DIRECT METAL LASER SINTERING OF TITANIUM ALLOYS FOR BIOMEDICAL APPLICATIONS

THYWILL CEPHAS KOMLA DZOGBEWU

Dissertation submitted in Fulfilment of the Requirement for the Degree

DOCTOR OF ENGINEERING IN MECHANICAL ENGINEERING

in the Department of Mechanical and Mechatronics Engineering

Faculty of Engineering and Information Technology

at the Central University of Technology, Free State

Promoter:	**Prof. Ihar Yadroitsau**
Co- Promoters:	**Prof. Pavel Krakhmalev**
	Dr. Ina Yadroitsava

October, 2017

BLOEMFONTEIN

DECLARATION

I, Thywill Cephas Komla Dzogbewu, student number , do hereby declare that this dissertation submitted to the Central University of Technology, Free State for the degree of Doctor of Engineering in Mechanical Engineering, is my own independent work, and complies with the code of Academic integrity, as well as other relevant policies, procedures, rules and regulations of the Central University of Technology, Free State; and has not been submitted previously to any institution by myself or any other person in fulfilment of the requirements for the attainment of any qualification.

Signature of student:  Date: 27/10/2017

ACKNOWLEDGEMENT

First of all, thanks be to the Almighty God for all His blessings bestowed on me.

I would like to express my deep-felt sincere gratitude to my supervisors, Prof. Ihar Yadroitsau (Igor Yadroitsev), Prof. Pavel Krakhmalev and Dr. Ina Yadroitsava for their outstanding effort, patient and excellent suggestions throughout this study. Dr. Ina has taught me many things in these past three years. Not only she has helped me to understand the principles that underpin this work, but also, she has been the first person to walk down to the labs to help whenever I needed. I felt highly honoured for the opportunity to work with Prof. Igor and Dr. Ina who are prominent figures in the world of Additive Manufacturing. They have certainly contributed to my growth as an individual and as a researcher, providing me with an outstanding example of professionalism and intelligence. I am forever indebted to you both! Thank you. I would also like to acknowledge the contributions of Prof. Pavel Krakhmalev for all the material analysis.

My gratitude goes to the staff of Mechanical Engineering Department and Centre for Rapid Prototype Manufacturing (CRPM) for their immeasurable contributions to my studies. They provided me with all the support and state-of-the-art laboratory facilities required for a doctoral study. To my colleagues and co-authors, I say thank you.

To all my innumerable comrades with whom I enjoyed my research and social life at CUT, thank you, you brought salt and light into my life.

Many thanks to my beloved uncles, Prof. D.Y Dzansi and Torgbe Dzogbewu (V): you two are rare personalities given to humanity. Many have excelled and achieved their dreams because of you. I am eternally grateful to my dearest parent and siblings for their evergreen love and support.

I would like to express my very special thanks to my lovely wife for her patience, prayers and sacrifice. I owe it all to you. You have brought untold joy into my life. I dedicate this book to you, Mrs. Melody Dzogbewu.

This work is based on the research supported by the South African Research Chairs Initiative of the Department of Science and Technology and National Research Foundation of South Africa (Grant №97994) and Collaborative Program in Additive Manufacturing (Contract №CSIR-NLC-CPAM-15-MOA-CUT-01).

ABSTRACT

Ongoing scientific progress shifts conventional methods to the much celebrated Additive Manufacturing (AM) due to its freedom of design, flexibility in feedstock and material optimization. It has shown that Direct Metal Laser sintering (DMLS), one of the AM technologies, is an attractive manufacturing route for the biomedical applications. Ti6Al4V is the most widely used titanium alloy for the implants. However, there still remain issues of relative low ductility of DMLS Ti6Al4V and infections after implantation which have triggered the current research into producing implants of high ductility with antibacterial properties by DMLS, while establishing a body of knowledge about the relationship between the laser-matter interaction, microstructure, and mechanical properties. The type of material used in biomedical applications depends on specific implant applications and different types of implant need different mechanical properties. The current study is designed to investigate DMLS lattice structures from traditional Ti alloy such as T6Al4V ELI and the possibility of producing novel alloys by *in-situ* alloying for DMLS process.

Learning from nature, it can be understood that cellular structures would be more preferable for biomedical implants than dense solid structures' since the architecture of bone tissues in the human body are not completely dense and solid. Cellular structures of different nodes and strut sizes were produced and mechanically investigated to mimic the anisotropic porous nature of bones. A finite element analysis (FEA) was conducted to determine the applicability of graded/gradient implant based on each patient requirement. From the FEA it was hypothesized that implant design with cellular structures with relative low Elastic modulus would bridge the Elastic modulus gradient between dense solid metallic implants and the porous bones. An advanced lightweight mandible model was proposed whereby a damaged mandible could be replaced with a graded material based on the functional requirements of the damaged part.

Mixing different elemental powders for *in-situ* alloying by DMLS would definitely increase the material pallet for AM. Understanding the effects of the parameters on DMLS process is paramount to gaining full control over density, microstructure and the mechanical properties of the DMLS parts. Only a careful combination of the process parameters would result in optimum process parameters for each type of powder.

A wide range of process parameters were investigated to gain in-depth knowledge into the interaction between the laser beam and the powder bed by *in-situ* alloying powders with vastly different melting points and similar particle size distribution (−45 µm). Due to difference in thermo-physical properties between the powders (Ti6Al4V, Cu, Mo, Ti), sintered materials were inhomogenous. Rescanning was employed but there was no significant change in the volume fraction of the unmelted Mo particles in the Ti15Mo alloy matrix. Due to the inherent high rate of heating and cooling simultaneously of the DMLS process, martensitic phase was found in the as-built Ti15Mo and Ti6Al4V–1at.%Cu samples. The martensitic properties reduce the ductility of the as-built samples significantly.

Optimum process parameters were determined for both molybdenum-bearing titanium alloy (85% Ti and 15% Mo) and copper-bearing titanium alloy (Ti6Al4V and 1at.%Cu). Successful manufacturing of non-porous samples was done. I*n-situ* alloying Ti6Al4V+1%Cu was successful and therefore there are promising ways to manufacture materials with embedded antibacterial properties. Incorporating copper into the bulk material by *in-situ* alloying would prevent the fall-off of antibacterial deposition coatings used in the past, since the material matrix (implant) would be antibacterial agent.

The mechanical properties investigations with mini-samples presented ductility values below what was recommended for biomedical materials. It was concluded that finer Mo particles have to be chosen for *in-situ* alloying Ti15Mo for producing biomedical objects. Future work have to be done with elaboration of heat treatment procedures for higher ductility for structural bearing implants in a single step by the DMLS process.

The results obtained developed new knowledge that is important for understanding the *in situ* alloying process during DMLS and new material production. The illustrated effects of process parameters on the properties of the synthesized material would be paramount for advanced implants with unique properties.

LIST OF PUBLICATIONS

1. **Dzogbewu T.C.**, 2017. Additive manufacturing of porous Ti-based alloys for biomedical applications – A Review, *Journal for New Generation Sciences*, 15 (1).

2. **Dzogbewu T.C.**, 2017. Evaluation of Ti15Mo alloy manufactured by DMLS from elemental powders, *Proceedings of the 18th International conference Rapid Product Development Association of South Africa*, 8-10 November 2017, Pretoria, South Africa.

3. **Dzogbewu T.C.**, Yadroitsev I., Krakhmalev P., Yadroitsava I. & du Plessis A., 2017. Optimal process parameters for *in-situ* alloyed Ti15Mo structures by Direct Metal Laser Sintering, *Proceedings of the 28th Annual International Solid Freeform Fabrication Symposium*, Austin Texas, August 7-9, 2017.

4. **Dzogbewu T.C.**, Monaheng L., Yadroitsava I., du Preez W.B. & I. Yadroitsev, 2016. Finite element analysis in design of DMLS mandible implants, "*Challenges for Technology Innovation: An Agenda for the Future". Proceedings of the International Conference on Sustainable Smart Manufacturing* (S2M 2016), October 20-22, 2016, Lisbon, Portugal. *Eds.*: F. M. da Silva, H. M. Bartolo, P. Bartolo, R. Almendra, F. Roseta, H. A. Almeida, A. C. Lemos, CRC Press, 458 p.

5. **Dzogbewu T. C.**, Monaheng L., Els J., van Zyl I., du Preez W. B., Yadroitsava I. & I. Yadroitsev, 2016. Evaluation of the compressive mechanical properties of cellular DMLS structures for biomedical applications, *Proceedings of the 17th International conference Rapid Product Development Association of South Africa*, 2-4 November 2016, Vaal University of Technology Vanderbijlpark, South Africa.

6. Kinnear A., **Dzogbewu T. C.,** Krakhmalev P., Yadroitsava I. & Yadroitsev I., 2017. Manufacturing, microstructure and mechanical properties of selective laser melted Ti6Al4V-*x*Cu. *Proceedings of the LiM– Lasers in Manufacturing, World of Photonics Congress*, 25 – 29 June, 2017, München, Germany.

7. Kinnear A., **Dzogbewu T. C.,** Yadroitsava I. & Yadroitsev I., 2016. *In-situ* alloying process of Ti6Al4V-*x*Cu structures by direct metal laser sintering, *Proceedings of the 17th International conference Rapid Product Development Association of South Africa*, 2-4 November 2016, Vaal University of Technology Vanderbijlpark, South Africa.

8. Kinnear A., **Dzogbewu T.C**., Yadroitsava I. & Yadroitsev I., 2015. Multimaterial powder delivering system for direct metal laser sintering, *Proceedings of the 16th International conference Rapid Product Development Association of South Africa*, 4-6 November 2015, Pretoria, South Africa.

TABLE OF CONTENTS

LIST OF FIGURES

LIST OF TABLES

CHAPTER 1: INTRODUCTION

1.1: Background

The progressive advancement of Additive Manufacturing (AM) technologies is a logical result of the digital and environmental revolutions when personalized, unique and material-saving manufacturing comes to the fore. Laser Powder Bed Fusion (LPBF), one of the prominent AM technology, is gradually gaining momentum in manufacturing medical objects. Different companies use various terms and have patents for LPBF equipment: ConceptLaser uses the term LaserCusing, Selective Laser Melting (SLM) is a registered trademark of SLM Solutions GmbH, Direct Metal Laser Sintering (DMLS) is a registered trademark of EOS GmbH. The LPBF technology is applied to build up objects layer-by-layer from a 3D CAD model instead of removing waste material in different steps as used by the conventional methods. The essential operation of the LPBF technique is scanning the laser beam over the surface of a thin powder layer deposited on a substrate. The forming process proceeds along the scanning direction of the laser beam where the metallic powder is melted layer-wise and solidified. It is eco-design topology optimization technology that allows very complex parts to be created monolithically. As opposed to the conventional methods of fabrications, LPBF techniques provide an almost unchallenged freedom of design. The high degree of freedom offered by LPBF technology of building complex geometries (*e.g.* back tapers, intricate cooling channels, customized porous structures and special lattices or hollow structures) that would otherwise be difficult or impossible to produce using conventional manufacturing processes makes it a preferable choice.

The biomechanical properties of products manufactured by DMLS[1] technology are significantly determined by the process parameters, nature of the materials used for the production, scanning strategy, geometry characteristics of the tracks and layers and the bonding strength between them. Parts produced by the DMLS process undergo a rapid cooling and solidification resulting in different microstructures and mechanical properties compared to those obtained by the conventional manufacturing methods.

[1] Since all samples for the present work were manufactured by EOSINT M280 system from EOS GmbH, the term "DMLS" has been used.

The Ti6Al4V alloy accounts for more than 50% of total titanium alloys usage. Its unique mechanical characteristics make it ideal for many high-performance engineering applications. It is mostly used in the aerospace, automotive and marine industries. Titanium-based alloys could basically be described as the backbone of the implant industry. Most importantly it is also a material of choice for the biomedical industry as a result of its outstanding biomechanical and chemical properties. Ti6Al4V alloys happen to be the most extensively used Ti-based alloy for biomedical application with laudable clinical success. Ti6Al4V grade 5 and grade 23 Ti6Al4V ELI (Extra Low Interstitial) alloys are similar, but grade 23 has lower levels of oxygen, nitrogen, carbon and iron elements. The low level of the interstitial elements enhances the ductility and increases fracture toughness of the Ti6Al4V alloy.

For replacing a critical damaged loadbearing structure such as the femur, the implant must be a good combination of low Elastic modulus and high ductility of which DMLS Ti6Al4V is not mechanically the most ideal biomaterial. The quest for a more suitable alternative alloy for manufacturing direct load bearing structural implants of high ductility has become increasingly important since the number of patients demanding implant are rapidly increasing due to the increase in the aging population.

The most serious complication in implantation surgery is bacterial infection at the interface between the implant and the bone. Materials such as silver, zinc and copper have shown antibacterial properties. The main advantage of using antibacterial materials is that it acts locally at the site of infection. Thus, production of Ti6Al4V-Cu-advanced implants by DMLS can reduce the risk of bacterial infection. The possibility of the DMLS technology to process multimaterials would permit production of parts with the required properties in strategic locations, such as copper-bearing titanium implants to control implant infections. The multimaterial- handling capacity of the DMLS process would enable the production of biometric objects of intricate shapes, delicate material variations, and internal configurations characterize implants close to the bone structure. Manufacturing implants with variable materials based on position-dependent requirements would definitely improve functionality and longevity of implants.

A thorough experimental investigation into the DMLS process parameters on specific selected Ti-based alloys would probably open the door of controlling manufacturing process of implants where tailored Elastic modulus, ductility and positional variation of material properties could be attained.

1.2: The Aim of the Studies

The study investigates and establishes optimum process parameters and strategy for DMLS manufacturing of advanced materials for biomedical applications. Cellular structures from Ti6Al4V alloy were investigated for biomedical applications. The suitability of using the DMLS process to in-situ alloy 15 wt.% of Mo with 85 wt.% of Ti and Ti6Al4V-1 at.% Cu for biomedical applications was explored. 3D objects were subsequently manufactured and mechanically examined for biomedical applications.

1.3: Thesis Statements

The mechanical properties of Ti-based alloys could be tailored more suitably for structural biomedical applications by adding β-stabilizing elements such as Mo. Incorporating antibacterial agent such as Cu into Ti-based alloy would enhance the antibacterial properties of the alloy. Cellular structures are known to mimic the anisotropic porous nature of bone, hence could easily be used as a biometric implant. The Elastic modulus of cellular structures could also be tuned over a wide range by varying the lattice properties.

1.4: The Scope of the Studies

The studies generally comprised of three main sections of theoretical and experimental investigations:

- Numerical simulation deformable behaviour of different Ti materials used for implants and comparison with the jaw bone deformations and stresses under loading.
- Producing cellular structures with DMLS α/β Ti6AL4V (ELI) alloy and bulk binary *in-situ* alloyed DMLS Ti15Mo material, investigating their mechanical properties with the aim of producing implants with Elastic modulus and low ductility similar to the bone.
- *In-situ* alloying Ti6Al4V-1%Cu for producing self-antibacterial implants.

The study is generally limited to the domain of investigating the possibility of using the DMLS technology to *in-situ* alloy titanium base alloys for biomedical applications. DMLS process

parameters would be examined and the most suitable for each alloy would be determined for implant manufacturing. Since part of the studies aim to produce implants with low Elastic modulus the unique characteristics of cellular structures of being structural bearing material as demonstrated by nature would be explored for biomedical applications.

1.5: Research Methodology

The research methodology would encompass the research design and all activities that would lead to successful completion of the studies. The research design would serve as a roadmap to the studies; it would be the cardinal navigator which would sequentially direct the various tasks to be performed.

The following research procedures were generally followed in executing the various tasks:

- Literature review and state of the art in the research fields
- Numerical simulation implants
- Studying the DMLS process and corresponding equipment
- Powder characterization
- Formation of single tracks over a wide range of processing parameters
- Top view and cross-sectional examination of the tracks and selection of optimum processing parameters
- Formation of single layers at different hatch distances at optimum scanning speeds and laser powers
- Analysis of the single layers by optical and scanning electron microscopy (top view and cross-section) was done for optimal process parameters
- Production of 3D objects for microstructural and mechanical examination

1.6: Research Objectives

The principal objective of this research work is to produce implants from titanium alloys with excellent mechanical and antibacterial properties by DMLS technology, by establishing a firm relationship between the process parameters of laser scanning, microstructure and properties of

DMLS samples from Ti alloys for biomedical applications. It will investigate the following major issues confronting the implant industry and find the appropriate solutions:

- To identify Ti alloys for the fabrication of the various implants by DMLS
- To simulate suitability of using cellular structures mechanical properties for implants and to compare numerical simulation with experimental data
- To produce by DMLS non-porous and cellular structured samples
- To study microstructure and mechanical properties of DMLS samples
- To suggest ways for the development of the next generational implants with add-value functionality by DMLS

1.8: Expected Contribution

DMLS is a relatively new technology and just as alloys were carefully customized for casting, forging, *etc*., technologies in the past, it is also of prime importance to purposefully formulate alloys for additive manufacturing. If *in-situ* alloying by DMLS could be used to process powder mixtures of different materials it would certainly broaden the material database of additive manufacturing. Successful realization of using the DMLS process for *in-situ* alloying and not relying on pre-alloys would give the material scientist a great freedom of mixing different elemental powders for specific applications. Such an attempt could possibly lead to automation of the DMLS process for each specific metallic powder (alloys).

Producing implants with low Elastic modulus and high ductility with antibacterial properties would greatly reduce implants' failures associated with the stress shielding effect and infections. Manufacturing biomimetic cellular structures which could serve the analogous function of epiphysis and metaphysis found in the human limbs would aid the homogenous load transferred stress stimulation of the bone which would enhance osseointegration. Implants with biomimetic characteristics would reduce the time of implantation and hospital stay, economic cost, and physical pain associated with implant failure.

This study would serve as a foundation and point of reference for many future works because the results obtained developed new important knowledge for understanding the *in situ* alloying process during DMLS and new material production.

CHAPTER 2: LITERATURE REVIEW

2.1: Titanium Alloys as Biomedical Materials

2.1.1: Introduction

Titanium found its way into the surgery industry in the 1950s, but prior to that, it was first used in the dentistry industry a decade earlier. It curtly has the recognition as a preferable metal for biomedical applications. Low density, high specific strength, relatively low Elastic modulus as the mechanical properties that put Ti alloys in the lead as a biomaterial (Nasab *et al.*, 2010). Titanium and its alloys are virtually used at every part of the human body as prosthetics and internal fixation (Figure 2.1.1). It is also used for manufacturing most medical instruments (Josefson, 2001; Niinomi, 2003; International Titanium Association, 2015).

Figure 2.1.1: Use of Ti-alloys at different parts of the human body (Hiromoto, 2008)**.**

Ti and its alloys are found in every facet of the orthopaedic and dental industry. They are used for bone conduction, hearing aids, false eye implants, spinal fusion cages, pacemakers, toe, shoulder, elbow, hip, knee implants and for neurosurgery purposes, *etc.* (Josefson, 2001; Elias *et al.*, 2008). Ti-based alloys are considered as a prime metal for biomedical purposes due to their biocompatibility, easy surface modifications, and bioactive surface. These characteristics can be

optimized to create suitable biological interactions between the implant and the host tissues (Leyens & Peters, 2003). Titanium and its alloys have the capacity to withstand the effect of the body fluids, stay inert in the human body, compatible with bone growth and stay strong and flexible during use (Sakamoto *et al.,* 2014). The unique biocompatibility properties of Ti and its alloys to be resistant to the effects of the body environments under stress fatigue and in crevice conditions is due to the formation of thin oxide film layer that forms spontaneously in the presence of oxygen. The thin protective layer cannot be transported chemically; it is also insoluble, highly adherent and inhibits the effect of body fluids on the implant (Semiatin *et al.,* 1997; Raabe *et al.,* 2007; Raines *et al.,* 2010). Raines *et al.* (2010) studied surface-dependent production growth factors by MG63 human osteoblast-like cells and normal human osteoblasts cultured on Ti surfaces with different roughness. It was shown that Ti substrate features controlled osseointegration by enhancing angiogenesis at the material/tissue interface. The above-mentioned surface attribute can be highly optimized to produce an ideal cellular response.

Ti- based alloys can be classified as α, α+β and β titanium alloys based on the type of alloying element (β or α stabilizer) and composition. The β-alloys offer an attractive alternative to the α-alloys and α+β alloys for biomedical applications due to their inherent ductility and superior fatigue properties. The β-alloys have a wide and unique range of strength-to-weight ratios, increased heat treatability and deep hardening potentials (Weiss & Semiatin, 1998). β type Ti alloys have *bcc* structure that results in a less dense bonding between the atoms in the lattice structure. Since it has the non-closed packed structure, its modulus of Elasticity is low as moduli of materials depend on the bonding force between atoms and the crystal structure (Padmavathi, 2011; Askeland & Wright, 2013).

In general, the Elastic modulus ranges from 50-80 GPa for β-Ti alloys and 80-130 GPa for α and α-β Ti alloys (Figure 2.1.2) (Niinomi *et al.,* 2016). Ti-based alloys are the preferable choice for biomedical applications. However, for them to remain in the frontier as superior biomaterials depends absolutely on the reduction of their Elastic modulus comparable to that of bone. Mechanical properties of the bones are shown in Table 2.1.1.

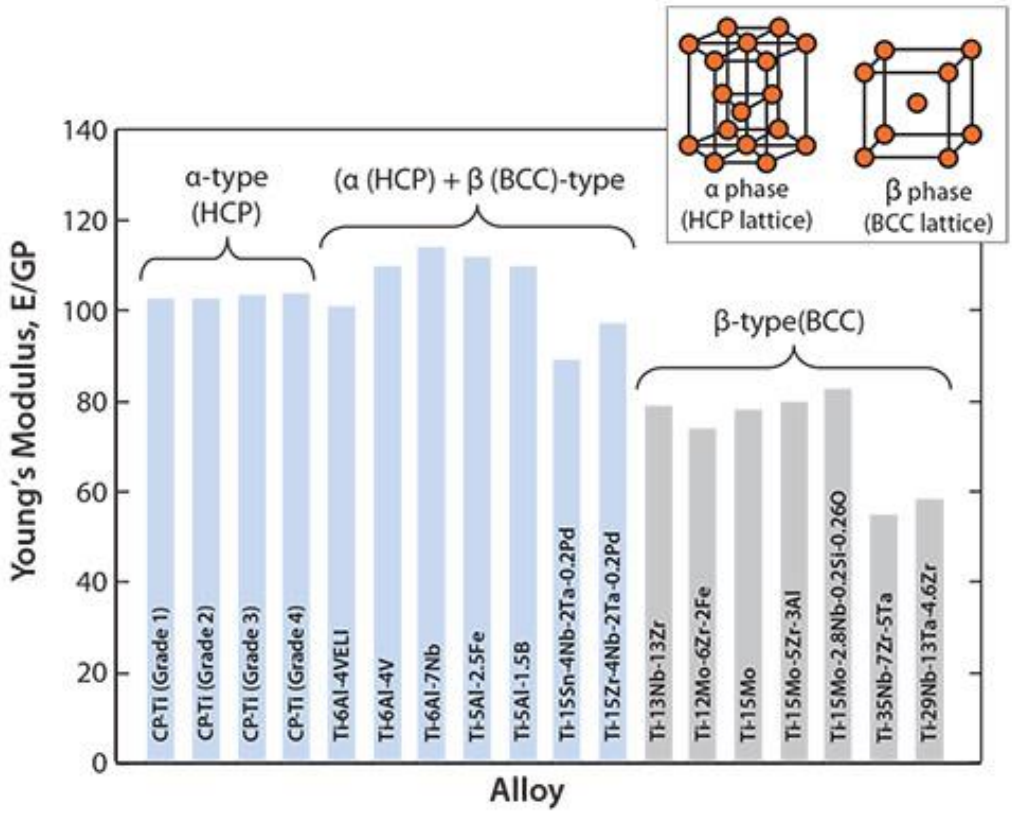

Figure 2.1.2: Comparison of Elastic modulus of Ti-based alloys (Niinomi et al., 2016).

Table 2.1.1: Mechanical properties of the human bones*

Mechanical properties	Value	Comments
Human Compact Bone, Haversian System		
Tensile strength at break	49.0 MPa	Normal to long axis
	148 MPa	Parallel to long axis
Tensile strength, ultimate	53.0 MPa	Transverse, Femur Cortical Bone
	135 MPa	Longitudinal, Femur Cortical Bone
Elongation at break	0.70 %	Normal to long axis; in tension
	2.6 %	Parallel to long axis; in compression
	2.8 %	Normal to long axis; in compression
	3.1 %	Parallel to long axis; in tension
Elongation at yield	0.40 %	Normal to long axis; in tension
	0.70 %	Parallel to long axis; in tension
	1.0 %	Parallel to long axis; in compression
	1.1 %	Normal to long axis; in compression
Modulus of elasticity	6.90 GPa	Radial, from ultrasonic testing
	8.50 GPa	Tangential, from ultrasonic testing

Mechanical properties	Value	Comments
	13.0 GPa	Radial, from ultrasonic testing
	14.4 GPa	Tangential, from ultrasonic testing
	17.0 GPa	Longitudinal, from mechanical testing
	18.4 GPa	Longitudinal, from ultrasound testing
	21.5 GPa	Longitudinal, from ultrasound testing
	27.4 GPa	Dry; Longitudinal, from ultrasound testing
Compressive strength	131 MPa	Transverse, Femur Cortical Bone
	133 MPa	Normal to long axis
	193 MPa	Parallel to long axis
	205 MPa	Longitudinal, Femur Cortical Bone
Poisson's ratio	0.31	Longitudinal-Tangential, from ultrasonic testing
	0.32	Longitudinal-Radial, from mechanical testing
	0.33	Longitudinal-Tangential, from ultrasonic testing
	0.40	Longitudinal-Radial, from mechanical testing
	0.42	Tangential-Radial, from ultrasonic testing
	0.62	Tangential-Radial, from ultrasonic testing
Shear modulus	2.40 GPa	Radial-Tangential, from ultrasonic testing
	3.60 GPa	Radial-Longitudinal, from ultrasonic testing
	4.70 GPa	Radial-Tangential, from ultrasonic testing
	4.90 GPa	Tangential-Longitudinal, from ultrasonic testing
	5.80 GPa	Radial-Longitudinal, from ultrasonic testing
	6.60 GPa	Tangential-Longitudinal, from ultrasonic testing
Shear strength	65.0 MPa	Femur Cortical Bone
Femur bone		
Modulus of elasticity	11.7 GPa	in compression, tangential direction
	11.7 GPa	in compression, radial direction
	12.0 GPa	in tension, radial direction
	13.4 GPa	in tension, tangential direction
	18.2 GPa	in compression, longitudinal direction
	20.0 GPa	in tension, longitudinal direction
Poisson's ratio	0.22	in tension radial-longitudinal
	0.24	in tension, tangential-longitudinal
	0.38	in tension, radial-tangential
	0.63	in compression, radial-tangential
Shear modulus	4.50 GPa	in tension, radial-tangential
	5.60 GPa	in tension, radial-longitudinal
	6.20 GPa	in tension, tangential
Cortical bone		
Tensile strength, ultimate	52.0 MPa	Tangential
	133 MPa	Longitudinal
Tensile strength, yield	114 MPa	Longitudinal
	0.70 %	Tangential

Mechanical properties	Value	Comments
Elongation at Break	3.1 %	Longitudinal
Modulus of elasticity	11- 20 GPa	
Compressive strength	67.0 MPa	Shear
	130 MPa	Tangential
	205 MPa	Longitudinal

* (MatWeb, 2015)

2.1.2: α/β Titanium Alloys

2.1.2.1: Conventional Ti6Al4V Alloy

The α+β Ti6Al4V alloy is the most extensively used titanium alloy and it is described as the 'backbone' of the titanium industry. It accounts for >50% of total Titanium usage due to its high strength, light weight, formability, machinability and corrosion resistance (Donachie, 2000; Beal *et al.,* 2006).

Since metallic materials are highly microstructurally sensitive, examination of Ti6Al4V microstructure could reveal adequate information about its mechanical properties. Understanding the relationship between microstructure and properties of metallic materials plays an important role in manufacturing and production controls, inspection and failure analysis and the development of novel materials (Petzow, 1999; Voort, 2003). Ti and its alloys can be manipulated (heat treated) – below or above the β-transus temperature (Figure 2.1.3). The β transus temperature is the minimum temperature at which 100% β phase can exist or the minimum temperature above which equilibrium alpha phase does not exist (Donachie, 2000; Qazi *et al.,* 2001)**.** It is very critical to understand the cooling mechanisms that enable the metal to transform from one phase to another in α/β Ti alloys.

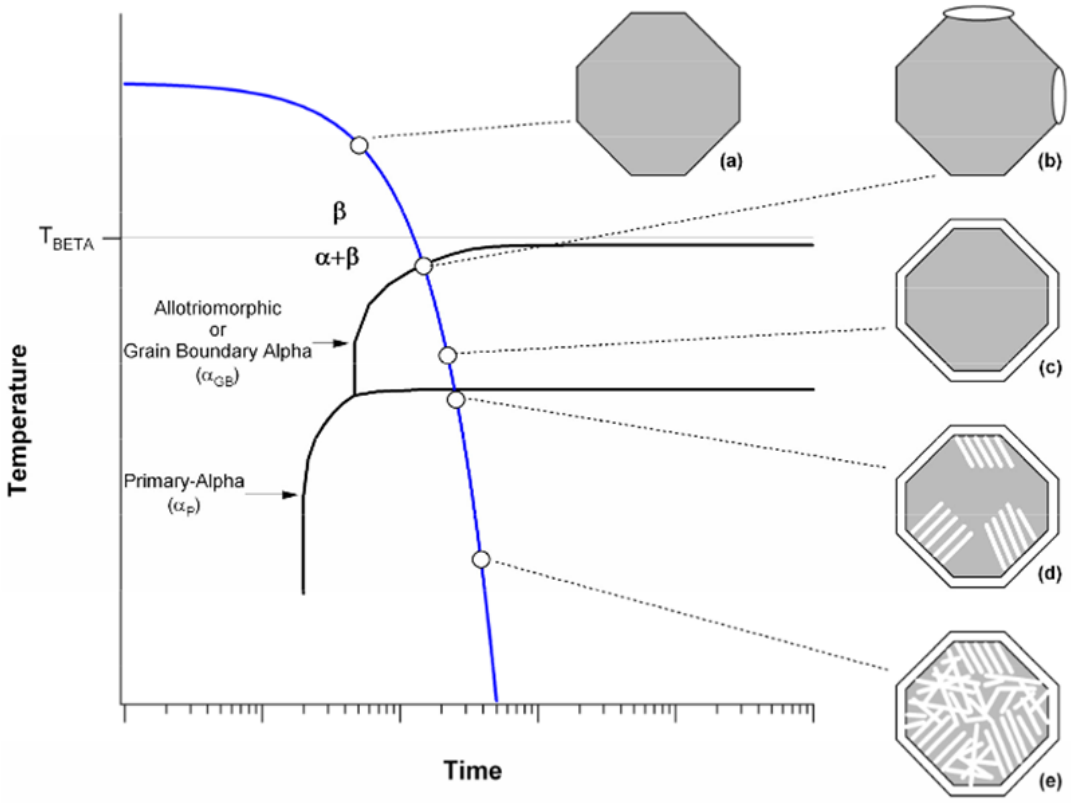

Figure 2.1.3: Schematic illustration of nucleation and growth of α to form an equilibrium α/β microstructure when cooling slowly from above the β-transus temperature (Kelly, 2004).

In Figure 2.1.3, case (a) represents a single β grain that exists above the β-transus temperature; (b) is the nucleation and growth of α at the grain-boundary of β at temperatures just beneath the β-transus, (c) is the completion of α grain-boundary; (d) represents the growth of a lamellae colony into the interior of the parent β, and (e) shows the nucleation and growth of lamellae (basket weave) in the interior of the parent β grain as cooling continues. Understanding the transformation behaviour of Ti-based alloys during cooling is the key to manipulating its microstructure. By applying the appropriate thermo-mechanical processing strategies, the microstructure can be highly manipulated which would result in varying mechanical properties that can be tailored for biomedical applications (Donachie, 2000). When α+β Ti-based alloy is heated above the β transus temperature, it would result in β phase (*bcc* structure) (Figure 2.1.3a). Upon slow cooling below the β-transus temperature α phase would begin to nucleate and grow at the grain boundary of β

(Figure 2.1.3b-c). Then α grows towards the interior of the β grains forming a colony called "α-colony" (Figure 2.1.3d-e).

Solidification occurs over a wide range of temperatures as the liquid transforms from the solid solution body centred cubic β phase (*bcc*) to the solid hexagonal closed packed α phase (*hcp*). The thermal conditions during the solidification process and the growth characteristics of the Ti alloy in conjunction with the nucleation rate determine the grain size, morphology and crystallographic texture of the solid. The microstructural transformation from β to α extensively depends on the cooling rate from the β-transus temperature. Heat treatment can alter the distribution, size and morphology of α phase but has less effect on the prior β grains. The geometrical arrangement of the two-phases **(**α and β), the crystallographic texture and the processing routes plays a vital role in determining the mechanical properties of the material (Kobryn & Semiatin, 2001; Babu, 2008). There exists also a thermo-mechanical process for developing different types of microstructures hence different mechanical properties (Figure 2.1.4).

Hom

Figure 2.1.4: Processing route for manipulating microstructure of Ti-based alloys (Lütjering, 1998)**.**

Bimodal microstructure (Figure 2.1.5) consisting of primary equiaxed grains in lamellar transformed β could be formed by homogenizing the Ti6Al4V alloy sample in stage I (Figure 2.1.4) and cool it down to form lamellar microstructure (Figure 2.1.36a-b). The lamellar microstructure is then deformed heavily in step II below the β-transus to provide sufficient dislocation density to trigger complete nucleation and recrystallization in the subsequent step III.

The sample is systematically cooled and then aged in step IV. The rate of cooling in steps III and IV would determine the morphology of the bimodal microstructure.

At a lower temperature of deformation, a high volume fraction of equiaxed α phase (Figure 2.1.5b) would be formed and at a higher deformation temperature, a high volume fraction of transformed β phase would be produced. As the size and volume fraction of the equiaxed grains increase the volume fraction and the size of transformed β grains decreases. The recrystallization temperature in step III (Figure 2.1.4) determines the volume fraction of the primary alpha while the cooling rate influences the size of the equiaxed grain size.

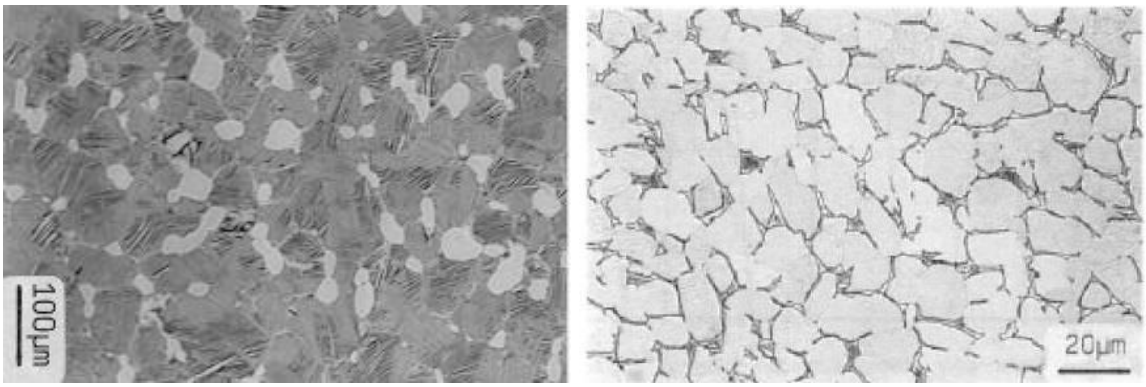

(a) (b)

Figure 2.1.5: Bimodal microstructure (a) and equiaxed microstructure (b) (Lütjering, 1998; Gammon *et al.*, 2004).

The bimodal microstructure is preferred to equiaxed or lamellar microstructure, due to the effective short slip length obtained by breaking the long continuous alpha plates at the grain boundaries of β through the deformation process in stage III. The resultant microstructure is associated with a high yield stress and resistance to crack propagation (Lütjering, 1998). In Ti6Al4V alloy, based on the degree of solubility, partitioning elements can partition within α and β phases during the formation of equiaxed primary α grains in stage III (Figure 2.1.4). These partitioning elements can cause micro-segregation and brittle precipitates such as Ti_3Al that can generally reduce the yield strength of the alloy as well as a decrease in high-cycle fatigue resistance. The adverse effects of the partitioning of the elements are more pronounced at low temperature than high-temperature regions (Nalla *et al*., 2002).

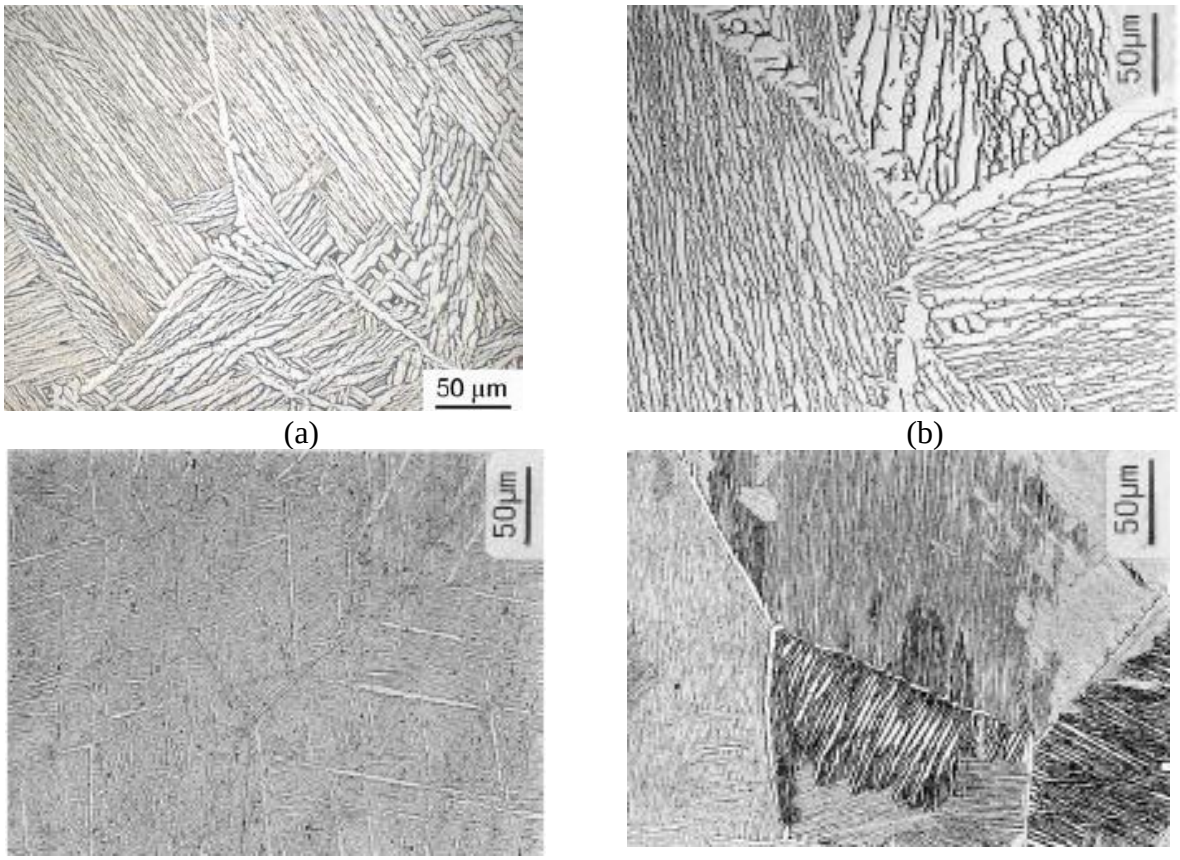

(a) (b)

(c) (d)

Figure 2.1.6: Ti6Al4V microstructure, cooled from 1050°C to 25°C and stress relieved at 700°C for 2 h (a) Ti alloy microstructures homogenized above the β transus and cool at the rate of 1°C/min (b) 100°C/min (c) and 8000 °C/min (d) (Lütjering, 1998; Benedetti & Fontanari, 2004)**.**

Widmanstätten microstructure (Figure 2.1.6d) is formed as a result of a new group of α lamellar nucleating and growing perpendicular from the boundaries of the already formed parallel α lamellar. The Widmanstätten microstructure is also referred to as basket weave. The new α colonies do not only nucleate on β-phase boundaries but also on boundaries of other α colonies, growing perpendicularly to the existing parallel α lamellae, hence forming a woven like stricture (basket weave). This type of microstructure has preferable tensile mechanical properties than the lamellar microstructure because of the perpendicular lamellar forming in-between the parallel lamellar which provide additional resistance to dislocation movement (Ahmed & Rack, 1998; Sieniawski *et al.,* 2013). At a very high cooling rate (8000°C/min) the microstructure is refined (martensitic microstructure) (Figure 2.1.6c) leading to a decrease in α colony size and lath thickness which would provoke a decrease in slip length (Figure 2.1.7).

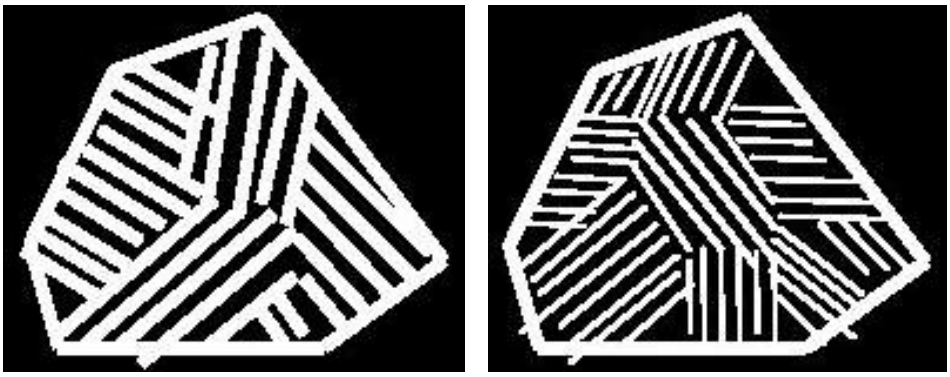

Figure 2.1.7: Schematic representation of decrease in lath thickness as cooling rate increases (Gaspar, 2012).

The major microstructural variables that determine the mechanical properties of lamellar microstructures are: β-grain size, size of α lamellar colony, thickness of the α lamellar and the morphology of the interlamellar interface (Malinov *et al.,* 2001; Sieniawski *et al.,* 2013) which are depicted in Figure 2.1.8.

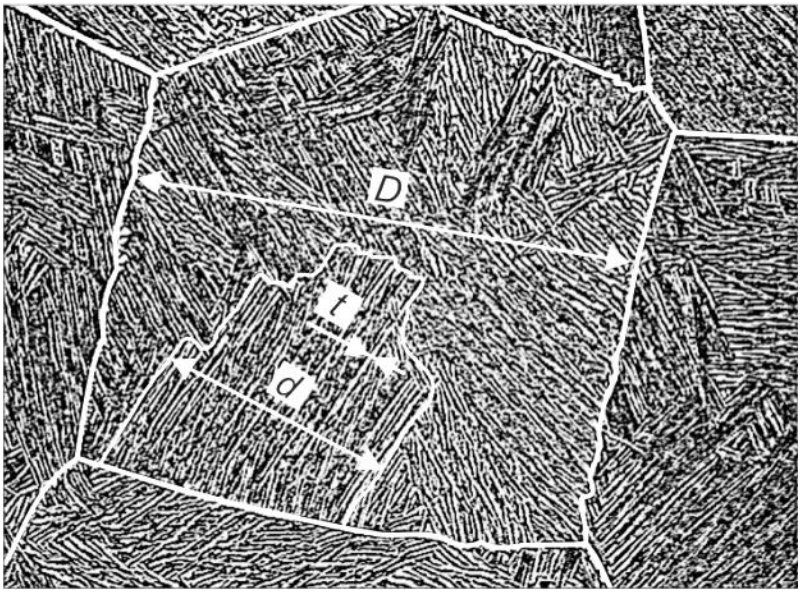

Figure 2.1.8: Mechanical property determinant of lamellar microstructure; *D* – prior β-grain size, *d* – size of the colony of parallel α-lamellae, *t* – thickness of α-lamellae (Sieniawski *et al.,* 2013).

As cooling rate increases, the slip length would decrease due to reduction in grain size, which would lead to higher yield stress (Figure 2.1.9a), crack nucleation resistance high cycle factige (HCF) strength, micro crack propagation resistance low cycle fatigue (LCF) strength as opposed to the lamellar microstructure which has the advantage of high toughness and macro-crack propagation resistance but weak in tensile properties (Vrancken *et al.*, 2012; Sieniawski *et al.*, 2013).

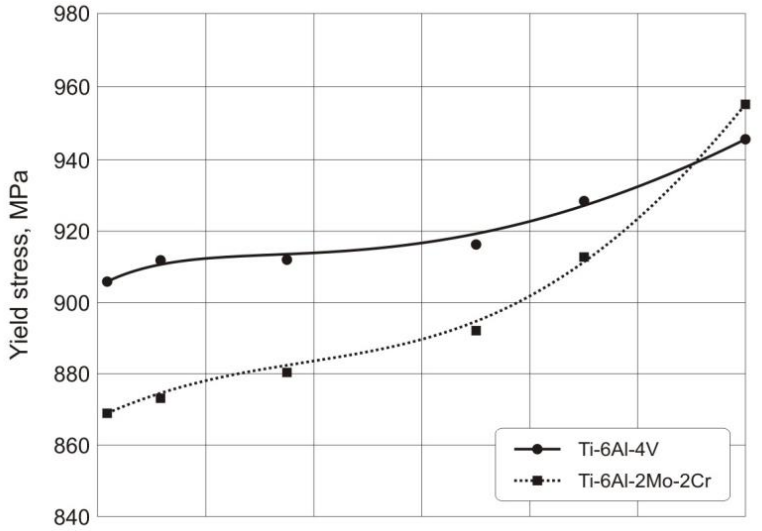

(a)

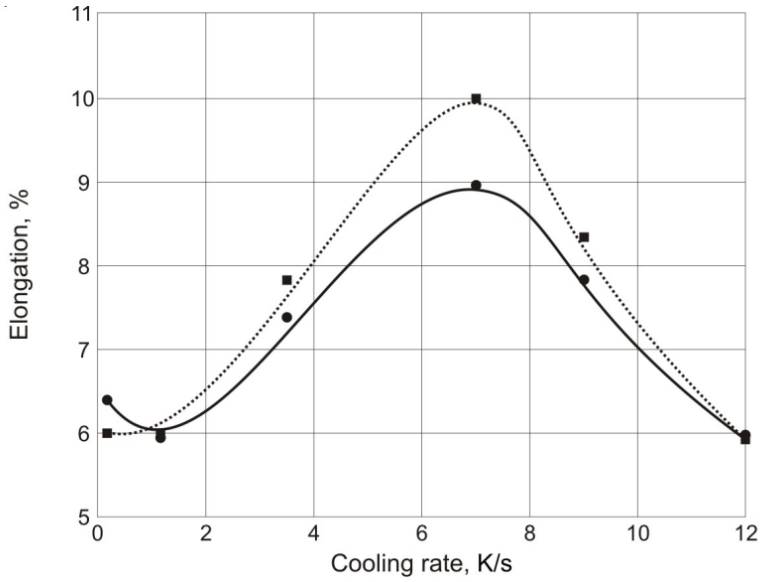

(b)

Figure 2.1.9: Yield stress (a) and tensile elongation (b) dependence on the cooling rate from β-phase for Ti6Al–4V and Ti-6Al-2Mo-2Cr alloys (Sieniawski *et al.*, 2013)**.**

At extremely fast cooling rate, the α colonies would reduce to single martensitic plate (Lütjering, 1999). For such samples, the ductility increases initially with increasing cooling rate and at maximum it declines drastically at high cooling rates (Figure 2.1.9b). Because at the maximum point of ductility the fracture mechanism changes from ductile trans-crystalline dimple type of fracture mode to ductile inter-crystalline dimple type of fracture mode along the continuous α-layers at β grain boundaries (Andres *et al.*, 1993).

Sieniawski *et al.* (2013) noted that the size of the prior β grains and the rate of cooling from the β-phase are the major determining factors of mechanical properties of lamellar microstructure, since the size of the prior β grain determines the size of the α colony which other variables depend on. As pointed out earlier, varied microstructure of Ti6Al4V could be produced based on each type of thermo-process as depicted in Figures 2.1.10–2.1.11. The various cooling rates (water quenched, air cooled and furnace cooled) lead to different mechanical properties as presented in Table 2.1.3. The tensile test results reveal that furnace cooled samples demonstrate the least response to the solution treatment process, followed by the air cooled samples. The water quenched samples register the most significant change in mechanical properties after the annealing process. It was observed that the water quench samples from the beta phase were poor in ductility which could be overcome by solution treating the samples at a relatively higher temperature in the alpha-beta field. Donachie (2000) also indicated that solution heat treatment of Ti6Al4V at varied temperatures would result in different microstructures which would definitely lead to varied mechanical properties (Figure 2.1.11). ASTM standards for surgical implant applications (ASTM F136-13, F1108-14 and F1472) require Ti6Al4V Ultimate tensile strength ≥ 825 MPa, Yield strength ≥758 MPa, elongation and reduction of area ≥8% and ≥14% correspondingly (Table 2.1.2)

Table 2.1.2: Recommended ASTM mechanical properties of Ti6Al4V for biomedical applications (ASTM F136-13, F1108-14 and F1472)

	UTS, MPa	YS (0.2% offset), MPa	Elongation in 4D, %	Reduction of Area, %
Cast (ASTM F1108)	860	758	8	14
Wrought annealed (ASTM F1472)	930	860	10	25
Ti6Al4V ELI wrought annealed (ASTM F136)	825	760	8	15

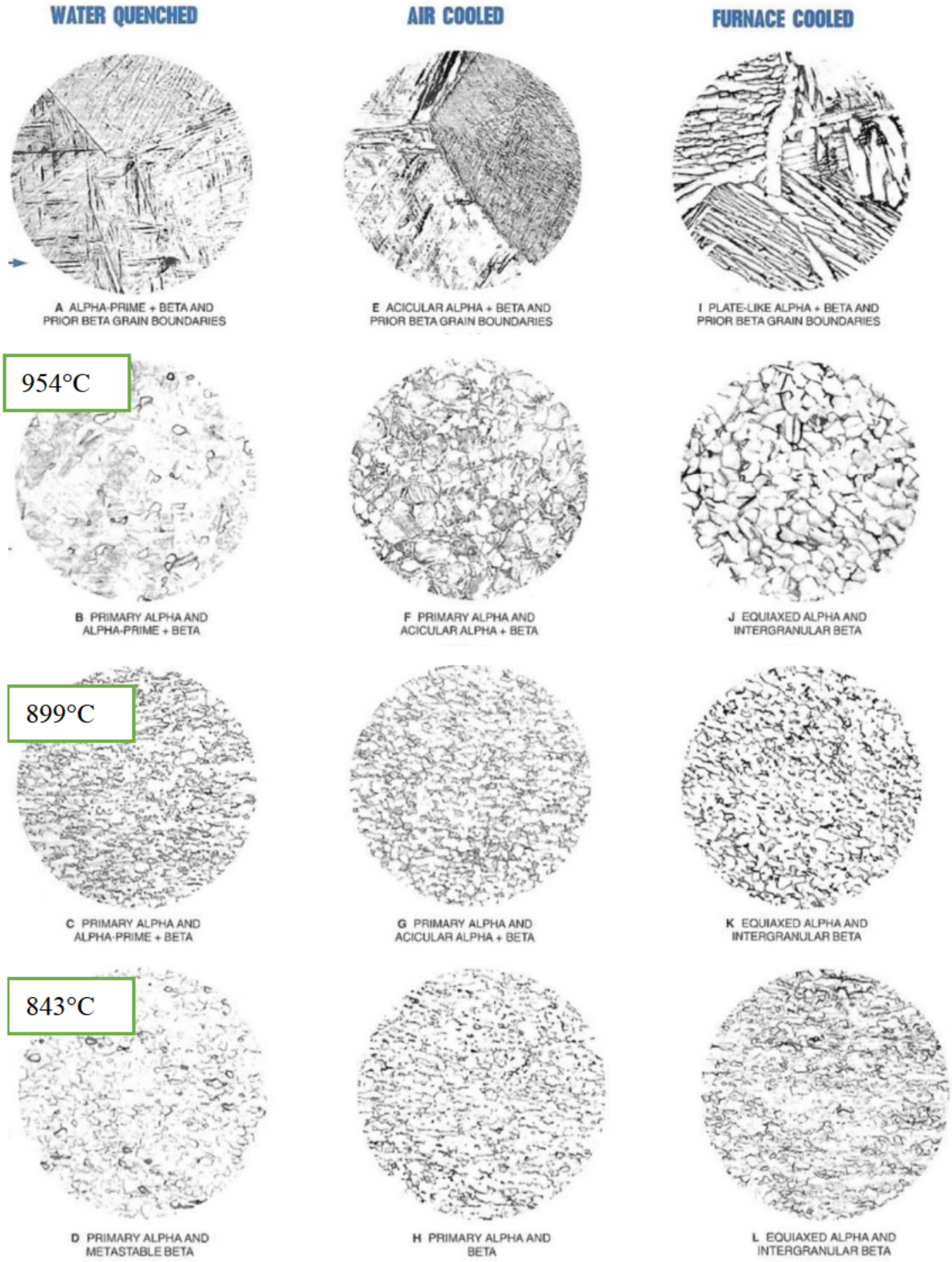

Figure 2.1.10: RMI Ti6Al4V 5/8" dia. bar microstructures resulting from various cooling rates from several temperatures (RMI Titanium Company, 2015).

Table 2.1.3: Mechanical properties of Ti6Al4V 5/8"·dia. bar following various heat treatments (RMI Titanium Company, 2015)

Type	Temperature,°C / Treatment	UTS, MPa	0.2% YS, MPa	Elongation, %	RA, %
A	1066/WQ	1108	953	7.7	19.2
	After aging	1170	1057	8.5	19.2
B	954/WQ	1119	953	17.0	60:2
	After aging	1183	1069	16.5	56.4
C	899/WQ	1117	924	15.2	53.9
	After aging	1117	1013	15.3	47.5
D	843/WQ	1009	772	20.0	54.7
	After aging	1077	977	16.5	48.8
E	1066/AC	1060	945	7.0	10.3
	After aging	1060	940	9.8	16.0
F	954/AC	995	846	17.8	54.1
	After aging	1020	896	16.1	45.7
G	899/AC	1002	869	17.5	54.7
	After aging	1029	938	17.3	50.2
H	843/AC	1020	878	17.8	477
	After aging	1034	931	16.8	46.9
I	1066/FC	1041	938	10.5	15.6
	After aging	1011	938	9.5	15.4
J	954/FC	940	836	18.8	46.0
	After aging	967	883	18.2	49.1
K	899/FC	963	855	16.5	43.3
	After aging	963	876	16.8	48.3
L	843/FC	997	924	17.3	48.9
	After aging	1062	954	17.0	49.6

Temperature	Water quenched	Air cooled	Furnace cooled
1065 C			
955 C			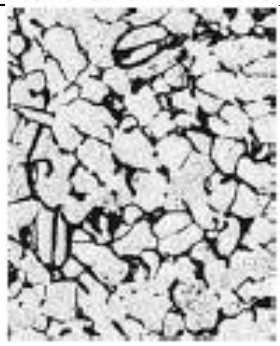
900 C		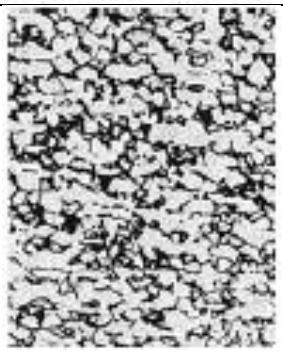	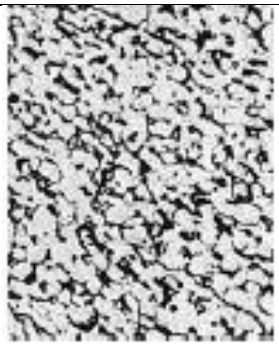
845 C	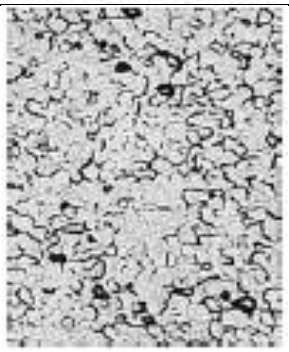	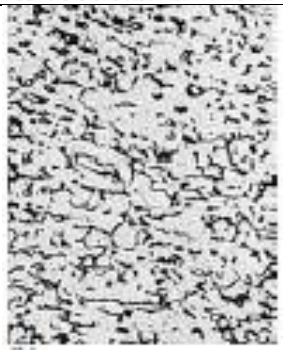	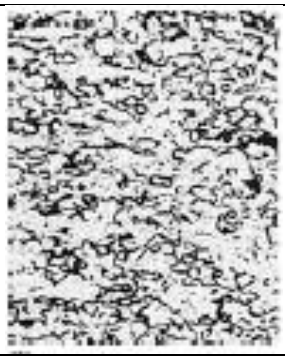

Figure 2.1.11: Ti6Al4V microstructures as a function of solution temperature and cooling rate (Donachie, 2000).

2.1.2.2: DMLS Ti6Al4V

2.1.2.2.2.1: Influence of Process Parameters and Strategies on Density, Microstructure and Mechanical Properties

Properties of DMLS objects depend greatly on laser power, scanning speed, scanning spacing (hatch distance), building strategy, powder layer thickness and powder properties. Song *et al.* (2012) investigated the effect of laser power and scanning speed on the mechanical properties and microstructure of Ti6Al4V samples manufactured by DMLS (Table 2.1.4).

Table 2.1.4: Selected processing windows (Song *et al.*, 2012)

Selected processing windows	Zone I	Zone II	Zone III
Laser power	120 W	110 W	110 W
Scanning speed	0.2 m/s	0.4 m/s	1.2 m/s

Sample manufactured with the parameters in the zone I reveal that the high laser energy input with high laser power and low scanning speed was able to melt the Ti6Al4V powder completely (Figure 2.1.12a). Complete continuous single track melting was obtained by using the second processing window (Figure 2.1.12b) and the last processing windows produce incomplete melting of the Ti6Al4V powder (Figure 2.1.12c). Surfaces of the samples manufactured with zone I parameters were split with many cracks, despite the relatively denser surface. The zone II samples have smooth continuous dense melted surfaces, which indicate a perfect metallurgical bonding of the single tracks. The zone III samples have balling surfaces (Figure 2.1.12c) as a result of melting instability, insufficient energy input and high scan speed that reduces the dwelling time of the laser spot. The parts manufactured by the optimum parameters (zone II parameters) have a density of 4.13 g/cm^3 which is comparable to the density (4.30 g/cm^3) of bulk Ti6Al4V alloy.

Scanning speed has been identified by several authors as one of the major determining factors of mechanical properties and microstructure of DMLS manufactured parts (Simchi & Asgharzadeh, 2004; Yadroitsev *et al.*, 2007; Li *et al.*, 2010; Mani *et al.*, 2015). Thijs *et al.* (2010) performed an initial experiment to determine optimum process parameters of manufacturing DMLS parts (Table 2.1.5.). After identifying the optimum process parameters, it was decided to vary the scanning speed from 0.05 to 0.2 m/s in order to verify the effect of the scanning speed on the

microstructure and mechanical properties of DMLS parts. The scanning speeds of 0.1 and 0.2 m/s demonstrate more control over the regularity of the scanning tracks. At a lower scanning speed of 0.05 m/s the width of the scan tracks varied considerably.

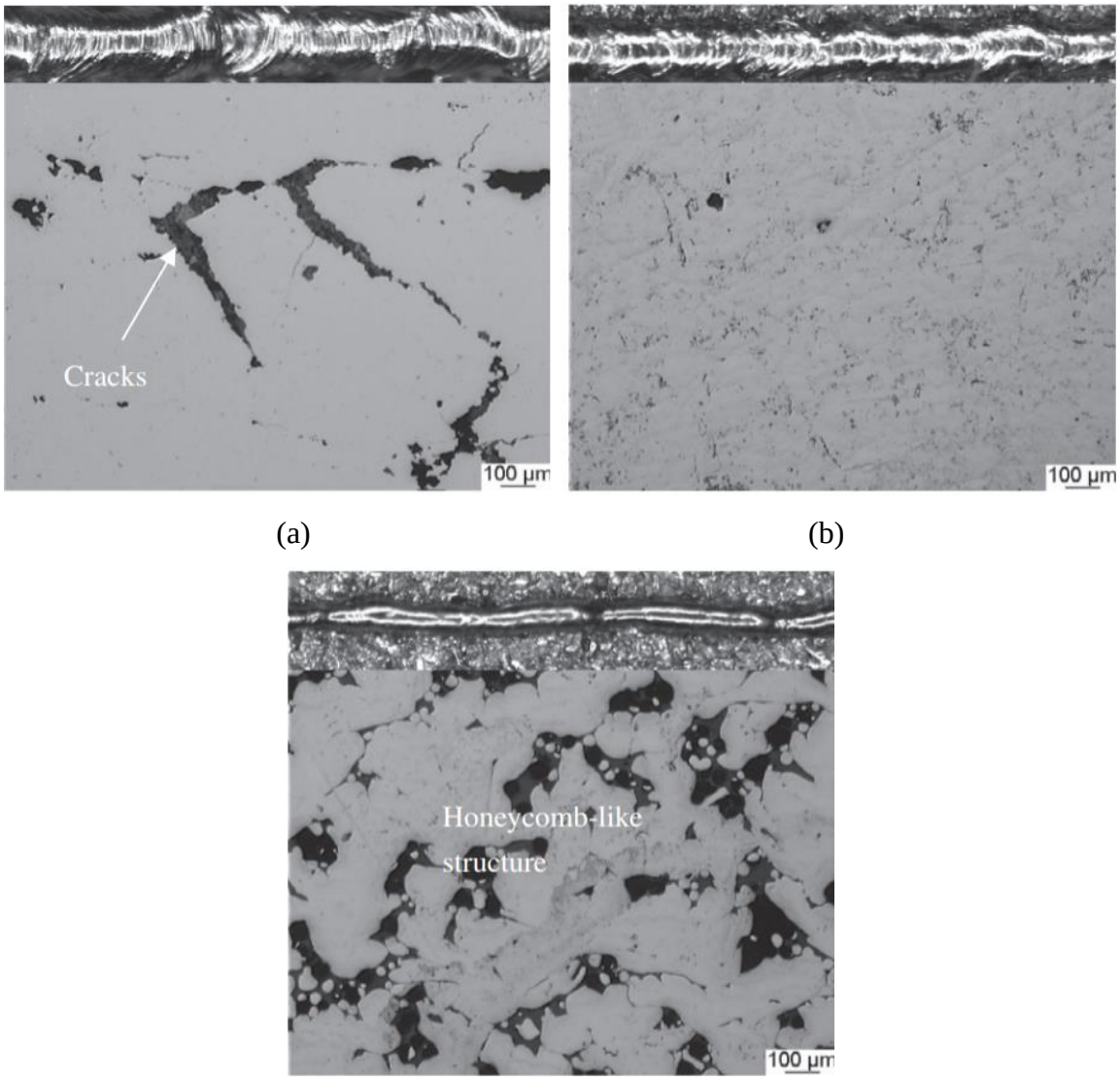

Figure 2.1.12: OM micrographs of single tracks (top) and cross-sectional Ti6Al4V parts (bottom) produced by different processing parameters: (a) 120 W, 0.2 m/s, (b) 110 W, 0.4 m/s and (c) 110 W, 1.2 m/s (Song *et al.*, 2012).

Table 2.1.5: Optimum processing parameters with varied scanning speed (Thijs *et al.*, 2010)

Scanning Variable	Sample A	Sample B	Sample C
Scanning speed	0.2 m/s	0.1 m/s	0.05 m/s
Hatch distance	75 µm	75 µm	75 µm
Laser power	42 W	42 W	42 W
Powder layer thickness	30 µm	30 µm	30 µm

Thijs *et al.* (2010) also investigated the effect of hatch distance on the microstructure and mechanical properties of DMLS manufactured parts with a laser spot diameter of 52 µm. Keeping all other parameters constant, they varied the hatch distance (Table 2.1.6) for three different sets (samples A-C) of Ti6Al4V alloy manufactured by DMLS method. Hatch spacing is the spacing between two consecutive scan lines (Figure 2.1.13).

Table 2.1.6: Processing parameters with different hatch spacing (Thijs *et al.*, 2010)

Operating parameters	Sample A	Sample B	Sample C
Hatch distance	50 µm	75 µm	100 µm
Laser power	42 W	42 W	42 W
Scanning speed	0.2 m/s	0.2 m/s	0.2 m/s
Powder layer thickness	30 µm	30 µm	30 µm

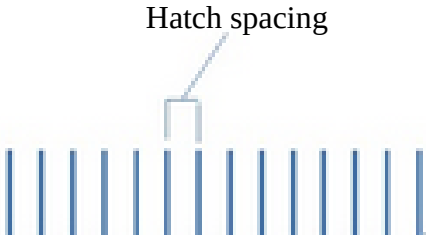

Figure 2.1.13: Schematic representation of hatch spacing

It was found that with a large hatch distance the neighbouring scanning tracks will hardly touch each other (100 µm) (Figure 2.1.14, sample C). But with a hatch spacing of 50 µm, the neighbouring scanning tracks overlap almost by 50%.

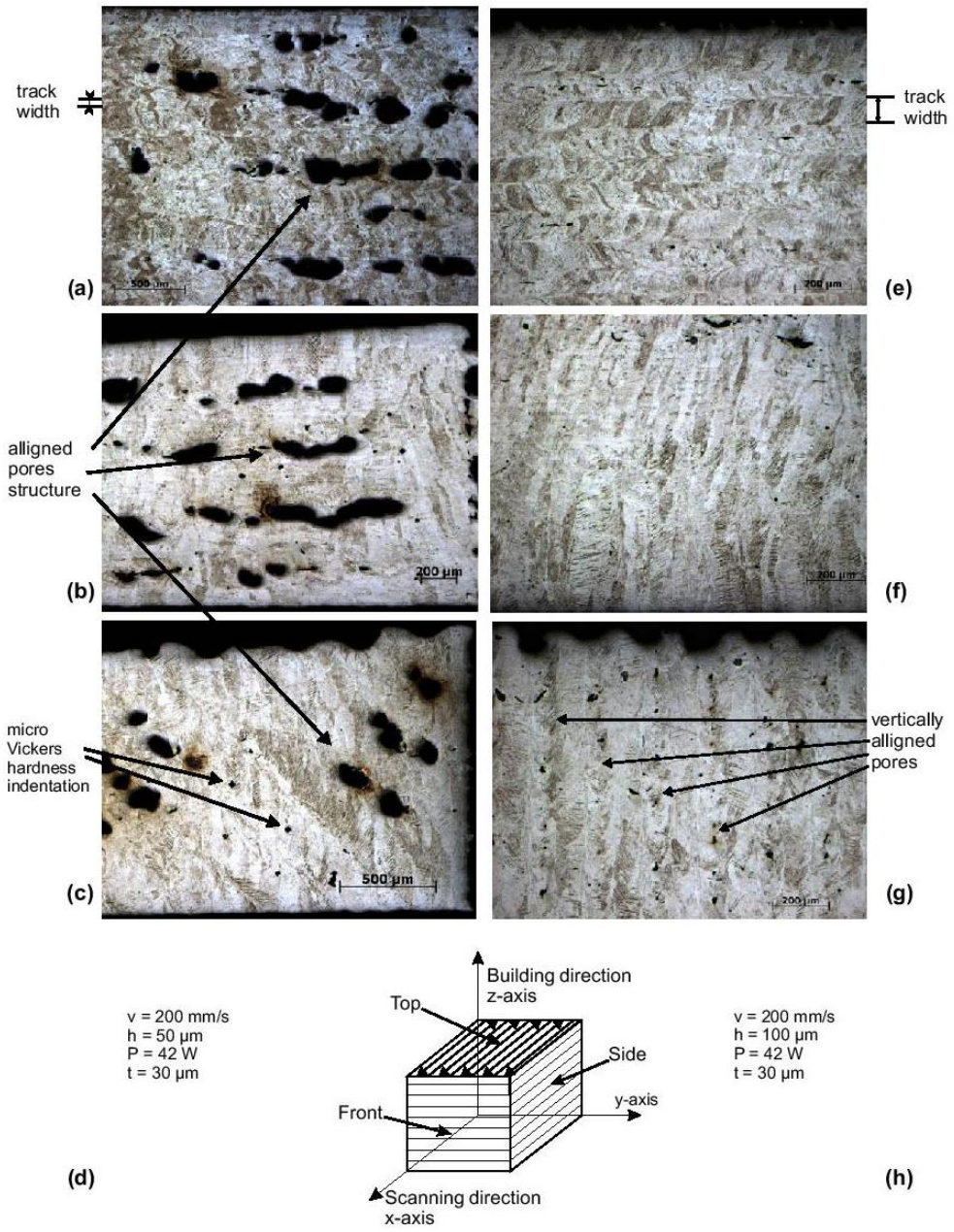

Figure 2.1.14: Influence of hatch spacing. Micrographs of sample A, scanned with a hatch spacing of 50 µm: (a) top view; (b) side view; (c) front view; and (d) the scanning strategy and parameters applied. Micrographs of sample C, scanned with a hatch spacing of 100µm: (e) top view; (f) side view; (g) front view; and (h) the scanning strategy and parameters applied (Thijs *et al.*, 2010).

Scanning strategies are known to have a great influence on the microstructure and mechanical properties of DMLS parts. Two major types of scanning strategies such as rotated strip pattern and

alternating block pattern are used in modern DMLS machines (Figure 2.1.15). To obtain a crosshatch pattern, the rotated stripe scanning strategy (Figure 2.1.15a) stripes are rotated counter clockwise by ~67° for every new layer in comparison with the previous layer which would result in creating of the crosshatch pattern. As can be seen on the DMLS resulted Inconel 625 microstructure (Figure 2.1.16), the angle between laser tracks of consecutive layers was found to be ~67° (Anam *et al.*, 2014).

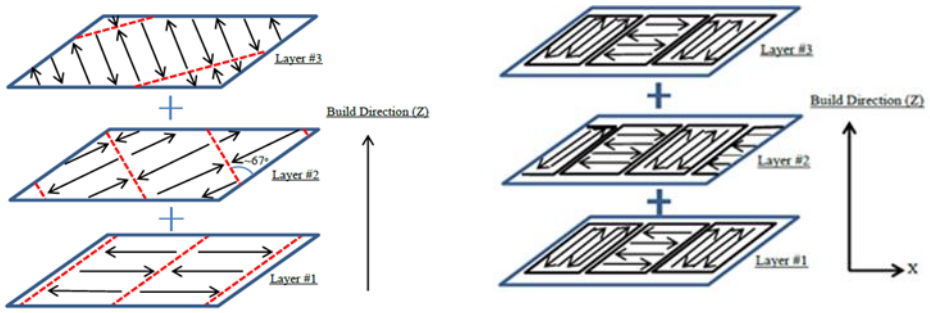

(a) (b)

Figure 2.1.15: Schematic representation of (a) rotated strip pattern (b) alternating block pattern (Anam *et al.*, 2014)**.**

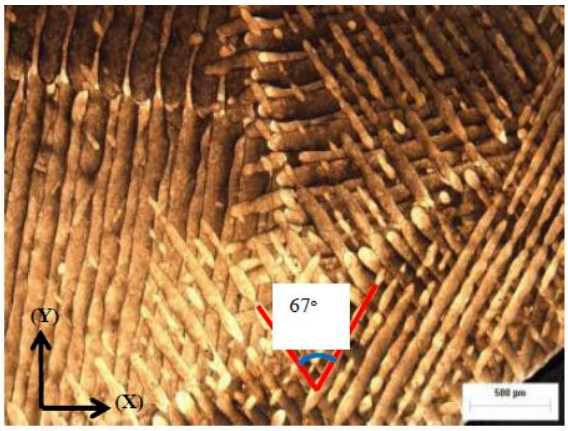

Figure 2.1.16: Microstructural evidence of the stripe pattern at 67° strip rotation creating a cross-hatch patterns (Anam *et al.*, 2014).

Kruth *et al.* (2010) investigated the effect of scanning strategies on the relative density of Ti6Al4V alloy manufactured by DMLS. They found out that zigzag alternating strategy produces the highest relative density (Figure 2.1.17), since the risk for having unmelted zones between adjacent scan

tracks is lower due to the rotation of the scan lines 90° in each new layer. Thijs *et al.* (2010) also noted that the cross-hatching scanning strategy (alternating zig-zag) produced the highest relative density.

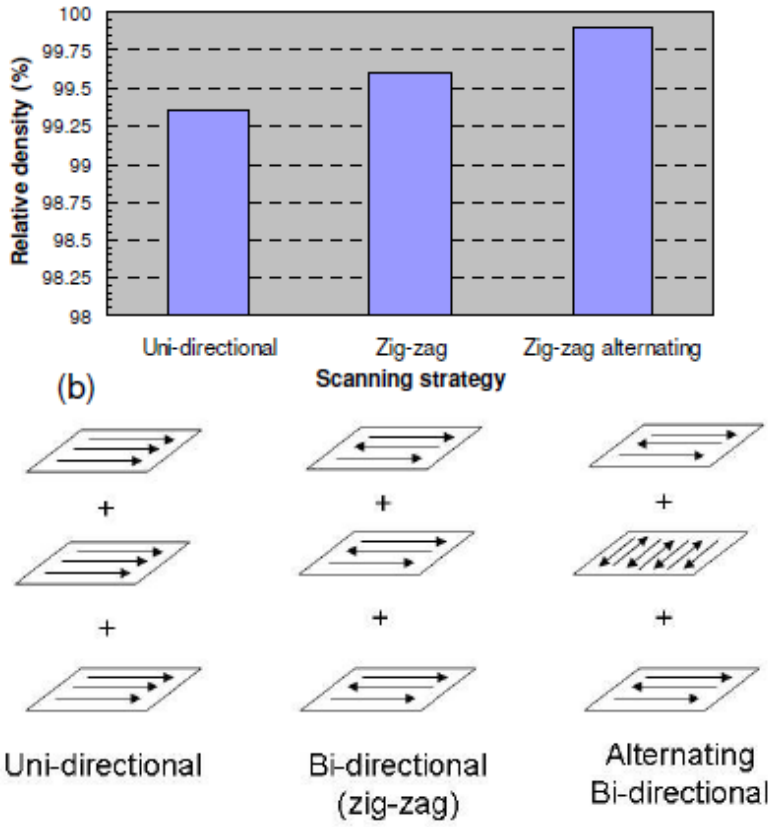

Figure 2.1.17: A graph of relative density against scanning strategy for Ti6Al4V material (a) type of scanning strategy applied (b) (Kruth *et al.*, 2010).

The effect of scanning strategies on the growth direction of the elongated grains was studied by Thijs *et al.* (2010). It was recorded that, for the unidirectional sample (Figure 2.1.18), the elongated grains are parallel to each other and the grains grow towards the melt pool. If the laser beam is moved from left to right, the grains are slanted as ///, from right to left as \\\. Therefore, it can be concluded that the orientation of grains is largely controlled by the heat conduction direction which depends on the type of laser scanning strategy.

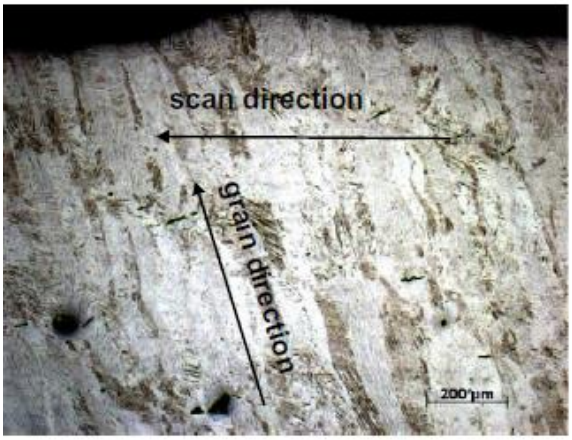

Figure 2.1.18: Influence of scan strategy on the grain direction in Ti6Al4V parts (Thijs *et al.*, 2010)**.**

Building direction is defined as "*an acute angle between the longitudinal axis of a given sample and the vertical axis*" (Hanzl *et al.*, 2015). Shifeng *et al.* (2014) investigated the effect of build direction on the mechanical properties of DMLS 316L stainless steel parts. Four samples with different orientations from 30° to 90° by a step size of 15° (Figure 2.1.19a) in the *X*–*Y* plane referred to as horizontal samples. Another set of samples were designed along the height direction (*Z*-axis) and referred to as vertical sample (Figure 2.1.19b). After optimum processing parameters (laser power 180 W, scanning speed 0.9 m/s, powder layer thickness 20 μm, hatch distance 0.06 mm), DMLS samples were manufactured. The results reveal a significant anisotropy characteristics and the sample build in the horizontal direction prove to have better mechanical properties than the samples build in the vertical direction. The sample built in the direction of 0° (the longitudinal axis parallel to the x-axis) showed the worst elongation and strength, while the sample build at an angle of 45° had the best combination of strength and ductility. The maximum elongation was noted for the angle of 60° samples.

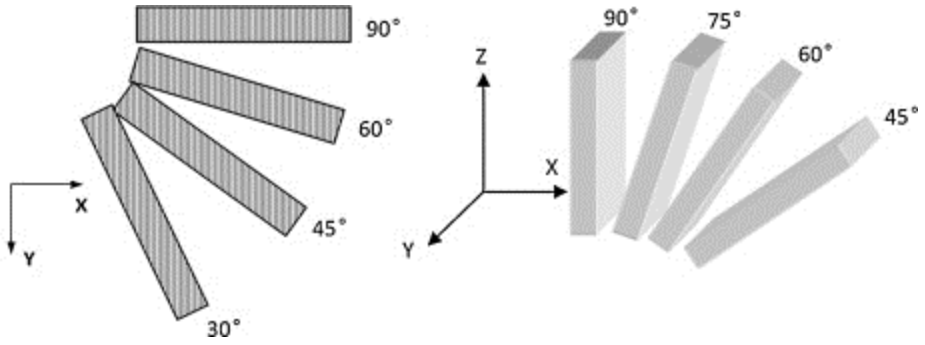

(a) (b)

Figure 2.1.19: Processing orientation (a) horizontal (b) vertical (Shifeng *et al.*, 2014).

Generally, during DMLS process the grains grow from the cooler side to the warmer side; since the upper surface is exposed to the laser beam it would be warmer while the bottom surface rests on a solidified metal substrate would be relatively cooler. The grains would orient towards the direction of the thermal gradient which lies in a plane parallel to the building platform. Hence, samples built with a different building direction would have differently grain orientation with different mechanical properties (Shifeng *et al.*, 2014). Hanzl *et al.* (2015) reported on the effect of build orientation on mechanical properties of Ti6Al4V parts, investigated by EOS company. The horizontal DMLS samples have better mechanical properties as compare to the vertical samples.

Non-optimal process parameters and difficulty of laying an even powder layer during the DMLS building process result to the manufacturing of less dense parts as compared to the conventional methods of manufacturing. Porosity in the form of micro-flaws, unmelted powder and voids serve have a direct effect on the mechanical properties of DMLS manufactured parts (Leuders *et al*., 2013).

2.1.2.2.2.2: Residual Stress

The high-temperature gradient due to the localized thermal input from the laser causes previously solidified layers to hinder the thermal expansion of the newly-formed areas which introduce thermal stress into DMLS manufactured parts. Residual stress poses a major challenge to the manufacturing of DMLS objects since it can cause degradation of mechanical properties, part distortion, and micro-crack formation (Van Zyl *et al.*, 2016).

Principal residual stresses were measured by XRD near the top surface in as-built Ti6Al4V LPBF samples produced with similar process parameters and attached to the substrate. Residual stresses were tensile in nature and varied from 200 MPa to 800 MPa. These values were similar to the ones reported for cantilever specimens in as-built conditions. Van Zyl *et al.* (2016) reported that maximum residual stress was found to be 1100 MPa. A high variability of residual stresses can be (at least partially) linked to the morphology of the processed layer and inhomogeneity of delivered powder layers which lead to different strains during cooling. The strain during cooling can be described as a superposition of elastic, thermal and plastic deformation, as well as creep strain components. The molten pool and the heat-affected zone had an elongated shape in the scanning direction. When the laser beam left the irradiated zone, the track solidified and cooled down. Various layers of material, cooled at different rates, therefore contraction also occurred at different speeds. During laser melting, high compressive and tensile stresses were under the front of the molten pool. As a result, deformations in the surrounding material and the solidifying track occurred (Yadroitsava *et al.*, 2015a). It was reported that preheating of the powder bed and build chamber temperature reduced the residual stress (Knowles et al., 2012; Leuders et al., 2013).

2.1.2.2.2.3: Microstructural Evolution and Mechanical Properties under Different Heat Treatment

The microstructure of DMLS α/β Ti6Al4V alloys consists of martensitic acicular α' phase due to the fast cooling rates and the layer-wise building process. The DMLS process results in a fine non-equilibrium phase and anisotropic mechanical behaviour. To obtain a balance of mechanical properties, the above mentioned negative effects of DMLS process must be eliminated through heat treatment. However, the microstructure of as built DMLS samples are vastly un-identical with the conventional microstructures, hence standard heat treatments might not necessarily produce the required expected microstructural result. Tailoring heat treatment strategies such as; holding time, varying temperature and the cooling rate among others must be applied to achieve the expected microstructural result was proposed (Vrancken *et al.*, 2012; Becker *et al.*, 2015; Huang *et al.*, 2015). Becker *et al.* (2015) investigated microstructural evolution and the mechanical properties of the DMLS Ti6Al4V parts under different heat treatment. The first set of the sample were heated above the β-transus temperature (1015^0C) for 0.5 hour, cool at a rate of 10 C/min to

730 C for 2 hours and furnace cool to room temperature as shown Figure 2.1.20a for treatment A (blue line). Decomposition of the martensitic microstructure, tailoring of the grain size and distribution took place in the first stage and the second stage stress relief the material.

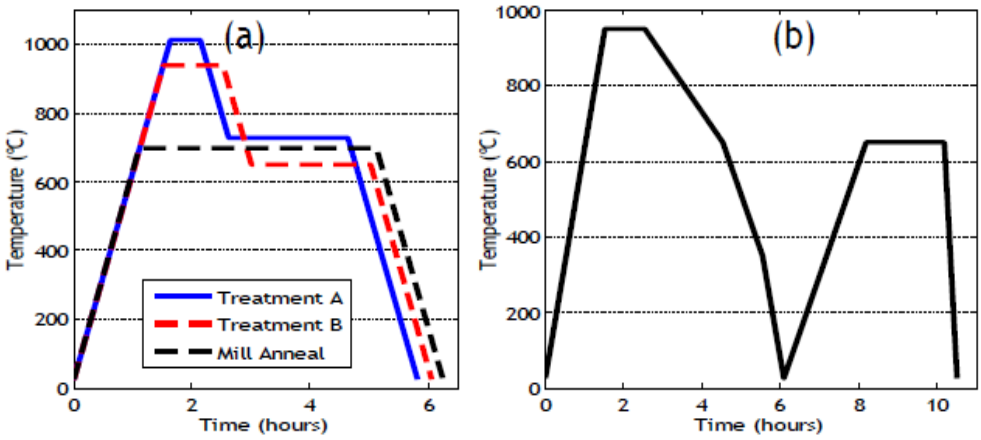

Figure 2.1.20: Tailored heat treatment plan (Becker *et al.*, 2015).

A bimodal microstructure dotted with regions of semi-equated β grains and lamellar α+β (Figure 2.1.21c) was obtained with a reduction in hardness value which would probably compensate for ductility. The super-transus treatment eliminates the presence of columnar β grains (Figure 2.1.21d). The second set of samples was heat treated in the α+β region below the β-transus temperature (940°C) of Ti6Al4V for 1 hour and cooled at a rate of 10 ^{0}C/min to 650°C for 2 hours and furnace cooled to room temperature (Figure 2.1.20a) the red dotted line – treatment B. The microstructure reveals the presence of fine alpha needles in β phase (Figure 2.1.21e) columnar grains are noted at the radial view (transverse section) as the results of α grain boundary formation (Figure 2.1.21f).

The third type of tailored heat treatment was meant to produce a Ti6Al4V sample with high strength and ductility. The first stage of the treatment induces ductility into the material while the second stage strengthens the material by cooling in a muffle furnace to prevent excessive grain growth (Figure 2.1.20b). The third type of tailored treatment leads to the production of equiaxed microstructure in the longitudinal direction of the sample (Figure 2.1.21g). Figure 2.1.21h reveals a fine needle-like structure within lean columnar β grains due to the slow cooling in the first stage. There is a reduction in the hardness value of the treated samples as compared to the untreated sample. It was also observed that the hardness values recorded after heat treatment in the axial

direction were different from the radial direction. This signifies that the DMLS sample still maintains anisotropic characteristics even after heat treatment.

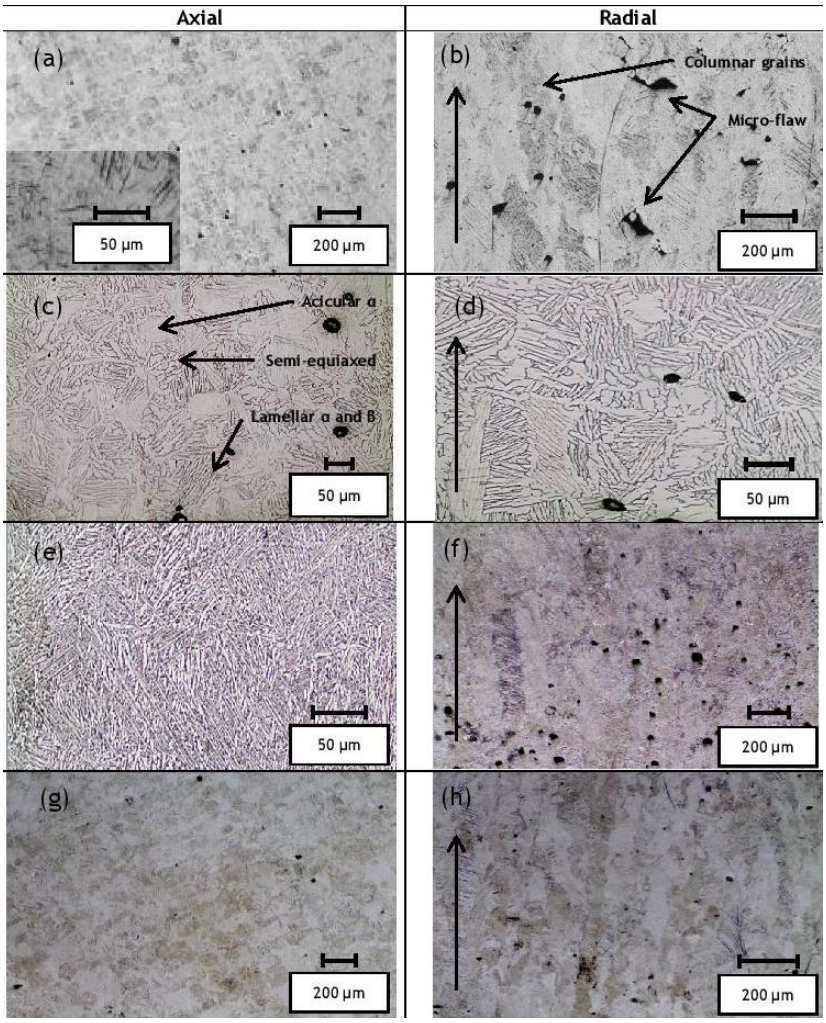

Figure 2.1.21: Effect of heat treatment on DMLS Ti6Al4V parts (a) (b); as build (c) (d); solution treated at 1015°C for 0.5 h, cooled at a rate of 10°C/min to 730°C for 2h and furnace cooled (e) (f); annealed at 9400C for 1h, cooled at a rate of 10°C/min to 650°C for 2h and furnace cooled (g) (h) heated to 950°C for 1h, cool at rate of 2.5°C/min to 6500C for 2h, cooled at a rate of 50C/min to 350°C and furnace cooled (Becker *et al.*, 2015).

Thöne *et al.* (2012) also proposed three types of tailored heat treatment to relief as-build DMLS parts of internal stress and improve its ductility (Figure 2.1.22). The first set of the sample (case 1) were heated at the rate 25 °C from 750 °C up to 850 °C for 2h under an Argon gas atmosphere and furnace cool. The second (case 2) and third (case 3) category of the experimental parts were

heat treated in a vacuum at 950 °C and 1050 °C respectively for 2h and furnace cooled. Case 1 involves annealing the as-build sample at a low temperature for a short time to relieve the material of internal stress. The case 2 heat treatment take place at a higher temperature and the microstructure of the Ti6Al4V DMLS manufactured samples change from α'-constellation to α + β-constellation (Figure 2.1.22-case 2). For the third case the Ti6Al4V DMLS fine microstructure evolved into coarse microstructure. The α lamellar (red) enlarges in a lean β matrix (green) (Figure 2.1.23). This type of heat treatment would increase the ductility of the sample for biomedical applications (Figure 2.1.24).

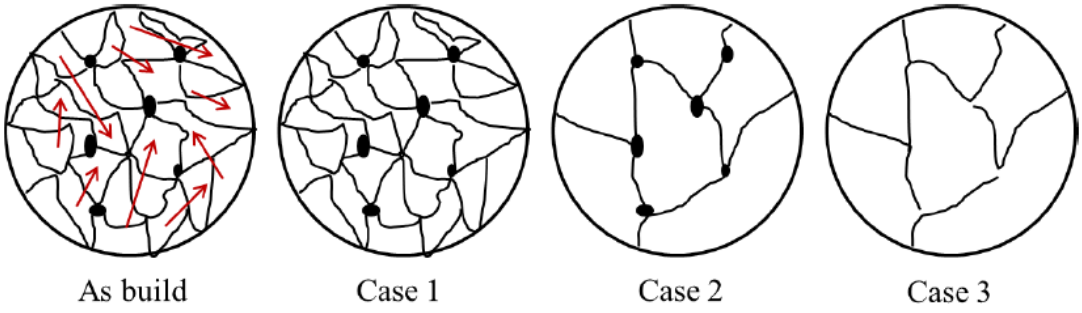

Figure 2.1.22: Heat treatment of DMLS manufactured parts (Thöne *et al.*, 2012).

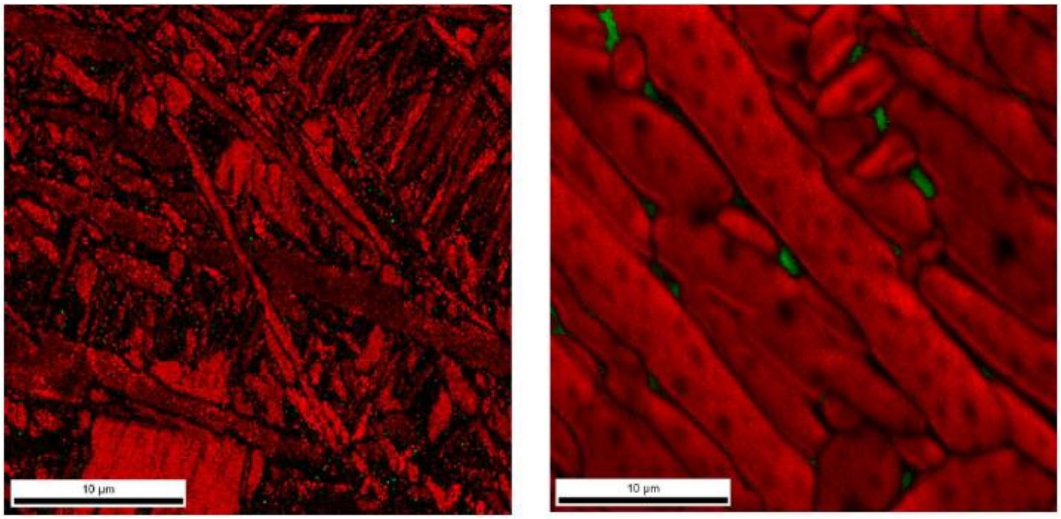

(a) (b)

Figure 2.1.23: As-build Ti6Al4V DMLS parts (a) and heat treated at 950°C in vacuum for 2h with furnace cooling (b) (Thöne *et al.*, 2012).

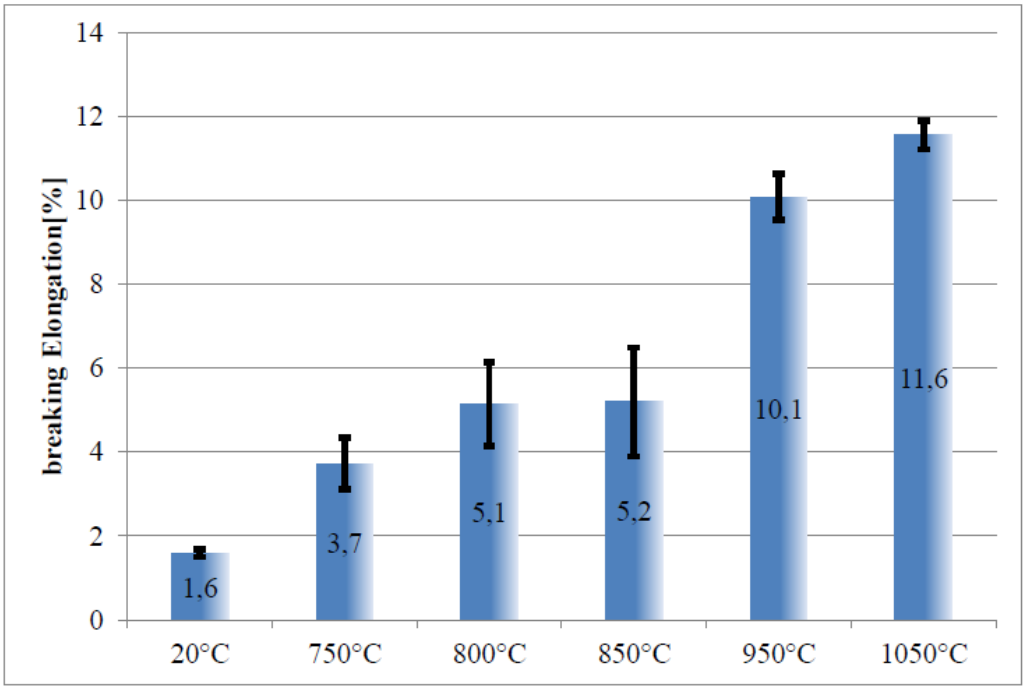

Figure 2.1.24: Increase in ductility (percentage elongation) as the heat treatment temperature increase (Thöne *et al.*, 2012).

Vrancken *et al.* (2012) study the effect of temperature on DMLS Ti6Al4V parts. The samples were annealed and solution treated for 2 hours. They noted that for heat treatment of Ti6Al4V DMLS parts below the β-transus temperature, the α-β morphology becomes coarser for higher holding temperatures. Ti6Al4V DMLS samples were heat treated at 940°C for 2 h and 20 h, it was noted that the width of α plates of the longer residence (holding time at a particular temperature) sample increase from 2.23±0.12 µm to 2.80±0.16 µm (Figure 2.1.25a–b). Heat treatment for longer residence time at higher temperature leads to increase in grain size (Figure 2.1.25c-d).

During heat treatment in the α+β region below the β-transus, α and the β phases will tend to coarsen but will hinder each other, thereby limiting grain growth in the two phases. This phenomenon is absent as the annealing temperature rises closer to the β-transus temperature, hence as the residence time increases in the α+β region closer to the β-transus temperature grain growth occurs. The effect of residence time is more pronounced when heating above the β-transus temperature since it is only a single phase region, the growing of the grains is not hindered. Lütjering (1998) mentions that the size of α colony is dependent on β grain size which in turn affect the mechanical properties.

Understanding the effect of residence time on DMLS heat treated part is very important. It can be observed from Figure 2.1.25c-d that longer residence time leads to increase in α colony size which would ultimately affect the mechanical properties of the material.

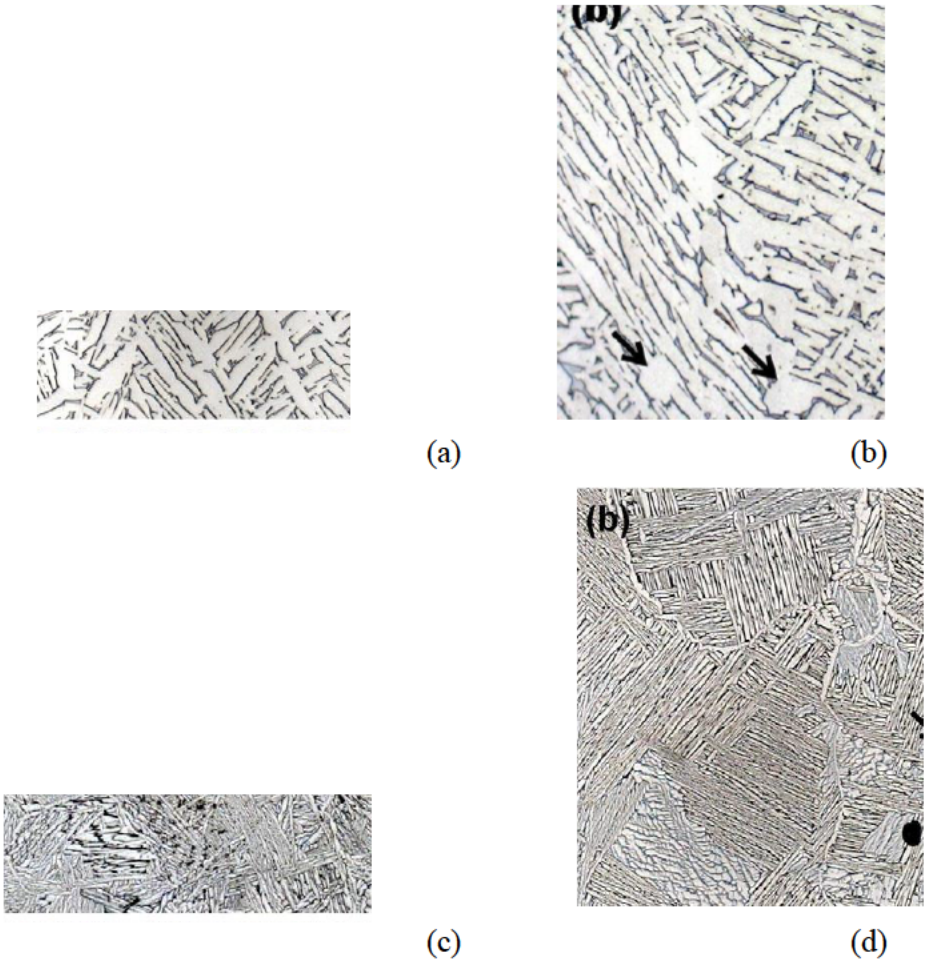

Figure 2.1.25: Comparison of the similarity in α plate colony size after 2 h at 940°C (a) and 20 h at 940°C (b) followed by furnace cooling; illustration of smaller α size after heat treatment at 2 h at 1020°C (c) compare to 20 h at 1040°C (d) followed by furnace cooling. Arrows in (b) indicate globularized α grains; the arrows in (c, d) indicate grain boundary of α (Vrancken *et al.,* 2012).

The mechanical properties response (Figure 2.1.26) of wrought and DMLS samples to heat treatment are vastly different since their microstructures are different. The fracture strain of wrought sample reduces with increasing temperature while that of DMLS Ti6Al4V heat treated parts increases (Figure 2.1.26a and c). The yield stress of DMLS samples reduced with increasing

temperature while the wrought sample does not demonstrate any drastic change (Figure 2.1.26b and d) (Vrancken *et al.*, 2012).

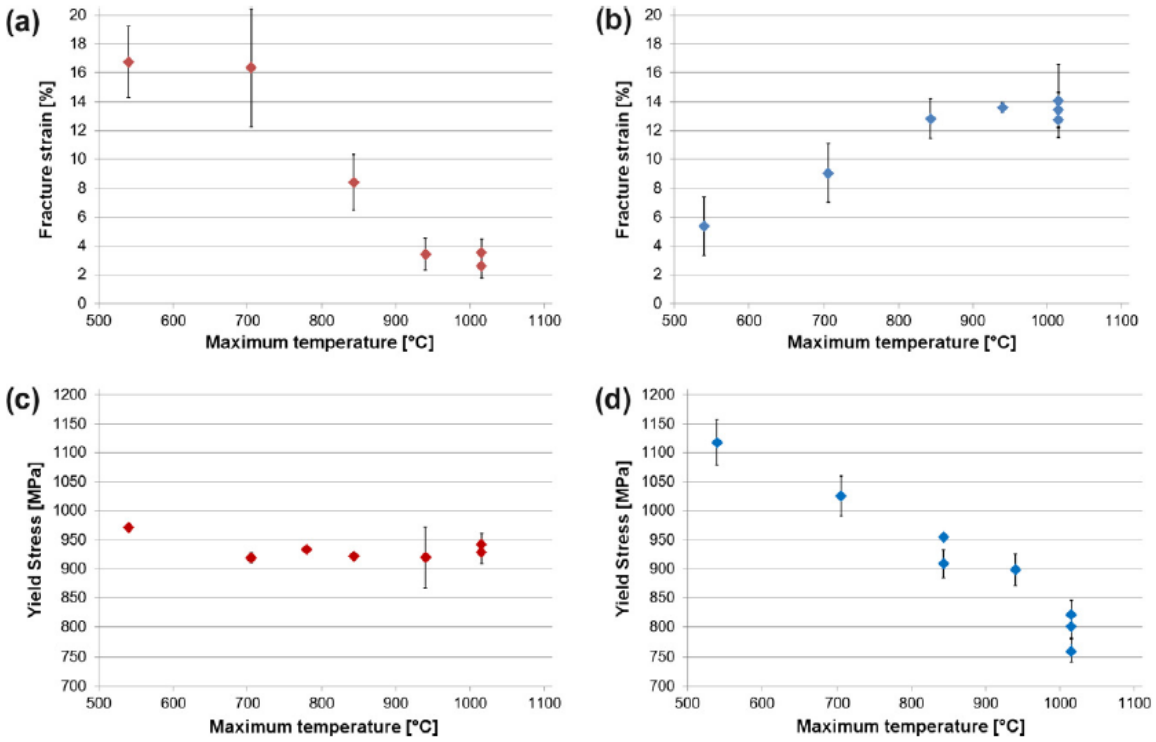

Figure 2.1.26: Fracture strain and yield stress of mill annealed (wrought) (a, c) and DMLS material (b, d) in function of the maximum heat treating temperature (Vrancken *et al.*, 2012).

2.1.2.2.2.4: Surface Roughness

Implants surface are supposed to be in direct contact with the human body tissue for osseointegration to occur. It is well proven that the surface quality of an implant has a direct influence on the anchoring process (Liu *et al.*, 2004; Bertol *et al.*, 2010; Longhitano *et al.*, 2015). Despite the appealing opportunities offered by the DMLS process, surface quality is a well-known inherent limitation of the DMLS process and it is of primary concern to users. If this limitation is well addressed it would make the DMLS process more agile and acceptable especially for sectors of high surface quality demand (Gharbi *et al.*, 2013; Mierzejewska 2015; Yasa *et al.*, 2016).

Longhitano *et al.* (2015) produced Ti6Al4V cylindrical samples with a EOSINT M270 machine and reported mean value of about 6.2 µm for *Ra* and about 30 µm for the mean roughness *Rz*. EOS

noted on their material data sheet that for a powder layer thickness of 60 µm the *Ra* value is in the range of 6-10 µm and *Rz* value in the range of 35-40 µm for Ti6Al4V alloy produced by EOS M280 with 400W laser power (EOS, 2014). Duleba *et al.* (2011) also, reported that DMLS as build parts has a surface roughness value of *Ra* = 8.75 µm.

Top and side surface roughness of as-build DMLS Ti6Al4V alloy was investigated by Król & Tański (2016). It was documented that the top surfaces roughness values for all the process parameters were less than the side surface roughness. This was attributed to the DMLS processing mechanisms. Measuring *Ra* value on the top surface (horizontal axis) would take into consideration only one layer. However, *Ra* value on the side surface (vertical axis) would take into consideration multiple layers. The multiple interlayer connections and possible entrained powder particles that adhere and agglomerate to the external edge cumulatively increase the *Ra* value of the side surface. At a laser power of 150 W and scanning speed of 250 mm/s, Król & Tański (2016) recorded *Ra* values of 8.8±0.2 µm and 11.4±0.4 µm for the top and side surfaces respectively.

A similar observation was made by Mumtaz & Hopkinson (2010) with Inconel 625 alloy. Pyka *et al.* (2012, 2013) also focused on top and bottom surface quality of DMLS struts. It was reported that the top surface of the struts was of appreciable quality than the bottom parts. *Ra* value of 7 µm and 12 µm was recorded for the top and bottom surface quality respectively. They realized that the bigger the strut size the less the surface quality. The bigger strut formation would result in larger amounts of attached powder particles, resulting in a higher surface roughness.

Kleszczynski *et al.* (2015) use a numerical simulation model to investigate the causes of surface roughness of DMLS process. Both the simulation and the experimental results attest that surface roughness is always higher than the mean diameter of the used powder. It came to light that process parameters that produce good part densities are most likely to produce good surface quality.

Build direction could also have a significance influence on surface quality (Taufik & Jain, 2013). The experimental results of Yasa *et al.* (2010) and Kinnear *et al.* (2016) demonstrated that increasing scanning speed and hatch distance would also increase surface roughness (Yasa *et al.*, 2010; Kinnear *et al.*, 2016). The stair step effect is the main reason for the low surface quality of

DMLS manufactured parts (Shi & Gibson, 1998; Hague *et al.*, 2003; Ahn *et al.*, 2009; Yasa *et al.*, 2016). To remedy the surface roughness situation, rescanning has been proposed (Yasa & Kruth, 2008; Kruth *et al.*, 2009; Kruth *et al.*, 2010; Król *et al.*, 2014; Becker *et al.*, 2015) as the primary procedure to improving the surface quality of DMLS as build parts. However, Yasa *et al.* (2016) is of the view that the re-scanning strategy would increase the cost of production due to machine time. Thin powder layer thickness has been identified as a possible technique for reducing surface roughness (Gharbi *et al.*, 2013; Mierzejewska, 2015). Using smaller powder particle size distribution would also contribute to surface quality (Spierings *et al.*, 2011).

2.1.2.3: Titanium-copper alloys

2.1.2.3.1: Properties of conventional Ti-Cu alloys

Implants and their associated infections still pose serious threats leading to possible complications such as prolonged hospitalization, complex revision procedures, complete removal, patient suffering, financial burden and even death. The original intent of designing antibacterial coating was to prevent the initial adhesion of bacteria onto the implant surface after implantation (Zhao *et al.*, 2009). However, the conventional antibiotic antibacterial agents have failed in combatting bacterial colonization of the implant surface (Bosco *et al.*, 2012; Goodman *et al.*, 2013). The bonding between the coating materials and the metal surface is generally not as firm as expected as a result of the great difference in the material characteristics which result in falling off of the antibacterial coating from the metal matrix in the long term (Ren *et al.*, 2014).

The studies of Liu *et al.* (2014) focus on antibacterial activity, cytotoxicity and the cell function of sintered Ti-10 wt% Cu alloy for suitable biomedical applications. The samples were ball-milled for 3–6 hours and subsequently hot pressure sintered. The results attest that the Cu ions possess strong antibacterial properties without cell cytotoxicity. Zhang *et al.* (2013) reported on the antibacterial and mechanical property of Ti–Cu alloy produced by powder metallurgy. It was concluded that the addition of copper provided the whole alloy with strong antibacterial property without a reduction in mechanical property and corrosion resistance.

Novel design of implant with self-antibacterial properties whereby the inorganic antimicrobial agent is incorporated into the bulk implant material from the initial stage of manufacturing would

be more desirable. Ren *et al.* (2014) fabricated by melting commercial medical grade Ti6Al4V-*x*Cu (x = 1, 3, 5 wt.%) alloys in a vacuum arc furnace. The Ti6Al4V-*x*Cu (x = 1, 3, 5 wt%) implant samples demonstrate excellent antimicrobial properties. It was revealed that as the percentage of copper increases in the Ti-alloy the potency of the implant against bacterial infection also increases and with no cytotoxicity. They further investigated the effect of Cu on the mechanical properties of Ti6Al4V alloy and found that, though there was the formation of intermetallic compound (Ti_2Cu) the amount of copper used did not have any major effect on the mechanical properties of the Ti alloy. A similar work done by Aoki *et al*. (2004) with a higher copper concentration Ti6Al4V– x Cu (x = 1, 4, 10 wt%) reveals a great effect of Cu on the mechanical properties of the Ti6Al4V alloy. As the copper content increases the ductility of the material reduces and the bulk material becomes more brittle, which is attributed to the presence of the intermetallic compounds.

Aoki *et al*. (2004) noted that the microstructure for 1% Cu composition in Ti6Al4V in cast alloy was Widmanstätten (Figure 2.1.27a), where α plates were dispersed in β-matrix. The microstructure for Ti6Al4V-4%Cu was termed α+β microstructure (Figure 2.1.27b).

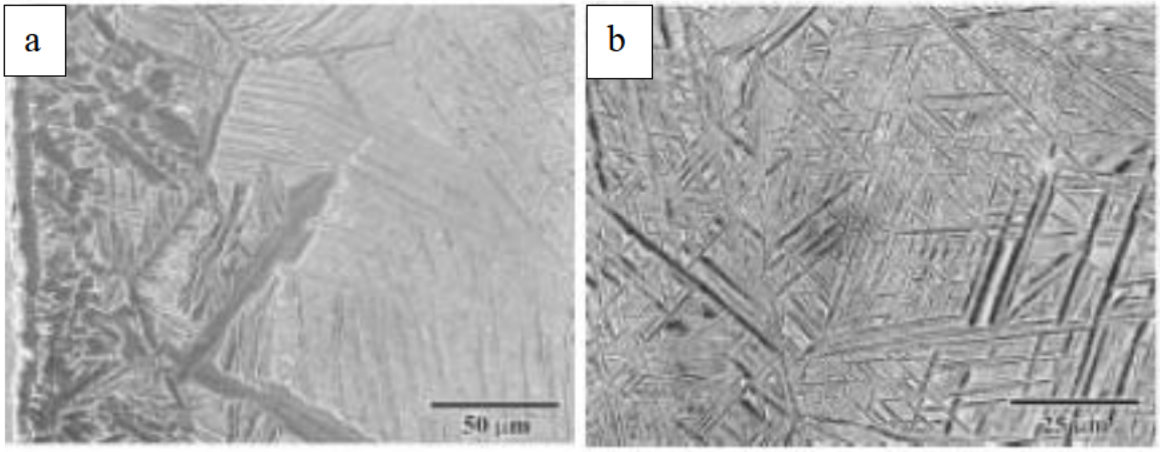

Figure 2.1.27: Typical microstructures of (a) Ti6Al4V-1% Cu (b) Ti6Al4V-4% Cu (Aoki *et al.,* 2004).

For copper-titanium alloy, heat treatment could have a significant effect on the mechanical properties of the alloy and its antibacterial properties. If the alloy is cooled from the β-phase at a very fast rate that does not permit atomic diffusion resulting in the formation of a hexagonal

martensitic phase instead of stable α phase (Dobromyslov & Elkin, 2001). For a hypoeutectoid Cu composition in the Ti6Al4V alloy, irrespective of the cooling rate the presence of the intermetallic compound (Ti_2Cu) is unavoidable (Cardoso *et al.*, 2011). However, previous researchers have demonstrated that at a lower concentration of Cu ≤4.5%, Ti_2Cu was not observed (Bhaskaran *et al.*, 1995; Kikuchi et al., 2003; Aoki *et al.*, 2004). Specific heat treatment such as aging with subsequent quenching could be used in controlling the precipitating of Ti_2Cu which would enhance the mechanical properties of the alloy (Yao *et al.*, 2009).

Ma *et al.* (2015) conducted a detailed study by investigating the effect of heat treatment on the microstructure, antibacterial property and cytocompatibility of Ti6Al4V-5wt.%Cu. The β-transus temperature for the alloy is 920±10°C. The Ti6Al4V-5wt.%Cu alloy was solution treated at 810°C, 930°C and 1050°C for 1 h and followed by water quenching. Half of the solution treated samples were aged at 600 °C for 7 hours. The heat treatment had a significant effect on the microstructure of the alloy. The microstructure of the solution treated samples at 810 °C consisted of α strips distributed evenly in the β matrix (Figure 2.1.28a). Whereas the samples solution treated at 930°C and 1050°C respectively demonstrated a decrease in α phase with increase in β-phase and large β grain size, especially for the 1050 °C solution treated sample (Figure 2.1.28b-c). The aged samples at 930°C and 1050°C demonstrate an increase in the volume fraction of the α phase, the primary α-phase in the β-matrix grow considerably (Figure 2.1.28e-f). The XRD patterns proved that the aged samples consist of α-phase, α+β-phase, β-phase and Ti_2Cu as a result of the eutectoid reaction.

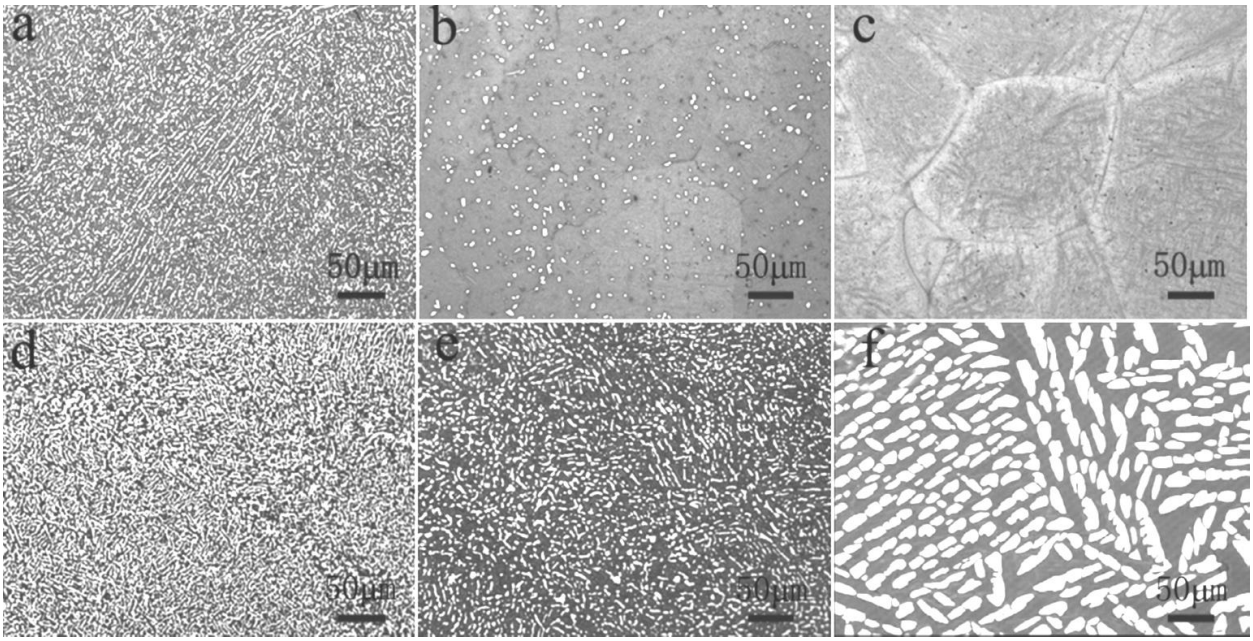

Figure 2.1.28: Microstructures of Ti6Al4V-5wt.%Cu alloy under different heat treatments: (a) S-810 °C, (b) S-930°C, (c) S-1050 °C, (d) SA-810 °C, (e) SA-930 °C and (f) SA-1050 °C. (Where 'S' = solution treated samples and 'SA' = solution treated first and subsequent age treated samples) (Ma *et al.,* 2015).

Regarding the antibacterial properties, the solution treated samples demonstrate more antibacterial potency as compared to the aged samples. When Cu is present in alloy as substitutional atoms, it was easier for release of Cu ions from the alloy in comparison with the stable intermetallic Ti_2Cu phase. With increase in solution temperature, more β phase formed, so solution treatment exhibited antibacterial ability. Therefore, the recommend heat treatment of the Cu-bearing titanium alloy for biomedical applications was 930 ^oC for 1 hour followed by water quenching. The samples were found to be non-cytotoxic base on WHO standard (IPCS, 1998).

Cardoso *et al.* (2011) investigated solution treatment of Ti-6.91wt.%Cu alloy at ~1000°C. The samples were either furnace cooled or water quenched at a rate of 150°C/s. The water quenched samples demonstrate a complete decomposition of the β-phase into hexagonal martensite which propagates through pre-existing β-grains due to the high cooling rate imposed on the samples. The furnace cooled samples present a basket weave microstructure. The SEM analysis reveals the presence of Ti_2Cu in both sets of samples (furnace cooled and water quenched). The samples were then age treated at 415 ^oC, 550 ^oC, 570 ^oC and 618 ^oC in order to investigate the mechanism of

Ti_2Cu precipitation from the hexagonal martensite. It was realized that the precipitation of Ti_2Cu occurs in two stages. For the first stage at 415^oC, coherent precipitations were observed with similar crystal structure as that of the hexagon martensite. During the second cycle of heat treatment at 550^oC semi-coherent and incoherent precipitates occur, leading to Ti_2Cu precipitation. The first type of coherent precipitation is known as Guinier–Preston zones (Reed-Hill & Abbaschian, 1973). A microhardness test was conducted to investigate the effect of Ti_2Cu on the alloy. An increase in hardness was observed for 415-550°C. Which was attributed to the Guinier–Preston zones phenomenon and the onset of incoherence decomposition of martensite into nanometric formation of Ti_2Cu compound. Such nanometric formation would impede dislocation movement which causes an increase in the hardness values (Sun *et al.,* 2004) as observed from 415 to 550 C (Figure 2.1.27). At higher temperature, (>550^oC) the Ti_2Cu grew in size leading to a reduction in their number (coalescence) and strain strength which cause a reduction in microhardness value (Figure 2.1.29). At a higher temperate range (570–618 ^oC) of aging complete decomposition of the martensite was observed and the Ti_2Cu peaks were more defined.

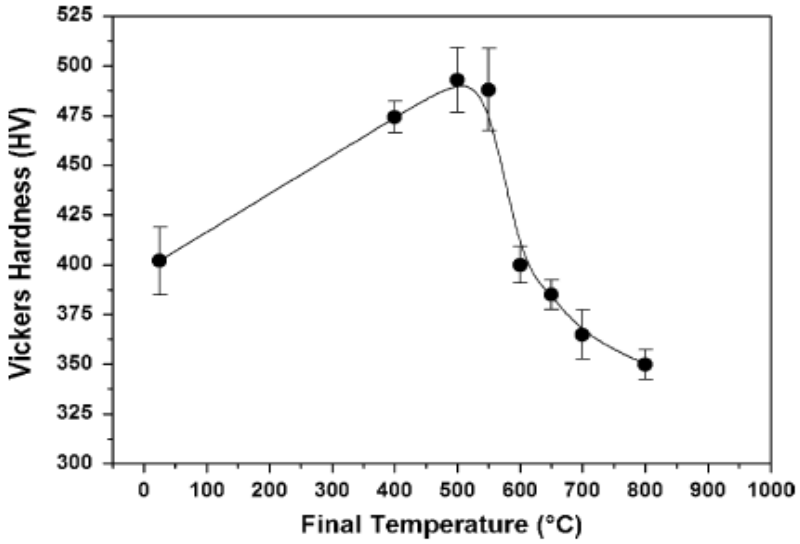

Figure 2.1.29: Effect of the aging temperature on microhardness of Ti–Cu samples (Cardoso *et al.,* 2011).

Contieri *et al.* (2014) studied the effect of cooling rate on near eutectoid Cu composition (Ti-5.5 at.% Cu). It was noted that for the three selected cooling rates used (fast cooling under

160 K/s, intermediate 9 K/s and slow 2 K/s cooling) the decomposition of the supersaturated β solid solution occurs as follows:

$$\beta \rightarrow \beta + \textit{Pro-eutectoid } \alpha \rightarrow \textit{Pro-eutectoid } \alpha + Ti_2Cu \textit{ (within } \alpha \textit{ plates)} + \textit{Eutectoid } (\alpha + Ti_2Cu)$$

With the decrease in the cooling rate, there was a substantial increase in the volume fraction of the lamellar eutectoid product and the composition of all decomposition products approached their equilibrium values. Also, the slowest cooling rate promoted the cooperative growth of lamellar $\alpha + Ti_2Cu$ occurred at the interface between the proeutectoid α plates and the β matrix.

Souza *et al.* (2009) found that the Elastic modulus of Ti–7.1wt.%Cu increased at lower cooling rate (2, 4, 9°C/s) and decreased at a higher cooling rate (24, 63, 160°C/s) as a results of higher volume fraction of Ti_2Cu present at lower cooling rate. The hardness value decreases at a lower cooling rate and increases at higher cooling rate opposite to the Elastic modulus behaviour. The reduction of hardness value at a lower cooling rate is as a result of large volume fraction of $\alpha+Ti_2Cu$ whiles the increase in hardness value at fast cooling rate is due to martensitic structure formation.

Yao *et al.* (2009) also heat treated Ti–2.5wt.% Cu alloy in order to investigate the effect of Ti_2Cu on the mechanical properties of Ti. It was found out that, during annealing treatment at 790 °C the shape of the intermetallic Ti_2Cu were spherical and acicular ones during age treatment. The acicular shape Ti_2Cu had a higher microhardness value than the spherical intermetallic Ti_2Cu produce during the annealing process.

2.1.2.3.2: DMLS Ti-Cu alloys

Current literature has revealed that DMLS has a superior manufacturing capability (Attar *et al.,* 2014) than all the above mentioned technologies which were used to manufacture Ti-based copper incorporated implants. As DMLS is undergoing intense academic research to permit production of end-user tailored multimaterial properties, manufacturing of position dependent microstructure, chemical composition, thermal properties, mechanical properties and electrical properties would ultimately be possible. This versatile technology could be used to produce Cu-bearing Ti-based

implant. This kind of manufacturing of implant with a self-antibacterial function from the design of chemical composition of the implant material would avoid the fall of coating material from the metal matrix as noted above. An implant with the inbuilt bacterial resistant ability (self-antibacterial implants) such as Ti6Al4V–Cu alloy would prevent the initial adhering of bacterial onto the implant surface which would prevent the formation of biofilms.

Most recently Guo *et al.* (2017) studied Ti6Al4V-*x*Cu (x = 0, 2, 4, 6 wt%) by DMLS for biomedical applications. The XRD analysis reveals that Cu was melted completely and existed in the formation of Ti_2Cu. The density, porosity, corrosion resistance and antibacterial properties of the alloy were found to increase with increasing copper content as noted by most of the previous authors. It was concluded that the addition of copper to Ti6Al4V did not cause cell cytotoxicity nor any negative effect on cell proliferation and activity.

2.1.3: Titanium β-Alloys

2.1.3.1: Conventional Ti-*x*Mo Alloys

Beta titanium alloys contain enough β-stabilizing elements to retain complete β-structure (*bcc*) upon quenching from the β- phase (Weiss & Semiatin, 1998). The driving force behind formulating of β-titanium alloys lies in their intrinsic ability to produce biomaterials with low Elastic modulus, high ductility, good fatigue properties, increased bio-corrosion resistance and improved tissue response (Oliveira *et al.,* 2007).

An early metastable beta alloy which is cold formable and age hardenable are part of what are also known as B120VCA alloys, was developed in the 1950s. Ti–8V–8Mo–2Fe–3Al (Ti–8–8–2–3), and Ti–11.5Mo–6Zr–4.5Sn (Beta III), Ti–3Al–8V–4Mo–4Zr (Beta C) were introduced between 1960 and 1980. There has been a progressive increase in the number of β-alloys formulating till date. Some of the current new β-type Ti alloys include Ti-Mo, Ti-Nb, Ti-Zr, Ti-Mn (binary), Ti-Nb-Mo, Ti-Mo-Zr, Ti-Nb-Ta (ternary) and Ti-Ta-Sn-Zr, Ti-Nb-Zr-Sn, Ti-Mo-Zr-Fe, Ti-Nb-Ta-Zr (quaternary) (Weiss & Semiatin, 1998; Mohammed *et al.*, 2014). The binary Ti-*x*Mo had considerable attention for biomedical applications (Niinomi, 1998; Niinomi, 2002; Oliveira et al., 2007; Júnior *et al.,* 2011).

Oliveira *et al.* (2007, 2008) studied microstructure and electrochemical characterization of binary Ti-xMo (x=4, 6, 8, 10, 15 & 20 Mo wt. %) alloys for biomedical applications produced by the arc-melting furnace method. The X-ray diffraction (XRD) analyses show that Mo concentration had a profound effect on the crystal structure of the alloy. At a concentration of 4 wt.% Mo, the X-ray diffraction pattern is made up of hexagonal α′ and orthorhombic α″ phases (Figure 2.1.30). From 6-8 wt.% Mo concentration, orthorhombic α″ phases were produced and higher concentrations of Mo wt.% were dominated entirely by β phase (Figure 2.1.30). Ringer solution chemical tests proved that the addition of Mo increase corrosion resistance of the alloy significantly.

A similar experiment was performed earlier by Ho *et al.* (1999), the X-ray diffraction pattern analysis results were similar to those obtained by Oliveira *et al*. (2007). The bending strength of the alloy at 7.5 wt.% Mo and 15 wt.% Mo were similar.

Elastic modulus, corrosion resistance, and biocompatibility of binary Ti-Mo alloy specimens with Mo contents of 3, 7, 10, and 15 wt% were investigated by Sung *et al*. (2015). The results point out that the Elastic modulus of the alloys decreases with increasing Mo content from 3 to 7 wt.% Mo concentration and increase with a subsequent increase in Mo content. Ti-7wt.% Mo alloy exhibited lowest Elastic modulus and low metal ion release in a simulated body fluid solution test. A cell proliferation test with MC3T3-E1 also indicated that Ti-7 wt.% Mo was the most active as compared to other Ti-xMo compositions. The authors mentioned that Ti-7 wt.% Mo is the most suitable for biomedical applications.

Zhou & Luo (2011) studied cold-rolled and heat treated Ti-*x*Mo (x=10 and 20) alloys for biomedical applications. The microstructure structure of Ti-10 wt.% Mo reveals (α″ + β) and (β + ω) phases; addition of Sn (Ti–Mo–Sn alloys) neutralised the ω phase and make the alloy more preferable for biomedical applications from a mechanical point of view.

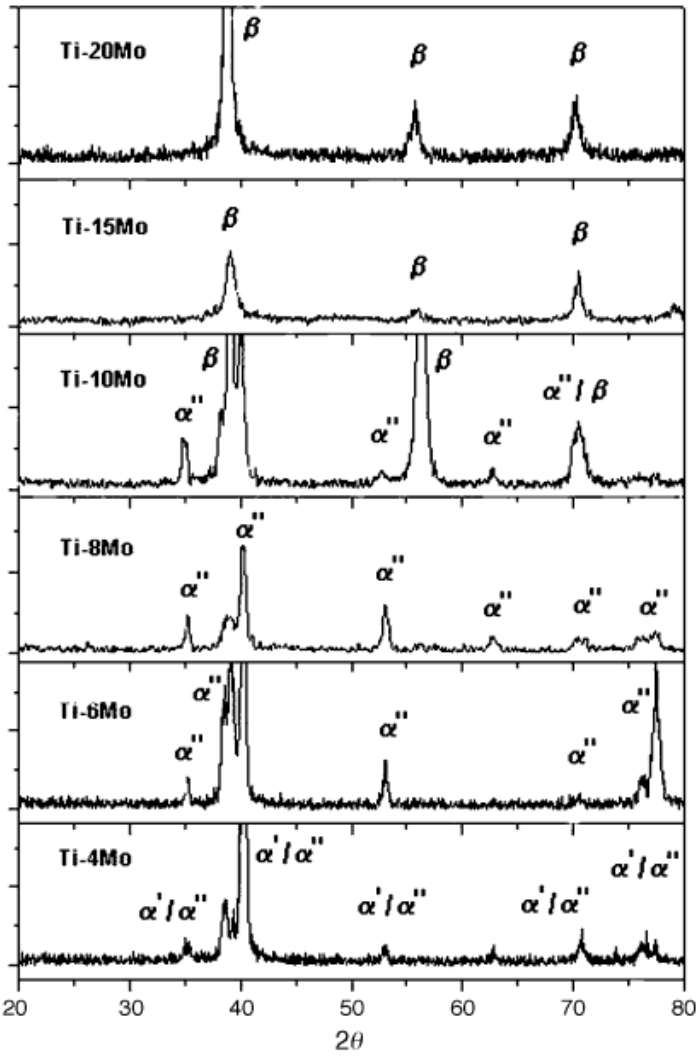

Figure 2.1.30: XRD diffractograms of Ti–Mo alloys from 4 to 20 wt.% Mo (Oliveira *et al.*, 2007).

Chen *et al*. (2006) experimented with Ti-*x*Mo (x=5,10,15 and 20 wt.%) alloys produced by arc-melting vacuum-pressure casting. It was found that Ti-5Mo consisted of the equiaxed crystal grains. At 10% Mo content, the equiaxed α crystal grains and fine needles β phase were found. When the Mo contents were 15%–20%, only the equiaxed β grains were observed. The lowest Elastic modulus was at 15 wt.% Mo concentration. Ti-10Mo was recommended for dental applications because the friction coefficient was the smallest and its wear track profile was very smooth, its depth and width were smaller for this alloy.

Júnior *et al.* (2011) noted that 15 wt.% Mo would yield optimum mechanical properties for biomedical applications. From the experimental results of Zhao *et al.* (2012) Ti–17Mo was

considered the best for spinal fixation applications because this alloy "*exhibits small springback and could be easily bent to the required shape during operation*".

Xie *et al. (*2015) produced porous Ti-xMo (x=4, 6, 8 and 10 wt.%) alloys from elemental powders by selective laser sintering method. They recognized that total porosity, pore size, open and closed pores depend entirely on the Mo content. Thus, the higher the Mo content the higher the above mention parameters. The mechanical properties of the porous structure do not only depend on the pore properties but also on the microstructure. Unexpectedly, samples with higher porosity value recorded higher Elastic modulus value. The authors explained that, although most literature has postulated that the mechanical properties of porous structures depend on porosity and density and thus mechanical properties decrease with increasing porosity. They noticed that in the case of Ti–(4–10 wt.% Mo) alloys microstructural effects play a significant role. The authors conducted a similar work by Xie *et al.* (2013) with Ti–(4–8 wt.% Mo) and obtained similar results, but noted in their earlier publication that the mechanical properties of the porous samples "*improved with the decrease of porosity*" as generally demonstrated by porous structures. This earlier statement does not tally with their current result; the authors prefer their latest explanation.

Collins *et al.* (2003) did detailed studies on microhardness and microstructural evolution of Ti-*x*Mo alloys produced by laser engineered net shaping (LENS™) process. A cylindrical compositional gradient samples of length 25 mm with varying Mo composition were manufactured from pure Ti to Ti–25 at.% Mo. The microstructure evolution indicated that as the Mo content increases the Ti-α phase decreases and the Ti-β phase increases. With the same magnification lens power, a series of backscattered SEM images were recorded in successively increasing Mo content (Figure 2.1.31a-f). A composition of Ti-0.8% Mo, produced a Widmanstätten α-Ti laths microstructure of different α orientations in a very small volume of β-Ti at the α-lath boundaries (Figure 2.1.31a). As the Mo content increased to 2.2% the volume fraction of β (*the lighter phase contrast in between the α-laths*) increased with a reduction in width of the α laths (Figure 2.1.31b). An intricate mixed multiple variants of the α-laths microstructure is noticed at 2.6% Mo content. The sharp variation from the Widmanstätten microstructure (Figure 2.1.31b) to the two phase distribution of the α laths within the β matrix (Figure 2.1.31c) could be explained by the solid-state

annealing phenomenon (thermo-physics processes) that normally occurs during LENS™ manufacturing process.

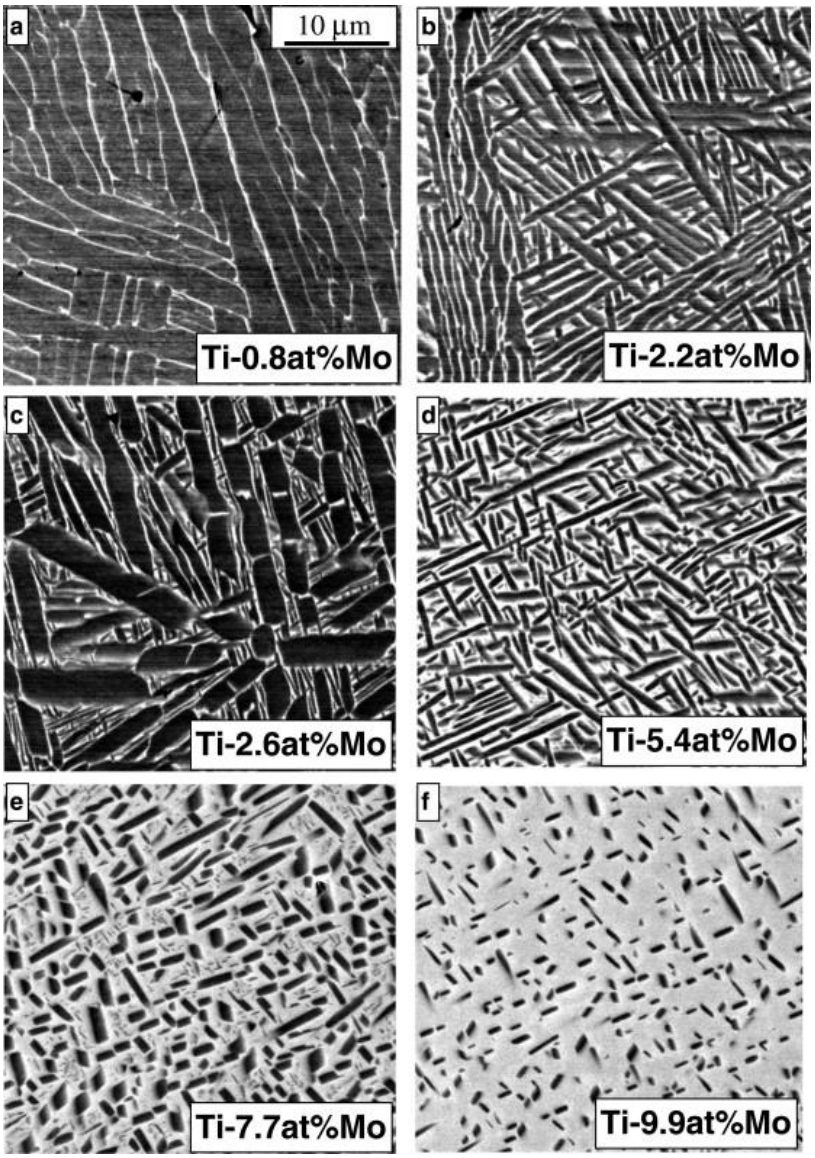

Figure 2.1.31: A series of backscatter SEM images from regions with progressively higher Mo content in the LENS™ deposited Ti–xMo (x= 0.8, 2.2, 2.6, 5.4, 7.7 and 9.9 at.%Mo) graded alloy (Collins *et al.*, 2003).

It was found the formation of prior β grain boundaries (Figure 2.1.32) perpendicular to the substrate surface. At a low Mo content (<at.% Mo) α precipitate at β grain boundaries in a thick continuous layer form, wetting the grain boundaries, while at a higher Mo composition (>5% Mo)

the thick continuous wetting layer reduces and form a discrete α precipitate at the β grain boundaries.

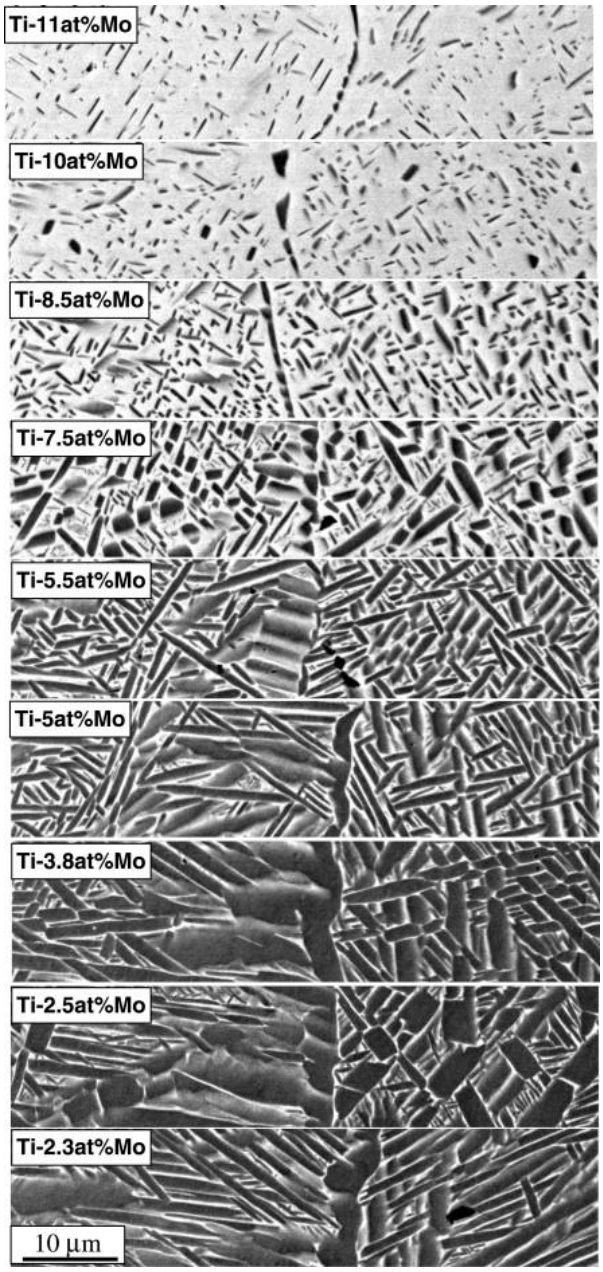

Figure 2.1.32: A series of backscatter SEM images tracing the microstructural variations along the same prior β columnar grain boundary with varying Mo content in the LENS™ Ti–*x*Mo graded alloy (Collins *et al.*, 2003).

Corrosion resistance of Ti-*x*Mo alloy in NaCl solution and Ringer solution *(potassium chloride (0.40g); calcium chloride dehydrate (0.27g); sodium chloride (6.00g); sodium lactate (3.17g); rest water up to 1000ml)* was studied by Magheru *et al.* (2013). It was noted that as the Mo content increases in the Ti-*x*Mo alloy, the rate of corrosion decreases significantly.

In terms of biocompatibility Ti–15Mo alloy seem to be acceptable for dental implant applications (Kumar & Narayanan, 2008). A survey of the literature reveals that the binary Ti15Mo alloy might be the most suitable for biomedical applications (Bowen, 1971; Disegi, 2003; Kumar & Narayanan, 2008; Júnior *et al.*, 2011; ATI Titanium Alloy Technical Data Sheet, 2014; Disegi *et al.*, 2016).

Ti15Mo alloy could be retained at room temperature as β or α+β alloy, based on the defined composition and the process route. At a nominal composition of 15 wt.% Mo the standard β phase annealing temperature is 800°C. The β transus temperature is documented as 750°C while the α+β annealing treatment temperature is reported as 725 °C (IMI Titanium 205, 2014). The thermal treatment at 800°C presents only β-phased microstructure upon rapid cooling (Figure 2.1.33a) while heat treatment at 725°C produces the α+β microstructure when cool slowly (Figure 2.1.33b) (Disegi *et al.*, 2016).

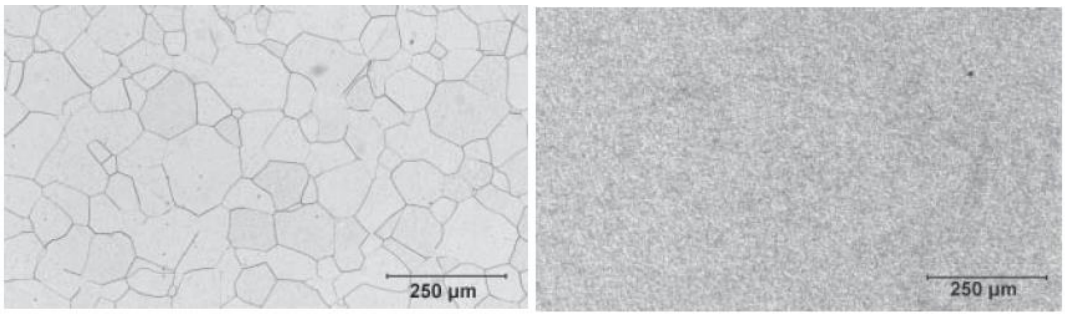

(a) (b)

Figure 2.1.33: Microstructure of Ti15Mo alloy (a) β-alloy (b) α+β alloy (Disegi, 2003).

The anneal-aged α+β Ti15Mo alloy microstructure (Figure 2.1.33b) is described as marble-like microstructure (Saito *et al.*, 2003). It is noted as a fine dispersion of α+β phase which does not

contain any continues α networks at prior β grains boundary nor a coarsened elongated α plates (Disegi *et al.*, 2016).

The Ti–Mo equilibrium phase diagram (Figure 2.1.34) indicates the transformation phases from α+β to β phase for various Mo at.% with the corresponding temperature. A highlight of the 15 at.% Mo is depicted in the phase diagram.

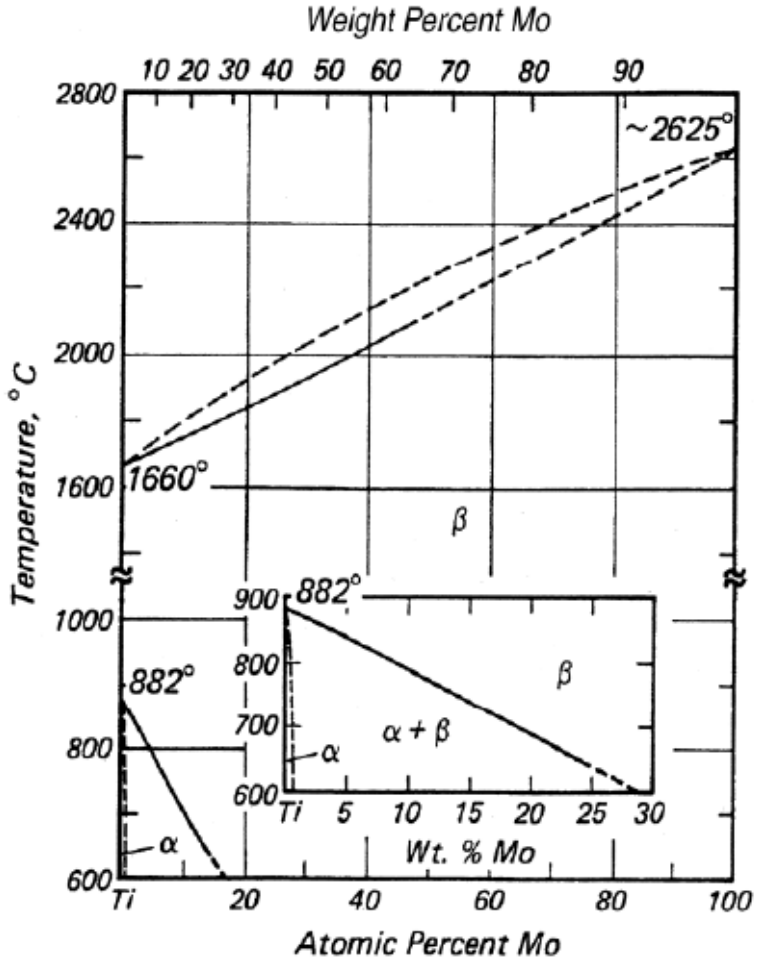

Figure 2.1.34: Ti-Mo binary phase diagram (Collings, 1988).

Disegi *et al*. (2016) annealed α+β Ti15Mo alloy at varied temperatures. It was found that the best combination of strength and ductility was obtained using an $\alpha + \beta$ annealing temperature of $705°C \pm 10°C$ followed by an aging treatment of $482°C \pm 10°C$. The mechanical properties obtained were more appropriate for high-strength implant applicationsas compared to Ti6Al4V alloy (Table 2.1.7).

Table 2.1.7: Mechanical properties of α+β Ti15Mo compared with Ti6Al4V after heat treatment (Disegi *et al.*, 2016)

Type of alloy	UTS (MPa)	0.2% YS (MPa)	Elongation 4D (%)
Ti15Mo (α+β)	1227	1130	16
Ti6Al4V	1103	1034	10

ATI (ATI Titanium Alloy Technical Data Sheet, 2014) reported that omega phase (ω) formation (embrittlement) is detrimental to the mechanical properties of Ti15Mo and should be avoided. This could be achieved by rapid cooling from the β-phased for the β-annealed condition or slow cooling below the β transus for the α+β condition. It was suggested following process routes of obtaining either β or α+β Ti15Mo alloy without ω phase. To obtain Ti15Mo β alloy, the alloy should be annealed in temperature range of 802 – 982 °C, hold for 0.5-1h and rapidly quench below 552 °C. A β alloy can also be produced by annealing at 816 °C for less than 10 minutes and rapidly quench below 552°C. α+β Ti15Mo alloy could be obtained by the above mentioned annealing temperatures and holding times at slow cooling rates below 552 °C. α+β Ti15Mo alloy could be produced alternatively by annealing below the β-transus temperature in the range of 538-649 °C, holding >4 hours and air cool.

Disegi *et al.* (2016) also proposed an optimum heat treatment process route to produce α+β Ti15Mo alloy. The ideal annealing and aging temperatures for Ti15Mo alloy for biomedical applications are "*705 °C±10 °C /1-hour minimum/water quench plus aging at 482 °C ±10 °C/4 hours/fan cool or faster quench*". Such annealing process would produce implants with low Elastic modulus and effective 'spring back' characteristics required for high strength implant applications.

A heat treatment at low temperatures (≤250°C) for a very long time (100 hours) could trigger ω phase formation (Bowen, 1971). Cardoso *et al*. (2014) heat treated Ti15Mo alloy at a relatively low temperature (250°C) for about 80 hours and found ω phase precipitation in the β matrix. At a higher temperature of aging (≥450 °C) the ω phase disappears after 12 hours of heat treatment.

The Ti15Mo alloy is very susceptible to contamination (hydrogen, oxygen, nitrogen, and carbon) during heat treatment. If not handled carefully, the alloy can be contaminated which would

adversely affect its ductility and notch sensitivity (ATI Titanium Alloy Technical Data Sheet, 2014). Recently Martins *et al*. (2016) investigated the effect of oxygen content on the mechanical properties of Ti-*x*Mo alloy. The results proved that the processed Ti-15Mo alloy with the least oxygen content had the lowest Elastic modulus.

2.1.3.2: DMLS Ti-xMo Alloys

The literature on DMLS manufactured parts is quite modest which have led to increasing in knowledge about the DMLS process. However, information about *in-situ* alloying by the DMLS process is sparse and almost non-existing for Ti-*x*Mo by DMLS.

Vrancken *et al*. (2014) *in-situ* alloyed Ti6Al4V-ELI with 10 wt.% Mo powder and focused on the solidification mechanism, microstructure, mechanical properties and response to heat treatment of the novel alloy. The results were compared to Ti6Al4V (ELI) manufactured by DMLS with the same process parameters. A cross sectional analysis of the microstructure reveals that the 10 wt.% of Mo has a significant effect on the microstructure. The expected columnar prior β grains which are normally observed in DMLS microstructure due to the layer wise building process and the partial remelting of the previously solidified layers (epitaxial growth) was completely absent. The Ti6Al4V-10Mo microstructure presents unmelted Mo particles distributed randomly in the β-titanium matrix (Figure 2.1.35).

Figure 2.1.35: BSE image of the top surface, showing compositional differences in the matrix due to rapid solidification and the low diffusion coefficient of Mo. The white particles are unmolten Mo dispersed randomly in the matrix (Vrancken *et al.,* 2014).

The Mo was not able to melt completely due to the thermophysical difference between the two materials. Mo has a melting point of 2623 °C while Ti6Al4V has a melting point of 1668 °C. Secondly the laser reflectance of Mo is higher than that of Ti (Lynch *et al.*, 1985). Ti6Al4V would absorb more laser radiation than Mo. These thermophysical differences induce the partial melting of the Mo leading to the formation of Mo particle – Ti matrix microstructure. Further analysis reveals that the solidification front change from the usual planar mode for Ti6Al4V to cellular solidification due to the severe solute distribution between liquid and solid phases. The mode of solidification contributed to the different microstructure and texture as compared to Ti6Al4V. The melt pool boundaries were delineated and within each grain a cellular substructure with an intercellular spacing of less than 1 μm was present.

Based on Murray (1981) experimental ideology that the β transus temperature lowers around 9 to 10°C per wt% Mo added, Vrancken *et al.* (2014) expected the β-transus temperature for Ti6Al4V+10Mo to be around 900 °C which was later validated through a heat treatment analysis. The heat treatment process eliminates the cellular substructure nature of the grains present in as build parts. The microhardness values decrease with increasing the annealing temperature. The as build samples were mechanically investigated. An Elastic modulus of 73 GPa with a remarkable elongation of 20% was recorded as compared to 7.3% of Ti6Al4V. The trade-off for the elongation was low yield stress of 858±16 MPa for Ti6Al4V+10Mo as compared to 1110± 9 MPa for Ti6Al4V.

Thus, in-situ alloying by DMLS could facilitate easier processing of many alloys, which would increase the material pallet for DMLS process. The possibility of tailoring alloying content to induce a particular microstructure and meeting a specific required mechanical or physical properties makes in-situ alloying via DMLS a prime technology of the day.

2.2: Additive Manufacturing of Porous Structures for Biomedical Applications

2.2.1: Introduction

Loosening of prosthetic joints is one of the main reasons for implant failure, due to the high Elastic modulus of metallic biomaterial (80-120 GPa) (Niinomi *et al.*, 2015). The Elastic modulus of human cancellous bone is <3 GPa and that of compact bone is between the ranges of 3-30 GP

(Long & Rack, 1998; Wen *et al.,* 2007; Parthasarathy *et al.*, 2010); as a result of this Elastic modulus mismatch, when a metallic implant is planted into a living bone, the metallic material bears the load without transmitting the load to the surrounding bone (*stress shielding effect*) which leads to implant failure (Barbas *et al.,* 2012).

Metals are considered the optimum choice for biomedical applications because of their structural advantages as compared to other biomaterials, with Ti-based alloys as the most preferable, due to its excellent specific strength, exceptional corrosion resistance, low weight, low toxicity, *etc.* (Niinomi, 2003, 2008; Zhou *et al.,* 2007; Mohammed *et al.,* 2014; Kulkarni *et al.,* 2014). Despite the outstanding biomechanical, physicochemical and biofunctionability properties of Ti and its alloys, it has a major drawback as a clinical biomaterial due to its high Elastic modulus and low ductility which would induce bone resorption (Hermawan *et al.,* 2011). However, there is a process called porosification of metal, which involves the introduction of a considerable number of interconnected pores into the material by additive manufacturing (AM) methods, in an attempt to reduce its Elastic modulus (Niinomi *et al.,* 2015). Another alternative to developing implants with low Elastic modulus is the production of beta Ti-based alloys, which have demonstrated a low Elastic modulus value of about 80 GPa, as discussed above.

Ti-based foams have also been produced with a low Elastic modulus between 40-60 GPa, but all these alternative results are still higher than the Elastic modulus of bone tissue (Mohammed *et al.,* 2014; Niinomi *et al.,* 2015). However, Van Bael *et al*. (2012) employed SLM technology to produce porous Ti-based (Ti6Al4V) implants with pores measured between 500 µm and 1000 µm in size with Elastic modulus ranging from 0.4-11 GPa, demonstrating that AM methods are possibly the only promising technology for producing implants with low elastic modulus that can mimic bone tissue.

Implants with such low Elastic modulus are recommended for areas of low bending stresses to ensure homogenous load transferred stress stimulation of the bone (Liu & Webster, 2007). The experimental work of Wieding *et al.* (2012) reveals that a low Elastic modulus implant could stimulate the growth of bone cells due to mechanical stimulus by physiological load application.

2.2.2: Porosity and Mechanical Properties

Mour *et al.* (2010) defined porosity of a material as "the percentage of void space in a solid material". Pores can be divided into three categories: closed pores *(pores that do not permit transportation of fluid through them),* blind pores *(pores that terminate inside the fabricated part)* and through pores (*pores that permit complete transportation of body fluid*) (Figure 2.2.1).

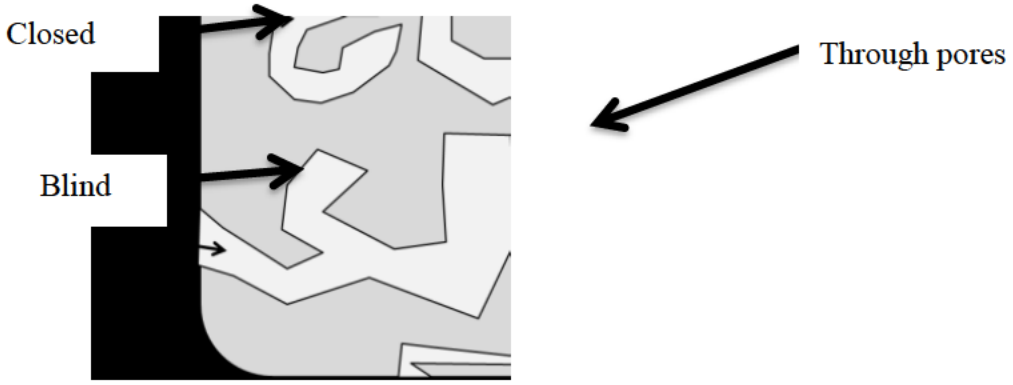

Figure 2.2.1: A schematic diagram of different types of pores (Stoffregen *et al.,* 2011).

The blind and open pores permit the transportation of fluid cells and bacteria between the implant and the surrounding tissues, but closed pores are surrounded by fully dense material and do not permit transmission of fluid (Mour *et al.,* 2010; Stoffregen *et al.,* 2011).

Li *et al.* (2014) and Miao & Sun (2009) indicated that porosity between the range of 1–100 μm is mostly observed in bone structures and is needed for optimum functionability. Those in the range of 100–350 μm are usually for bone ingrowth, and those between the range of 350–1000 μm have the function of reducing Elastic modulus. While those in the range of 350–3500 μm are normally useful during the surgical procedures for wiring-like sutures. The larger pores also provide a great surface area for cell attachment and a good medium of transportation of nutrients and metabolic waste out of the pores. The small pores would also enhance cartilage ingrowth. Mour *et al*. (2010) also noted that pore sizes of more than 100 μm are considered suitable for rapid bone ingrowth.

As noted by most of the previous reviews (Miao & Sun, 2009; Hannink & Arts, 2011; Wally *et al*., 2015), the optimum pore size value for bone ingrowth and fluid transportation is yet to be

determined. Nevertheless, there is an upper limit on porosity set by constraints associated with mechanical properties; hence any arbitrary increase in porosity of an implant would adversely affect its mechanical properties (Figure 2.2.2).

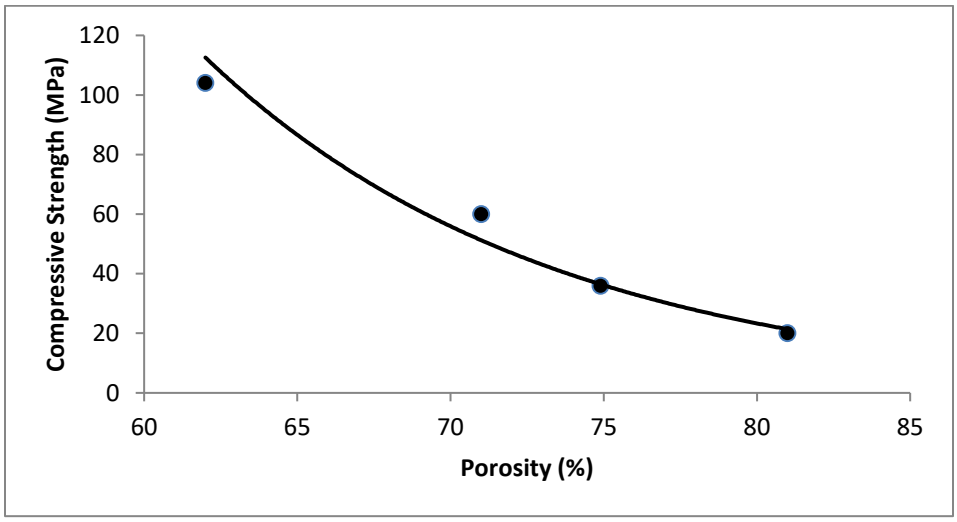

Figure 2.2.2: A graph of compressive strength decreasing as porosity increases (Data from Mullen *et al.*, 2009).

Parthasarathy *et al.* (2010) evaluated the mechanical properties of porous Ti-based implant fabricated by the Electron Bean Melting (EBM) process. The manufactured patient-specific custom porous implants have porosity ranging from 50%–70% with effective stiffness values ranging from 0.57±0.05 – 2.92±0.17 GPa. The authors concluded that the mechanical properties of the implants are very suitable for craniofacial applications. The experimental work of Lin *et al.* (2007) led to the manufacture of porous Ti implants with an average compressive modulus of 2.97±0.90 GPa, which is comparable to bone tissue.

The work of Harrysson *et al.* (2008) focused on design and fabrication of titanium hip stems by the EBM process with tailored mechanical properties that will reduce stress shielding. The porous Ti bone substitute structure has porosities ranging from 60% to 96.2%, with average modulus of 12 GPa which were close to the mechanical properties of compact bone.

Yavari *et al.* (2013) studied fatigue behaviour of porous titanium alloy manufactured by the selective laser melting process. Four different porous microarchitectures were produced with

porosities between 68 and 84% and the fatigue S–N curves of the four bone substitutes were determined. The authors found that generally, given the same absolute stress level, the fatigue life is much shorter for structures with higher porosity.

2.2.3: Manufacturing of Porous Ti-based Biomedical Objects by AM Methods

Some of the AM methods which have been used recently to manufacture porous bone substitute are: Direct Metal Laser Sintering (DMLS) or Selective Laser Melting (SLM), selective laser sintering (SLS), direct laser forming (DLF), electron beam melting (EBM), and laser engineered net shaping (LENS). AM technology could be used to produce intricate structures (Yadroitsev & Smurov, 2011; Niinomi *et al.*, 2015; Kim *et al*., 2014). By controlling the processing parameters, the porosity of the manufactured samples could be tailored to precisely predetermined dimensions. The ability to control the processing parameters would permit greater control over the final structure of very complex interconnected strut designs to produce customized tailored pore and strut sizes for a specific medical application. SLM technology enables a continuous connected pore network to be produced throughout the manufactured parts which is probably impossible with the traditional methods of fabrication. By controlling the pore size, shape, pore size distribution and interconnectivity the mechanical properties of the porous fabricated objects can be greatly tailored to desired values (Yadroitsev *et al.*, 2009; Cheng *et al.*, 2014).

The fundamental difference between the DMLS and EBM process is that the DMLS process uses a laser to melt/sinter the metallic powders while the EBM process uses an electron beam for the melting process. Both methods can be used to manufacture patient-specific implants to suit the patient morphology which does not required plastic deformation during surgery, contrary to implants manufactured by the conventional methods (Barbas *et al*., 2012). Implants manufactured by these methods have the advantage of graded composition and macrostructure in a controllable manner for a specific biomedical application (Stamp *et al.*, 2009). DMLS and EBM technologies have proven to manufacture highly porous micro-topography Ti-based alloy bone substitute with several hundred micrometres' accuracy (Fukuda *et al.*, 2011), which made available a large surface area for better bone-implant-contact micro-interlocking (Liu *et al*., 2015) without affecting the biocompatibility of the implant.

Pattanayak *et al*. (2011) used the DMLS to manufacture porous Ti metal structures similar to that of human cancellous bone with different porosities. Cancellous bone images data obtained from a CT scans were used to create three-dimensional CAD models of porous metallic structures. Fibre laser with a nominal beam diameter of 100 μm was used. To obtain optimum process parameters, a boundary contour beam of 58.5 W power was followed by a hatch beam of 117 W while a hatch space of 180 μm and a hatch offset of 20 μm were used. With a constant powder deposition layer of 30 μm thickness, the hatch lines were rotated with respect to the previous layer by 66.7° to melt the powder completely at a constant scanning speed of 225 mm s^{-1}. With powder particle size less than 45 μm, the biomimic Ti6Al4V cancellous-like structures manufactured have a porosity of 75–55% and a compressive strength of 35–120 MPa which were found similar to some bone structures in the body.

To establish basic data for developing a porous osteoinductive Ti alloy implant, Fukuda *et al*. (2011) melted Ti powder with a Yb fibre laser at a power of 117 W, at a scanning speed of 225 mm/s, a hatch spacing of 90 μm and a hatch offset 20 μm in an argon gas atmosphere. With a powder deposition thickness of 30 μm, they manufactured four cylindrical implants with lengths of 15 mm and diameters of 3.3 mm. The implants were made with longitudinal square channels acting as pores with different diagonal widths of 500, 600, 900, and 1200 μm. These were implanted in the dorsal muscles of eight mature beagle dogs (weight 10–11 kg), for periods of 16, 26, or 52 weeks. It was evident that the amount of bone formation increased with time and the total induced bone formation showed a tendency to increase with increasing pore size at 52 weeks. The record showed osteoinduction might occur at approximately 5 mm from both ends at 16 weeks and continue to 7 mm at 52 weeks, which is far above 2.5–3 mm noted in the research work of Fujibayashi *et al*. (2004), Habibovic *et al*. (2005) and Takemoto *et al*. (2005), probably due to the relatively bigger diameter (5-6 mm) but shorter length (10-11mm) of their experimental implants. They concluded that the longer length (15 mm) of their implant is what made the difference; hence a wider pore throat might be necessary for larger implants.

Barbas *et al*. (2012) used the DMLS method to produce porous titanium with a particular periodic internal architecture close to the mechanical properties of bone. Mechanical anisotropy of bone was their focus, and by adopting a porosity of 53% and pore sizes in the range of 860–1500 μm,

they produced porous implants from Commercially Pure Titanium (CpTi) mimicking the orthotropic properties of the human bone following several mechanical and geometrical criteria which could possibly permit bone ingrowth. Their efforts led to the manufacturing of porous Ti parts with mechanical properties mimicking those of human bone.

In the quest to determine the bone mass and bone density of newly formed bone, Nakano *et al*. (2011) conducted bone regenerative test by embedding novel unidirectional interconnected porous cylindrical implants of Ti6Al4V alloy manufactured by EBM method in rabbits. An Arcam, EBM S12 device with accelerating voltage, 60 kV; beam current, 2 mA; beam scan rate, 100 mm/s; lamination pitch, 0.1 mm with grating wall thickness of 0.73±0.11 mm was adopted. The porous manufactured implant has the ability to attach to bone over a long period of time without causing bone resorption. Parthasarathy *et al*. (2010) also focused on evaluating porous Ti6Al4V parts fabricated by EBM for use in craniofacial applications for cortical bone and load-bearing reconstruction. With porosity between 50% to 70% and pore sizes from 500 – 2000 μm respectively, well-interconnected porous implants which can facilitate tissue ingrowth were manufactured with elastic modulus values ranging between 0.57 to 2.92 GPa.

Matena *et al*. (2015) also demonstrated that bone formation is strongly dependent on fast vascularization of fluid through the interconnected pores of the implants by using DMLS technology to manufacture Ti6Al4V implant of pore size 250 μm to enable vessel ingrowth. The development of a scanning strategy for the manufacture of porous biomaterials by selective laser melting was experimented by Stamp *et al*. (2009). The porosity (pore size, pore distribution and interconnectivity) and mechanical properties of manufacture porous implants can be greatly controlled to a tailored value. Warnke *et al*. (2008) also mention that altering pore width of a Ti-based implant manufactured by DMLS can help tailor the mechanical properties of the implant for a particular biomedical application.

DMLS technology was used by Wang *et al.* (2010) to produce a Ti alloy implant with high porosity (~ 70 %), interconnected Ti walls and open porous structures with macroscopic pores (about 200–500 μm). The laser power and scanning speed were 1000 W and 0.02 m/s respectively. The authors noted that as the scanning speed increased from 0.01 to 0.03 m/s, the porosity increased, but then

decreased when the scan speed increased further to 0.05 m/s, which they attributed to laser input energy.

In order to investigate the influence of different porous structures on osteoinduction, Fujibayashi *et al.* (2004) manufactured porous metallic bioactive Ti structures by plasma sprayed or powder sintered method. Realizing that the conventional method does not produce well-defined concavities such as precise control porosity, pore size and interconnectivity as required for biomaterial objects, they performed another experiment in 2011 using an AM method, which resulted in well-defined concavities (Fukuda *et al.,* 2011), demonstrating that AM methods can produce substitutional porous bone structures with well-defined concavities (Figure 2.2.3).

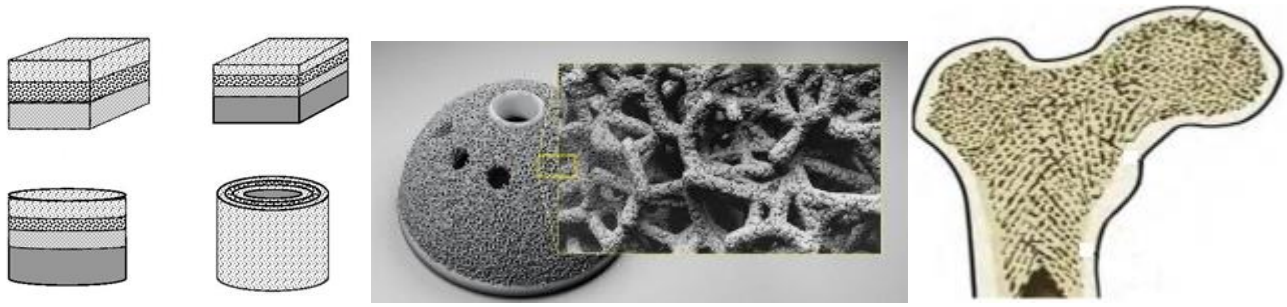

(a) (b) (c)

Figure 2.2.3: (a) Different types of graded pore structures, (b) Micro porous acetabular hip cup, (c) Porous nature of cancellous bone (Miao & Sun, 2009; Bankoff, 2012; Austin-Morgan, 2015).

As it can be learned from nature, the architectural nature of the human bones is of graded or gradient pores (2.2.4c), and it is only a similar graded or gradient implant that can suitably replace any affected part of the body (Simske *et al.,* 1997; Keaveny *et al.,* 2004; Miao & Sun, 2009; Choi *et al.,* 2009).

The capability of AM methods to manufacture a biomimic bone substitute of graded porosity was demonstrated by Lin *et al.,* (2012), who used SLS and SLM strategies to produce cylindrical Ti6Al4V specimens with “dense outer skin + porous inner core” structure to reflect the natural geometrical nature of bones. With a laser power of 170 W, they produced fully melted outer skin

of their biomimic implant samples and with laser power ranging from 43-85 W they produced sintered (partially melted) a graded porous inner core to form fully dense skin and gradient pore inner core prototype implants. The Elastic moduli of the samples were close to that of human bone. A graded or gradient porous structure by AM technologies depends on the laser energy, comprising laser power, scanning velocity, spacing between scan lines and powder layer thickness, which combine to determine the quantity of energy input into the material during the fabrication process. The variation of these fabrication parameters would control the solidification and cooling process to produce varied porosity. It is revealed that there are no automation universal optimum processing parameters. Careful selection of the principal processing parameters for specific desired mechanical properties is crucial in DMLS. If the amount of laser energy injected into the powder bed is too high, there would be excessive melting. On the contrary, if it is too low the powder would not melt completely (Yadroitsava *et al.,* 2015; Spears & Gold, 2016).

Li *et al.* (2010a) produced graded pore metallic implants by using 316L stainless steel. The investigation reveals that the porosity gradients depend majorly on the scanning speed; as the scanning speed increases, porosity increases (Figure 2.2.4).

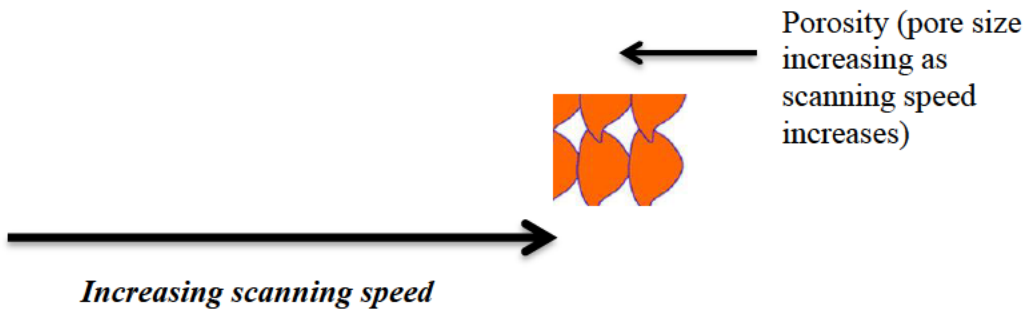

Figure 2.2.4: Schematic representation of porosity increasing as scanning speed increases (Li *et al.,* 2010a).

By scanning speeds of 50 mm/s to 1000 mm/s and laser beam power in the range of 20 W to 195 W, Emmelmann *et al.* (2011) manufactured Ti6Al4V implant with an osseointegrative surface using the DMLS method. Porosity between 68-87 % was obtained with powder deposition layers

of 30 microns, as a result of change in the energy inputs per unit length from 0.3 – 1.0 J/mm leading to change in beam diameter, which triggered the change in porosity (*graded pore*). The manufactured implants had the capacity to avoid the stress-shielding effect since their Elastic modulus ranges between 0.4–1.2 GPa.

The Elastic moduli of the porous structures decrease with increasing porosity (Figure 2.2.5). By using EBM Murr *et al.* (2009) also produced open cellular porous cells with different cell wall structures (Figure 2.2.6)

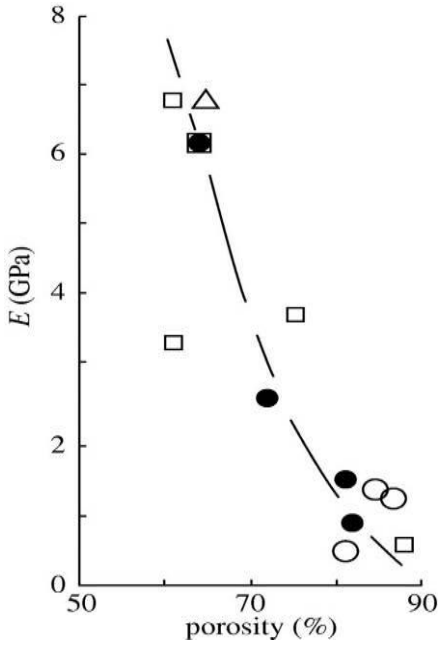

Figure 2.2.5: A graph demonstrating reduction in elastic modulus as porosity increases (Murr *et al.*, 2010).

Traini *et al*. (2008) investigated the possibility of using SLS technology to manufacture functional porous isoelastic dental implants by using graded master alloy powder (Ti6Al4V) with a particle size of 1–10 µm to produce a dense core implant with porous surface. It was concluded that the Elastic modulus of the graded dental implant porous surface is comparable to that of bone tissue. Tolochko *et al*. (2002) also manufactured dental root implants by selectively melting Ti powders to produce a dense core and selectively sintering an irregular porous Ti powder shell on the dense core.

Most of the porous implants produced currently are of dense core with porous surface (Figure 2.2.6b) (Ryan *et al.*, 2006; Mangano *et al.*, 2014). Simske *et al*. (1997) declared in their review work "*Porous materials for bone engineering*" that *"an area of future clinical research will be the construction of implants with gradients of porosity*". They also mention that "*the ultimate porous bone implant, perhaps, is yet to be designed; however, there is reason to believe that such a material is not long in coming*".

(a) (b) (c)

Figure 2.2.6: (a) Porous Ti6Al4V implant manufactured by EBM method; (b) Dense core implant with porous surface CAD model of graded porous implant (Li *et al.*, 2010; Murr *et al.*, 2010).

2.3: Summary

The literature review reveals that Ti-based alloys have been used extensively for biomedical applications especially Ti6Al4V alloy. Ti-based alloys are preferred for biomedical applications due to their exceptional biomechanical properties. Their mechanical properties depend largely on the type of crystal structure, composition, method of production and thermo-mechanical process. The β titanium alloys are gaining preference over other type of titanium alloys due to their inherent capability of producing implants of low Elastic modulus. The binary Ti–Mo has taken the canter stage among the β-titanium alloys because of its low Elastic modulus, good mechanical properties, excellent corrosion resistance and well characterized biological response.

To mitigate the implant failure as a result of implant infections the conventional methods of manufacturing has been used extensively to produce titanium coated implants. But the differences in material matrix do not permit strong adhesion of the antibacterial agents onto the implant surface. It came to light that the versatility of DMLS technology could be used to produce copper bearing titanium implants to prevent bacterial infections of implants. The effects of DMLS process parameters on manufactured parts were extensively discussed. Tailored heat treatment of Ti-based alloys manufactured by DMLS were also identified since the microstructure of DMLS parts are diametrically opposed to that of the conventional methods.

The current research data has emphatically pointed out that porous Ti-based implants could be manufactured by DMLS methods. There is a perceived idea presented in the literature that the fundamental principles of producing graded or gradient porous implants by DMLS method has come to maturity. But more needs to be done to harness the various ideas to reality, by practically using the DMLS method to manufacture reproducible non-homogenous porous implants, possibly in one step at an "affordable" cost for biomedical applications. Micromechanical interlocking fixation improvement could be achieved by bone tissue growing into and through a porous matrix of metal to ensure a stronger bone-implant-contact (BIC) which would enhance rapid osseointegration and a suitable Elastic modulus. Pore-graded implants are more desirable than homogenous pores, due to their ability to mimic natural bone tissue.

2.4: References

Ahmed, T. & Rack, H.J., 1998. Phase transformations during cooling in α+ β titanium alloys. *Materials Science and Engineering:* A, 243(1), pp. 206-211.

Ahn, D., Kim, H. & Lee, S., 2009. Surface roughness prediction using measured data and interpolation in layered manufacturing. *Journal of Materials Processing Technology*, 209(2), pp. 664-671.

Anam, M. A., Dilip, J.J.S., Pal, D. & Stucker, B., 2014. Effect of scan pattern on the microstructural evolution of inconel 625 during selective laser melting. *Annual International Solid Freeform Fabrication Symposium*, Austin, Texas, 2014.

Andres, C., Gysler, A. & Lutjering, G., 1993. *Titanium '92 Science and Technology*. Ed. Froes, F.H & Caplan, I., Warrendale, PA.

Aoki, T., Okafor, I.C.I., Watanabe, I., Hattori, M., Oda, Y. & Okabe, T., 2004. Mechanical properties of cast Ti-6Al-4V-xCu alloys. *Journal of Oral Rehabilitation*, 31(11), pp. 1109-1114.

Askeland, D.R. & Wright, W.J., 2013. *Essentials of materials science & engineering*. Michigan: Cengage Learning, 624 p.

ASTM F1472 - *08e1.Standard Specification for Wrought Titanium-6Aluminum-4Vanadium Alloy for Surgical Implant Applications*, UNS R56400 (2008), DOI:10.1520/F1472-08E01.

ASTM F1108-14, *Standard Specification for Titanium-6Aluminum-4Vanadium Alloy Castings for Surgical Implants*, UNS R56406, (2014), DOI: 10.1520/F1108-14.

ASTM F2066 - 13e1. *Standard Specification for Wrought Titanium-15 Molybdenum Alloy for Surgical Implant Applications*, UNS R58150 (2013) DOI: 10.1520/F2066.

ASTM F136 – 13. *Standard Specification for Wrought Titanium-6Aluminum-4Vanadium ELI (Extra Low Interstitial) Alloy for Surgical Implant Applications*, UNS R56401 (2013) DOI: 10.1520/F0136.

ATI Titanium Alloy Technical Data Sheet, 2014. *ATI 15Mo*, Pittsburgh, PA USA: ATI.

Attar, H., Calin, M., Zhang, L.C., Scudino, S. & Eckert, J., 2014. Manufacture by selective laser melting and mechanical behaviour of commercially pure titanium. *Material Science Engineering A*, 593, pp. 170–177.

Austin-Morgan, T., 2015. Eureka – the site for engineering design (Transforming what's possible for 3D-printed orthopaedic implants). [Online] Available at: http://www.eurekamagazine.co.uk [Accessed 06 01 2016].

Babu, B., 2008. *Physically based model for plasticity and creep of Ti-6Al-4V*. Licentiate thesis. Luleå University of Technology.

Bankoff, A.D.P., 2012. *Biomechanical characteristics of the bone*. INTECH Open Access Publisher. ISBN: 978-953-307-638-6.

Barbas, A., Bonnet, A.S., Lipinski, P., Pesci, R. & Dubois, G., 2012. Development and mechanical characterization of porous titanium bone substitutes. *Journal of the Mechanical Behavior of Biomedical Materials*, 9, pp. 34-44.

Beal, J. D., Boyer, R. & Sanders, D., 2006. *Forming of titanium and titanium alloys.* Metalworking: Sheet Forming (ASM Handbook).

Becker, T., van Rooyen, M. & Dimitrov, D., 2015. Heat treatment of Ti-6Al-4V produced by lasercusing. *South African Journal of Industrial Engineering*, 26(2), pp. 93-103.

Becker, T., Beck, M. & Scheffer, C., 2015. Microstructure and mechanical properties of direct metal laser sintered Ti-6AL-4V. *South African Journal of Industrial Engineering*, 26(1), pp. 1-10.

Benedetti, M. & Fontanari, V., 2004. The effect of bi-modal and lamellar microstructures of Ti-6Al-4V on the behaviour of fatigue cracks emanating from edge-notches. *Fatigue & Fracture of Engineering Materials & Structures,* 27(11), pp.1073-1089.

Bertol, L.S., Júnior, W.K., da Silva, F.P. & Aumund-Kopp, C., 2010. Medical design: direct metal laser sintering of Ti–6Al–4V. *Materials & Design*, 31(8), pp. 3982-3988.

Bhaskaran, T.A., Krishnan, R.V. & Ranganathan, S., 1995. On the decomposition of β phase in some rapidly quenched titanium-eutectoid alloys. *Metallurgical and Materials Transactions A*, 26(6), pp. 1367-1377.

Bosco, R., Van Den Beucken, J., Leeuwenburgh, S. & Jansen, J., 2012. Surface engineering for bone implants: a trend from passive to active surfaces. *Coatings*, 2(3), pp. 95-119.

Bowen, A.W., 1971. Omega phase embrittlement in aged Ti-15% Mo. *Scripta Metallurgica*, 5(8), pp. 709-715.

Cardoso, F.F., Cremasco, A., Contieri, R.J., Lopes, E.S.N., Afonso, C.R.M. & Caram, R., 2011. Hexagonal martensite decomposition and phase precipitation in Ti–Cu alloys. *Materials & Design*, 32(8), pp. 4608-4613.

Cardoso, F.F., Ferrandini, P.L., Lopes, E.S., Cremasco, A. & Caram, R., 2014. Ti–Mo alloys employed as biomaterials: effects of composition and aging heat treatment on microstructure and mechanical behavior. *Journal of the Mechanical Behavior of Biomedical Materials*, 32, pp. 31-38.

Chen, Y.Y., Xu, L.J., Liu, Z.G., Kong F.T., Chen, Z-Y., 2006. Microstructures and properties of titanium alloys Ti-Mo for dental use. *Transactions of Nonferrous Metals Society of China*, 16, pp. s824-s828.

Cheng, A., Humayun, A., Cohen, D.J., Boyan, B.D. & Schwartz, Z., 2014. Additively manufactured 3D porous Ti-6Al-4V constructs mimic trabecular bone structure and regulate osteoblast proliferation, differentiation and local factor production in a porositand surface roughness dependent manner. *Biofabrication*, 6(4), pp.045007.

Choi, S.W., Zhang, Y. & Xia, Y., 2009. Fabrication of microbeads with a controllable hollow interior and porous wall using a capillary fluidic device. *Advanced Functional Materials*, 19(18), pp. 2943-2949.

Collings, E.W., 1988. *Introduction to titanium alloy design*. ASM International, Alloying, pp. 257-370.

Collins, P.C., Banerjee, R., Banerjee, S. & Fraser, H.L., 2003. Laser deposition of compositionally graded titanium–vanadium and titanium–molybdenum alloys. *Materials Science and Engineering: A*, 352(1), pp. 118-128.

Contieri, R.J., Lopes, E.S.N., Caram, R., Devaraj, A., Nag, S. & Banerjee, R., 2014. Effects of cooling rate on the microstructure and solute partitioning in near eutectoid Ti–Cu alloys. *Philosophical Magazine*, 94(21), pp. 2350-2371.

Disegi, J., 2003. *Wrought Titanium-15% Molybdenum Implant Material. Original Instruments and Implants of the Association for the Study of International Fixation —AO ASIF*. West Conshohocken.

Disegi, J.A., Roach, M.D., McMillan, R.D. & Shultzabarger, B.T., 2016. Alpha plus beta annealed and aged Ti–15 Mo alloy for high strength implant applications. *Journal of Biomedical Materials Research Part B: Applied Biomaterials.* 105 (7), pp. 2010–2018.

Dobromyslov, A.V. & Elkin, V.A., 2001. Martensitic transformation and metastable β-phase in binary titanium alloys with d-metals of 4–6 periods. *Scripta Materialia,* 44(6), pp. 905-910.

Donachie, M.J., 2000. *Titanium: A Technical Guide, 2nd Edition*. Michigan: ASM International.

Duleba, B., Greškovič, F. & Sikora, J.W., 2011. Materials and finishing methods of DMLS manufactured parts. *Transfer Inovácií,* 21, pp. 143-148.

Elias, C.N., Lima, J.H.C., Valiev, R. & Meyers, M.A., 2008. Biomedical applications of Titanium and its alloys. *Journal of Minerals, Metals and Materials Society,* 60(3), pp. 46-49.

Emmelmann, C., Scheinemann, P., Munsch, M. & Seyda, V., 2011. Laser additive manufacturing of modified implant surfaces with osseointegrative characteristics. *Physics Procedia*, 12, pp. 375-384.

EOS, 2014. *Material data sheet, EOS Titanium Ti64*: EOS GmbH - Electro Optical Systems.

Fujibayashi, S., Neo, M., Kim, H.M., Kokubo, T. & Nakamura, T., 2004. Osteoinduction of porous bioactive titanium metal. *Biomaterials,* 25(3), pp. 443-450.

Fukuda, A., Takemoto, M., Saito, T., Fujibayashi, S., Neo, M., Pattanayak, D.K., Matsushita, T., Sasaki, K., Nishida, N., Kokubo, T. & Nakamura, T., 2011. Osteoinduction of porous Ti implants with a channel structure fabricated by selective laser melting. *Acta Biomaterialia*, 7(5), pp. 2327-2336.

Gammon, L.M., Briggs, R.D., Packard, J.M., Batson, K.W., Boyer, R. & Domby, C.W., 2004. *Metallography and microstructures of titanium and its alloys*. Materials Park, OH: ASM International.

Gaspar, B., 2012. *Microstructural characterization of Ti-6Al-4V and its relationship to sample geometry*. Master's thesis. Cal Poly – San Luis.

Gharbi, M., Peyre, P., Gorny, C., Carin, M., Morville, S., Le Masson, P., Carron, D. & Fabbro, R., 2013. Influence of various process conditions on surface finishes induced by the direct metal

deposition laser technique on a Ti–6Al–4V alloy. *Journal of Materials Processing Technology*, 213(5), pp. 791-800.

Goodman, S.B., Yao, Z., Keeney, M. & Yang, F., 2013. The future of biologic coatings for orthopaedic implants. *Biomaterials*, 34(13), pp. 3174-3183.

Guo, S., Lu, Y., Wu, S., Liu, L., He, M., Zhao, C., Gan, Y., Lin, J., Luo, J., Xu, X. & Lin, J., 2017. Preliminary study on the corrosion resistance, antibacterial activity and cytotoxicity of selective-laser-melted Ti6Al4V-xCu alloys. *Materials Science and Engineering: C*, 72, pp. 631-640.

Habibovic, P., Li, J., Van Der Valk, C.M., Meijer, G., Layrolle, P., Van Blitterswijk, C.A. & De Groot, K., 2005. Biological performance of uncoated and octacalcium phosphate-coated Ti6Al4V. *Biomaterials*, 26(1), pp. 23-36.

Hague, R., Campbell, I. & Dickens, P., 2003. Implications on design of rapid manufacturing. *Proceedings of the Institution of Mechanical Engineers, Part C. Journal of Mechanical Engineering Science*, 217(1), pp. 25-30.

Hannink, G. & Arts, J.C., 2011. Bioresorbability, porosity and mechanical strength of bone substitutes: what is optimal for bone regeneration? *Injury*, 42, pp. S22-S25.

Hanzl, P., Zetek, M., Bakša, T. & Kroupa, T., 2015. The Influence of processing parameters on the mechanical properties of SLM parts. *Procedia Engineering*, 100, pp. 1405-1413.

Harrysson, O. L., Cansizoglu, O., Marcellin-Little, D.J., Cormier, D.R. & West, H.A., 2008. Direct metal fabrication of titanium implants with tailored materials and mechanical properties using electron beam melting technology. *Materials Science and Engineering: C*, 28(3), pp. 366-373.

Hermawan, H., Ramdan, D. & Djuansjah, J. R., 2011. *Metals for biomedical applications*. Intech Open Access Publisher, pp. 411-430.

Hiromoto, S., 2008. Corrosion of metallic biomaterials in cell culture environments. *The Electrochemical Society Interface*, 17(2), p. 41.

Ho, W.F., Ju, C.P. & Lin, J.C., 1999. Structure and properties of cast binary Ti–Mo alloys. Biomaterials. *Biomaterials*, 20(22), pp. 2115-2122.

Huang, Q., Liu, X., Yang, X., Zhang, R., Shen, Z. & Feng, Q., 2015. Specific heat treatment of selective laser melted Ti–6Al–4V for biomedical applications. *Frontiers of Materials Science*, 9(4), pp. 373-381.

IMI Titanium 205, 2014. *Alloy Data Sheet*, IMI Titanium Ltd, Birmingham England: ATI.

International Titanium Association, 2015. Developing tomorrow applications… building a stronger titanium industry. [Online] Available at: www.titanium.org [Accessed 14 10 2015].

IPCS, 1998. *Environmental Health Criteria 200, International Programme on Chemical Safety*. Geneva: World Health Organization.

Josefson, D., 2001. US surgeons implant new artificial heart. *British medical journal*, 323(7304), pp. 66.

Júnior, M., Severino, J.R., Nogueira, R.A., Araújo, R.O.D., Donato, T.A.G., Arana-Chavez, V.E., Claro, A.P.R.A., Moraes, J.C.S., Buzalaf, M.A.R. & Grandini, C.R., 2011. Preparation and characterization of Ti-15Mo alloy used as biomaterial. *Materials Research*, 14(1), pp. 107-112.

Keaveny, T.M., Morgan, E.F. & Yeh, O.C., 2004. *Bone mechanics. Standard Handbook of Biomedical Engineering and Design*. McGraw-Hill.

Kelly, S.M., 2004. *Thermal and microstructure modeling of metal deposition processes with application to Ti-6Al-4V*. Doctoral thesis: Virginia Polytechnic Institute and State University.

Kikuchi, M., Takada, Y., Kiyosue, S., Yoda, M., Woldu, M., Cai, Z., Okuno, O. & Okabe, T., 2003. Mechanical properties and microstructures of cast Ti–Cu alloys. *Dental Materials*, 19(3), pp. 174-181.

Kim, T.B., Yue, S., Zhang, Z., Jones, E., Jones, J.R. & Lee, P.D., 2014. Additive manufactured porous titanium structures: Through-process quantification of pore and strut networks. *Journal of Materials Processing Technology*, 214(11), pp. 2706-2715.

Kinnear, A., Dzogbewu, T. C., Yadroitsava, I. & Yadroitsev, I., 2016. *In-situ* alloying process of ti6al4v-xcu structures by direct metal laser sintering. *Proceedings of the 17th International conference Rapid Product Development Association of South Africa*, 2-4 November 2016, Vaal University of Technology Vanderbijlpark, South Africa.

Kleszczynski, S., Ladewig, A., Friedberger, K., zur Jacobsmühlen, J., Merhof, D. & Witt, G., 2015. Position dependency of surface roughness in parts from Laser Beam Melting Systems. *In Proceedings of the 26th Internation Solid Freeform Fabrication (SFF) Symposium*, Austin Texas.

Knowles, C.R., Becker, T.H. & Tait, R.B., 2012. The effect of heat treatment on the residual stress levels within direct metal laser sintered Ti-6Al-4V as measured using the hole-drilling strain gauge method. *Proceedings of the 13th International conference Rapid Product Development Association of South Africa*, Sun City, South Africa.

Kobryn, P.A. & Semiatin, S.L., 2001. The laser additive manufacture of Ti-6Al-4V. *Journal of The Minerals, Metals & Materials Society*, 53(9), pp. 40-42.

Król, M. & Tański, T., 2016. Surface quality research for Selective Laser Melting of Ti-6Al-4V alloy. *Archives of Metallurgy and Materials*, 61(3), pp. 1291-1296.

Król, M., Kujawa, M., Dobrzański, L. A. & Tański, T., 2014. Influence of technological parameters on additive manufacturing steel parts in Selective Laser Sintering. *Archives of Materials Science and Engineering*, 67(2), pp. 84-92.

Kruth, J. P., Badrossamay, M., Yasa, E., Deckers, J., Thijs, L. & Van Humbeeck, J., 2010. Part and material properties in selective laser melting of metals. *In Proceedings of the 16th International Symposium on Electromachining*, Belgium.

Kruth, J.P., Yasa, E. & Deckers, J., 2009. Experimental investigation of laser surface re-melting for the improvement of selective laser melting process. *Proceedings of Solid Free Fabrication Symposium*, Austin, Texas, USA, 321-322.

Kulkarni, M., Mazare, A., Schmuki, P. & Iglič, A., 2014. Biomaterial surface modification of titanium and titanium alloys for medical applications. *Nanomedicine*, 111, pp. 111.

Kumar, S. & Narayanan, T.S., 2008. Corrosion behaviour of Ti–15Mo alloy for dental implant applications. *Journal of Dentistry*, 36(7), pp. 500-507.

Leuders, S., Thöne, M., Riemer, A., Niendorf, T., Tröster, T., Richard, H.A. & Maier, H.J., 2013. On the mechanical behaviour of titanium alloy TiAl6V4 manufactured by selective laser melting: Fatigue resistance and crack growth performance. *International Journal of Fatigue*, 48, pp. 300-307.

Leyens, C. & Peters, M., 2003. *Fundamentals and Applications: Titanium and Titanium Alloys*. Weinheim: Wiley-VCH.

Li, R., Liu, J., Shi, Y., Du, M. and Xie, Z., 2010a. 316L stainless steel with gradient porosity fabricated by selective laser melting. *Journal of Materials Engineering and Performance*, 19(5), pp. 666-671.

Li, X., Wang, C., Zhang, W. & Li, Y., 2010b. Fabrication and compressive properties of Ti6Al4V implant with honeycomb-like structure for biomedical applications. *Rapid Prototyping Journal*, 16(1), pp. 44-49.

Li, Y., Yang, C., Zhao, H., Qu, S., Li, X. & Li, Y., 2014. New Developments of Ti-Based Alloys for Biomedical Applications. *Materials*, pp. 1709-1800.

Lin, C.Y., Wirtz, T., LaMarca, F. & Hollister, S.J., 2007. Structural and mechanical evaluations of a topology optimized titanium interbody fusion cage fabricated by selective laser melting process. *Journal of Biomedical Materials Research Part A*, 83(2), pp. 272-279.

Lin, W.S. Starr, T.L., Harris, B.T., Zandinejad, A. & Morton, D., 2012. Additive manufacturing technology (direct metal laser sintering) as a novel approach to fabricate functionally graded titanium implants: preliminary investigation of fabrication parameters. *The International Journal of Oral & Maxillofacial Implants*, 28(6), pp. 1490-1495.

Liu, H. & Webster, T.J., 2007. Bioinspired nanocomposites for orthopedic applications. *Nanotechnology for the Regeneration of Hard and Soft Tissues*, pp. 8.

Liu, J., Han, G., Pan, S., Ge, Y., Feng, H. & Shen, Z., 2015. Biomineralization stimulated peri-titanium implants prepared by selective laser melting. *Journal of Materiomics*, 1(3), pp. 253-261.

Liu, J., Zhang, X., Wang, H., Li, F., Li, M., Yang, K. & Zhang, E., 2014. The antibacterial properties and biocompatibility of a Ti–Cu sintered alloy for biomedical application. *Biomedical Materials*, 9(2), p. 025013.

Liu, X., Chu, P. K. & Ding, C., 2004. Surface modification of titanium, titanium alloys, and related materials for biomedical applications. *Materials Science and Engineering: R: Reports*, 47(3), pp. 49-121.

Long, M. & Rack, H.J., 1998. Titanium alloys in total joint replacement—a materials science perspective. *Biomaterials*, 19(18), pp. 1621-1639.

Longhitano, G.A., Larosa, M.A., Munhoz, A.L.J., Zavaglia, C.A.D.C. & Ierardi, M.C.F., 2015. Surface finishes for Ti-6Al-4V alloy produced by Direct Metal Laser Sintering. *Materials Research*, 18(4), pp. 838-842.

Lütjering, G., 1998. Influence of processing on microstructure and mechanical properties of (α+ β) titanium alloys. *Materials Science and Engineering: A*, 243(1), pp. 32-45.

Lütjering, G., 1999. Property optimization through microstructural control in titanium and aluminum alloys. *Materials Science and Engineering: A*, 263(2), pp. 117-126.

Lynch, D.W., Hunter, W.R. & Palik, E.D., 1985. *Handbook of optical constants of solids*. Orlando: Academic press.

Ma, Z., Ren, L., Liu, R., Yang, K., Zhang, Y., Liao, Z., Liu, W., Qi, M. & Misra, R.D.K., 2015. Effect of heat treatment on Cu distribution, antibacterial performance and cytotoxicity of Ti–6Al–4V–5Cu Alloy. *Journal of Materials Science & Technology*, 31(7), pp. 723-732.

Magheru, A.M., Ghiban, B., Ghiban, N. & Miculescu, M., 2013. Corrosion resistance of new TiMo alloys for biomedical applications. *UPB Scientific Bulletin, Series B: Chemistry and Materials Science* 75(3), pp.187-196.

Malinov, S., Guo, Z., Sha, W. & Wilson, A., 2001. Differential scanning calorimetry study and computer modeling of $\beta \Rightarrow \alpha$ phase transformation in a Ti-6Al-4V alloy. *Metallurgical and Materials Transactions A*, 32(4), pp. 879-887.

Mangano, F., Chambrone, L., Van Noort, R., Miller, C., Hatton, P. & Mangano, C., 2014. Direct metal laser sintering titanium dental implants: a review of the current literature. *International Journal of Biomaterials.*

Mani, M., Donmez, A., Feng, S., Moylan, S. & Fesperman, R., 2015. Measurement Science Needs for Real-time Control of Additive Manufacturing Powder Bed Fusion Processes. *National Institute of Standards and Technology, Gaithersburg, MD, Standard No. NISTIR, 8036*.

Martins, J.R.S., Araújo, R.O., Nogueira, R.A. & Grandini, C.R., 2016. Internal friction and microstructure of Ti and Ti-Mo alloys containing Oxygen. *Archives of Metallurgy and Materials*, 61(1), pp. 25-30.

Matena, J., Petersen, S., Gieseke, M., Kampmann, A., Teske, M., Beyerbach, M., Escobar, H.M., Haferkamp, H., Gellrich, N.C. & Nolte, I., 2015. SLM produced porous titanium implant improvements for enhanced vascularization and osteoblast seeding. *International Journal of Molecular Sciences*, 16(4), pp. 7478-7492.

Matweb, 2015. Human Compact Bone, Haversian System. Available at: www.matweb.com [Accessed 14 10 2015]

Miao, X. & Sun, D., 2009. Graded/Gradient porous biomaterials. *Materials*, 3(1), pp. 26-47.

Mierzejewska, Ż.A., 2015. Process optimization variables for direct metal laser sintering. *Advances in Materials Science*, 15(4), pp. 38-51.

Mohammed, M.T., Khan, Z.A. & Siddiquee, A.N., 2014. Beta titanium alloys: the lowest elastic modulus for biomedical applications: a review. *International Journal of Chemicla Molecular Nuclear Material Metallurgy Engineering*, 8, pp. 788-793.

Mour, M., Das, D., Winkler, T., Hoenig, E., Mielke, G., Morlock, M.M. & Schilling, A.F., 2010. Advances in porous biomaterials for dental and orthopaedic applications. *Materials*, 3(5), pp. 2947-2974.

Mouritz, A.P., 2012. *Introduction to aerospace materials. 2nd edition*. New Delhi: Elsevier.

Mullen, L., Stamp, R.C., Brooks, W.K., Jones, E. & Sutcliffe, C.J., 2009. Selective laser melting: A regular unit cell approach for the manufacture of porous, titanium, bone in-growth constructs, suitable for orthopedic applications. *Journal of Biomedical Materials Research Part B: Applied Biomaterials*, 89(2), pp. 325-334.

Mumtaz, K. & Hopkinson, N., 2010. Selective laser melting of Inconel 625 using pulse shaping. *Rapid Prototyping Journal*, 16(4), pp. 248-257.

Murr, L. E., Gaytan, S.M., Medina, F., Lopez, H., Martinez, E., Machado, B.I., Hernandez, D.H., Martinez, L., Lopez, M.I., Wicker, R.B. & Bracke, J., 2010. Next-generation biomedical implants using additive manufacturing of complex, cellular and functional mesh arrays. *Philosophical Transactions of the Royal Society of London A: Mathematical, Physical and Engineering Sciences*, 368(1917), pp. 1999-2032.

Murr, L.E., Quinones, S.A., Gaytan, S.M., Lopez, M.I., Rodela, A., Martinez, E.Y., Hernandez, D.H., Martinez, E., Medina, F. & Wicker, R.B., 2009. Microstructure and mechanical behavior of Ti–6Al–4V produced by rapid-layer manufacturing, for biomedical behavior of Ti–6Al–4V produced by rapid-layer manufacturing, for biomedical applications. *Journal of the Mechanical Behavior of Biomedical Materials*, 2(1), pp. 20-32.

Murray, J.L., 1981. The Mo− Ti (Molybdenum-Titanium) system. *Bulletin of Alloy Phase Diagrams*, 2(2), pp. 185-192.

Nakano, T., Fujitani, W., Ishimoto, T., Lee, J.W., Ikeo, N., Fukuda, H. & Kuramoto, K., 2011. Formation of new bone with preferentially oriented biological apatite crystals using a novel cylindrical implant containing anisotropic open pores fabricated by the electron beam melting (EBM) method. *ISIJ International*, 51(2), pp. 262-268.

Nalla, R.K., Boyce, B.L., Campbell, J.P., Peters, J.O. & Ritchie, R.O., 2002. Influence of microstructure on high-cycle fatigue of Ti-6Al-4V: bimodal vs. lamellar structures. *Metallurgical and Materials Transactions A*, 33(13), pp. 899-918.

Nasab, M. B., Hassan, M. R. & Sahari, B. B., 2010. Metallic biomaterials of knee and hip - A Review. *Trends Biomater. Artif. Organs*, 24(1), pp. 69-82.

Niinomi, M., 1998. Mechanical properties of biomedical titanium alloys. *Materials Science and Engineering: A*, 243(1), pp. 231-236.

Niinomi, M., 2002. Recent metallic materials for biomedical applications. *Metallurgical and Materials Transactions A*, 33(3), pp. 477-486.

Niinomi, M., 2003. Recent research and development in titanium alloys for biomedical applications and healthcare goods. *Science and Technology of Advanced Materials*, 4(5), pp. 445–454.

Niinomi, M., 2008. Biologically and mechanically biocompatible titanium alloys. *Materials Transactions*, 49(10), pp. 2170-2178.

Niinomi, M., Liu, Y., Nakai, M., Liu, H. & Li, H., 2016. Biomedical titanium alloys with Young's moduli close to that of cortical bone. *Regenerative biomaterials*, 3(3), pp. 173–185.

Niinomi, M., Narushima, T. & Nakai, M., 2015. *Advances in Metallic Biomaterials: Tissues, Materials and Biological Reactions. 3rd edition*. Berlin: Springer.

Oliveira, N. T., Aleixo, G., Caram, R. & Guastaldi, A. C., 2007. Development of Ti–Mo alloys for biomedical applications: microstructure and electrochemical characterization. *Materials Science and Engineering: A*, 452, pp. 727-731.

Oliveira, N.T.C. & Guastaldi, A.C., 2008. Electrochemical behavior of Ti–Mo alloys applied as biomaterial. *Corrosion Science*, 50(4), pp. 938-945.

Padmavathi, D.A., 2011. Potential energy curves & material properties. *Materials Sciences and Applications,* 2(2), pp. 97.

Parthasarathy, J., Starly, B., Raman, S. & Christensen, A., 2010. Mechanical evaluation of porous titanium (Ti6Al4V) structures with electron beam melting (EBM). *Journal of the Mechanical Behavior of Biomedical Materials,* 3(3), pp. 249-259.

Pattanayak, D.K., Fukuda, A., Matsushita, T., Takemoto, M., Fujibayashi, S., Sasaki, K., Nishida, N., Nakamura, T. & Kokubo, T., 2011. Bioactive Ti metal analogous to human cancellous bone: fabrication by selective laser melting and chemical treatments. *Acta Biomaterialia,* 7(3), pp. 1398-1406.

Petzow, G., 1999. *Metallographic etching: techniques for metallography, ceramography, plastography. 2nd edition*: ASM International.

Pyka, G., Burakowski, A., Kerckhofs, G., Moesen, M., Van Bael, S., Schrooten, J. & Wevers, M., 2012. Surface modification of Ti6Al4V open porous structures produced by additive manufacturing. *Advanced Engineering Materials,* 14(6), pp. 363-370.

Pyka, G., Kerckhofs, G., Papantoniou, I., Speirs, M., Schrooten, J. and Wevers, M., 2013. Surface roughness and morphology customization of additive manufactured open porous Ti6Al4V structures. *Materials,* 6(10), pp. 4737-4757.

Qazi, J.I., Rahim, J., Fores, F.H., Senkov, O.N. & Genc, A., 2001. Phase transformations in Ti-6Al-4V-xH alloys. *Metallurgical and Materials Transactions A,* 32(10), pp. 2453-2463.

Raabe, D., Sander, B., Friák, M., Ma, D. & Neugebauer, J., 2007. Theory-guided bottom-up design of β-titanium alloys as biomaterials based on first principles calculations: Theory and experiments. *Acta Materialia,* 55(13), p. 4475–4487.

Raines, A.L., Olivares-Navarrete, R., Wieland, M., Cochran, D.L., Schwartz, Z. & Boyan, B.D., 2010. Regulation of angiogenesis during osseointegration by titanium surface microstructure and energy. *Biomaterials,* 31(18), p. 4909–4917.

Reed-Hill, R. E. & Abbaschian, R., 1973. *Physical metallurgy principles. 3rd edition*. Boston: PWS Publishing Company.

Ren, L., Ma, Z., Li, M., Zhang, Y., Liu, W., Liao, Z. & Yang, K., 2014. Antibacterial properties of Ti–6Al–4V–xCu alloys. *Journal of Materials Science & Technology,* 30(7), pp. 699-705.

RMI Titanium Company [online], 2015. *Titanium Armor*. Available at www.titanium.org/resource/resmgr/Technical_Library/RMI_Metallography_brochure.pdf [Accessed 28 January 2016].

Ryan, G., Pandit, A. & Apatsidis, D. P., 2006. Fabrication methods of porous metals for use in orthopaedic applications. *Biomaterials,* 27(13), pp. 2651-2670.

Saito, T., Furuta, T., Hwang, J.H., Kuramoto, S., Nishino, K., Suzuki, N., Chen, R., Yamada, A., Ito, K., Seno, Y. & Nonaka, T., 2003. Multifunctional alloys obtained via a dislocation-free plastic deformation mechanism. *Science,* 300(5618), pp. 464-467.

Sakamoto, M., Watanabe, H., Higashi, H. & Kubosawa, H., 2014. *Titanium alloy stem as a cause for adverse reaction to metal debris after bipolar hemiarthroplasty*, Case Reports in Orthopedics, 2014 (4), ID 209461.

Semiatin, S. L., Seetharaman, V. & Weiss, I., 1997. The thermomechanical processing of alpha/beta titanium alloys. *Journal of Materials,* 49(6), pp. 33-39.

Shi, D. & Gibson, I., 1998. Surface finishing of selective laser sintering parts with robot. *In Proceedings of the 9th Solid Freeform Fabrication Symposium,* Austin, Texas (pp. 27-35).

Shifeng, W., Shuai, L., Qingsong, W., Yan, C., Sheng, Z. & Yusheng, S., 2014. Effect of molten pool boundaries on the mechanical properties of selective laser melting parts. *Journal of Materials Processing Technology*, 214(11), pp. 2660-2667.

Sieniawski, J., Ziaja, W., Kubiak, K. & Motyka, M., 2013. Microstructure and mechanical properties of high strength two-phase titanium alloys. *Titanium Alloys-Advances in Properties Control.* Eds. Sieniawski, J., Ziaja, W. InTech, pp. 69-80.

Simchi, A. & Asgharzadeh, H., 2004. Densification and microstructural evaluation during laser sintering of M2 high speed steel powder. *Materials Science and Technology,* 20(11), pp. 1462-1468.

Simske, S. J., Ayers, R. A. & Bateman, T. A., 1997. Porous materials for bone engineering. *In Materials science forum,* 250, pp. 151-182.

Song, B., Dong, S., Zhang, B., Liao, H. & Coddet, C., 2012. Effects of processing parameters on microstructure and mechanical property of selective laser melted Ti6Al4V. *Materials & Design*, 35, pp. 120-125.

Souza, S.A., Afonso, C.R.M., Ferrandini, P.L., Coelho, A.A. & Caram, R., 2009. Effect of cooling rate on Ti–Cu eutectoid alloy microstructure. *Materials Science and Engineering: C*, 29(3), pp. 1023-1028.

Spears, T.G. & Gold, S.A., 2016. In-process sensing in selective laser melting (SLM) additive manufacturing. *Integrating Materials and Manufacturing Innovation*, 5(1), p. 2.

Spierings, A. B., Herres, N. & Levy, G., 2011. Influence of the particle size distribution on surface quality and mechanical properties in AM steel parts. *Rapid Prototyping Journal*, 17(3), pp. 195-202.

Stamp, R., Fox, P., O'neill, W., Jones, E. & Sutcliffe, C., 2009. The development of a scanning strategy for the manufacture of porous biomaterials by selective laser melting. *Journal of Materials Science: Materials in Medicine,* 20(9), pp. 1839-1848.

Stoffregen, H., Fischer, J., Siedelhofer, C. & Abele, E., 2011. Selective laser melting of porous structures. *In Proceedings of the 22nd Annual International Solid Freeform Fabrication (SFF) Symposium*, University of Texas, Austin.

Sun, Q.Y., Yu, Z.T., Zhu, R.H. & Gu, H.C., 2004. Mechanical behavior and deformation mechanisms of Ti–2.5 Cu alloy reinforced by nano-scale precipitates at 293 and 77 K. *Materials Science and Engineering: A*, 364(1), pp. 159-165.

Sung, B. S., Park, T. E. & Yun, Y. H., 2015. Microstructures and electrochemical behavior of Ti-Mo alloys for biomaterials. *Advances in Materials Science and Engineering*, 2015.

Takemoto, M., Fujibayashi, S., Neo, M., Suzuki, J., Kokubo, T. & Nakamura, T., 2005. Mechanical properties and osteoconductivity of porous bioactive titanium. *Biomaterials,* 26(30), pp. 6014-6023.

Taufik, M. & Jain, P. K., 2013. Role of build orientation in layered manufacturing: a review. *International Journal of Manufacturing Technology and Management*, 27(1-3), pp. 47-73.

Thijs, L., Verhaeghe, F., Craeghs, T., Van Humbeeck, J. & Kruth, J.P., 2010. A study of the microstructural evolution during selective laser melting of Ti–6Al–4V. *Acta Materialia*, 58(9), pp. 3303-3312.

Thöne, M., Leuders, S., Riemer, A., Tröster, T. & Richard, H.A., 2012. Influence of heat-treatment on selective laser melting products–eg Ti6Al4V. *In Solid Freeform Fabrication Symposium SFF*, Austin, Texas.

Tolochko, N.K., Savich, V.V., Laoui, T., Froyen, L., Onofrio, G., Signorelli, E. & Titov, V.I., 2002. Dental root implants produced by the combined selective laser sintering/melting of titanium powders. *Journal of Materials Design and Applications*, 216(4), pp. 267-270.

Traini, T., Mangano, C., Sammons, R.L., Mangano, F., Macchi, A. & Piattelli, A., 2008. Direct laser metal sintering as a new approach to fabrication of an isoelastic functionally graded material for manufacture of porous titanium dental implants. *Dental Materials*, 24(11), pp. 1525-1533.

Van Bael, S., Chai, Y.C., Truscello, S., Moesen, M., Kerckhofs, G., Van Oosterwyck, H., Kruth, J.P. & Schrooten, J., 2012. The effect of pore geometry on the in vitro biological behavior of human periosteum-derived cells seeded on selective laser-melted Ti6Al4V bone scaffolds. *Acta Biomaterialia*, 8(7), pp. 2824-2834.

Van Zyl I., Yadroitsava I., Yadroitsev I., 2016. Residual stress in Ti6Al4V objects produced by direct metal laser sintering. *The South African Journal of Industrial Engineering*, 27(4), pp. 134-141.

Voort, G., 2003. *Using Microstructural Analysis to Solve Practical Problems.* Lake Bluff, Illinois: Buehler Ltd.

Vrancken, B., Thijs, L., Kruth, J. P. & Van Humbeeck, J., 2014. Microstructure and mechanical properties of a novel β titanium metallic composite by selective laser melting. *Acta Materialia*, 68, pp. 150-158.

Vrancken, B., Thijs, L., Kruth, J. P. & Van, H. J., 2012. Heat treatment of Ti6Al4V produced by Selective Laser Melting: microstructure and mechanical properties. *Journal of Alloys and Compounds*, 541, pp. 177-185.

Wally, Z.J., van Grunsven, W., Claeyssens, F., Goodall, R. & Reilly, G.C., 2015. Porous Titanium for dental implant applications. *Metals*, 5(4), pp. 1902-1920.

Wang, Y., Shen, Y., Wang, Z., Yang, J., Liu, N. & Huang, W., 2010. Development of highly porous titanium scaffolds by selective laser melting. *Materials Letters*, 64(6), pp. 674-676.

Warnke, P.H., Douglas, T., Wollny, P., Sherry, E., Steiner, M., Galonska, S., Becker, S.T., Springer, I.N., Wiltfang, J. and Sivananthan, S., 2008. Rapid prototyping: porous titanium alloy scaffolds produced by selective laser melting for bone tissue engineering. *Tissue Engineering Part C: Methods*, 15(2), pp. 115-124.

Weiss, I. & Semiatin, S. L., 1998. Thermomechanical processing of beta titanium alloys—an overview. *Materials Science and Engineering: A*, 243(1), pp. 46-65.

Wen, C. E., Yamada, Y., Nouri, A. & Hodgson, P. D., 2007. Porous titanium with porosity gradients for biomedical applications. *In Materials science forum, Trans Tech Publications*, 539, pp. 720-725.

Wieding, J., Jonitz, A. & Bader, R., 2012. The effect of structural design on mechanical properties and cellular response of additive manufactured titanium scaffolds. *Materials*, 5(8), pp. 1336-1347.

Xie, F., He, X., Cao, S., Mei, M. & Qu, X., 2013. Influence of pore characteristics on microstructure, mechanical properties and corrosion resistance of selective laser sintered porous Ti–Mo alloys for biomedical applications. *Electrochimica Acta*, 105, pp. 121-129.

Xie, F., He, X., Lv, Y., Wu, M., He, X. & Qu, X., 2015. Selective laser sintered porous Ti–(4–10) Mo alloys for biomedical applications: Structural characteristics, mechanical properties and corrosion behaviour. *Corrosion Science*, 95, pp. 117-124.

Yadroitsava I., Grewar S., Hattingh D., Yadroitsev I., 2015a. Residual stress in SLM Ti6Al4V alloy specimens. *Materials Science Forum*, 828-829, pp. 305-310.

Yadroitsava, I., Els, J., Booysen, G. & Yadroitsev, I., 2015. Peculiarities of single track formation from TI6AL4V alloy at different laser power densities by selective laser melting. *South African Journal of Industrial Engineering*, 26(3), pp. 86-95.

Yadroitsev, I. & Smurov, I., 2011. Surface morphology in selective laser melting of metal powders. *Physics Procedia*, 12, pp. 264-270.

Yadroitsev, I., Bertrand, P. & Smurov, I., 2007. Parametric analysis of the selective laser melting process. *Applied Surface Science*, 253(19), pp. 8064-8069.

Yadroitsev, I., Shishkovsky, I., Bertrand, P. & Smurov, I., 2009. Manufacturing of fine-structured 3D porous filter elements by selective laser melting. *Applied Surface Science*, 255(10), pp. 5523-5527.

Yadroitsev, I., Yadroitsava, I., Bertrand, P. & Smurov, I., 2012. Factor analysis of selective laser melting process parameters and geometrical characteristics of synthesized single tracks. *Rapid Prototyping Journal*, 3(18), pp. 201-208.

Yao, X., Sun, Q. Y., Xiao, L. & Sun, J., 2009. Effect of Ti_2Cu precipitates on mechanical behavior of Ti–2.5 Cu alloy subjected to different heat treatments. *Journal of Alloys and Compounds*, 484(1), pp. 196-202.

Yasa, E. & Kruth, J. P., 2008. Experimental study of the combined process of selective laser melting and selective laser erosion. *In Proceedings of the Rapid 2008 Conference & Exposition*. Florida

Yasa, E., Demir, F., Akbulut, G., Cızıoğlu, N. & Pilatin, S., 2014. Benchmarking of different powder-bed metal fusion processes for machine selection in additive manufacturing. *In Proceedings of International Solid Freeform Fabrication Symposium.* Austin Texas.

Yasa, E., Kempen, K., Kruth, J.P., Thijs, L. & Van Humbeeck, J., 2010. Microstructure and mechanical properties of maraging steel 300 after selective laser melting. *In Solid Freeform Fabrication Symposium Proceedings.* Austin Texas.

Yasa, E., Poyraz, O., Solakoglu, E.U., Akbulut, G. & Oren, S., 2016. A Study on the stair stepping effect in Direct Metal Laser Sintering of a Nickel-based superalloy. *Procedia CIRP*, 45, pp. 175-178.

Yavari, S. A., Wauthlé, R., van der Stok, J., Riemslag, A.C., Janssen, M., Mulier, M., Kruth, J.P., Schrooten, J., Weinans, H. & Zadpoor, A.A., 2013. Fatigue behavior of porous biomaterials manufactured using selective laser melting. *Materials Science and Engineering: C,* 33(8), pp. 4849-4858.

Zhang, E., Li, F., Wang, H., Liu, J., Wang, C., Li, M. & Yang, K., 2013. A new antibacterial titanium-copper sintered alloy: preparation and antibacterial property. *Material Science Engineering: C Material Biology*, 33(7), pp. 4280-7.

Zhao, L., Chu, P. K., Zhang, Y. & Wu, Z., 2009. Antibacterial coatings on titanium implants. *Journal of Biomedical Materials Research Part B: Applied Biomaterials*, 91(1), pp. 470-480.

Zhao, X., Niinomi, M., Nakai, M. & Hieda, J., 2012. Beta type Ti–Mo alloys with changeable Young's modulus for spinal fixation applications. *Acta Biomaterialia*, 8(5), pp. 1990-1997.

Zhou, Y. L. & Luo, D. M., 2011. Microstructures and mechanical properties of Ti–Mo alloys cold-rolled and heat treated. *Materials Characterization*, 62(10), pp. 931-937.

Zhou, Y.L., Niinomi, M., Akahori, T., Nakai, M. & Fukui, H., 2007. Comparison of various properties between titanium-tantalum alloy and pure titanium for biomedical applications. *Materials Transactions*, 48(3), pp. 380-384.

CHAPTER 3: MATERIALS AND METHODS

3.1: Introduction

This chapter gives a detailed description of the various powder materials, a manufacturing machine, and measuring equipment used during the experimental work in this research. For repeatability of a scientific investigation, the capacity of the various machines and the characteristic of the materials used for an experiment must be properly known. The fundamental principles of the manufacturing machine (EOSINT M 280) and the various items for measuring equipment were described. The powder characteristics, the accuracy of the manufacturing machine and the measuring equipment would have a direct impact on the results.

3.2: Materials

3.2.1: Powder Characteristics

For the parts manufactured by additive manufacturing to be consistent, predictable, reliable and repeatable the input material (metallic powders) must be characterized and standardized. Powder characterization for additive manufacturing is very important and especially for manufacturing biological object where the powder is converted directly (layer by layer) into a functional part. Powder properties such as size, morphology (shape), surface area, porosity and impurity content can have a direct effect on the manufacturing process and the mechanical properties of the final part (Spierings *et al.,* 2011; Schade *et al.,* 2014; Dawes *et al.,* 2015).

Benson & Snyders (2015) listed major powder parameters (Figure 3.2.1) that should be taken into consideration when characterizing a metallic powder for additive manufacturing. They mention that powder characterization is an extremely obligatory step in the additive manufacturing process to ensure total quality and consistency in the mechanical prosperities of the manufactured parts.

Figure 3.2.1: Major powder characterization parameters for AM (Benson & Snyders, 2015).

The relationships between the aforementioned powder characteristics and their cumulative effects on a manufactured parts are extensively discussed in the literature (McGeary, 1961; Zou & Yu, 1996; Simchi, 2004; German & Park, 2008; Liu *et al.*, 2011; Vincent *et al.*, 2012; Chang & Zhao, 2013; Schade *et al.*, 2014; Clayton, 2014; Dawes *et al.*, 2015).

3.2.2: Characterization of the Employed Powders

It was not possible to characterize the whole batch of the powders due to the large lot sizes, therefore small fractions of the selected powders were examined to represent the characteristics of the bulk powder. The powders were selected under motion to ensure that the sample represents the entire batch of powder (Cooke & Slotwinski, 2012). As already mention in the first chapter, the studies generally comprised of three main sections of experimental investigations, hence three sets of powders were used:

1. Ti6Al4V (ELI)
2. Cp Ti and Mo
3. Ti6Al4V (ELI) and Cu

3.2.2.1: Ti6Al4V (ELI) Powder

Employed Ti6Al4V (ELI) powder perfectly fulfils the ASTM F1472 requirement of the maximum concentration of impurities (Table 3.2.1: Chemical composition of Ti6Al4V (ELI) powder (in weight %). The typical physical and mechanical properties of the Ti6Al4V alloy are shown in Table 3.2.2: Typical physical and mechanical properties of wrought Ti6Al4V (ELI). The morphology of the gas atomized Ti6Al4V is represented in Figure 3.2.3.

Table 3.2.1: Chemical composition of Ti6Al4V (ELI) powder (in weight %)

Ti		Al	V	O	N	H	Fe	C
	ASTM standard for Ti6Al4V (ELI) alloy, grade 23							
88.1 - 91		5.5-6.5	3.5-4.5	≤0.13	≤0.030	≤0.0125	≤0.25	≤0.080
	Employed powder							
89.263		6.31	4.09	0.12	0.009	0.003	0.20	0.005

Table 3.2.2: Typical physical and mechanical properties of wrought Ti6Al4V (ELI)

Property	Ti6Al4V (ELI)
Density, Kgm^{-3}	4430
Melting point, ^oC	1604 - 1660
Solidus, ^oC	1604
Liquidus, ^oC	1660
Beta Transus ^oC	980
Specific heat, $J{\cdot}kg^{-1}K^{-1}$	526
Thermal conductivity, $Wm^{-1}K^{-1}$	6.7
Ultimate tensile strength, MPa	860
Yield strength, MPa	790
Elasticity modulus, GPa	113.8
Shear modulus, GPa	44.0
Elongation at break, %	14-15%
Notched Tensile Strength MPa	1450
Hardness, Vickers	341
Poison ration	0.342
Fracture Toughness	75 MPa-m½

(AZO, 2015)

The 10^{th}, 50^{th} and 90^{th} percentiles of equivalent diameter (weighted by volume) of the Ti6Al4V ELI powder were d_{10}=12.64 μm, d_{50}=22.93 μm and d_{90}=37.03 μm respectively (Figure 3.2.2).

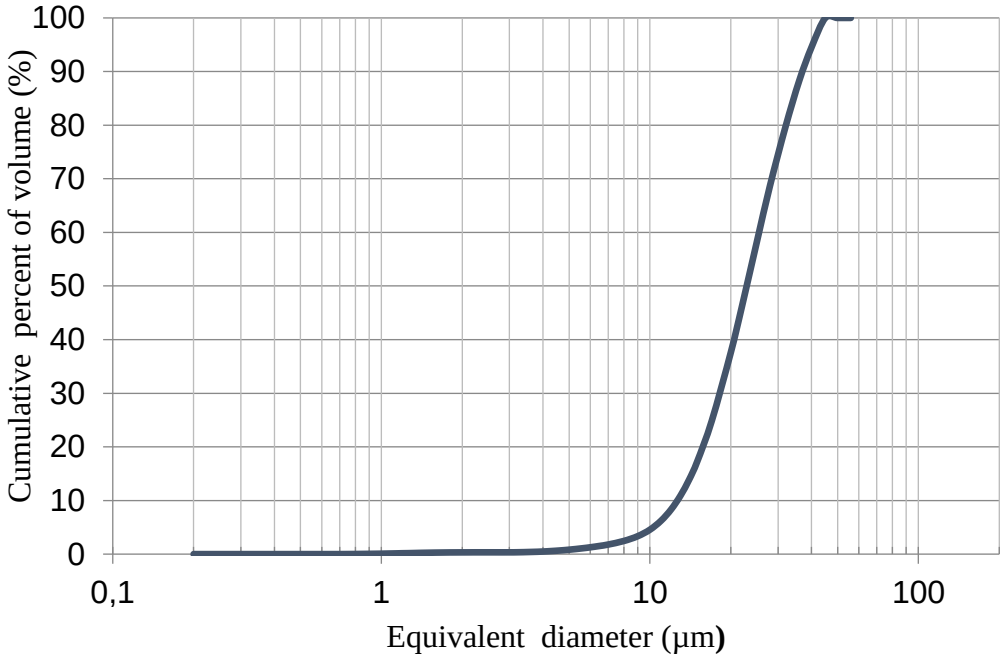

Figure 3.2.2: Particle size distributions for employed Ti6Al4V ELI.

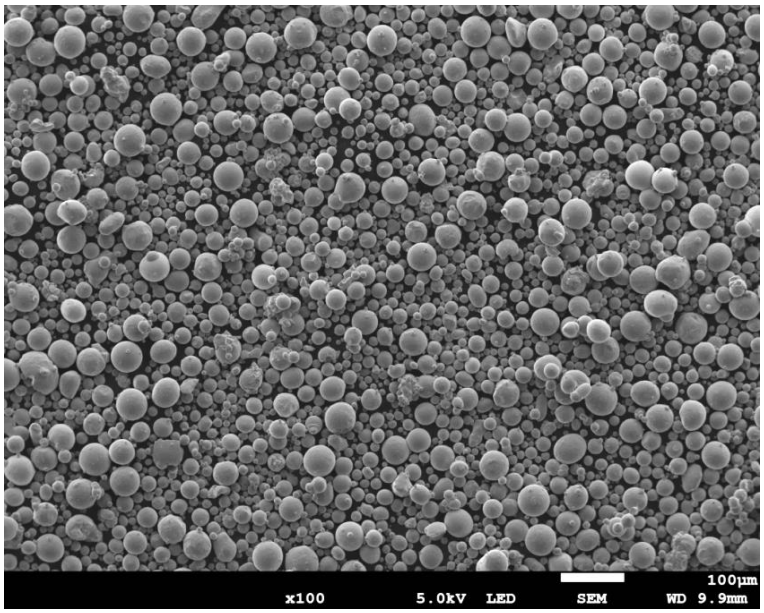

Figure 3.2.3: SEM micrograph of the employed Ti6Al4V powder.

3.2.2.2: Copper Powder

Copper has been extensively used as a constituent element for various metal alloys and it is a trace dietary mineral element in the body. Copper was one of the earliest metals to be extracted and have contributed immensely to civilization and industrialization. It is generally characterized by high ductility, electrical and thermal conductivity. It has a wide range of applications in the construction industry, power generation and transmission, automobile and production of industrial machine, etc. (Gayle *et al.*, 1998).

Copper has emerged as antibacterial agent which makes it very important to the current studies (O'gorman & Humphreys, 2012; Zhang *et al.*, 2013; Liu *et al.*, 2014). The antibacterial properties of copper have made it a metal of choice for frequently touched surfaces such as doorknobs and handles where the antibacterial properties of copper mitigate the transfer of germs and diseases (Berman, 2015), hence producing copper bearing titanium alloy would eliminate bacterial adhesion to implant surfaces (O'gorman & Humphreys, 2012). Copper occurs in different grades and the amount of impurities present in each type of grade differs, however in its pure forms it contains ≥ 99.3% Cu (Harrer, 2016). Copper has a face-centred cubic (*fcc)* structure. Typical physical and mechanical properties for oxygen-free pure Cu are shown in Table 3.2.3.

Table 3.2.3: Typical physical and mechanical properties of Cu

Property	Cu
Density, Kgm^{-3}	8890 - 8940
Melting point, ^oC	1083
Solidus, ^oC	1065
Liquidus, ^oC	1086
Beta Transus ^oC	
Specific heat, $J{\cdot}kg^{-1}K^{-1}$	387
Thermal conductivity, $Wm^{-1}K^{-1}$	398-401
Ultimate tensile strength, MPa	220
Yield strength, MPa	70
Elasticity modulus, GPa	115
Share modulus GPa	44.0
Elongation at break, %	60%
Notched Tensile Strength MPa	
Hardness, Vickers	75.0 - 105
Poison ration	0.310
Fracture Toughness	

(Everhart, 1975; MatWeb, 1996; Davis, 2001; AZO, 2015)

The chemical composition of the employed Cu (–45 µm) powder shows 99.9% pure Cu purity. The 10th, 50th and 90th percentiles of equivalent diameter (weighted by volume) of the powder are d_{10}=9.45 µm, d_{50}=21.9 µm and d_{90}=37.54 µm, respectively (Figure 3.2.4). The employed Cu powder was gas atomised and spherical in shape (Figure 3.2.5).

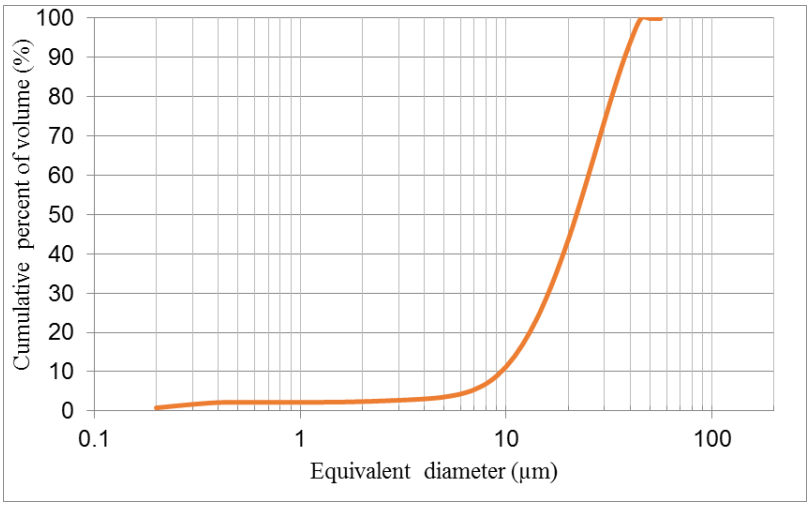

Figure 3.2.4: Particle size distributions for employed Cu powder.

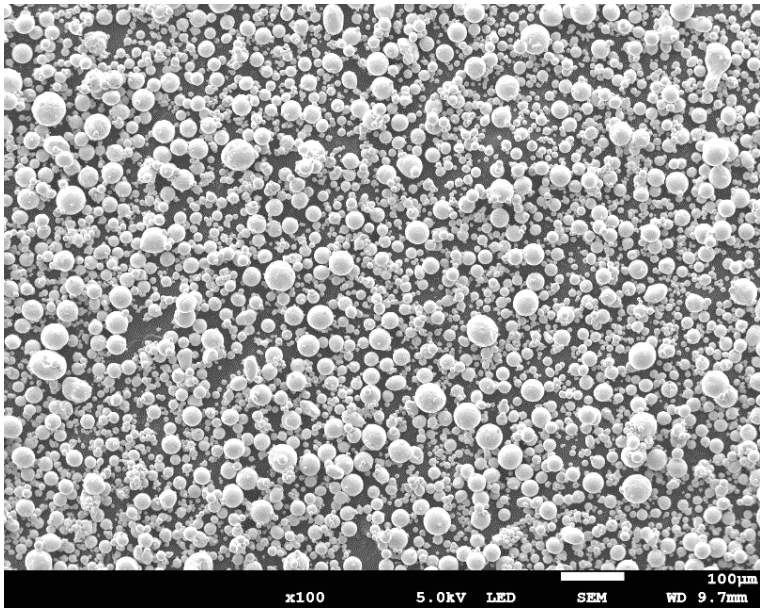

Figure 3.2.5: SEM micrograph showing spherical sphape of Cu powder.

3.2.2.3: Titanium Powder

Commercially pure titanium (Cp Ti) is unalloyed material and available in four different grades, 1, 2, 3 and 4. The grade 2 is preferred for several applications due to its excellent formability, superior corrosion resistance and moderate strength (Elagli *et al.*, 1989). It is a single phase material and its properties greatly depend on levels of interstitial elements (oxygen, nitrogen, carbon and iron) and grain size. It could undergo an allotropic transformation from hcp alpha phase to bcc beta phase based on the operational temperature. It has wide applications in the aircraft industry, manufacturing of marine and chemical vessels, jewelry and medical industries (Donachie, 2000). The most desirable feature of Cp Ti is its ability to osseointegrate within the human body. The chemical composition of employed powder is noted in Table 3.2. and the typical physical and mechanical properties of pure Ti are recorded in Table 3.2..

Table 3.2.4: Chemical composition of Cp Ti powder (in weight %)

Ti	O	Fe	C	H	N
ISO 5832-2 (Cp-Ti grade 2)					
Bal	≤0.45	≤0.30	≤0.10	≤0.0125	≤0.05
Employed powder					
Bal	0.17	0.062	0.006	0.002	0.012

Table 3.2.5: Typical physical and mechanical properties of pure Ti (grade 2)*

Property	CpTi (grade 2)
Density, Kgm^{-3}	4500
Melting point, ^{o}C	1650-1670
Specific heat, $J{\cdot}kg^{-1}K^{-1}$	528
Thermal conductivity, $Wm^{-1}K^{-1}$	17
Thermal diffusivity, m^2s^{-1}	7.15×10^{-6}
Heat of fusion kJ/kg	435.4
Boiling point, °C	3287
Ultimate tensile strength, MPa	220
Yield strength, MPa	140
Elasticity modulus, GPa	116
Elongation at break, %	54
Hardness, Vickers	60

*(ASM, 2016)

The particle size distribution of the CpTi powder is represented in Figure 3.2.6. The equivalent diameters of the 10th, 50th and 90th percentiles were d_{10}=11.6 µm, d_{50}=24.6 µm and d_{90}=38.4 µm respectively. The powder was gas atomized and spherical in shape (Figure 3.2.7).

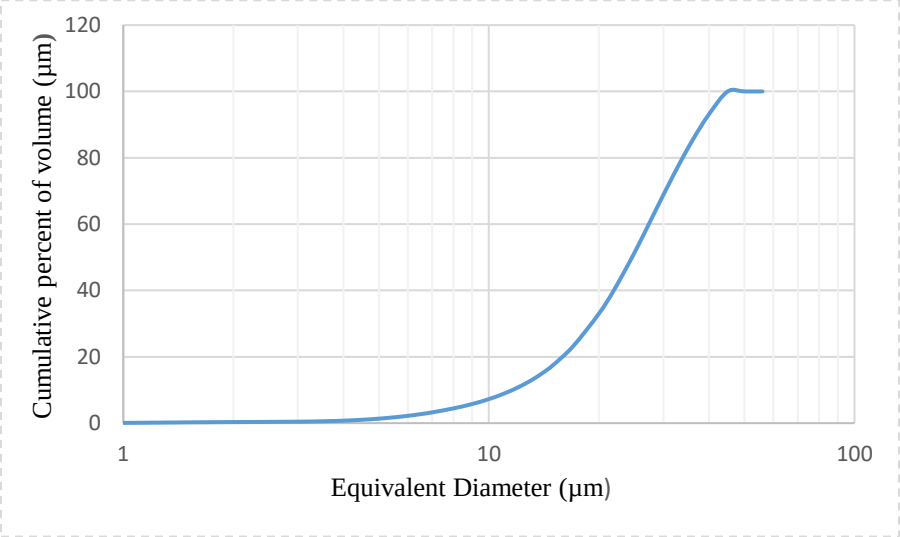

Figure 3.2.6: Particle size distributions for employed Cp Ti powder.

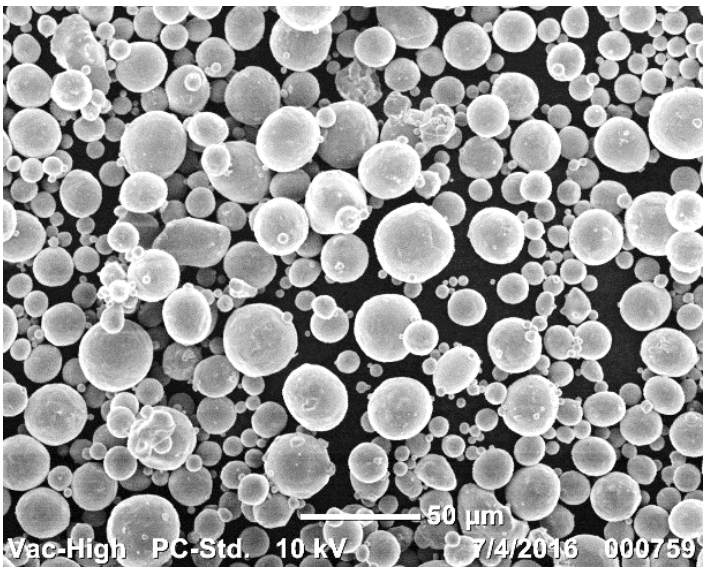

Figure 3.2.7: SEM micrograph of Cp Ti grade 2.

3.2.2.4: Molybdenum Powder

Molybdenum (Mo) is a pure silvery white element with high melting point which promotes it used as a refectory element. It is normally used as an alloying agent for a variety of metals for specific applications. It is also used in nuclear energy applications, aerospace industry, and petroleum refinery. The versatility of molybdenum in enhancing a variety of alloy properties has ensured it a significant role in contemporary industrial technology where ductility, toughness, reverse bending notch sensitivity and exceptional high fatigue strength to resist repetitive loading are required (USGS, 2017; Lenntech, 2017). The aforementioned characteristics make it worth alloying Mo with CpTi for biomedical applications.

Table 3.2.6: Typical physical and mechanical properties of Mo*

Property	Mo
Density, Kgm^{-3}	10220
Melting point, ^{o}C	2617
Specific heat, $J{\cdot}kg^{-1}K^{-1}$	276
Thermal conductivity, $Wm^{-1}K^{-1}$	138
Thermal diffusivity, m^2s^{-1}	54.3×10^{-6}
Heat of fusion kJ/kg	289
Boiling point, °C	4640
Ultimate tensile strength, MPa	515
Yield strength, MPa	415
Elasticity modulus, GPa	330
Elongation at break, %	17
Hardness, Vickers	230

*(Glemco, 2016; AZO, 2015)

The chemical analysis reveals >99,9 % Mo purity. The typical physical and mechanical values of the material are reported in Table 3.2.6 and the particle size distribution in Figure 3.2.8. The shape of the employed powder (Mo) is spherical (Figure 3.2.9). The equivalent percentiles of the 10th, 50th and 90th was recorded as d_{10}=10.87 µm, d_{50}=22.36 µm and d_{90}=31.92 µm respectively.

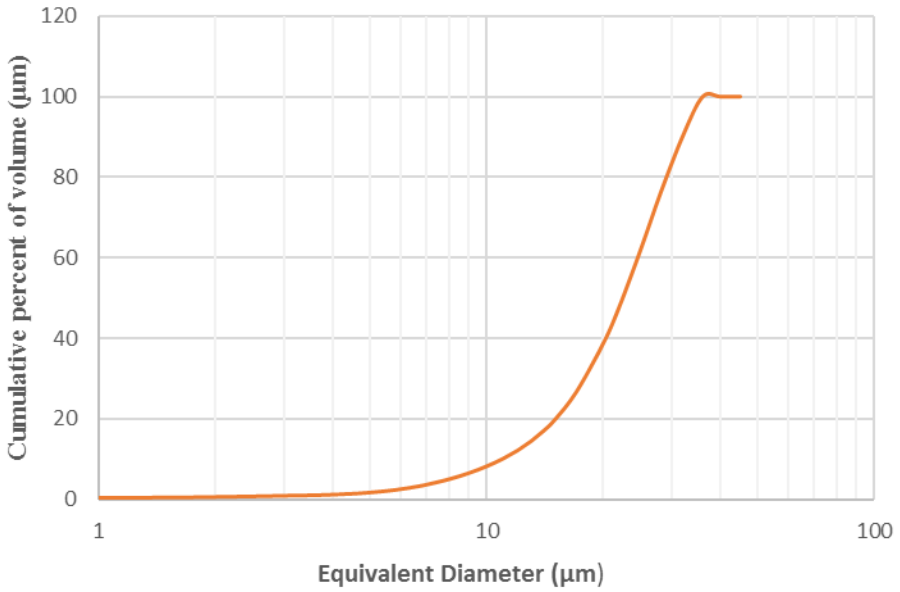

Figure 3.2.8: Particle size distributions for employed Cp Ti powder.

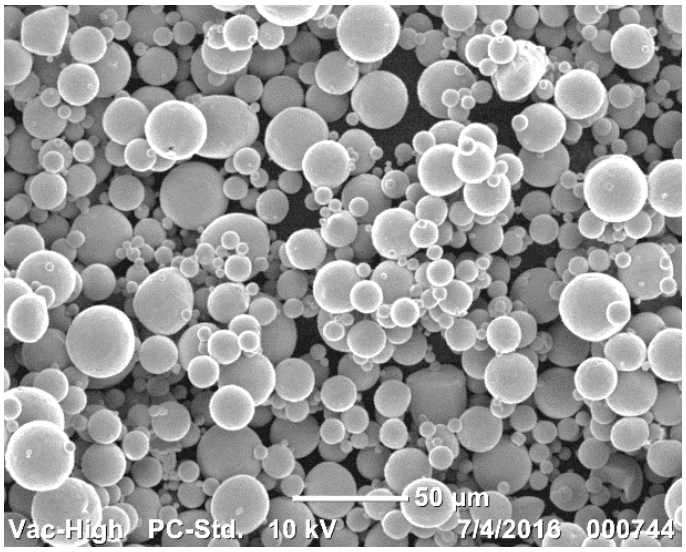

Figure 3.2.9: SEM micrograph of the employed Mo powder

3.2.3. Flowability of Employed Powders

For DMLS process, powder flowability has a significant effect on the build product. In most cases to estimate flowability of the powder, Hausner ratio (ratio of tapped density ρ_{tap} to loose-packed bulk density, or apparent density ρ_{app}) and Carr index (Carr, 1965; Hausner, 1967) are applied:

$$Carr\ index = \frac{\rho_{tap} - \rho_{app}}{\rho_{tap}} \times 100\%$$

A Hausner ratio of <1.25 indicates a powder that is free flowing while powder with values higher than 1.25 indicates weaker powder flow. Likewise, Carr index is indicated as the difference between the tap density and the apparent density as a percentage of the tapped density. Powders with smaller Carr index values have better flow properties, powders with values <15% tend to be free flowing (Hausner, 1967; Zou & Yu, 1996; Hassan & Lau, 2009).

Apparent density of metal powder is defined as the actual volume occupied by a mass of loose powder. It is the weight of a unit volume of loose powder expressed in grams per cubic centimetre. To determine the tap density of the employed powders, a clean dry 50 ml cylinder was filled with powder, taking care that a level surface of powder is obtained. The powder is settled in the cylinder by mechanical tapping. The measurements were done in 3 fold and an average value was reported. The employed powders showed good/excellent flow (Table 3.2.).

Table 3.2.7: Flowability of employed powders

Powder	ρ_{app}, g/cm^3	ρ_{tap}, g/cm^3	Hausner ratio	Carr index	Flow properties
Ti6Al4V ELI	2.51	2.79	1.11	10	Excellent
CpTi	2.46	2.89	1.17	14.88	Good
Cu	4.76	5.39	1.13	11.6	Good
Mo	2.89	3.12	1.08	7.37	Excellent

3.3: Numerical simulations

3.3.1: Finite Element Analysis for Mandible

The implant was modelled to resemble the geometry and function of the natural mandible (Figure 3.3.1). To reduce the computational time during FEA, only half of the symmetric mandible bone was designed. The region A1 in Figure 3.3.1a corresponds to region A2 in Figure 3.3.1b. Rotation was allowed about the point A2 as in normal clenching of the teeth (A1), but it could not translate or move up and down. The applied load during the simulation was applied at an angle of 69^0 (Figure 3.3.1b point C2) to mimic the function of the masseter muscle. Furthermore, the implant was fixed at point B (Figure 3.3.1b) so that it could not translate nor rotate when performing the

simulation. Since only half of the mandible was designed for this analysis, only half (1000 N) of the total resultant force exerted by the mastication muscle during mastication was used in the simulation (Hattori *et al.*, 2009). The hole at point C2 where the force is applied represents the location of the masseter muscle attachment (C1).

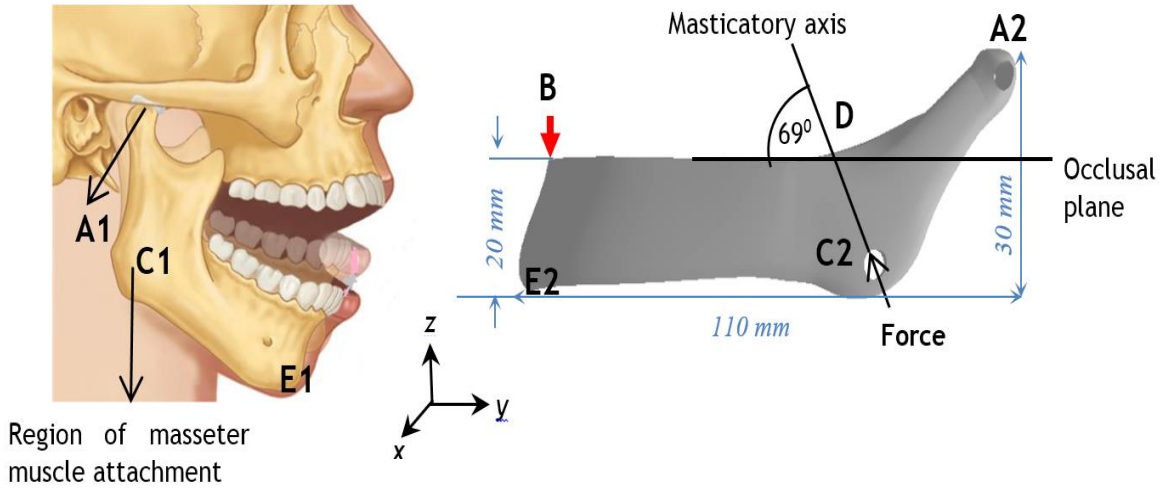

(a) (b)

Figure 3.3.1: Symmetry representation of the mandible (a) and a CAD model of a mandible implant (b).

The FEA mesh was verified and mesh equivalence was obtained to ensure that the model was seen as one body by the FEA software. The kinematic boundary conditions for the simulation were selected based on how the experimental test would be performed and the natural boundary conditions set for movement of the mandible. The model was constrained not to rotate nor translate in the *x*,*y*, *z*-direction at point B (Figure 3.3.1b). Under a static load of 1000 N at an angle of 69° in the *z*-direction a force was applied to the hole (C2). The uniaxial force at the specified angle of application was transmitted throughout the model. As the simulation was performed the motion in the *z*-direction with respect to the fixed contact, was transmitted vertically and horizontally to register any deformation in the simulation model. The maximum Von Mises stress and strains were used as the main indicators to evaluate the maximum load that the material could bear and the stress distribution behaviour throughout the model.

3.3.2: Defining the CAD model

Due to the complexity and regional variation of human body parts (Heylighen, 1999), a compromise must be reached between the experimental model in turns of geometrical accuracy and material properties.

Strait *et al*. (2005) noted that finite element results could be adversely affected and misleading if the right material properties are not selected to define the model, especially oversimplifying the skeletal system as isotropic and not incorporating the elastic properties. But Ichim *et al*. (2007) explained that although bone is an anisotropic material, skeletal model like mandible which were assigned isotropic properties were capable of producing "discerning meaningful strain differences when replicating functional loading". Daegling & Hylander (1998) also defined mandibular corpus morphology as "homogeneous, isotropic symmetrical body" other researchers (Korioth *et al.,* 1992; Ichim *et al.,* 2006; Chen *et al.,* 2011) also assigned similar properties to their experimental CAD mandible model and obtained meaningful results. Hence, the CAD model in the current studies would also be assumed to be homogenous and linearly isotropic.

The choice of Elastic modulus to defined the CAD model was based on the fact that AM technology could be used to produce Ti-based alloys with such low Elastic modulus (Heinl *et al.,* 2008; Hanzl *et al.,* 2015). Elastic modulus from 1.6 – 30 GPa would be used to define the CAD models representing trabecular and cortical bone. For the implant sections of the model Elastic modulus of 110 GPa would be used, representing the Elastic modulus of Ti6Al4V.

Bone constituent properties and Elastic modulus for human cortical mandible in the radial, axial and circumferential direction (Ashman & Van Buskirk, 1987; Korioth & Hannam, 1994; Ichim *et al.,* 2006) were taken from literature. Poison ratio of 0.35 would be used for the simulation as demonstrated elsewhere (Wirtz *et al.,* 2000; Fraser *et al.,* 2016).

3.4: Experimantal Methods

3.4.1: EOSINT M 280 Machine

EOSINT M 280 system, a Direct Metal Laser Sintering (DMLS) machine from EOS GmbH (Figure 3.4.1), was used for the studies. The machine mainly comprises of a process chamber with

the recoating system, computer control elevating systems, platform module, an optical system with a laser, a process gas management system and a process computer with control software. There are other vital accessories such as vacuum cleaner and platform handling trolley which makes the machine ergonomic.

The machine is equipped with 400 watts Yb-fibre laser which provides excellent beam and power stability to ensure manufacturing of quality parts. The operating atmosphere is protected by argon gas which permits processing of a wide range of reactive metallic powders. The EOSINT M 280 machine scanner can scan up to a speed of 7 m/s and could have exposure area of 250 mm x 250 mm.

The EOSINT M 280 machine is a computer controls system with a Process Soft Ware called PSW software. The PSW software virtually controlled the whole machine; it is used to protocol the building process prior to the manufacturing process. The graphical layout of the parts which would be built could also be displayed on the computerized screen by the PSW software.

Figure 3.4.1: EOSINT M280 machine installed in CRPM (CUT)

To obtain optimum result when using DMLS machine, a systematic procedure must be followed. A careful consideration must be given to each step; any step that is not performed accurately would defiantly affect the final product. The machine set-up generally comprises of sieving and refilling

of powder container, platform preparation, selection of the right recoater blade, levelling the recoater blade with the platform and flushing the building environment with argon or nitrogen gas to ensure the minimum acceptable oxygen content (0.07-0.12%).

3.4.1.1: Sieving of the Powder

The EOSINT M280 machining has a sieving component: by regulating the elevating system the dispenser or the collector system could be moved up/down to enable collecting and sieving of the powder manually, thus if the powder was previously used (non-virgin powders). The powder needs to be sieved before use to remove any agglomerates or other large particles to ensure even consistency of the metal powder that has been conveyed from the dispenser duct, building duct and collector duct. During the sieving process, it is critically important to wear the recommend protective clothes such as mask, gloves, lab coats and antistatic shoes.

3.4.1.2: Platform Preparation

Pure Ti and Ti6Al4V plates were used as the base plate for the research. The first step involved grinding/machining the building plate to have a smooth surface after which it is cleaned with acetone. The base plate is held in place by four corner screws onto the elevating system on the carrier plate in the process chamber. The platform is set to move down at precise predetermined value base on the desired powder layer thickness.

3.4.1.3: Recoater Blade Settings

Setting the gap between the re-coater and the base plate accurately is very important since it is the main tool that controls powder deposition on the substrate. The manual setting of the gap between the re-coater and the base plate is a complicated task (Khaing *et al.,* 2001). This part of the preliminary activities seems very crucial since it can affect the densification of the build parts if the powder is not deposited evenly by the re-coater. Gauge clock and feeler gauge were used to level and determined the gap between the base plate and the re-coater for this research.

The gauge was mount (clamp) firmly at 90^{o} to the re-coater blade and the tip of the plunger touch the surface of the re-coater blade. The pointer on the surface of the gauge was set to zero by moving the bezel. The gauge clock was moved across the whole length of the re-coater blade. If the pointer

moves from the zero mark while moving across the length of the re-coater blade it means the re-coater is not level properly and was adjusted accordingly. The filler gauge determines the gap between the base plate and the recoater blade which basically determined the deposited powder layer thickness. For the current experiment, the powder layer thickness was 50 µm hence a filler gauge of 0.05 mm thickness was used to set the gap between the base plate and the recoater blade. The operational speed of the recoater blade was 150 mm/s. The recoater blade used for the experiment was made of high-speed steel alloys.

3.4.1.4: Protective Atmosphere

For highly reactive metallic powders like Ti-based alloys, it is highly recommended that it should be processed under an inert atmosphere. Since the EOSINT M280 machine building atmosphere is made up of the entire building environment, inert gas (argon) was flushed continually into the building chamber. The type of gas used could influence the depth of penetration of the laser beam into the subtract (Kurzynowski *et al.,* 2012). The level of oxygen gas content in the build chamber is also of great concern since it can cause oxidation of the manufactured part. It is demonstrated that the use of higher laser power would contribute greatly to the efficient removal of oxygen in the build chamber (Dadbakhsh & Hao, 2014).

It is perceived that, the higher the temperature of the build chamber the lesser the residual stress effect on the sample. Bertol *et al.* (2010) kept the temperature of the build chamber at 230°C during SLS (Selective laser stintring) process and found out that the residual stress is virtually eliminated and there was no need for post heat treatment. Higher temperature is preferred for processing metallic powder because at higher temperatures the flowability of the powder increases. The manufactures of the EOSINT M280 matching (EOS GmbH, 2010) also recommends operating temperature between 60 – 100 °C. Knowles *et al*. (2012) postulated that raising the powder bed and build chamber temperature to 650 °C would reduce the residual stress. However, Izgar (2014) caution that operating at high temperatures is detrimental to the lifespan of the base plate and the entire manufacturing system.

3.4.1.5: CAD Modelling

An additive manufacturing process normally starts with designing a 3D CAD data with various CAD data software. The basic requirement of selecting any of the modeling software is its

capability of converting the selected CAD data into .STL (Standard Tessellation Language) file format. The main task of the .STL software is to convert the 3D design structure into a sequence of two-dimensional (2D) layers called "slices". This conversion is necessary to create the Specific Layer Interface (SLI) data which are required for the building process. The conversion process made it possible to process the data in a Computer Aided Manufacturing (CAM) platform.

After slicing the 3D CAD data into 2D layers by STL file, EOS RP-Tools which is the EOS software specifically designated for generating and manipulating part data in STL format or in CLI (Common Layer Interface) is used. The software converts the part data from STL or CLI into EOS-specific CLI format by separating the layer data of the solid bodies into skin and core data. The various steps and the software used in this particular research are documented in the flow chart (Figure 3.4.2).

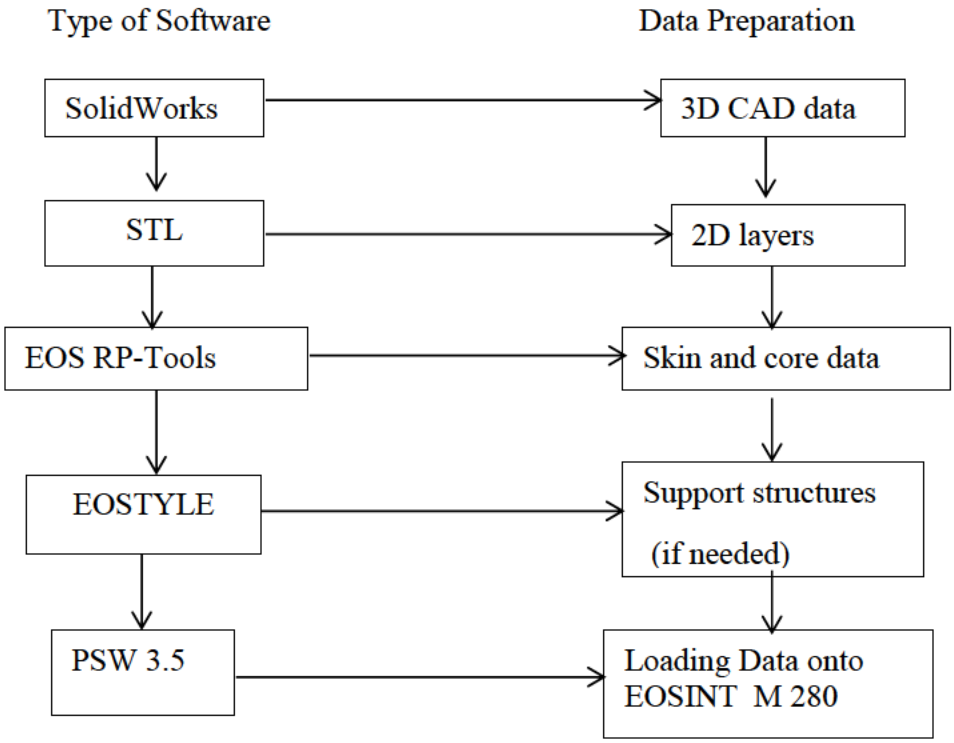

Figure 3.4.2: CAD modeling steps and the required software used.

3.4.1.6: Support Structures

Another important step in the data preparation process is generating support structures for hanging parts. The building of support structures for hanging parts during the DMLS process is mandatory.

Lack of support structures at the appropriate place can cause parts to wrap severely. EOSTYLE is the software package for support structure generating.

3.4.1.7: Loading and Controlling DMLS Building

By the PSW 3.5 computer interface software, the parts and supports are placed on the EOSINT M280 machine building platform. The operating engineer is able to control and regulate operating parameters such as laser power, scanning speed, scan spacing (hatch distance) and powder layer thickness. The software permits the user to know about the temperature of the building environment, oxygen level and the estimated time a particular job would be completed. Information about the movement of the building platform (vertically, up and down), the powder deposition blade (horizontally, back and forth), available powder in the dispensary duct or the collector duct are also provided by the software interface. After all the processing parameters have been set at their optimum value based on the selected powder properties the start button is pressed.

3.4.2: Metallographic Analysis

For metallographic analyses, samples were removed from the build plate via wire Electrical Discharge Machining and section/cross-section into smaller units for mounting. Struers CitoPress-1 machine (Figure 3.4.3a) was used for mounting the samples in MultiFast non-conductive resin. The mounting of each sample took 3.5 min at a temperature of 180 C at a pressure of 250 bar. The samples were subsequently cooled by water at high rate for 2 min. Grinding and polishing of the specimens were conducted with Struers Tegramin-25 (Figure 3.4.3b) according to the protocol suggested by Struers for Ti-based alloys. The details of the grinding and polishing steps recommended by Struers are recorded in Table 3.4.1.

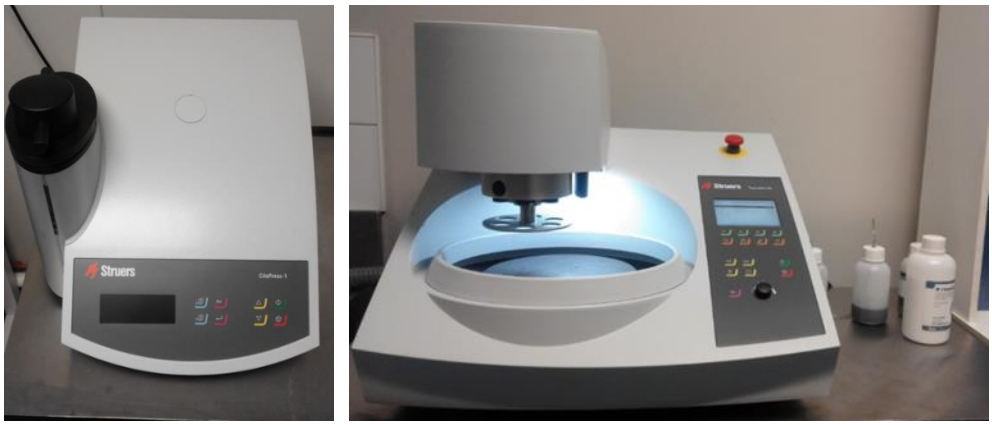

(a) (b)

Figure 3.4.3: CitoPress-1 (a) and polishing machine Tegramin-25 (b).

Table 3.4.1: The recommended polishing procedure by Struers adopted for the studies

Process	Wheel/Cloth	Lubricant	Force	Speed	Time
Coarse Grinding	320 SIC	Water	25 N	300 rpm	1.50 min
Fine Grinding	MD-Largo	DiaPro All/Lar.9	30 N	150 rpm	5.00 min
First Polishing	MD-Mol	DiaPro Mol.3	25 N	150 rpm	2.20 min
Final Polishing	MD-CHEM	OP-S Suspension	20 N	150 rpm	1.50 min

The OP-S colloidal silica suspension for the final stage of the polishing in conjunction with the MD-CHEM polishing disk ensure that the surface of the sample was mirror finished and free of mechanical deformation. Each sample is first cleaned under tap water and then in Lab Companion UC-02 Ultrasonic Cleaner for 3 min (Figure 3.4.4a). The sample is then washed with alcohol and dried by air at room temperature.

The sample is subsequently etched in ESCO Ductless Fume Hood (Figure 3.4.4b) with Kroll's reagent. The Kroll etchant is a dilute aqueous solution containing HF and HNO_3, which is mostly used for etching titanium alloys. It is made up of: 5ml of HNO3 + 10ml of HF (48% concentration) + 85 ml H_2O.

(a) (b)

Figure 3.4.4: Ultrasonic cleaner (a) and fume hood (b).

After etching the samples were ready for microstructural examinations. A ZEISS Axio Scope.A1 Optical Microscope (Figure 3.4.5a) was used for the microstructural analysis. AxioVision SE64 software was used for capturing the micro-images. To obtain further detailed information about the samples, Scanning Electron Microscope (SEM) analyses were conducted on the samples. Secondary Electron (SE) and Backscatter Electron (BSE) imaging were employed for the analyses. JEOL JSM-7800F SEM (Figure 3.4.5b) with integrated Energy Dispersive X-ray Spectroscopy (EDS) detector was used for the studies.

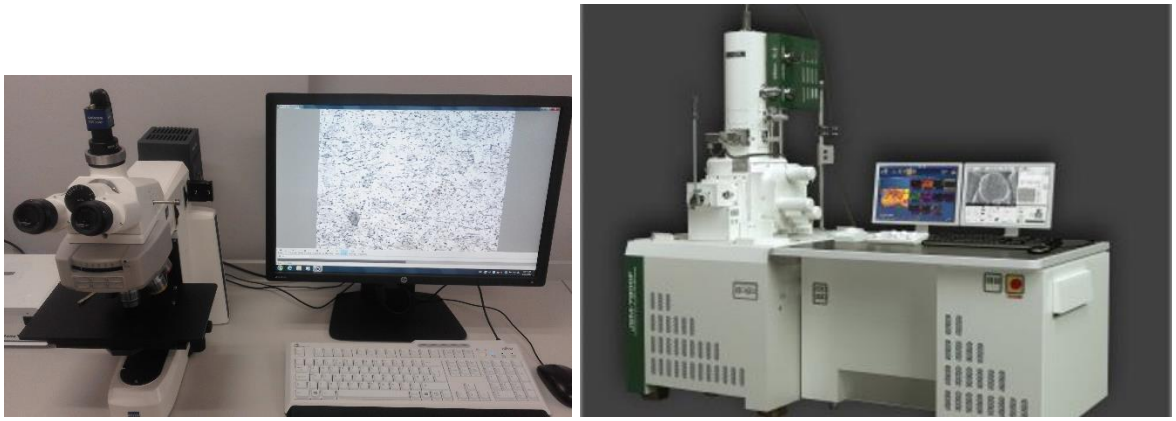

(a) (b)

Figure 3.4.5: ZEISS Axio Scope.A1 Optical Microscope (a) and JEOL JSM-7800F SEM (b).

The morphology of the samples and powders was conducted in the SE and BSE mode under 15-20 kV and working distance up to 10 mm. The chemical analysis and elemental mapping of the samples to determine the degree of homogenous distribution of the alloying elements in the master alloys was conducted in the EDS mode.

3.4.3: Mechanical Properties Investigations

3.4.3.1: Tensile and Compressive Tests

Mini-samples were used for the tensile tests. It has been experimentally proven that mini samples for tensile test produce accurate results just like the standard tensile test specimen (LaVan, 1999; Kartal *et al.*, 2007; Seguineau *et al.*, 2008; Molak *et al.*, 2009; Kashaev *et al.*, 2013; Rund *et al.*, 2015; van Zyl *et al.*, 2016). The dimensional characterization of the mini tensile test samples for the current studies is represented in Figure 3.4.6. The specimens have a rectangular shape with 10 mm gauge length, 2 mm width and 1 mm thickness.

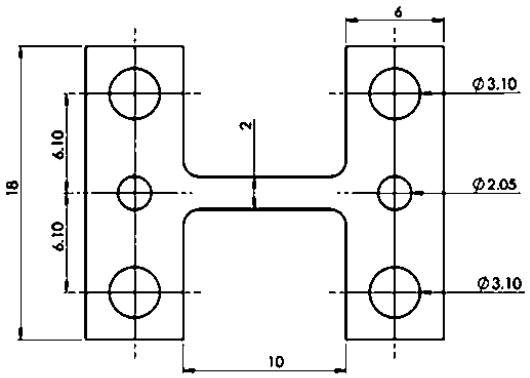

Figure 3.4.6: Dimensions sketch of mini specimens (van Zyl *et al*., 2016).

The tensile test was carried out using MTS Criterion model 43 Universal Test machine (Figure 3.4.7). The samples were strained at a rate of 0.5 mm/s through the 0.2% yield until fracture.

Figure 3.4.7: MTS Criterion model 43 Electromechanical Universal Test Systems machine.

The tensile test was conducted on the Ti15Mo and Ti6Al4V+xCu samples only while the Ti6Al4V cellular structures were tested in compressive mode. As opposed to tensile test where a sample is pulled and elongate, for a compressive test the sample experiences opposing forces that push inward upon it from opposite sides (biaxial) pressing the material together (flattened). For the compressive test the experimental samples were placed in between two plates that distribute the applied load across the entire surface area of two opposite faces of the test sample and then the plates were pushed together by the MTS Criterion model 43 Universal Testing machine system (30kN max load cell) under 0.3 mm/min strain rate causing the sample to crushed/flattened.

3.4.3.2: Microhardness Tests

For the current studies the microhardness test was conducted with FM-700 Digital Vickers Microhardness Tester from Future-Tech Corporation (Figure 3.4.8). The samples were placed individually in the specimen holder and the pyramid-shaped diamond indenter was pressed into the surface of the material at a constant load of 200 g for about 10 to 15 seconds.

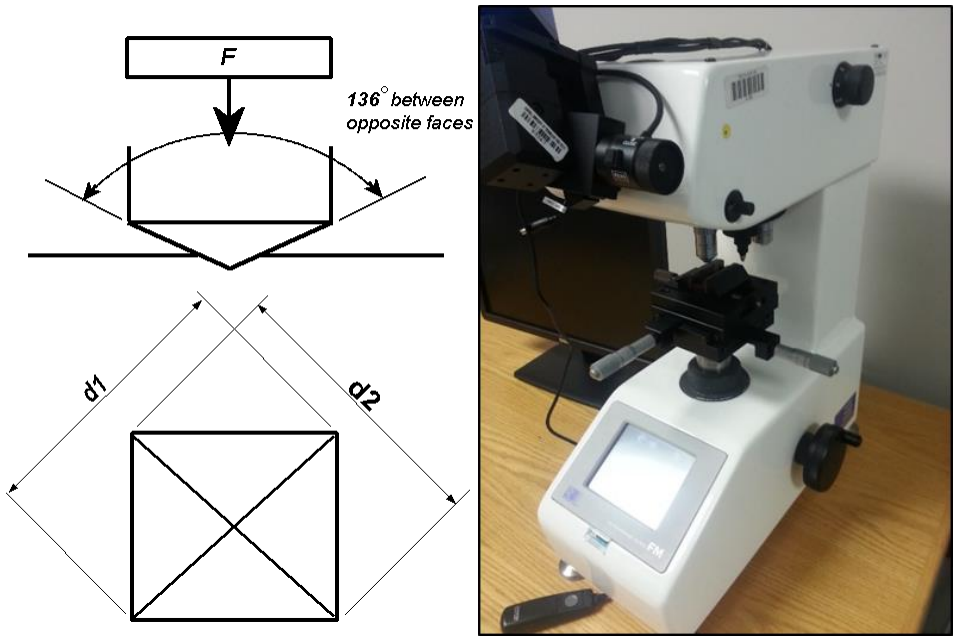

(a) (b)

Figure 3.4.8: Indenter for Vicker's hardness test (a) and FM-700 microhardness tester (b).

3.4.3.3: Surface Roughness Measurements

For DMLS manufactured parts to be suitable for biomedical applications the quality of the surface is very important since the quality of an implant surface has a direct effect on its anchoring process. Surface roughness measurement is a quantification of the fine irregularities on the surface of a manufactured object. The fine irregularities could be categorized by height and depth (*Rz*) and interval (*Ra*) of the irregularities. The surface roughness of the samples was measured with Surftest SJ-210 portable surface roughness tester from Mitutoyo Corporation (Figure 3.4.9). The set parameters on the Surftest SJ-210 that were used to conduct the measurements are documented ISO 1997 standard for roughness measurements.

Figure 3.4.9: Surftest SJ-210 portable surface roughness tester.

3.5: Summary

The chapter espoused the materials and methods that were used for the research. For repeatability and predictability of a manufactured part the various material and methods that were employed must be carefully documented. The employed powders were gas atomized and spherical in shape and demonstrate a good/excellent flowability. The capacity and the operation of the EOSINT M280 machine which was used for the research was discussed. The selected measuring equipment which were used to characterize the metallographic and mechanical properties of the manufactured samples were presented.

3.6: References

ASM, 2016. ASM aerospace specification metals Inc. [Online Available at: http://www.matweb.com/[Accessed 28 November 2016].

ASTM F 2066 13, 2013. *ASTM F 2066 Standard Specification for Wrought Titanium-15 Molybdenum Alloy for Surgical Implant Applications surgical implant application (UNSR 8150).* west Conshohocken, PA.

AZO, 2015. AZO materials. [Online] Available at: http://www.azom.com [Accessed 28 November 2016].

Benson, J. M. & Snyders, E., 2015. The need for powder characterisation in the additive manufacturing industry and the establishment of a national facility. *South African Journal of Industrial Engineering,* 26(2), pp. 104-114.

Berman, J., 2015. Copper Surfaces Prevent Spread of Respiratory Viruses on Contact. [Online] Available at: http://www.voanews.com [Accessed 21 March 2017].

Bertol, L. S., Júnior, W. K., da Silva, F. P. & Aumund-Kopp, C., 2010. Medical design: direct metal laser sintering of Ti–6Al–4V. *Materials & Design,* 31(8), pp. 3982-3988.

Carr, R. L., 1965. Classifying flow properties of solids. *Chemical Engineering*, 72(3), pp. 69-72.

Chang, I. & Zhao, Y., 2013. *Advances in powder metallurgy: Properties, processing and applications*. New Delhi: Woodhead Publishing.

Clayton, J., 2014. Optimising metal powders for additive manufacturing. *Metal Powder Report*, 69(5), pp. 14-17.

Cooke, A. & Slotwinski, J., 2012. *Properties of metal powders for additive manufacturing: a review of the state of the art of metal powder property testing*. US Department of Commerce, National Institute of Standards and Technology.

Dadbakhsh, S. & Hao, L., 2014. Effect of layer thickness in selective laser melting on microstructure of Al/5 wt.% Fe2O3 powder consolidated parts. *The Scientific World Journal*, 2014 (2014), pp. 1-10.

Davis, J. R., 2001. *Copper and copper alloys*. Materials Park, Ohio 44073-0002: ASM international.

Dawes, J., Bowerman, R. & Trepleton, R., 2015. Introduction to the additive manufacturing powder metallurgy supply chain. *Johnson Matthey Technology Review*, 59(3), pp. 243-256.

Donachie, M. J., 2000. *Titanium: a technical guide, 2nd Edition*. Michigan: ASM International.

Elagli, K., Hildebrand, H. F. & Hamme, G., 1989. Biocompatibility of titanium and its alloys. *Le Chirurgien-dentiste de France*, 59(457), p. 35.

EOS GmbH, 2010. *Technical Description EOSINT M 280*. EOS GmbH – Electro Optical Systems.

Everhart, J. L., 1975. *Copper and copper alloy powder metallurgy: Properties and applications*. New York: Metal Powder Industries Federation.

Gayle, M., Look, D. W. & Waite, J. G., 1998. *Metals in America's historic buildings*. U.S Department of Interior, Washinton: Diane Publishing.

German, R. M. & Park, S. J., 2008. *Mathematical relations in particulate materials processing*. John Wiley & Sons, Inc.

Glemco, 2016. Molybdenum, Mo (wt 100%) Material Notes. [Online] Available at: www.glemco.com [Accessed 28 November 2016].

Harrer, S. L., 2016. How to Test Copper Purity. [Online] Available at: http://sciencing.co [Accessed 21 March 2017].

Hassan, M. S. & Lau, R. W. M., 2009. Effect of particle shape on dry particle inhalation: study of flowability, aerosolization, and deposition properties. *Aaps PharmSciTech*, 10(4), p. 1252.

Hausner, H. H., 1967. Friction conditions in a mass of metal powders. *International Journal of Powder Metallurgy*, 3(4), pp. 7-13.

Indentec, 2017. Indentec Hardness Testing Machines. [Online] Available at: http://www.indentec.com [Accessed 20 March 2017].

Izgar, A. A., 2014. *Direct Metal Laser Sintering of Titanium Implant with Tailored Structure and Mechanical Properties*. Doctoral thesis. The university of Waikato.

Kartal, M., Molak, R.M., Turski, M., Gungor, S., Fitzpatrick, M.E. & Edwards, L., 2007. Determination of weld metal mechanical properties utilising novel tensile testing methods. In Applied Mechanics and Materials. *Trans Tech Publications*, 7, pp. 127-132.

Kashaev, N., Horstmann, M., Ventzke, V., Riekehr, S. & Huber, N., 2013. Comparative study of mechanical properties using standard and micro-specimens of base materials Inconel 625, Inconel 718 and Ti-6Al-4V. *Journal of Materials Research and Technology*, 2(1), pp. 43-47.

Khaing, M. W., Fuh, J. Y. H. & Lu, L., 2001. Direct metal laser sintering for rapid tooling: processing and characterisation of EOS parts. *Journal of Materials Processing Technology*, 113(1), pp. 269-272.

Knowles, C. R., Becker, T. H. & Tait, R. B., 2012. The effect of heat treatment on the residual stress levels within direct metal laser sintered Ti-6Al-4V as measured using the hole-drilling strain gauge method. *In Proceedings of the 13th International conference Rapid Product Development Association of South Africa*.

Kurzynowski, T., Chlebus, E., Kuźnicka, B. & Reiner, J., 2012. Parameters in selective laser melting for processing metallic powders. *International Society for Optics and Photonics, In SPIE LASE* pp. 823914-823914.

LaVan, D. A., 1999. Microtensile properties of weld metal. *Experimental Techniques*, 23(3), pp. 31-34.

Lenntech, 2017. Molybdenum - Mo. [Online] Available at: http://www.lenntech.com [Accessed 17 March 2017].

Liu, B., Wildman, R., Tuck, C., Ashcroft, I. & Hague, R., 2011. Investigation the effect of particle size distribution on processing parameters optimisation in Selective Laser Melting process. *International solid freeform fabrication symposium: an additive manufacturing conference*. University of Texas at Austin, Austin.

Liu, J., Zhang, X., Wang, H., Li, F., Li, M., Yang, K. & Zhang, E., 2014. The antibacterial properties and biocompatibility of a Ti–Cu sintered alloy for biomedical application. *Biomedical Materials*, 9(2), pp. 025013.

MatWeb, 1916. Material property data. [Online] Available at: http://www.matweb.com [Accessed 26 March 2017].

McGeary, R. K., 1961. Mechanical packing of spherical particles. *Journal of the American Ceramic Society*, 44(10), pp. 513-522.

Molak, R. M., Paradowski, K., Brynk, T., Ciupinski, L., Pakiela, Z. & Kurzydlowski, K.J., 2009. Measurement of mechanical properties in a 316L stainless steel welded joint. *International Journal of Pressure Vessels and Piping*, 86(1), pp. 43-47.

O'gorman, J. & Humphreys, H., 2012. Application of copper to prevent and control infection. Where are we now? *Journal of Hospital Infection*, 81(4), pp. 217-223.

Rund, M., Procházka, R., Konopík, P., Džugan, J. & Folgar, H., 2015. Investigation of Sample-size Influence on Tensile Test Results at Different Strain Rates. *Procedia Engineering*, 114, pp. 410-415.

Schade, C., Murphy, T. & Walton, C., 2014. *Development of Atomized Powders for Additive Manufacturing.* New Jersey: Hoeganaes Corporation, Cinnaminson.

Seguineau, C., Ignat, M., Malhaire, C., Brida, S., Lafontan, X., Desmarres, J.M., Josserond, C. & Debove, L., 2008. Micro-tensile tests on micromachined metal on polymer specimens: Elasticity, plasticity and rupture. *In Design, Test, Integrationand Packaging of MEMS/MOEMS, 2008. MEMS/MOEMS 2008.*

Simchi, A., 2004. The role of particle size on the laser sintering of iron powder. *Metallurgical and Materials Transactions B*, 35(5), pp. 937-948.

Spierings, A. B., Herres, N. & Levy, G., 2011. Influence of the particle size distribution on surface quality and mechanical properties in AM steel parts. *Rapid Prototyping Journal*, 17(3), pp. 195-202.

USGS, 2017. Minerals Information. [Online] Available at: minerals.usgs.gov [Accessed 17 March 2017].

van Zyl, I., Moletsane, M., Krakhmalev, P., Yadroitsava, I. & Yadroitsev, I., 2016. Validation of miniaturised tensile testing on DMLS TI6AL4V (ELI) specimens. *South African Journal of Industrial Engineering*, 27(3), pp. 192-200.

Vincent, C., Silvain, J. F., Heintz, J. M. & Chandra, N., 2012. Effect of porosity on the thermal conductivity of copper processed by powder metallurgy. *Journal of Physics and Chemistry of Solids*, 73(3), pp. 499-504.

Zhang, E., Li, F., Wang, H., Liu, J., Wang, C., Li, M. & Yang, K., 2013. A new antibacterial titanium–copper sintered alloy: preparation and antibacterial property. *Materials Science and Engineering: C*, 33(7), pp. 4280-4287.

Zou, R. P. & Yu, A. B., 1996. Evaluation of the packing characteristics of mono-sized non-spherical particles. *Powder Technology*, 88(1), pp. 71-79.

CHAPTER 4: FINITE ELEMENT ANALYSIS IN DESIGN OF DMLS MANDIBLE IMPLANTS

4.1: Introduction

The use of cadaveric and human specimen for biomechanics and orthopedics research have proven to give researchers tremendous understanding about how the bones in the body respond to different loading systems. However, considering the fundamental human rights of using human participants in an experiment and the destructive experimental testing of cadaveric samples make it costly, that has placed a great limitation on such methods as an experimental tool. Fortunately, the use of numerical simulation as a feasible alternative for predicting the response of bone under a variety of loading conditions have made biomechanics and orthopedic research more robotic and repeatable with great accuracy (Rogge *et al.*, 2002; Burkhart *et al.*, 2013).

FEA (finite element analysis) is the major tool used to predict the biomechanical behaviour of various implant designs as well as clinical factors on implant success. The advent of advanced computer technology such as CT scans has helped to obtain more precise individual patient base data for accurate simulated results in recent years (Gultekin *et al.*, 2012). Using FEA to envisage how stresses would be transferred between the implant and the bone interface would greatly prevent try and error methods and implant failure.

Chen *et al*. (2011) uses FEA method to study the effect of Stress distribution at implant−bone interface. It was designed hollow and solid implants; the hollow model represented cancellous bone and solid model - cortical bones. The model implants were assumed to be homogenous, isotropic and linearly elastic. A static force of 50-300 N in the axial direction was applied. From the simulation results, it was noted that the main factors contributing to implants stability are the structure of the implants, the distribution of the interface stress and the combination mode of the interface.

The type of material used in biomedical applications depends on specific implant applications; different types of implant need different mechanical properties. Since the architectures of bone tissues in the human body are not completely dense and solid, it is desirable to produce biomimetic

structures as a replacement for damaged bone tissues (Wang *et al.,* 2016). Using the undoubted capabilities of AM technology, it is possible to produce graded material with varying mechanical properties of lower Elastic modulus for biomedical applications (Beaman *et al.,* 2000). To ascertain the suitability of graded biomaterial applications, a preliminary study was conducted by simulating a mandible CAD model with graded material properties of Ti-based alloys.

4.2: Mechanisms of Mastication

The mandible (lower jaw) is noted as the strongest bone of the skull which is capable of moving independently from the head movement. It supports the lower teeth and provides a place of attachment for the mastication muscle (Saladin, 1998). Mastication is the combined action of the jaw biomechanics and reflex mechanisms by the jaw elevator muscles to produce the necessary forces for mastication (Koc *et al.,* 2010). More than 20 muscles are involved in the jaw biomechanics during mastication (Palastanga, 1998) but the complex movement of these muscles could be simplified to three primary muscles (*temporal, pterygoid and masseter muscles*) (Daumas *et al.,* 2005). The masseter muscle is the principal mastication muscle which is responsible for retracting and elevating the mouth (opening and closing of the mouth). It must be able to exert enough force for biting and chewing of food (Santana-Mora *et al.,* 2014). The magnitude of the resultant force produced by the mastication muscles on the dental arches during clenching of the teeth in maximum intercuspation for normal human being's ranges from 246.9 to 2091.9 N (Hattori *et al.,* 2009). The resultant force during clenching of the teeth is said to act at an angle of 69^0 approximately. This is because the angle between the occlusal plane and the anterior boarder of the masseter muscle remains approximately 69^0 (Figure 4.1b point D) based on the cephalogram analysis of Sato *et al.* (2007).

4.3: Results and Discussions

4.3.1: FEA for Jaw Bone and Ti6Al4V Alloy Implant

The first model (Model 1, Figure 4.3.1a) was assigned an Elastic modulus of 11.7 GPa and Poisson's ratio of 0.35 representing cortical bone. At the angle of incidence of the force (69^o), the implant model would experience most stress at the upper part of the mandible. This correlates with the normal function of mandible, since that is the part that translates around a fixed point (point A2 in Figure 4.2.1b) when retracting and elevating the mouth and bears the maximum load during

opening and closing of the mouth (de Jong *et al.,* 2011). The second model (Model 2, Figure 4.3.1b) was defined by the material properties of Ti6AlV alloy (Elastic modulus of 110 GPa and Poisson's ratio of 0.35). Due to the higher Elastic modulus, the material experiences less deformation (strain) indicating its ability to bear more load as compared to Figure 4.3.1a. Nevertheless, the model defined by 11.7 GPa (Figure 4.3.1a) is very suitable for biomedical applications, since the maximum strain value is about 0.01 below the peak strain of 0.0275 as reported by Horch *et al.* (2011) for human cortical bone.

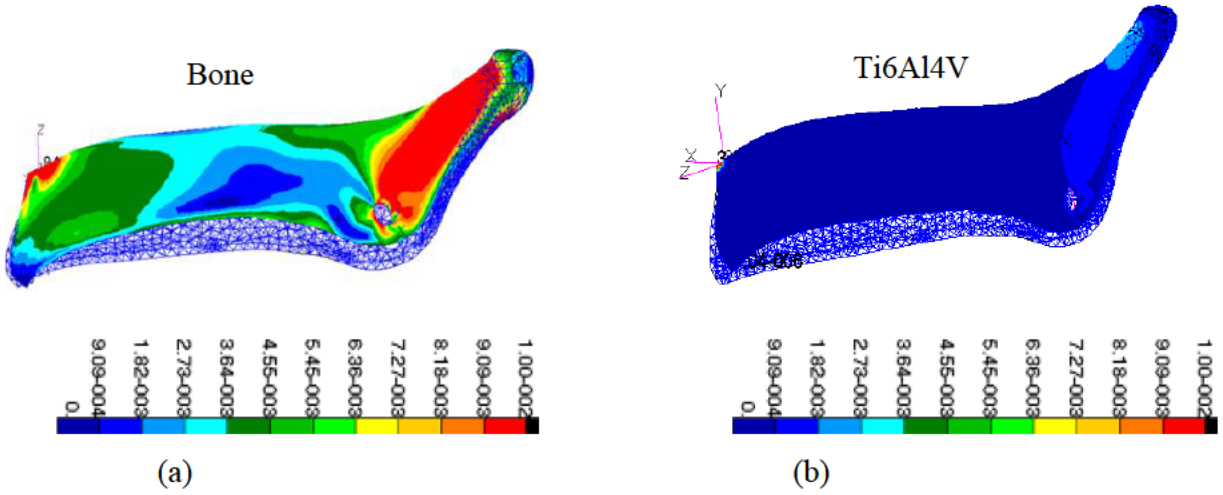

Figure 4.3.1: Numerical simulations for mandible models: true strains for bone (a) and Ti6Al4V alloy (b).

4.3.2: FEA for Segmented Implant with the Cellular Middle Part

Complex mandible CAD models were designed (Figure 4.3.2a and b), where the implants were segmented into three sections. Sections 1 and 3 were defined by the material properties of dense solid Ti6Al4V (Elastic modulus of 110 GPa and Poisson's ratio of 0.35) and the mid portion was assigned lower Elastic modulus of porous Ti6Al4V alloy (Elastic modulus of 1.6 GPa and Poisson's ratio of 0.35). The segmented models were meshed with tetrahedral elements after the proper element size was selected on the basis of mesh convergence analysis in order to obtain mesh independent solutions at areas expected to be critical areas for stress raisers like the regions around the holes (Figure 4.2.2.1b point A2 and C2).

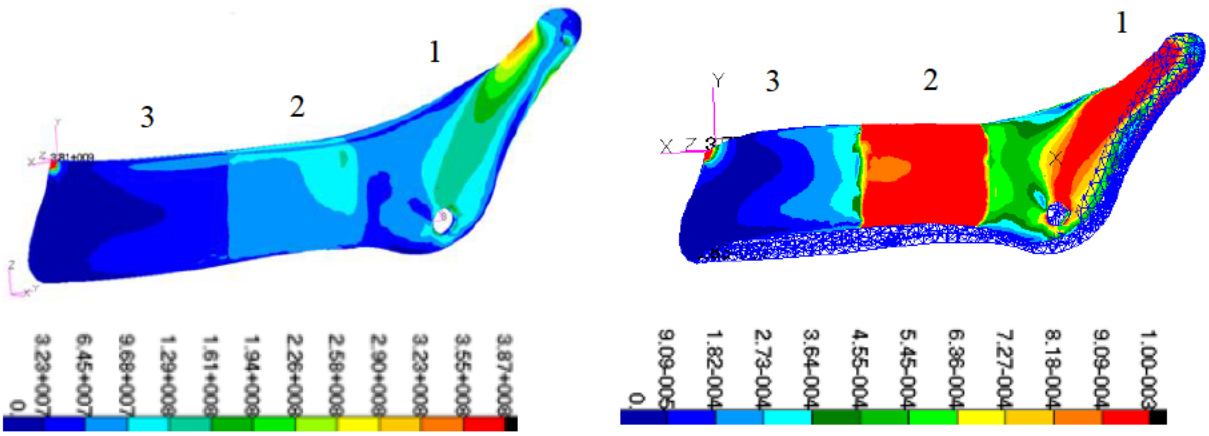

Figure 4.3.2: Simulated three-sections CAD mandible model: von Mises stress (a) and true strain (b).

The maximum Von Mises stress recorded under the loading conditions corresponding to the complex mandible implant CAD model in section 1 was 387 MPa (Figure 4.3.2a). This maximum stress indicated that the implant would not fail at the load of 1000 N, because the maximum stress generated on the implant due to the applied force was less than the yield stress of dense solid Ti6Al4V which could range between 703–933 MPa (Niinomi, 1998; Niinomi, 2008). The stress value recorded for section 2 of the complex mandible (Figure 4.3.2a) was less compared to section 1. The Elastic modulus for section 1 is higher than section 2, and it is expected to bear more load as it is heavier and stronger than section 2. Section 2 serves as a place of attachment for other facial muscles and does not experience much stress during mastication like section 1. Section 1 is the place the masseter muscle is attached to and requires a stronger region for attachment to bear the necessary load required for biting and chewing.

It is also noted that one major reason for most mandible failure is as the result of the mismatch of the Elastic modulus between implants and bone tissue (Barbas *et al.,* 2012). To reduce the total weight of the implant, it is prudent to produce a complex mandible implant with a strong region (higher Elastic modulus, section 1) that can bear the force exerted by the masseter muscle without fracture and a region with lower Elastic modulus (section 2). Such reduction in the weight of the mandible implant would definitely translate to a reduction in implant failure (due to the stress-shielding effect, bone resorption and implant loosening) and better quality of life for implant patients.

The maximum Von Mises stress recorded by section 2 of the complex implant was 129 MPa which is below compression stress of bones (Öhman *et al.,* 2011). The result of the Von Mises strain simulation (Figure 4.3.2b) also revealed that the implant models deformed heavily at the upper part (section 1) and region two of lower Elastic modulus. Section 3 of both complex implant models did not experience much stress or strain, probably due to the angle at which the force was applied and its distance from the point of application. The force was directly applied in section 1 and then transmitted to section 2. Therefore, it is expected that the effect of the applied force would mainly be experienced in section 1, which actually needs to bring about biting and chewing by opening and closing the mouth. Section 3 served as a region for attachment of facial muscles and the digastric muscle (point E1 in Figure 4.2.1a), which does not experience much stress as compared to section 1 (point A1, A2 and C1, C2 in Figure 4.2.1a and b). Section 2 would probably not require a very strong material to bear stress during mastication. It is therefore proposed that in designing an implant, region 1 should be designed with a strong material (high Elastic modulus) while regions 2 and 3 should be built with a material with relatively lower Elastic modulus.

The degree of displacement of the complex simulated mandible models were compared with the displacement of solid Ti6Al4V alloy and cortical bone. It is evident that displacement is inversely proportional to elastic modulus. The material with the least Elastic modulus has the highest displacement and the one with the highest Elastic modulus (Ti6Al4V alloy) has the least displacement. The complex implant with the least resultant elastic modulus was displaced more than the one with the highest resultant Elastic modulus. The displacements recorded during the simulation were higher than the maximum displacement of the human mandible (0.42 mm) (Ichim *et al.,* 2007) during mastication. The large displacement could be attributed to the difference between the average wall thickness of the human mandible (2-3 mm) (de Souza Fernandes *et al.,* 2012) and the wall thickness of the CAD model (2 mm).

4.3.3: FEA for the Replacing of the Damaged Part of the Jaw Bone

Further investigation was carried out on the complex CAD models. The models were segmented into three parts (Figure 4.3.3). The mid-section of the models was assigned the material properties of solid Ti6Al4V alloy (Elastic modulus of 110 GPa) or material with lower Elastic modulus of

30 GPa (Models 4 and 5 respectively) and the outer sections (sections 1 and 3) with Elastic modulus of 11.7 GPa represented jaw bone. This complex arrangement was meant to investigate the strain (deformation) at the mid-portion (section 2) of the models and to ascertain its suitability for patients who may not need total mandible replacement but replacement of a damaged part of the jaw bone.

The model with the lower Elastic modulus (Figure 4.3.3b) demonstrates a more uniform retrogressive deformation from region 1 to 2 than the one with the higher Elastic modules at the middle (Figure 4.3.3a). For bone-implant contact interlocking and avoiding of the stress shielding effect, replacing a damaged part of a mandible with a relatively lower Elastic modulus would probably prevent implant failure since the stress/strain induce by the mastication forces are most likely to be distributed uniformly.

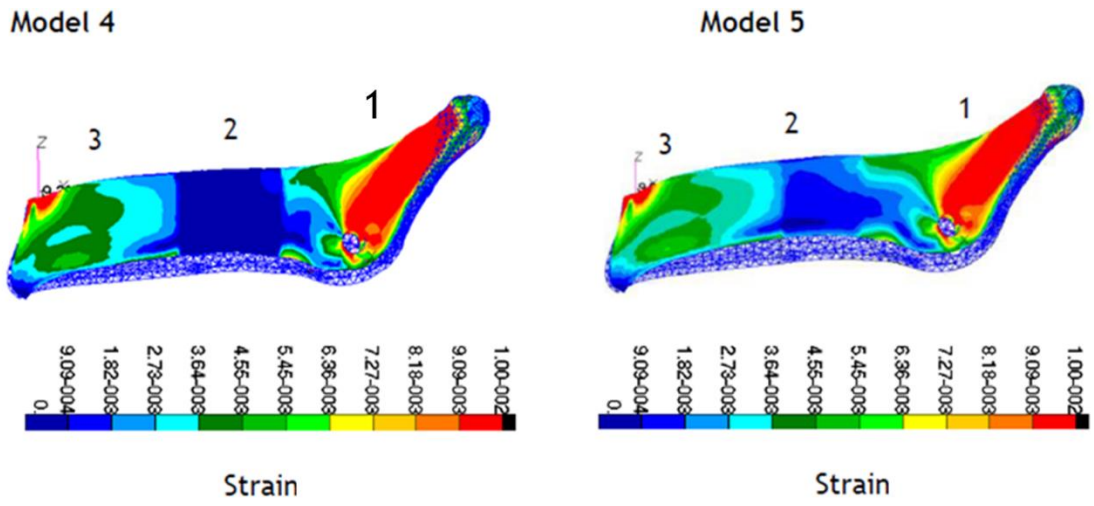

Figure 4.3.3: Simulated three-sections CAD mandible models with replacement by (a) solid DMLS Ti6Al4V and (b) material with lower Elastic modulus.

4.4: Summary

Replacing damage mandibular or part with graded material properties based on the functioning requirements would definitely lead to the production of advanced lightweight implants. The FEA analysis clearly demonstrated that it is worth manufacturing complex implants defined by varied mechanical properties. The region that the masseter muscle is attached to and the point of rotation (A2) should be designed with a relatively high Elastic modulus and sections 2 and 3 could be built with a lightweight material to reduce the total weight of the implant. Care should be exercised in

selecting the mechanical properties of the material that should be used to replace just a part of a damaged mandible since the sharp change in the Elastic modulus of the materials could lead to implant failure.

4.5: References

Ashman, R. B. & Van Buskirk, W. C., 1987. The elastic properties of a human mandible. *Advances in Dental Research*, 1(1), pp. 64-67.

Barbas, A., Bonnet, A.S., Lipinski, P., Pesci, R. & Dubois, G., 2012. Development and mechanical characterization of porous titanium bone substitutes. *Journal of the Mechanical Behavior of Biomedical Materials*, 9, pp. 34-44.

Beaman, J., Bourell, D., Jackson, B., Jepson, L., McAdams, D., Perez, J. & Wood, K., 2000. Multi-material selective laser sintering: empirical studies and hardware development. *In Proceedings of the 2000 NSF Design and Manufacturing Grantees Conference.* Austin, Texas.

Burkhart, T., Andrews, D. M. & Dunning, C. E., 2013. Finite element modeling mesh quality, energy balance and validation methods: A review with recommendations associated with the modeling of bone tissue. *Journal of Biomechanics*, 46(9), pp. 1477-1488.

Chen, L. J., Hao, H.E., Li, Y.M., Ting, L.I., Guo, X.P. & Wang, R.F., 2011. Finite element analysis of stress at implant–bone interface of dental implants with different structures. *Transactions of Nonferrous Metals Society of China*, 21(7), pp. 1602-1610.

Daegling, D. J. & Hylander, W. L., 1998. Biomechanics of torsion in the human mandible. *American Journal of Physical Anthropology*, 105(1), pp. 73-88.

Daumas, B., Xu, W. L. & Bronlund, J., 2005. Jaw mechanism modeling and simulation. *Mechanism and Machine Theory*, 40(7), pp. 821-833.

de Jong, W. C., Korfage, J. A. M. & Langenbach, G. E. J., 2011. The role of masticatory muscles in the continuous loading of the mandible. *Journal of Anatomy*, 218(6), pp. 625-636.

de Souza Fernandes, A. C., de Quadros Uzeda-Gonzalez, S., Mascarenhas, M.L., Machado, L.A. & de Moraes, M., 2012. Direct and tomographic dimensional analysis of the inter-radicular distance and thickness of the vestibular cortical bone in the parasymphyseal region of adult human mandibles. *British Journal of Oral and Maxillofacial Surgery*, 50(4), pp. 350-355.

Fraser, H. L., Imam, M.A., Kosaka, Y., Rack, H.J., Chatterjee, A. & Woodfield, A., 2016. The determination of residual stress in extruded Ti-6Al-4V by contour method and finite element analysis. *In 2015 World Conference on Titanium*. John Wiley & Sons.

Gultekin, B. A., Gultekin, P. & Yalcin, S., 2012. *Application of finite element analysis in implant dentistry*: INTECH Open Access Publisher.

Hanzl, P., Zetek, M., Bakša, T. & Kroupa, T., 2015. Procedia Engineering. The influence of processing parameters on the mechanical properties of SLM parts. *Procedia Engineering*, 100, pp. 1405-1413.

Hattori, Y., Satoh, C., Kunieda, T., Endoh, R., Hisamatsu, H. & Watanabe, M., 2009. Bite forces and their resultants during forceful intercuspal clenching in humans. *Journal of Biomechanics*, 42(10), pp. 1533-1538.

Heinl, P., Müller, L., Körner, C., Singer, R.F. & Müller, F.A., 2008. Cellular Ti–6Al–4V structures with interconnected macro porosity for bone implants fabricated by selective electron beam melting. *Acta Biomaterialia*, 4(5), pp. 1536-1544.

Heylighen, F., 1999. The growth of structural and functional complexity during evolution. *The Evolution of Complexity*, pp. 17-44.

Horch, R. A., Gochberg, D. F., Nyman, J. S. & Does, M. D., 2011. Non-invasive predictors of human cortical bone mechanical properties: T 2-discriminated 1 H NMR compared with high resolution X-ray. *PloS One*, 6(1), pp. e16359.

Ichim, I., Kieser, J. A. & Swain, M. V., 2007. Functional significance of strain distribution in the human mandible under masticatory load: numerical predictions. *Archives of Oral Biology*, 52(5), pp. 465-473.

Ichim, I., Swain, M. V. & Kieser, J. A., 2006. Mandibular stiffness in humans: numerical predictions. *Journal of Biomechanics*, 39(10), pp. 1903-1913.

Koc, D., Dogan, A. & Bek, B., 2010. Bite force and influential factors on bite force measurements: a literature review. *European Journal of Dentistry*, 4(2), pp. 223-232.

Korioth, T. W. P. & Hannam, A. G., 1994. Deformation of the human mandible during simulated tooth clenching. *Journal of Dental Research*, 73(1), pp. 56-66.

Korioth, T. W., Romilly, D. P. & Hannam, A. G., 1992. Three-dimensional finite element stress analysis of the dentate human mandible. *American Journal of Physical Anthropology*, 88(1), pp. 69-96.

Niinomi, M., 1998. Mechanical properties of biomedical titanium alloys. *Materials Science and Engineering: A*, 243(1), pp. 231-236.

Niinomi, M., 2008. Biologically and mechanically biocompatible titanium alloys. *Materials Transactions*, 49(10), pp. 2170-2178.

Öhman, C., Baleani, M., Pani, C., Taddei, F., Alberghini, M., Viceconti, M. & Manfrini, M., 2011. Compressive behaviour of child and adult cortical bone. *Bone*, 49(4), pp. 769-776.

Palastanga, N., 1998. *Anatomy and Human Movement: Structure and Function*. Boston: Butterworth-Heinemann, Oxford.

Rogge, R. D., Adams, B. D. & Goel, V. K., 2002. An analysis of bone stresses and fixation stability using a finite element model of simulated distal radius fractures. *The Journal of Hand Surgery*, 27(1), pp. 86-92.

Saladin, K. S., 1998. *Anatomy & physiology, 2nd Edition.* Mishawaka: WCB/McGraw-Hill.

Santana-Mora, U., Martínez-Ínsua, A., Santana-Penín, U., del Palomar, A.P., Banzo, J.C. & Mora, M.J., 2014. Muscular activity during isometric incisal biting. *Journal of Biomechanics*, 47(16), pp. 3891-3897.

Sato, M., Motoyoshi, M., Hirabayashi, M., Hosoi, K., Mitsui, N. & Shimizu, N., 2007. Inclination of the occlusal plane is associated with the direction of the masticatory movement path. *The European Journal of Orthodontics*, 29(1), pp. 21-25.

Strait, D. S., Wang, Q., Dechow, P.C., Ross, C.F., Richmond, B.G., Spencer, M.A. & Patel, B.A., 2005. Modeling elastic properties in finite-element analysis: How much precision is needed to produce an accurate model? *The Anatomical Record Part A: Discoveries in Molecular, Cellular, and Evolutionary Biology*, 283(2), pp. 275-287.

Wang, X., Xu, S., Zhou, S., Xu, W., Leary, M., Choong, P., Qian, M., Brandt, M. & Xie, Y.M., 2016. Topological design and additive manufacturing of porous metals for bone scaffolds and orthopaedic implants: A review. *Biomaterials*, 83, pp. 127-141.

Wirtz, D. C., Schiffers, N., Pandorf, T., Radermacher, K., Weichert, D. & Forst, R., 2000. Critical evaluation of known bone material properties to realize anisotropic FE-simulation of the proximal femur. *Journal of Biomechanics*, 33(10), pp. 1325-1330.

CHAPTER 5: EVALUATION OF THE MECHANICAL PROPERTIES OF DMLS CELLULAR STRUCTURES

5.1: Introduction

Most researchers have focused on optimizing the DMLS process to manufacture dense non-porous parts (Kruth *et al.,* 2005; Kruth *et al.,* 2010; Thijs *et al.,* 2010), but more recently great attention has been given to manufacturing low-density lattice structures for biomedical applications (de Damborenea *et al.,* 2015; Wally *et al.,* 2015).

Cellular structures can perform the function of the irregular rod and plate-like trabeculae in the middle of the cranial bone. In a case when the first outer cortical bone fractures the second still protects the brain before the cranial surgery. A biomimetic replacement is also required for cranial traumatic patients to minimize implant failure. The response of the head to traumatic loading is intrinsically linked to the anatomy and mechanical properties of the crania, hence any replacement which does not comprehensively take necessary anatomical consideration in the design process could lead to implant failure. As indicated by Singh *et al.* (2016), three-dimensional open porous interconnected structures (scaffolds) can be used to repair or fill the defective bone sites of the human body. The conventional technologies did not permit manufacturing of graded biomimicry anatomical devices. However, with the advent of AM technologies and the superior capabilities of the DMLS manufacturing process, it is most likely to manufacture implants with anatomical compatibility.

Despite the celebrated biomechanical properties of Ti6Al4V alloy, it is well documented that its Elastic modulus (110-114 GPa) is far above that of human bone (Table 5.1.1). In view of this, there is a need to produce novel biomaterial with better mechanical properties similar to that of bone tissue and to use cellular structures for advanced implants. Since cellular structures are known to mimic the anisotropic porous nature of bone and with the possibility of tuning their Elastic modulus over a wide range by varying the lattice properties (Soman *et al.,* 2012), such structures would probably provide the much-needed solution by reducing the effective Elastic modulus of Ti6Al4V alloy (Lin *et al.,* 2013). The creation of open space within the lattices would also translate to minimal material usage and the discrete pore volumes in micron dimensions would in addition

produce a perfect surface for bone-implant interlocking with suitable biomechanical properties (Murr *et al.*, 2010).

Table 5.1.1: Mechanical properties of adult human bones (Nouri *et al.*, 2010)

	Cortical bone		Cancellous bone
	longitudinal direction	transverse direction	
Tensile strength, MPa	79-151	51-56	
Compressive strength, MPa	131-224	106-133	2-5
Elastic moduli of compact bone, GPa	17-20	6-13	0.76-4
Apparent density, g/cm^3	1.99		0.05-1.0

Ohman *et al*. (2011) found that a child's cortical bone tissue had significant lower compressive Elastic modulus (−34%), yield stress (−38%) and ultimate stress (−33%) than an adult's bones.

Table 5.1.2 presents values of porosity and Elastic modulus of various forms of AM Ti6Al4V cellular structures. Wieding *et al.* (2012) noted that a low Elastic modulus can stimulate growth of bone cells due to mechanical stimulus by physiological load application, and avoid stress shielding caused by high stiffness gradients between bones and implants.

Table 5.1.2: Mechanical properties of DMLS and EBM Ti6Al4V cellular structures

Type of lattice structure	Technology	Porosity, %	Elastic Modulus (GPa)	Reference
Scaffold with rectangular struts	DMLS	70.2 ± 0.4	5.1±0.3	(Wieding *et al.*, 2012)
Scaffolds with shifted strut alignment		71.9 ± 0.2	3.7±0.2	
Scaffolds with diagonal struts		68.7 ± 0.2	6.7±0.3	
Unit cell in the form of prisms	DMLS	69	0.341	de Damborenea *et al.*, 2015
Diamond structure	EBM	80.5	1.6	Heinl *et al.*, 2008
Hatched structure		59.5	12.9	
Honeycomb-like structure	EBM	66.3	2.5	Li *et al.*, 2009
Rhombic dodecahedron	EBM	70.32	2.13	Parthasarathy *et al.*, 2010
Rhombic dodecahedron		60.41	2.68	
Rhombic dodecahedron		50.75	2.92	

As demonstrated earlier in Chapter 4 of this study, finite element modeling was used to modify the Elastic modulus of different parts of Ti6Al4V mandibular implant closely matching with the mechanical properties of human bone, while still retaining the required strength for normal functionality. The FEA in the preliminary studies has demonstrated that implant failure has been attributed to the mismatch between the Elastic modulus of the bone and the implants. To avert the situation, it was indicated that manufacturing implants with the relatively low Elastic modulus of cellular structures would prevent implant failure due to stress shielding effect. The mandible CAD models demonstrated that implants with a low Elastic modulus in the range of mechanical properties of bone would permit a homogeneous load transferred stress stimulation of the bone. It was hypothesized that implant design with cellular structures with relative low Elastic modulus would bridge the Elastic modulus gradient between dense solid metallic implants and the porous bones. It came to light that advanced light weight implant could be manufactured with cellular structures due to the advantage of high strength accompanied by a relatively low mass offered by cellular structures.

The current chapter provides experimental backing to the FEA claims in chapter 4. The mechanical properties of selected cell structures were determined to demonstrate the extent to which the effective Elastic modulus of Ti6Al4V cellular structures could be modified to approach that of bone through a selection of appropriate cellular lattice structures. The choice of the structures was based on lattice structures that produce Elastic modulus close to that of cortical or trabecular bone (Table 5.1.1). A preliminary investigation was conducted with polyamide 12 (PA 2200) powder to determine the appropriate struts sizes of the cellular structures that could be manufactured. The results that were obtained from the PA2200 serve as a gateway for the real experiment with Ti6Al4V alloy.

5.2: Cellular structures

The specimens for compression tests were cubes with periodic cellular lattice structures and solid top and bottom layers of 1 mm in thickness. Cubes with size 25x25x25 mm^3 were designed with 25%, 50% and 75% volume fraction with rhombic nodes (types A, B, C) and 2 cubes with similar size but 50% and 75% volume fraction (types D and E) (Figure 5.2.1). Volume fraction was defined as the volume percentage of solid material in the CAD cellular lattice structure. A fixed

unit cell size of 5 mm was chosen. The strut diameters of the unit cells are indicated in Figure 5.2.1. Three cubes in each series were produced from PA 2200 powder (polyamide 12) by an EOSINT P380 machine while the Ti6Al4V cellular structures were manufactured by the EOSINT M280 machine.

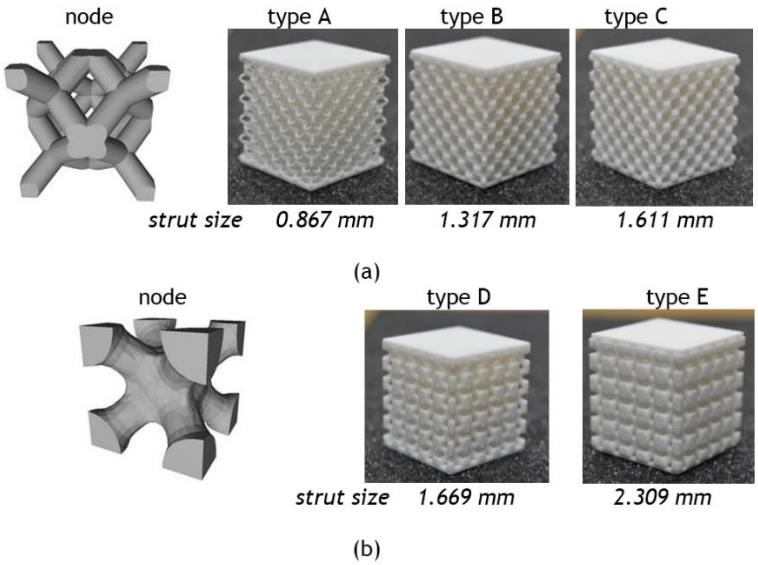

Figure 5.2.1: CAD models of nodes for cellular structures and PA 2200 cubes with rhombic (a) and diagonal cellular structures (b).

The Ti6Al4V cellular structures were manufactured from Ti6Al4V (ELI) powder (Table 3.2.1); specimens attached to the substrate were subjected to heat treatment post-processing in Ar atmosphere at 650°C (3 hours) for stress relieving, then were separated from the base plate and cut into 4 parts each via wire Electrical Discharge Machining (Figure 5.2.2).

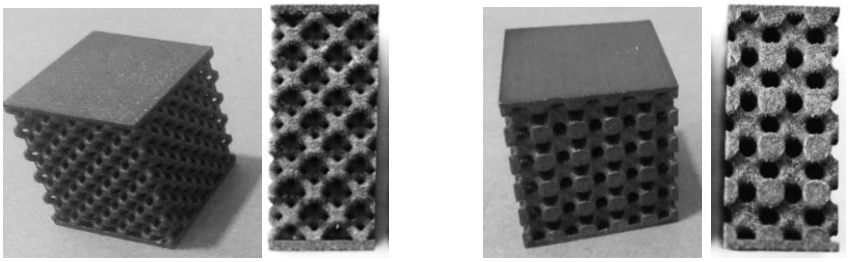

(a) (b)

Figure 5.2.2: General and frontal views of Ti6Al4V (ELI) DMLS objects with rhombic (a) and diagonal structures with 50% CAD volume fraction (b).

Mechanical properties of the Ti6Al4V and PA 2200 specimens were obtained through uniaxial compression tests. Compressive stress was calculated as the ratio of load (N) to the top surface area in direct contact during compression tests.

5.3: Results and Discussion

5.3.1: PA 2200 Cellular Structures

Stress-strain diagrams of compression tests for PA 2200 samples are shown in Figure 5.3.1. Elastic moduli for manufactured cellular structures were calculated as chord 0.1–0.5 MPa for type A samples, 1–4 MPa for type B samples, 2–10 MPa for types C–E.

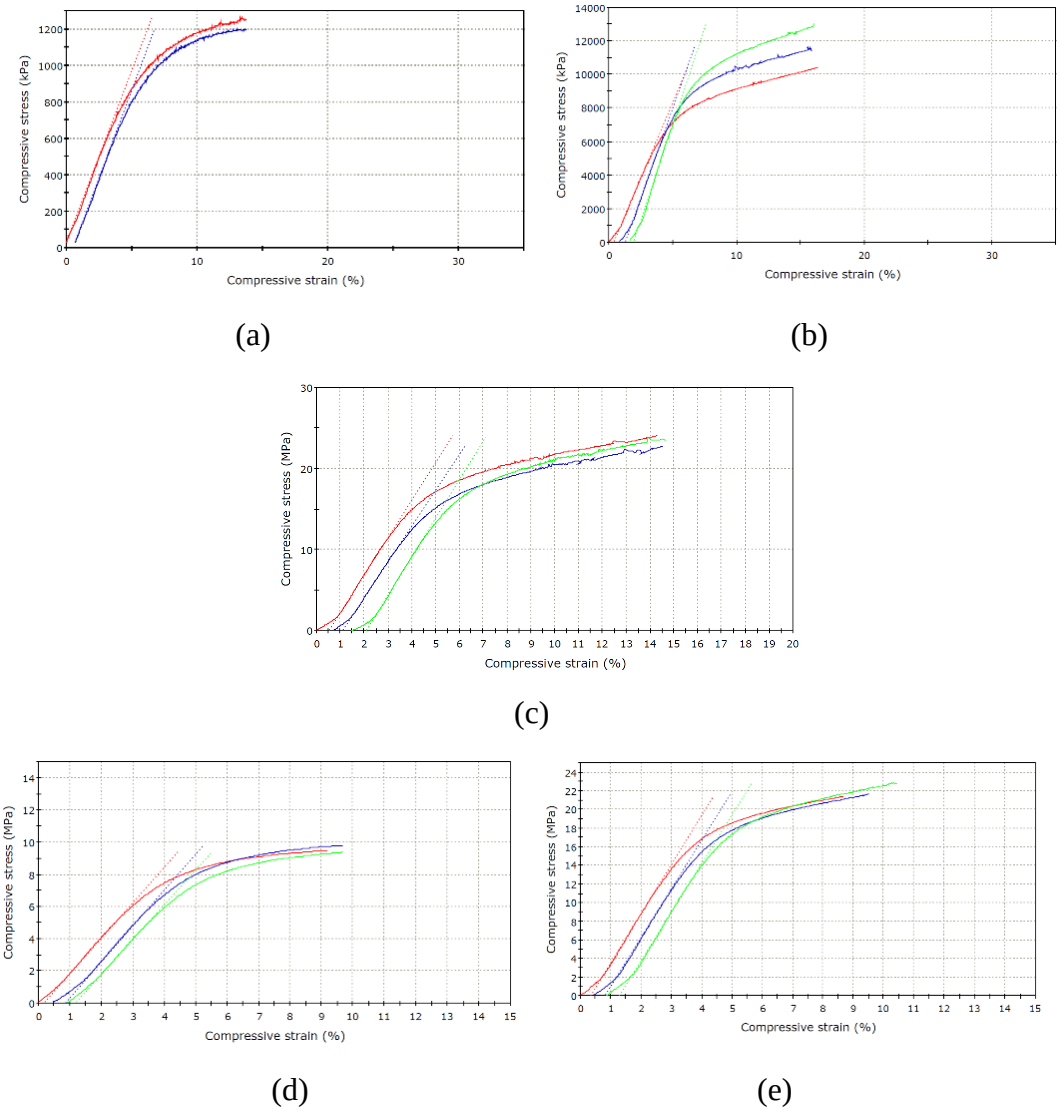

Figure 5.3.1: Compressive characteristic diagrams for different PA 2200 cellular samples: a (type A), b (type B), c (type C), d (type D) and e (type E) series.

The mechanical properties of the cellular structures measured from the compression test data are summarized in Table 5.3.1. The strain-stress behaviour at compression was similar for both types of nodes, but diagonal scaffolds (samples D–E) were stiffer than rhombic structures (samples B–C).

For solid PA 2200 samples obtained by Miron-Borzan *et al*. (2015) Elastic modulus was E_0=1.2–1.38 GPa. For 50% porous cellular structures, Elastic modulus was about 6 times lower in comparison with solid material (Table 5.3.2). Gibson &Ashby (1997) predicted the response to load for cellular structures as

$$\frac{E}{E_0} = k(\frac{\rho}{\rho_0})^r$$

where E_0 and ρ_0 are Elastic modulus and density for solid material, k and r depend on the type of structure. Figure 5.3.2 shows the elastic modulus of PA 2200 cellular structures as a function of volume fraction and maximum strut size for rhombic and diagonal scaffolds at a fixed unit cell size of 5 mm. The Elastic modulus increases with the volume fraction, as was predicted by the Gibson–Ashby model. Compressive strength also increases with strut size, but more drastic changes were observed for the rhombic type nodes (Table 5.3.1, Figure 5.3.2).

Table 5.3.1: Mechanical properties of different PA 2200 cellular samples

Types	Relative CAD porosity, %	Maximum load, N	Elastic Modulus, MPa	Compressive stress at maximum compressive load, MPa	Compressive strain at maximum compressive load, %
A	75	765±27	19±0.2	1.23±0.04	12.8±0.7
B	50	7384±816	208.5±24.4	11.69±1.3	15.2±1.0
C	25	15114±464	461.6±16.9	23.5±0.7	13.5±0.9
D	50	5917±150	219.2±4.3	9.5±0.2	9.0±0.2
E	25	14227±529	524.3±4.2	22.0±0.1	9.1±0.4

PA 2200 of 50-75% volume fraction cellular diagonal and rhombic structures had peak stress of 9.5-23.5 MPa. The proposed structures had stable mechanical properties and can be used in biomedical applications, depending on the required strength characteristics. Additional studies on regenerative properties of the tissue cells at the indicated shapes and sizes should be carried out.

Cerardi *et al*. (2013) use cubic nodes which were reinforced diagonally to produced cellular structures with porosities ranging from 40% – 80%. The Elastic modulus values obtained were higher (663±63 - 1143±207) than what was recorded for the current experiment due to the diagonal reinforcement of the nodes. It is also of interest to point out that the difference between Fig. 5.3.1 and Fig. 5.3.3 is due the difference in their material properties- thus PA 2200 and Ti6Al4V respectively.

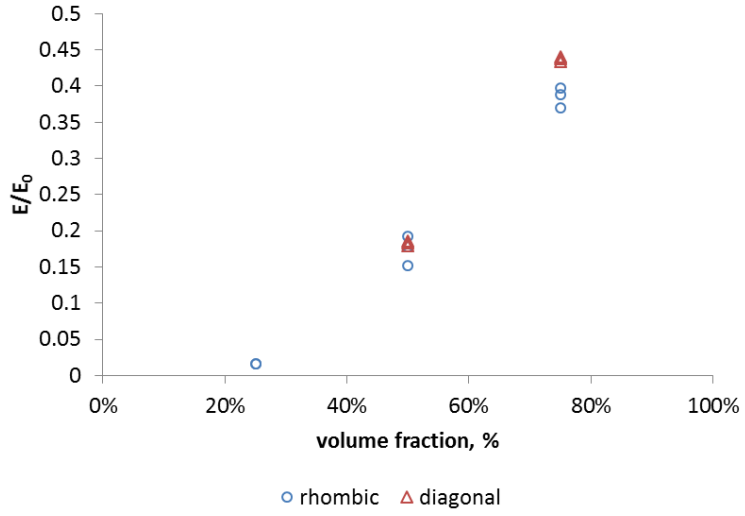

(a)

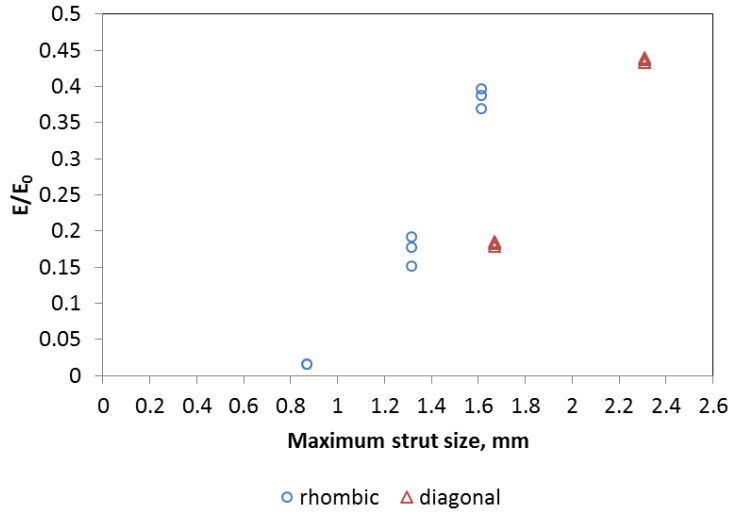

(b)

Figure 5.3.2: Elastic modulus *versus* volume fraction (a) and maximum strut size (b) of PA2200 cellular structures.

5.3.2: Ti6Al4V (ELI) Cellular Structures

Stress-strain diagrams of compression tests for DMLS Ti6Al4V samples are shown in Figure 5.3.3 and the resultant mechanical properties are presented in Table 5.3.2.

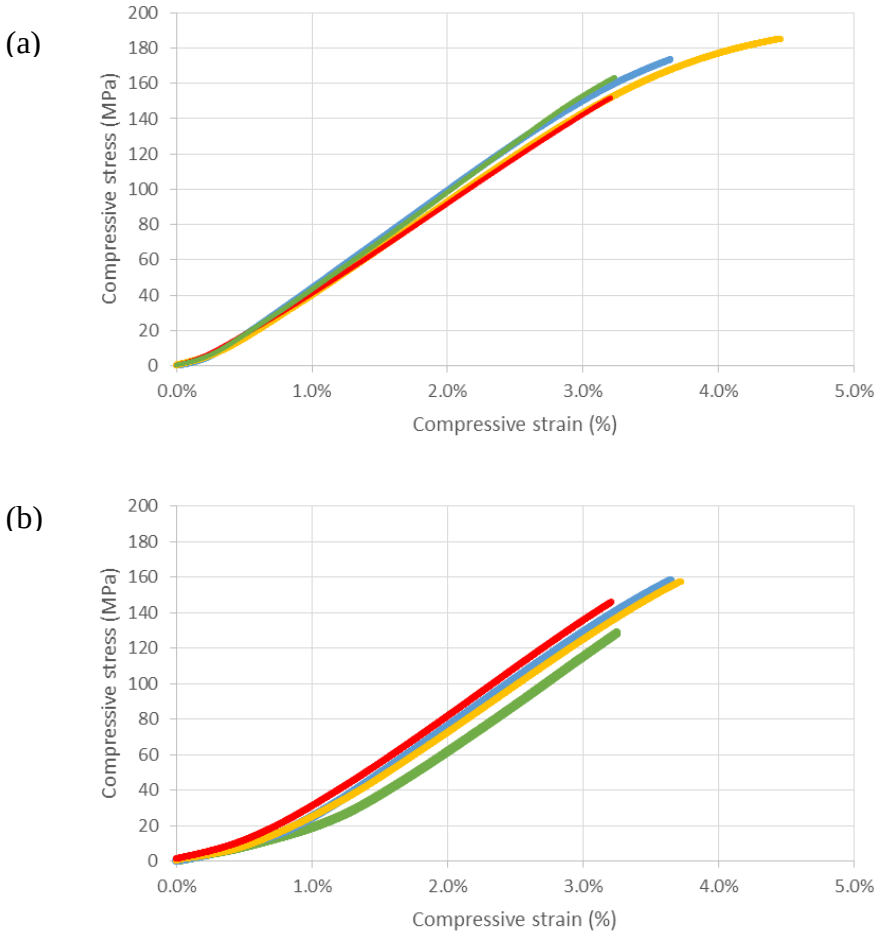

Figure 5.3.3: Compressive characteristic diagrams for Ti6Al4V cellular samples: structures of B (a) and D (b) types.

The macroscopic Elastic modulus for Ti6Al4V cellular structures was estimated as the slope of the linear part of the compressive characteristic diagram. The yield stress, defined as the inflection point between the linear and non-linear parts of the stress-strain diagram, was about 140-160 MPa and higher (Figure 5.3.3). Taking into account the trends from Figure 5.3.2(a) and assuming similar behaviour of DMLS cellular samples, manufacturing of 50% volume fraction will result in closely similar modulus of elasticity for the rhombic and diagonal structures for the same unit cells. Elastic moduli were found to be similar for the Ti6Al4V rhombic and diagonal scaffolds: 5.3 GPa and 5.1 GPa, respectively, as shown in Table 5.3.2.

Table 5.3.2: Mechanical properties of different DMLS Ti6Al4V cellular samples

Types	Max load, kN	Elastic Modulus, GPa	Compressive stress at maximum load, MPa	Compressive strain at maximum load, %
B	25	5.3±0.2	168.4±14.4	3.40±0.58
D	25	5.1±0.1	162.7±4.8	3.19±0.07

Phase transformations, texture effects and microstructural strengthening, as well as surface roughness, can affect the mechanical properties of the AM cellular structures (Hernández-Nava *et al.,* 2015). The microstructure of as-built Ti6Al4V alloy typically consists of α´ martensite. After stress-relieving heat treatment no significant changes in the microstructures have been found. The microstructures of the nodes of the DMLS cellular structures are shown in Figure 6.34 and Figure 6.3.5. Primary β grains were oriented almost parallel to the building direction (Figure 5.3.4b and Figure 5.3.5b); at perpendicular cross-sections the grain boundaries of the primary β phase also were well distinguished (Figure 5.3.4a).

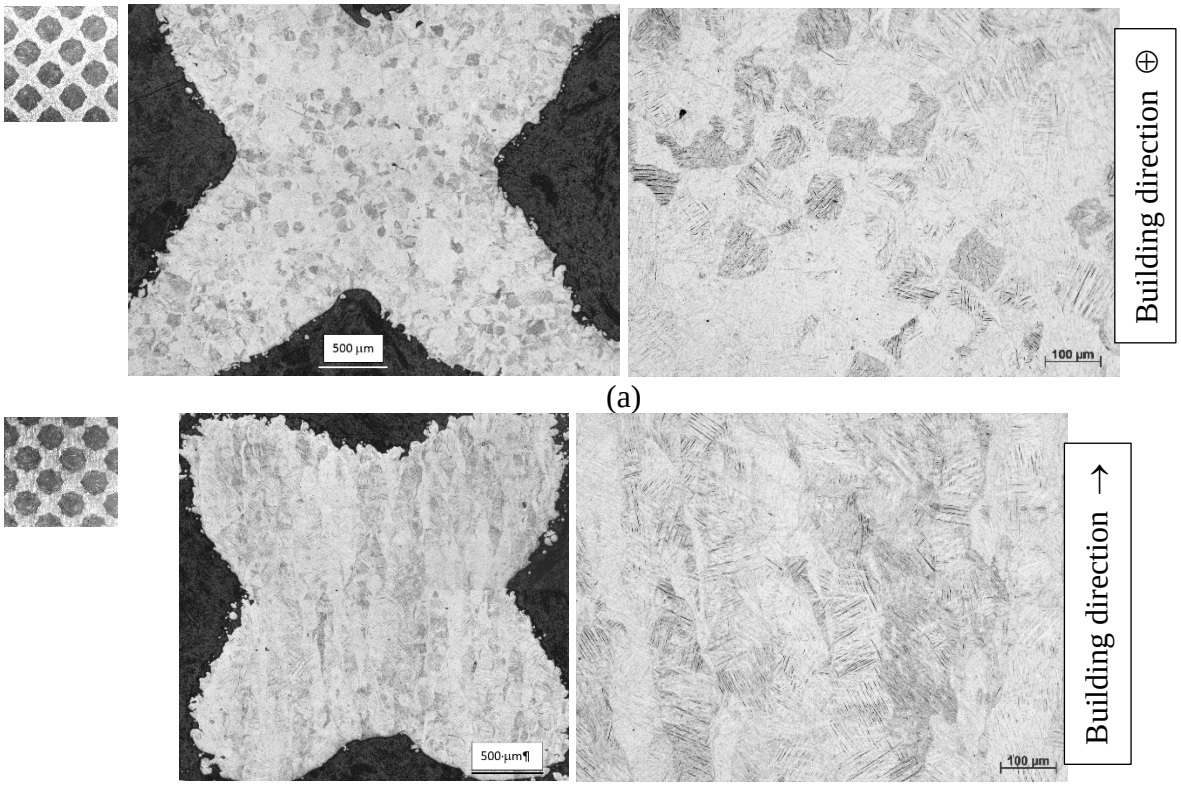

Figure 5.3.4: Cross-sections of Ti6Al4V rhombic nodes (type B): perpendicular (a) and along building direction (b).

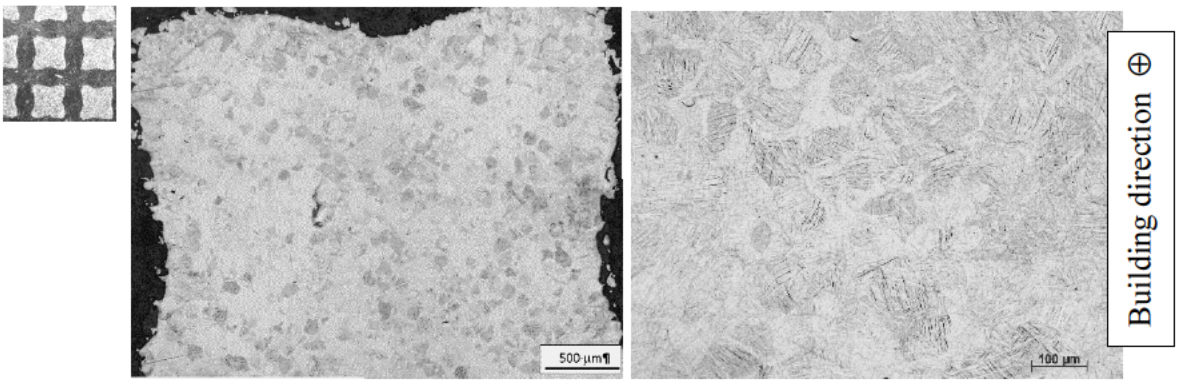

(a)

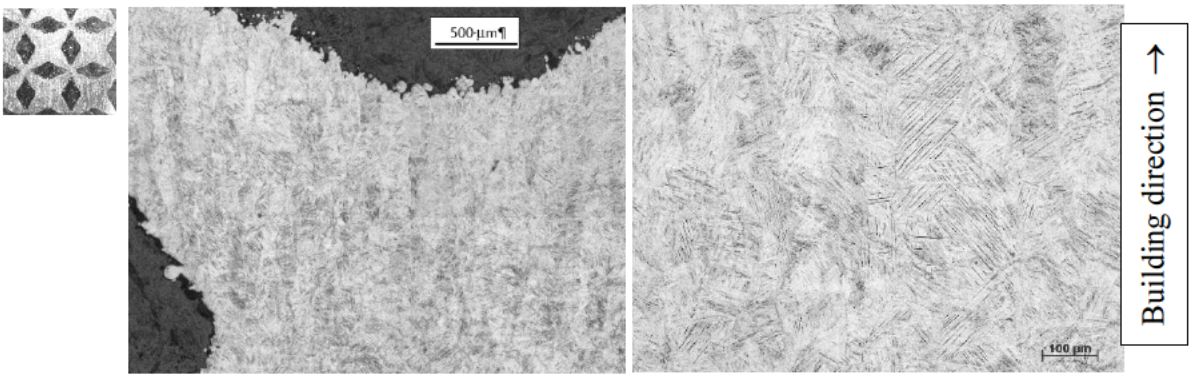

(b)

Figure 5.3.5: Cross-sections of Ti6Al4V diagonal nodes (type D): perpendicular (a) and along building direction (b).

Attached powder particles inside the cellular structures are visible in the cross-sections (Figure 5.3.4a and Figure 5.3.5a). No pores bigger than 20 µm were found in the analysed cross-sections of the struts. DMLS material had stable mechanical properties when loading was applied co-axial to the building direction. Compressive tests showed that the proposed DMLS Ti6Al4V cellular structures are suitable for fabrication of light-weight implants because their mechanical properties are close to the properties of human bone (Table 5.3.1 and Table 5.3.2).

5.4: Summary

When selecting the implant material to replace a part of a damaged bone, distinct differences between the Elastic moduli of these materials can lead to bone–implant discontinuities resulting in interfacial failure. The finite element analysis clearly demonstrated that it would be worth designing and manufacturing complex implants based on the mechanical properties of cellular structures. Manufacturing complex implants with the inherent mechanical properties of lattice

structures would definitely lead to advanced light-weight implants with biocompatible mechanical properties.

The Elastic modulus as well as compressive strength of PA 2200 DMLS structures increased with strut size and volume fraction. Proposed geometry of cellular structures from this material can be used as scaffolds in regenerative surgery to repair the body quickly and effectively.

Ti6Al4V DMLS rhombic and diagonal cellular structures have Elastic modulus and strength similar to the cancellous human bone. It must be noted that compression tests were done on uniaxially and cellular structures were tested along building direction. Further investigations of mechanical properties of DMLS cellular structures are needed to improve the Elastic modulus and to achieve satisfactory strength with respect to the loading direction and required strength for the specific implants.

5.5: References

Cerardi, A., Caneri, M., Meneghello, R., Concheri, G. & Ricotta, M., 2013. Mechanical characterization of polyamide cellular structures fabricated using selective laser sintering technologies. *Materials & Design*, 46, pp.910-915.

de Damborenea, J. J., Larosa, M.A., Arenas, M.A., Hernández-López, J.M., Jardini, A.L., Ierardi, M.C.F., Zavaglia, C.A., Maciel Filho, R. & Conde, A., 2015. Functionalization of Ti6Al4V scaffolds produced by direct metal laser for biomedical applications. *Materials & Design*, 83, pp. 6-13.

Gibson, L. J. & Ashby, M. F., 1997. Cellular Solids Structure and Properties. Cambridge: Cambridge University Press.

Heinl, P., Müller, L., Körner, C., Singer, R.F. and Müller, F.A., 2008. Cellular Ti–6Al–4V structures with interconnected macro porosity for bone implants fabricated by selective electron beam melting. *Acta Biomaterialia*, 4(5), pp. 1536-1544.

Hernández-Nava, E., Smith, C.J., Derguti, F., Tammas-Williams, S., Léonard, F., Withers, P.J., Todd, I. & Goodall, R., 2015. The effect of density and feature size on mechanical properties of isostructural metallic foams produced by additive manufacturing. *Acta Materialia*, 85, pp. 387–395.

Kruth, J. P., Badrossamay, M., Yasa, E., Deckers, J., Thijs, L. & Van Humbeeck, J., 2010. Part and material properties in selective laser melting of metals. *In Proceedings of the 16th international symposium on electromachining.*

Kruth, J. P., Mercelis, P., Van Vaerenbergh, J., Froyen, L. & Rombouts, M., 2005. Binding mechanisms in selective laser sintering and selective laser melting. *Rapid Prototyping Journal*, 11(1), pp. 26-36.

Kulkarni, M., Mazare, A., Schmuki, P. & Iglič, A., 2014. Biomaterial surface modification of titanium and titanium alloys for medical applications. *Nanomedicine*, 5, pp. 112-130.

Li, X., Wang, C., Zhang, W. & Li, Y., 2009. Fabrication and characterization of porous Ti6Al4V parts for biomedical applications using electron beam melting process. *Materials Letters*, 63(3), pp. 403-405.

Miron-Borzan, C. S., Dudescu, M.C., Elghany, K.A., Ceclan, V. & Berce, P., 2015. Analysis of Mechanical Properties of Selective Laser Sintered Polyamide Parts Obtained on Different Equipment. *Material Plastic*, 52, pp. 39.

Murr, L. E., Gaytan, S.M., Medina, F., Lopez, H., Martinez, E., Machado, B.I., Hernandez, D.H., Martinez, L., Lopez, M.I., Wicker, R.B. & Bracke, J., 2010. Next-generation biomedical implants using additive manufacturing of complex, cellular and functional mesh arrays. *Philosophical Transactions of the Royal Society of London A. Mathematical, Physical and Engineering Sciences*, 368(1917), pp. 1999-2032.

Nouri, A., Hodgson, P. D. & Wen, C., 2010. Biomimetic porous titanium scaffolds for orthopaedic and dental applications. *InTech*, pp. 415-50.

Öhman, C., Baleani, M., Pani, C., Taddei, F., Alberghini, M., Viceconti, M. & Manfrini, M., 2011. Compressive behaviour of child and adult cortical bone. *Bone*, 49(4), pp. 769-776.

Parthasarathy, J., Starly, B., Raman, S. & Christensen, A., 2010. Mechanical evaluation of porous titanium (Ti6Al4V) structures with electron beam melting (EBM). *Journal of the Mechanical Behavior of Biomedical Materials*, 3(3), pp. 249-259.

Singh, J. P., Pandey, P. M. & Verma, A. K., 2016. Fabrication of three dimensional open porous regular of PA-2200 for enhanced strength of scaffold using selective laser sintering. *Rapid Prototyping Journal*, 22(4), pp. 752-765.

Thijs, L., Verhaeghe, F., Craeghs, T., Van Humbeeck, J. and Kruth, J.P., 2010. A study of the microstructural evolution during selective laser melting of Ti–6Al–4V. *Acta Materialia*, 58(9), pp. 3303-3312.

Wally, Z. J., van Grunsven, W., Claeyssens, F., Goodall, R. & Reilly, G.C., 2015. Porous titanium for dental implant applications. *Metals*, 5(4), pp. 1902-1920.

Wieding, J., Jonitz, A. & Bader, R., 2012. The effect of structural design on mechanical properties and cellular response of additive manufactured titanium scaffolds. *Materials*, 5(8), pp. 1336-1347.

Yadroitsev, I., Krakhmalev, P. & Yadroitsava, I., 2015. Hierarchical design principles of selective laser melting for high quality metallic objects. *Additive Manufacturing*, 7, pp. 45-56.

CHAPTER 6: *IN-SITU* DMLS ALLOYING OF Ti15Mo

6.1: Introduction

According to the review publication of Spears & Gold (2016), there are about fifty (50) different DMLS processing parameters that determined the mechanical properties of the finished DMLS build parts. The hierarchical design principles of Yadroitsev *et al.* (2015) pointed out that laser power, spot size and scanning speed are the main process parameters that determined the energy input and the interaction time between the laser beam and the powder bed. These principal variables influence the mechanical properties of DMLS manufactured parts. It is also noted that for each type of metallic powder only particular combinations of the main process parameters would produce the optimum result (Rehme *et al.,* 2006; Yadroitsev, 2009; Gusarov & Smurov, 2010). It is therefore obligatory to determine the optimum processing parameters for each type of metallic alloy, which is the focus of the current chapter.

Though DMLS built parts have successfully evolved from the novelty stage (prototype) to the commercial end user production phase there still remain many challenges in tailoring the mechanical properties of each product for a specific application. Understanding the effects of each processing parameter on each specific powder's characteristics would empower the manufacturing engineer to have full control over the mechanical properties of DMLS built parts. To ensure process automation of DMLS technology, a comprehensive understanding of the melt pool dynamics of each individual metallic powder is paramount.

6.2: Experimantal Procedure

A uniform powder layer of 60 µm thickness was deposited on the Cp Ti substrate. Single tracks were sintered at different laser powers and scanning speeds with laser spot of ~80 µm. Figure 6.2.1 indicates laser powers (*P*), scanning speeds (*V*) and the linear energy density as the ratio of laser power and scan speed (*P/V*).

All tracks were of a 20 mm length (Figure 6.2.2). For each scanning speed, three single scan lines were produced. A gap of 1.0 mm was used between adjacent single tracks to avoid any interaction

between neighbouring scan tracks. To easily differentiate each set of scan lines a gap of 2 mm was placed between each set of single tracks produced by a particular scanning speed (Figure 6.2.2).

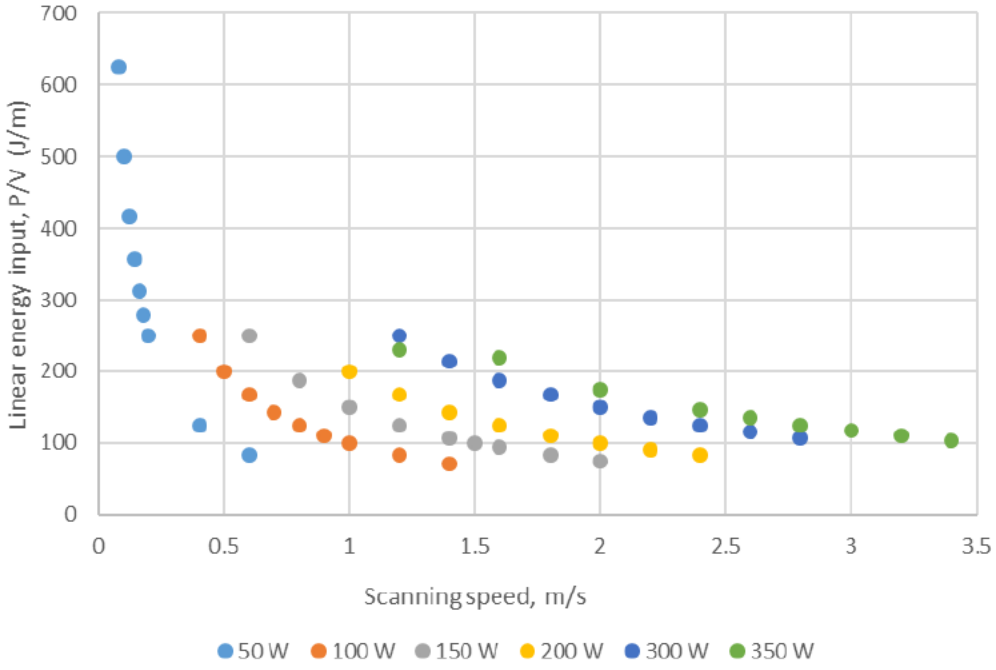

Figure 6.2.1: Scanning speed and the corresponding linear energy density.

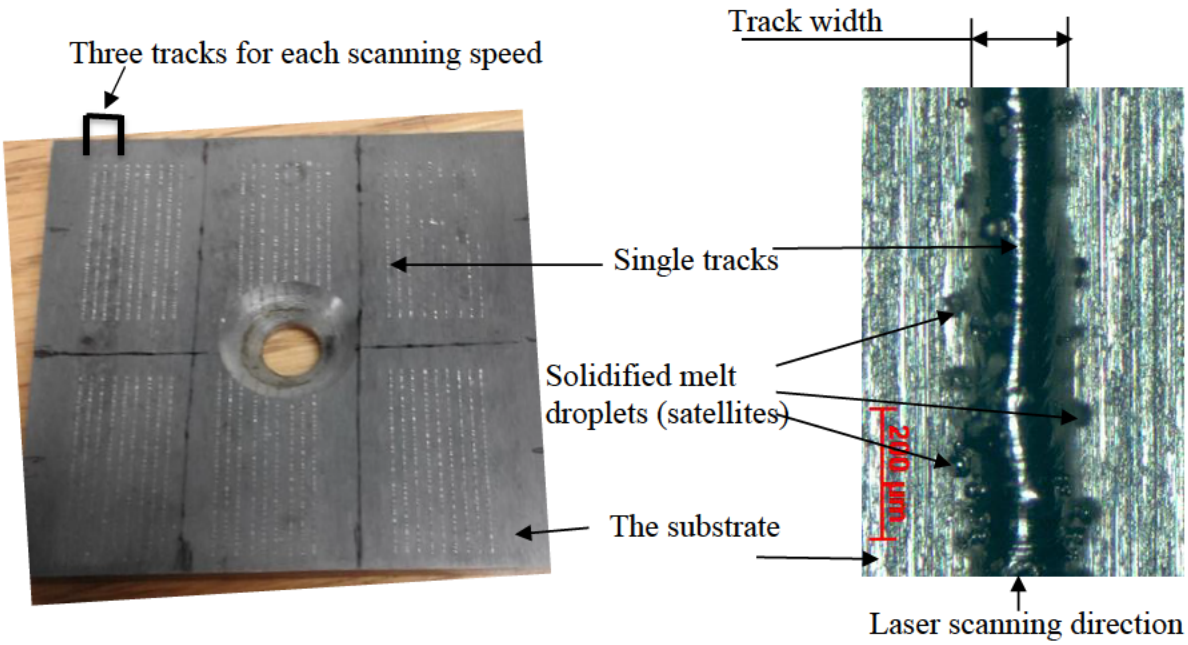

Figure 6.2.2: Top view of the substrate and single tracks.

The samples were prepared for metallographic analyses according to the procedures discussed in Chapter 3. The prepared samples were examined under an optical microscope where measurements were made of the width of the tracks, the height of the tracks above the build plate and the depth of the tracks into the build plate (Figure 6.2.3).

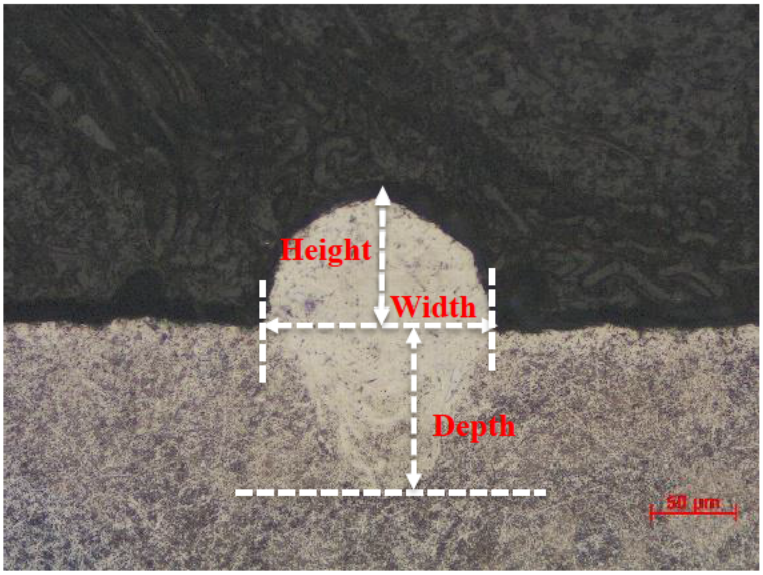

Figure 6.2.3: The cross-section of the DMLS single track.

6.3: Optimization of DMLS Single Tracks

6.3.1: Analysis of the Continuity of Single Tracks

The quality, reproducibility, and reliability of DMLS build parts are dependent on the quality of the various sintered single tracks and layers. A hierarchical approach, including a systematic analysis of SLM parameters is necessary to control the final product quality on every level – tracks and layers (Yadroitsev *et al.,* 2015). As it was indicated, a high-quality stable single track, i.e. continuous tracks with stable geometrical characteristics, without the balling effect and irregularities and adequate penetration depth for providing strong metallurgical bonding between the substrate and track is the first step in the algorithm for finding optimal DMLS process parameters.

Single tracks produced by DMLS could be discontinuous (balling effect) (Yadroitsau, 2009; Yadroitsev *et al.,* 2010). The underlying physics of the balling effects has been discussed

extensively in the available literature (Islam *et al.*, 2012). Chandrasekar (1961) stated that a free liquid cylinder is unstable if the ratio of its length L to diameter *W* exceeds π. Which implies that liquid cylinders with high aspect ratio would break down to lower their surface energy. Lord Rayleigh advanced the theory and postulated an equation to determine the breaking time for cylindrical molten metals above their liquidus temperature (Rayleigh, 1892). This phenomenon is currently known as Plateau-Rayleigh effect.

Khairallah & Anderson (2014) used a 3D mesoscopic model to elucidate the interplay between stainless steel 316 powder bed and the building processing parameters that lead to continuous or discontinuous track formation. It was noted that balling effects is as a result of Plateau-Rayleigh instability. Lee & Zhang (2015) also came to a similar conclusion with their 3D numerical model. The coupled radiation and heat transfer model of Gusarov & Smurov (2010) also agrees with that of the previous authors. Thus, the breaking of the cylindrical melt into droplets can be caused by the Plateau-Rayleigh instability.

Körner *et al.* (2011) noted that instability of molten pool can be caused by local powder arrangnment, wetting, gravity, and capillary forces. They arrive at this conclusion by performing a mesoscopic simulation of selective beam melting processes. The model demonstrates that the packing density of the powder bed has a significant effect on the melt pool characteristics. Das (2003) also indicated that balling effect can depend on the wettability of the powder and the underlying substrate by the molten liquid. Balling becomes very pronounced if the molten liquid fails to wet the powder or the plate.

Marangoni convection of thermocapillary-driven flow (Lu et al., 2004; Tam *et al.*, 2009) influences on the shape of the molten pool. The Marangoni convection in fluids is associated with a gradient in surface tension, where fluids flow from regions of lower surface tension to regions of higher surface tension:

$$M_a = \frac{d\gamma_{LV}}{dT}\frac{dT}{dr}\frac{L}{2\eta\alpha} \qquad \textit{Eq. 6.1.1}$$

Where *Ma* is the Marangoni number, $\left(\frac{d\gamma_{LV}}{dT}\right)$ is the surface tension gradient, $\frac{dT}{dr}$ *is* the temperature gradient, L is the length of the melt pool, η is the viscosity and α is the thermal diffusivity.

The surface tension gradient determined the direction of flow. If the surface tension gradient is negative, thus a shallow and broad melt pool of the laser melt would be formed, but if it is positive, a deep narrow melt pool would be formed. The surface tension gradient for many pure metals and alloys has been reported to be negative, with exception of group VI elements in molten iron (Keene, 1993). Hence it is expected that the Ti-Mo alloy should exhibit shallow and broad molten pool of cylindrical liquids with high surface energy. Fragmentation of the thermocapillary-driven flow cylinder is required to lower the free surface energy of the molten metal.

During DMLS of thick powder layer, the laser beam energy is initially absorbed in a narrow layer of the individual powder particles at the surface which causes high temperature at the surface of the powder particles. The high temperature causes surface melting of the powder particles. After the homogenization of the temperature, the heat flows towards the core of the remaining powder particles until a local steady state of the temperature within the sintering powder particles system is reached. The amount of liquid formation and its characteristics behaviour depends on the temperature which is influenced by the material properties, laser energy input (laser power, spot size and scanning speed) and the thickness of the deposited powder layer. The hydrodynamic movement of the molten liquid and the final geometry of the solidified liquid are determined by the laser energy density (Fischer *et al.*, 2003).

For the present investigations, process map for continuous/discontinuous single tracks was generated on the base of top view analysis (Figure 6.3.1). The continuity of the initial tracks (Figure 6.3.1) is due to the optimal combination of the powder layer thickness, laser powers and scanning speeds. The range of scanning speeds for producing continuous single tracks increased with laser power (Yadroitsau, 2009).

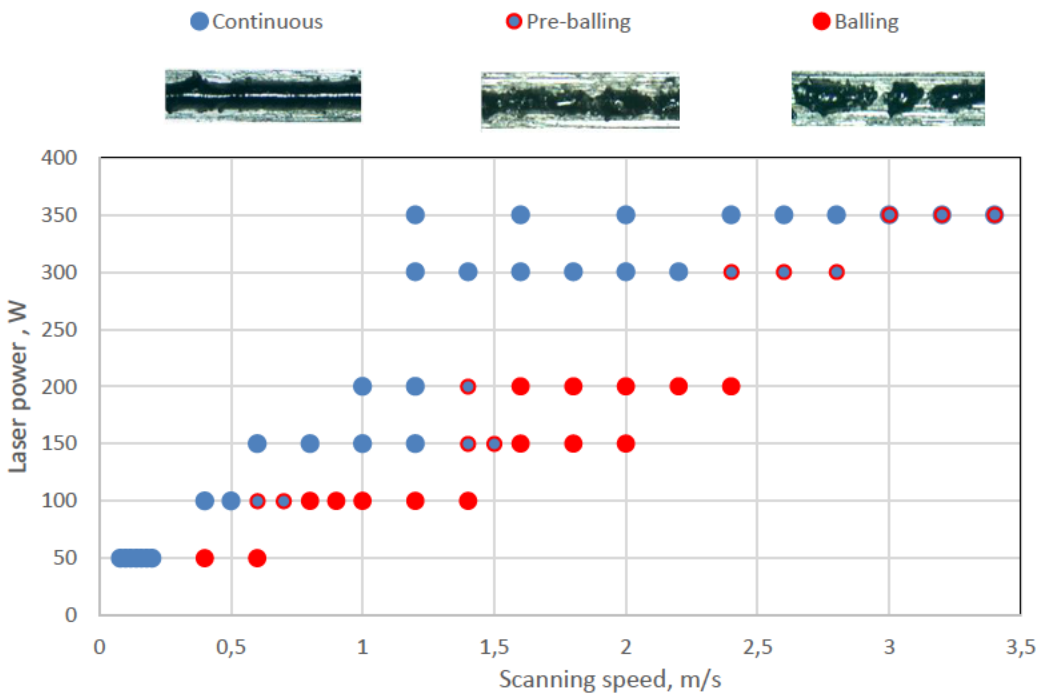

Figure 6.3.1: Process map for Ti15Mo single tracks produced at laser powers from 50 W to 350 W with varied scanning speeds (0.08–3.4 m/s).

Just as in nature as a boat moves through water 'bow wave' develops in front of the motion (Krehl, 2008); during laser melting process, molten liquid builds up ahead of the laser spot. The advancing molten liquid could spill over onto the powder particles ahead of the laser beam and pinched off onto the powder bed as spatter particles (Matilainen *et al.,* 2015). In the current experiment, it was observed that the molten pool dives onto the powder bed and forms droplets at the edge of the tracks (Figure 6.3.1 and Figure 6.3.2).

Yadroitsev *et al.* (2010, 2013) also observed spattering of stainless steel molten pool and termed it satellite. Satellites are surface defects and could be formed due to "melt spattering and partial powder melting in the peripheral zone of laser spot". Sames *et al.* (2016) also came to a similar conclusion that satellites are formed due to sintering of powder at the part edges. Yadroitsev *et al.* (2013) defined the satellites as particles sticking to the surface of the scan tracks and emphasized that increase in energy input would results to increase in satellites formation.

Aboulkhair *et al*. (2016) focused on the distinction between the morphology and microstructure of satellites and other surface defects during DMLS process of AlSi10Mg powder. It was realized that the microstructure of the satellites was similar to the as received AlSi10Mg powder micrograph. Such an observation "*support the suggestion that satellites are formed by the spatter of particles on the single track toward the end of its solidification with less energy transferred to the particle*". Since the energy transferred to the spatter particles is not enough for them to be melted and incorporated into the bulk material they stack to the surface of the DMLS build parts. It was noted that at constant laser powder the number of satellites increases with increasing scanning speed. The experimental work of Mumtaz & Hopkinson (2010) also demonstrated that the smaller the powder particle size the smaller the size of the satellites. Though such a conclusive statement could not be made regarding the number or size of the satellites in relation to the scanning speeds in the current experiment, it was generally observed that the number of satellites is much higher at lower laser power than at similar energy input (Figure 6.3.2).

The disperse melt splashing could form dents/discontinuity or cave-like pores on the track which can significantly affect the mechanical properties of internal structures especially for thin-walled and fine channel structures (Yadroitsev *et al.,* 2013; Qiu *et al.,* 2015).

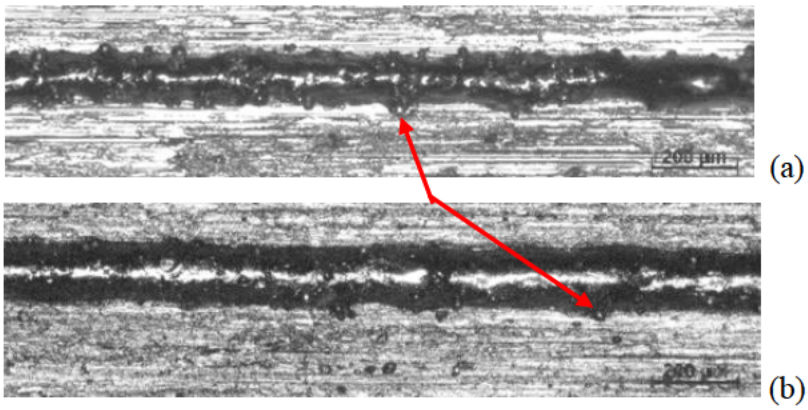

Figure 6.3.2: Top view of the tracks at similar linear energy input (~200 J/m): P=100 W, V=0.5 m/s (a) and P=350 W and V=1.6 m/s (b) (satellites – red arrows)

Observation of the process map (Figure 6.3.1) signifies that the initially selected scanning speeds and the corresponding laser powers radiate adequate energy for continuous track formation. It is already noted that progressive increase in the scanning speed has a significant effect on the

capillarity instability of the molten laser cylindrical liquid tracks (Simchi & Asgharzadeh, 2004; Yadroitsev *et al.*, 2007). As the scanning speed increases, there is general reduction in tracks width at the same laser power (Figure 6.3.3). Yadroitsava *et al.,* (2015) experimented with different powder layers of Ti6Al4V and reported a reduction in tracks width with increasing scanning speed as noted in the current experiment. A similar observation was made by Yang *et al.,* (2016) with Ti6Al4V alloy. This information is very important when producing surfaces. It helps in determining hatch distance in order to ensure accurate overlapping between the tracks.

Increase in the scanning speeds reduces the linear energy density (Figure 6.3.4). The reductions in the energy density lead to reduction of temperature in the molten pool. The low sintering temperature would produce a limited molten fluid of high viscosity which would obstruct the free movement of the powder particles. The high viscous liquid would form semi-discontinuous tracks known as pre-balls and subsequent spherical drops on the substrate known as balling effect.

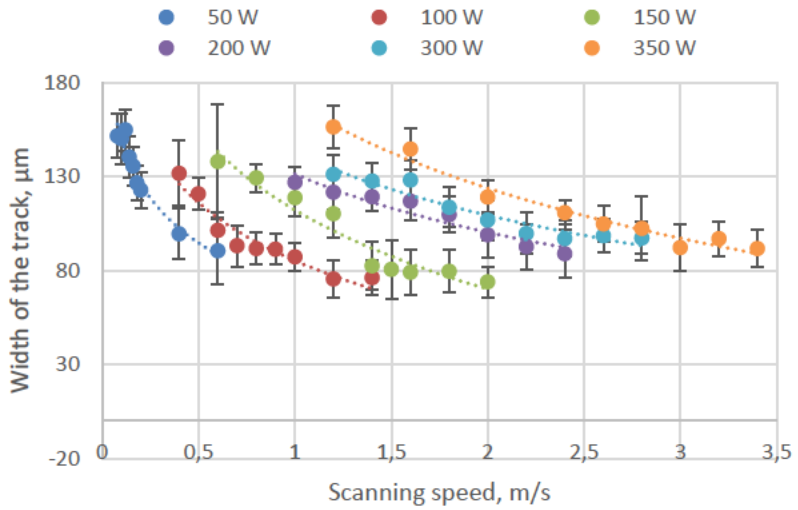

Figure 6.3.3: The width of the single tracks at different scanning speeds and laser power.

The higher energy input increases the temperature of the molten pool and subsequent production of large amount of liquid phase with low viscosity which enhances easy flowing of the molten pool. Additionally, at low scanning speeds the conduction phenomena promote heating of the substrate and powder material thus creating conditions for involvement new material into the

fusion process. Complex mechanisms of interaction of laser radiation with a system of powder - substrate, the flows in the molten pool, the possible variable thickness of powder layer and non-homogeneous distribution particles in the layer – all these factors further complicate the continuity of the tracks.

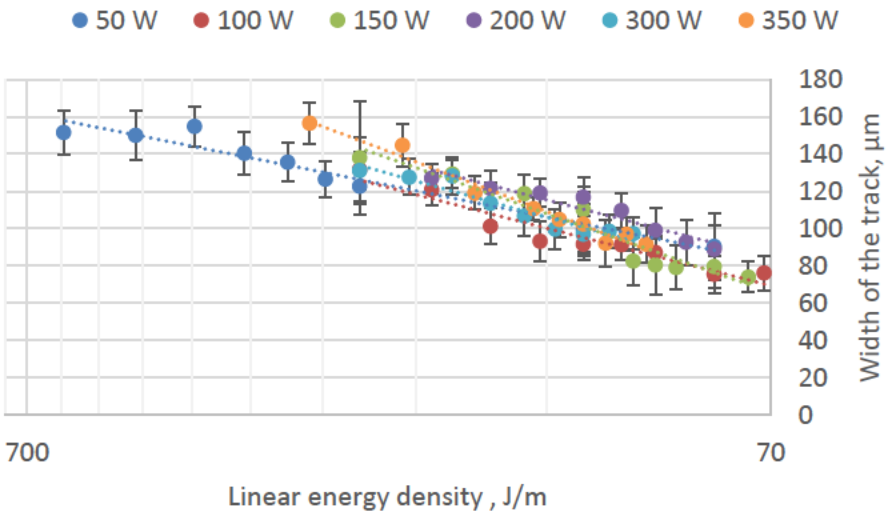

Figure 6.3.4: Width of the single tracks *versus* linear energy density.

6.3.2: Cross-Sections of Single Tracks

After the initial micrograph observation of the top view and measurements of the tracks widths, the plates were sectioned for further analysis to determine the extent of the re-melted depth and height of the tracks. For the layer by layer DMLS processes, if the selected process parameters lead to sufficient laser energy density to melt the powder and penetrate into the pre-existing layer; metallurgical bonding between the substrate (previous layers) would take place. Remelting of the subtract is always required to 'weld' the current layer to the previous layer. The re-melting of the previous layer also would enhance the stability of the molten cylindrical liquid (Yadroitsev *et al.,* 2010). Cross-section of the single tracks can be contingently divided into 3 cases as presented in Figure 6.3.5: a) lack/small penetration, b) with penetration and c) deep (like keyhole) penetration into the substrate.

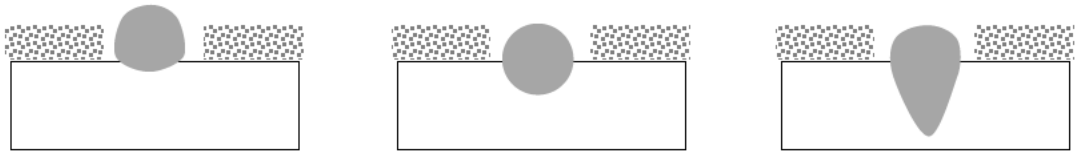

(a) (b) (c)

Figure 6.3.5: Schematic representation of the laser sintered single layer tracks at the substrate.

According to Eagar & Tsai (1983), the cross-section of solidified molten pool formed in conduction mode is about semi-circular. Yang *et al*. (2016) also describe the morphology of conduction mode tracks as (U-shape) and keyhole mode as (V-shape).

In DMLS, similar to laser welding, if the combination of the processing parameters exceeds a certain threshold the mode of thermal conduction in the molten pool could change to the so-called keyhole mode. In the keyhole mode, the laser energy density is sufficient enough to cause evaporation of the metal leading to plasma (vapour) formation. The vapor formation enhances laser energy absorption into the substrate and subsequent 'drilling' of the substrate. The collapse of the vapour cavity could leave a void (pore) in the wake of the laser beam which would contribute to pore defect of the final product (Rai *et al.,* 2007; Verhaeghe *et al.,* 2009; King *et al.,* 2014).

Laser ray-tracing energy deposition in the powder-scale model was used by Khairallah *et al*. (2016) to study the recoil pressure for laser powder bed fusion process. The recoil pressure which creates depression of the molten pool is closely related to the keyhole mode. The depression region of a track is the area directly under the laser beam which registers the highest temperature. Due to the exponential dependence of the recoil temperature the ensuing liquid has a high speed lateral flow component and accelerates the liquid away from the center of the track. The process leads to a vertical negative velocity component which creates a noticeable topological depression. The recoil force 'drill' into the substrate and it is noted to be responsible for the keyhole mode in laser melting phenomenon. King *et al*. (2014) experimentally estimate the recoil temperature close to the boiling temperature of a material. Klassen & Carolin (2014) also focused on increasing the accuracy of predicting the penetration depth during laser melting process. They proposed a model based on a set of semi-empirical equations and proved that depth of penetration had a strong influence on the quality of the fabricated parts.

Hann *et al*. (2011) investigated laser interaction and the effect of processing parameters on different materials in order to optimize the processing system. Based on the assumption that the ratio of the deposited energy density is equal to the normalized enthalpy ($\Delta H/h_s$), the transition from conduction to keyhole mode can be predicted. Deposited laser energy density was written as

$$\Delta H = \frac{A \cdot C \cdot P}{\rho \cdot \sqrt{r_0^3 \cdot \propto \cdot V}} \qquad \textit{Eq. 6.3.1}$$

where V is scanning speed, r_0 is half-width of Gaussian beam at the surface, α is the thermal diffusivity, C is a constant with no dimensions, ρ is the density of the material at melting, A is the absorptivity of the surface and P is laser power. The theoretical threshold enthalpy was estimated as 6 (Eq. 5.3):

$$\frac{\Delta H}{h_s} > \frac{\pi T_b}{T_m} \approx 6 \qquad \textit{Eq. 6.3.2}$$

where ΔH is the specific enthalpy, h_s is enthalpy at melting, T_b and T_m respectively are the boiling and melting temperate of the material. By substituting the thermophysical parameters of stainless steel grade 316L into the threshold equation, King *et al*. proposed that the threshold for laser bed fusion of steel to change from the conduction mode to keyhole mode is $\Delta H/h_s > (30 \pm 4)$. It was shown that a threshold for transition from conduction to keyhole mode depends on power, speed, and beam size for a certain powder layer thickness (50 μm layer thickness was used). It was also indicated that the threshold is expected to depend on layer thickness and possibly powder size distribution. Khairallah *et al*. (2016), also used the enthalpy equation of King *et al.*, and arrived at a threshold value of $\Delta H/h_s > 33$ for stainless steel grade 316L.

Yang *et al.* (2016) indicated that powder layer thickness might be the reason for the vast deviation of the theoretical value from the experimental value. The powder layer thickness was incorporated into the derivation of the threshold equation and rephrased the equation as:

$$\frac{P}{dhV} \geq \frac{kT_b\sqrt{\pi^3}}{0.865A\alpha} \qquad \textit{Eq. 6.3.3}$$

where Gaussian beam with spot size is d, P is laser power, h is layer thickness, α is thermal diffusivity of molten material, A is absorption coefficient. Yang *et al.* substitute thermophysical properties of Ti6Al4V alloy into the equation and obtained a threshold value of $\Delta H/h_s \geq 5.4$.

King *et al.* (2014) caution that "*going far below the threshold results in insufficient melting and going too far above results in an increase in voids due to keyhole mode melting*". It was concluded that keyhole mode could be realized when penetration depth is greater than half the width of the tracks.

6.3.3: Analysis of the Cross-sections of Ti15Mo Single Tracks

Analysis of the cross-sections shows that for chosen layer thickness laser power of 50 W could not produce sufficient energy to penetrate the substrate, though just enough to melt the metal powder (Figure 6.3.6). Maximum remelted depth was about 10 µm, single tracks had only small metallurgical bonding to the substrate. It is worth pointing out that it is not necessarily a high magnitude of the laser energy density that is needed to melt the powder and penetrate the substrate.

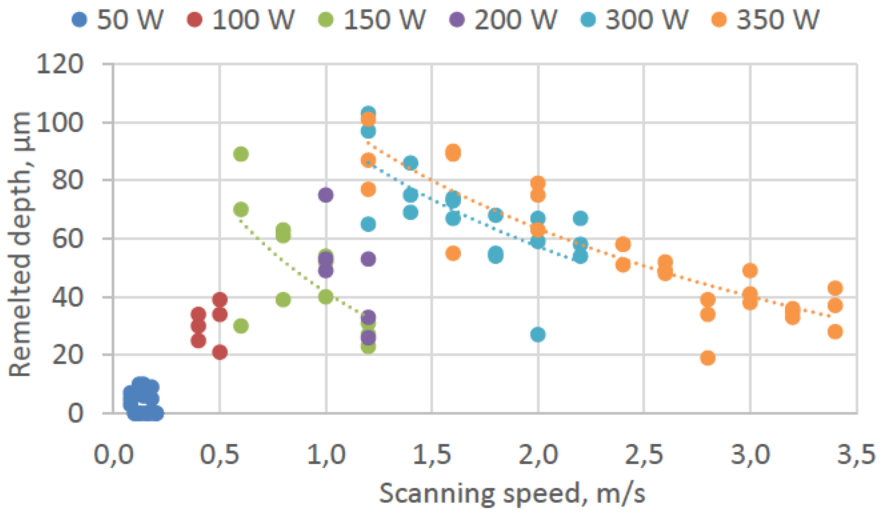

Figure 6.3.6: Remelted depth for continuous tracks for different scanning speed and laser power.

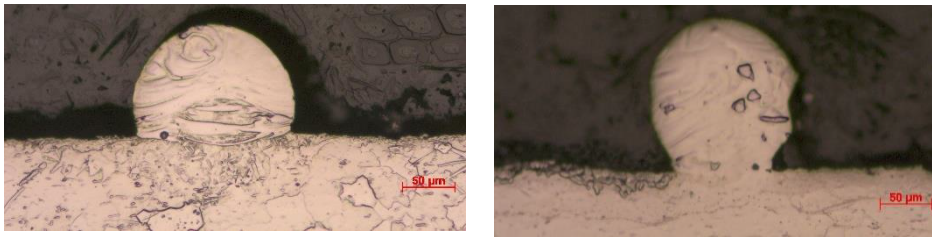

V=0.08 m/s *P/V*=625 J/m *V*=0.2 m/s *P/V*=250 J/m

(a)

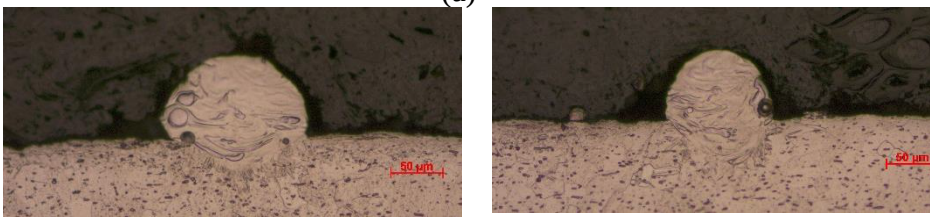

V=0.4 m/s *P/V*=250 J/m V=0.5 m/s *P/V*=200 J/m

(b)

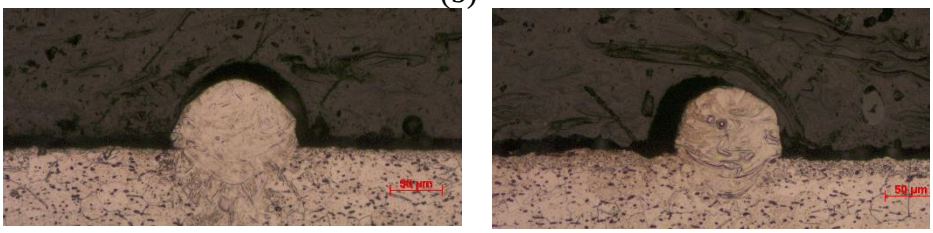

V=0.6 m/s *P/V*= 250 J/m *V*=1.2 *P/V*=125 J/m

(c)

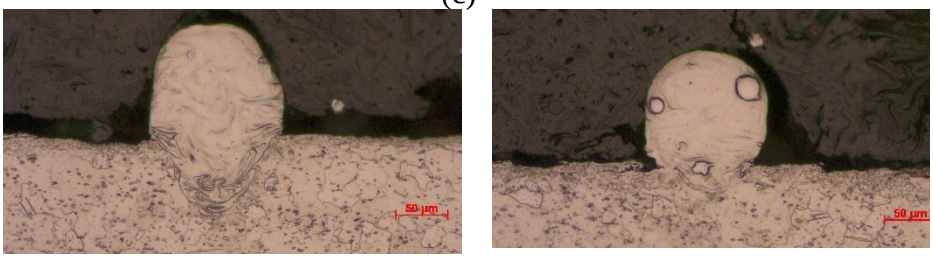

V=1.0 m/s *P/V*= 200 J/m *V*=1.2 *P/V*=167 J/m

(d)

Figure 6.3.7: Cross-sectional view of single laser tracks at a laser power of 50 W (a), 100 W (b), 150 W (c) and 200 W (d) at different scanning speeds.

As depicted in Figure 6.3.7 (a) for the 50 W laser power, the linear energy density at 0.08-0.2 m/s produce the same result of not making a metallurgical bond to the substrate despite the difference in their *P/V* values. The 50 W laser power and the corresponding scanning speeds were of the highest *P/V* values (Table 6.2.1) but the least to make perfect metallurgical contact with the substrate. This emphasized the importance of experimental investigation of determining optimum process parameters for each type of powder for DMLS process.

For laser power of 100, 150 and 200 W with scanning speeds ranging from 0.4-0.5, 0.6-1.2 and 1.0-1.2 m/s respectively (Figure 6.3.7b-d) the laser energy was enough to melt the powder completely and have sufficient enthalpy to melt the underlying material (substrate) to form a metallurgical bonding.

The shape of the single tracks formed at laser powers of 100 and 150 W and their corresponding scanning speeds of 0.4-0.5, and 1.0-1.2 m/s respectively nearly resemble a semi-circular or *U*-shape. Such conductive mode would lead to good bonding between the tracks and the substrate, hence could be referred to as optimum processing parameters. At 200 W, remelted depth was unstable and varied greatly (Figure 6.3.7d) that can be linked with non-homogeneous powder layer.

More stable results were received for tracks produced at laser powers of 300 W and 350 W (Figure 6.3.8). It could be observed that for scanning speeds in the range of 1.2-1.6 m/s and 1.2-2.0 m/s for corresponding laser powers of 300 W and 350 W respectively laser beam melts the powder and drill very deep into the substrate. This is as the result of the excessive laser energy which causes the laser beam to create a topological depression in the substrate (keyhole) (Khairallah *et al.,* 2016). As it was indicated above, the keyhole mode phenomenon would lead to a situation whereby the laser beam would penetrate too deep into the previous melted-solidified layers, resulting in pore formation and other metallurgical defect. With increasing scanning speed at a constant laser power of 300 W, the linear energy density decreases, leading to a reduction in penetration depth at scanning speeds of 1.8-2.2 m/s for the 300 W (Figure 6.3.8a).

For the current experiment a uniform layer of 60 µm powder deposition was used for single tracks and single layer experiments. It is expected that powder layer has 50% apperent density (Yadroitsev, 2009). The final layer ideally would be expected to be about 30 µm. Thus, next laser scanning at 150 W and 0.6 m/s; 300 W and scanning speed less than 1.8 m/s and 250 W and scanning speed lower 2.0 m/s will remelt 2 previously solidified layers. In terms of keyhole mode, *i.e.* taking into account ratio of remelted depth to half width of the single track, keyhole mode happened minimum in 2 cases at P=150 W at V≤0.6 m/s *P*=300 W and *P*=350 W at scanning speed lower than 2 and 2.2 m/s correspondingly (Figure 6.3.9).

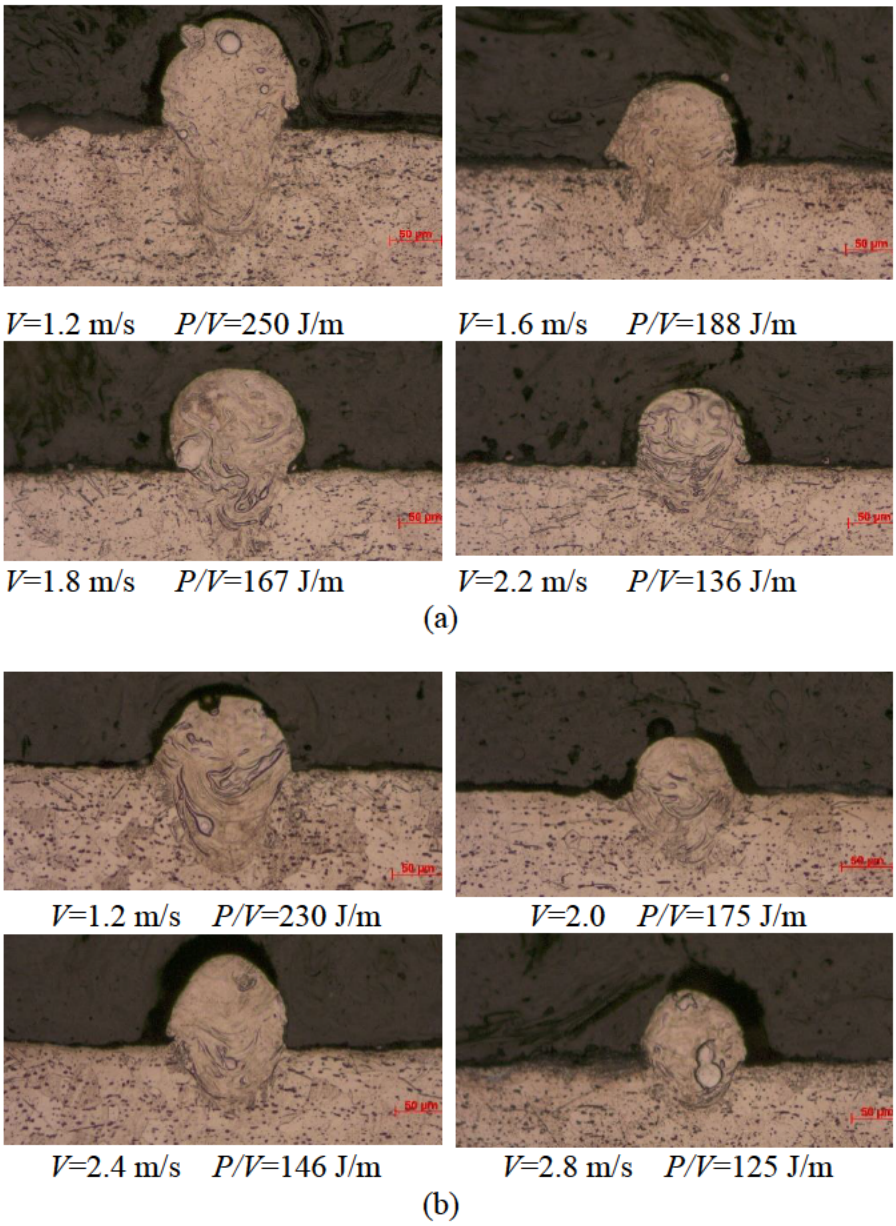

Figure 6.3.8: Cross-sectional view of single laser tracks at a laser power of 300 W (a), 350 W (b) different scanning speeds.

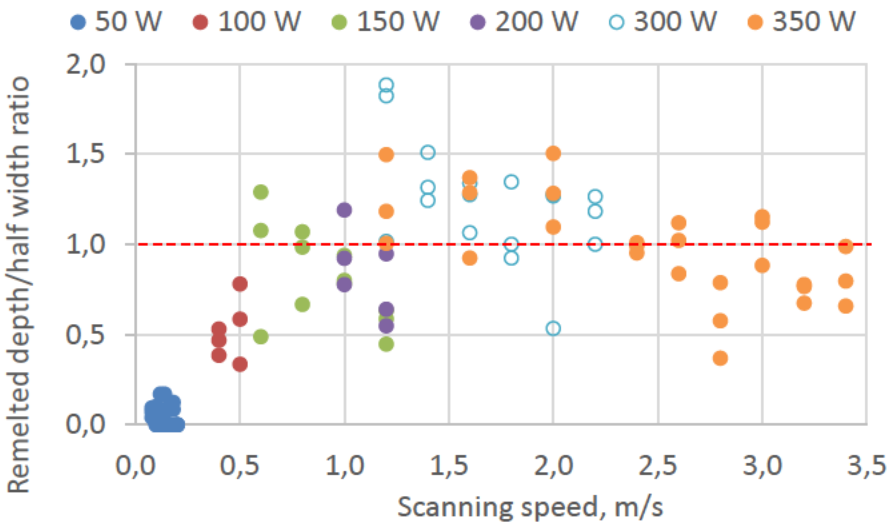

Figure 6.3.9: Ratio of remelted depth to half width of the single tracks.

Laser power of 350 W with scanning speeds ranging from 2.4-2.8 m/s perfectly demonstrate conduction mode laser process. The penetration depth values (Figure 6.3.9), and the shape of the molten pool correspond to the conduction mode. Since the experimental powders consists of 85% of pure Ti, its properties were used to calculate the threshold enthalpy ratio. Laser spot size of 80 μm, 50–350 W laser power, scanning speeds for continuous tracks, enthalpy of melting (Table 3.2.4), C=1 and Eq. 6.3.2, were used for calculations (Figure 6.3.10).

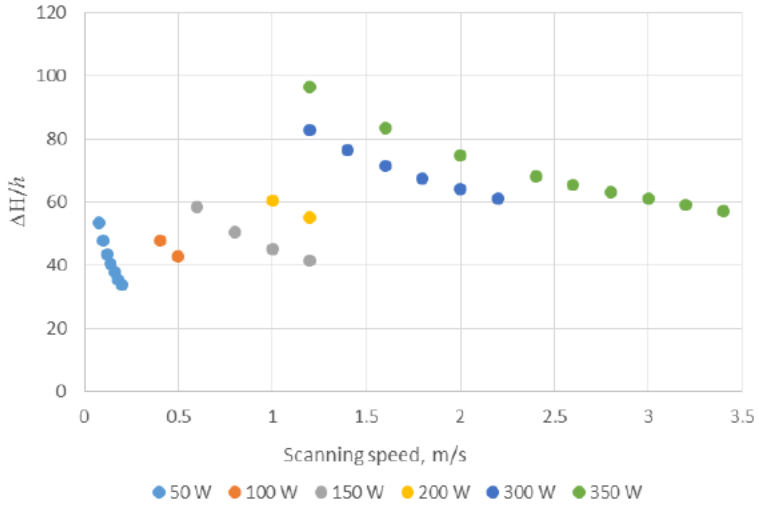

Figure 6.3.10: Ratio of the deposited energy density to the enthalpy at melting for continuous tracks for Ti-15Mo alloy.

From the cross-sectional analysis, it was observed that penetration depth increases with increasing laser power and decrease with increasing scanning speed (Figure 6.3.6). Yang *et al.,* (2016) keep scanning speed and powder layer thickness constant while varying laser power from 100 to 500 W. They noted that the critical laser power for transition from conduction mode to keyhole mode start from 300 W for Ti6Al4V alloy. Yadroitsava *et al.* (2015) found that at 30-45 µm Ti6Al4V powder layer thickness a keyhole mode started at P=150 W and scanning speed V=0.6 m/s just as observed for the Ti15Mo alloy in the current experiment.

Figure 6.3.11 shows that the aspect ratio of remelted depth/half width is plotted against the enthalpy ratio of the DMLS Ti-15% Mo mixture. At high laser power (more than 150 W), high laser energy input ($\Delta H/h_s$ ~58-70) will lead to V-shape molten pool, if this ratio exceeds 70, deep penetration and the probability of the keyhole mode is very high.

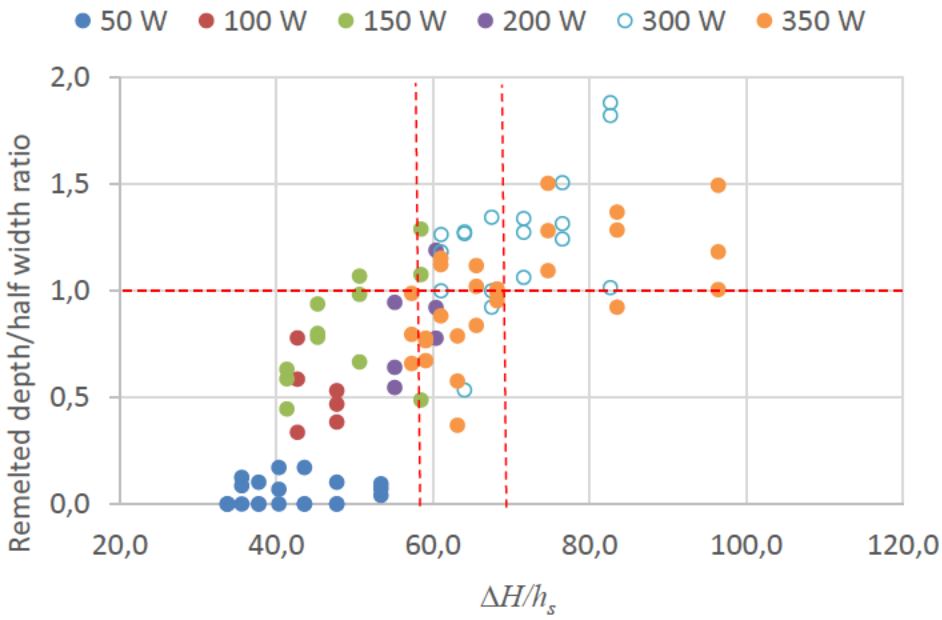

Figure 6.3.11: Ratio of remelted depth to half width of the single tracks *versus* enthalpy ratio.

A keyhole mode provokes pore formation: as the laser beam passes the hottest spot (depression region), a decrease in temperature is accompanied by an exponential decrease in the recoil force. However, as the temperature decrease, surface tension increases and overcome the effect of the recoil force which was keeping the depression open (keyhole). The high surface tension reverses

the direction of the melt flow velocity vector field towards the center of the molten pool. The reverse is very rapid (about 5 μs) and traps gas bubbles within the melt resulting into pores formation at the rear of the track (Khairallah *et al.*, 2016). Under chosen process-perameters, there were no pores in the keyhole mode DMLS in the current experiment.

Since the distribution of the Gaussian laser beam is not uniform, it leads to non-uniform temperature gradient of the molten pool. The center of the molten pool is normally of higher temperature than the edge of the molten liquid. The temperature difference triggers surface tension gradient between the center and the edges of the molten metal (Chan *et al.*, 1987). The difference in the surface tension would lead to recirculating flow within the molten pool, which would change the shape of the molten pool. Kou *et al.*, (2011) has shown that Marangoni flow which is also a function of temperature gradient would induce waves in the liquid. The waves within the molten pool would amplify deformation and oscillation of the pool surface, and ripple formation as the molten metal solidifies (corrugated surfaces). The modeling results of Qiu *et al.*, (2015) predicted that the complex melt flow behaviour within the melt pool could move in a dispersed and random way which could lead to different track head geometry. The complex melting process which is governed by laser beam absorption, viscosity, surface tension, capillary effects, gravity, *etc.*, would lead to stochastic melt tracks with irregular, corrugated track head appearance (Körner *et al.*, 2011; Körner *et al.*, 2013). Due to the hydrodynamics movement, the geometry of the molten pool could deviate significantly resulting in different track head (height) shape.

The measured heights of the tracks presented in Figure 6.3.12 and Figure 6.3.13 clearly demonstrated a corrugated (uneven) nature of the tracks height. A similar result was obtained by Yadroitsava *et al.* (2015) at single tracks of Ti6Al4V that was attributed to inhomogeneous deposition of powder layer and melt hydrodynamics. At low layer thickness (20-40 μm) Yang *et al.* (2016) demonstrated nearly a uniform track height for Ti6Al4V alloy single tracks at 100–400 W. It was indicated that the heights of molten pools under various scanning speeds remain nearly constant – about 30 μm.

The side-by-side and subsequent layer-by-layer melting of the irregular, corrugated track head would produce a rough surface. The rough surface would cause inhomogeneous powder deposition

which would trigger inconsistency in melt flow in the subsequent layers. Optimization of the melt flow to enhance homogenous single tracks formation is one of the main step to produce non-porous dense DMLS object.

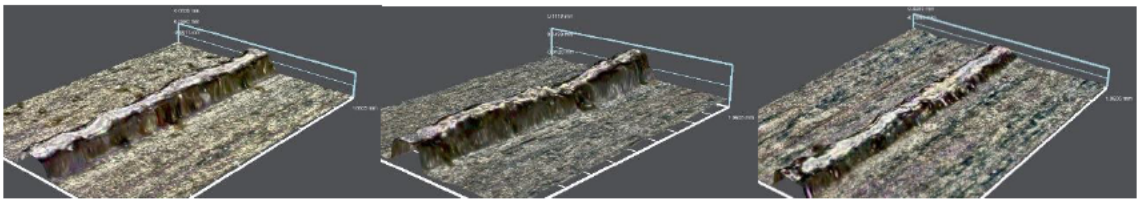

0.6 m/s 0.8 m/s 1.0 m/s

(a)

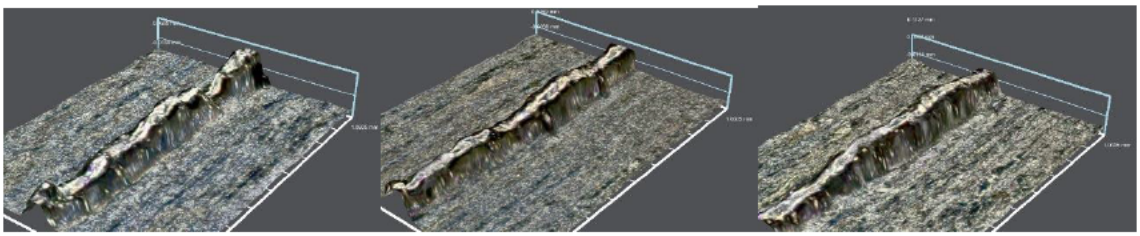

2.4 m/s 2.6 m/s 2.8 m/s

(b)

Figure 6.3.12: Single tracks on the substrate at 150 W (a) and 350 W laser power and different scanning speeds.

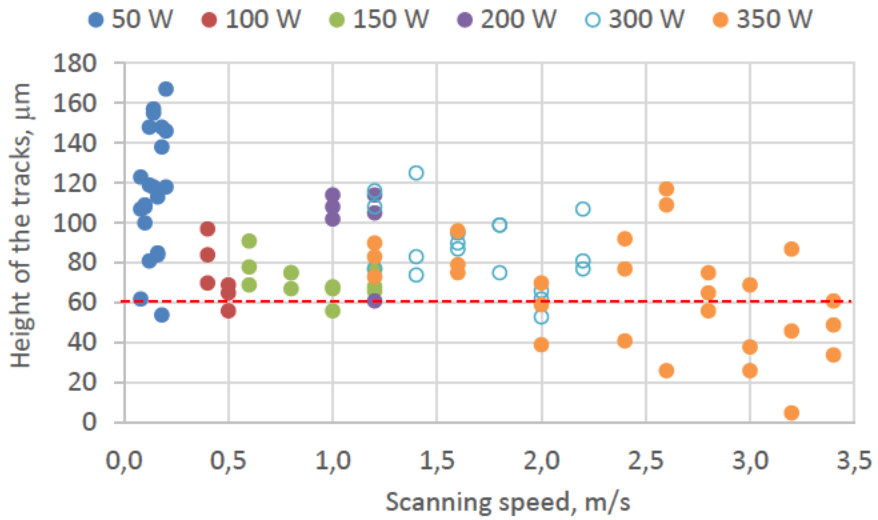

Figure 6.3.13: Height of the Ti15Mo tracks at varied laser power and scanning speed.

Selected process parameters under investigation start from keyhole mode, followed by optimum conduction mode, then proceed to pre-balling and the subsequent balling effect. It could be concluded that for the current experiment there always exists a particular range of scanning speed that would produce optimum results, except for 50 W laser power (Figure 6.3.14). Therefore, by selecting a 'reasonable' laser power there would be a range of scanning speeds that would produce the desired mechanical properties.

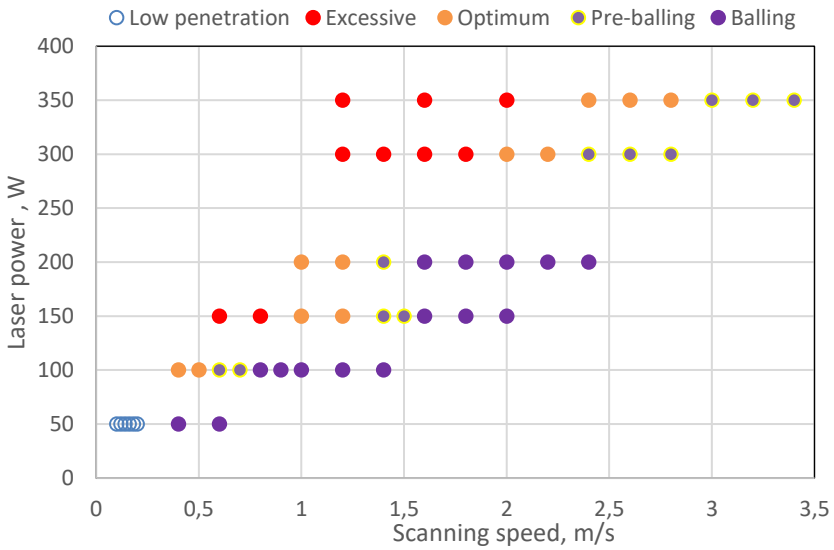

Figure 6.3.14: Process map for DMLS Ti15Mo single tracks.

6.4: Optimization of DMLS Single Layer

6.4.1: Top Surface Analysis

Hierarchical design algorithm stated that the basic building blocks of DMLS objects are set of single tracks which are placed side by side (Yadroitsev *et al.*, 2015). The previously solidified layer served as the substrate for the subsequent layer-by-layer formation. The layer wise process continues until the object is manufactured. The superposition of the various tracks and layers lead to the manufacturing of 3D objects. The quality of the individual set of single tracks determined the morphology and mechanical properties of the final object. Key parameters such as laser power, spot diameter, scanning speed, hatch distance, powder layer thickness and powder characteristics have a decisive effect on the surface morphology of DMLS parts. The interaction between radiation and properties of the powder and the substrate also has a significant effect on the molten pool dynamics hence the solidified layers (Childs *et al.*, 2004; Kruth *et al.*, 2005). The relationship

between the various parameters has proven to be non-linear (Yadroitsev *et al.,* 2010). It is therefore important to perform an experimental investigation to identify which combination of the various parameters could produce the desired surface quality.

From the abovementioned analysis of the single tracks, optimum process parameters of 150 W and 350 W with corresponding scanning speeds of 1.0 m/s and 2.4 m/s respectively were selected to produce single layers from the same powder (Ti15Mo). Different hatch distances of 80 µm,90 µm and 100 µm were produced under single scan and rescanning.

The width of single tracks that form the scan and rescan samples ranges from 80-160 µm (Figure 6.3.3 and Figure 6.3.4). Therefore, the selected hatch distance permits perfect overlapping of the various single tracks that form the layers. It could be observed that (Figure 6.4.1) for both samples the layers overlap completely at the various process parameters forming metallurgical bonding with fully dense sintered surfaces.

It is also observed that surface roughness of the samples increases with an increasing in hatch distance. At a lower hatch distance, a larger surface area of the previously solidified layer is remelted which could melt any unmelted powder particles. Since size of molten surface area increases in order 80>90>100µm hatch distances, it is expected that surface roughness would increase with increasing hatch distance (Figure 6.4.2 and Figure 6.4.3).

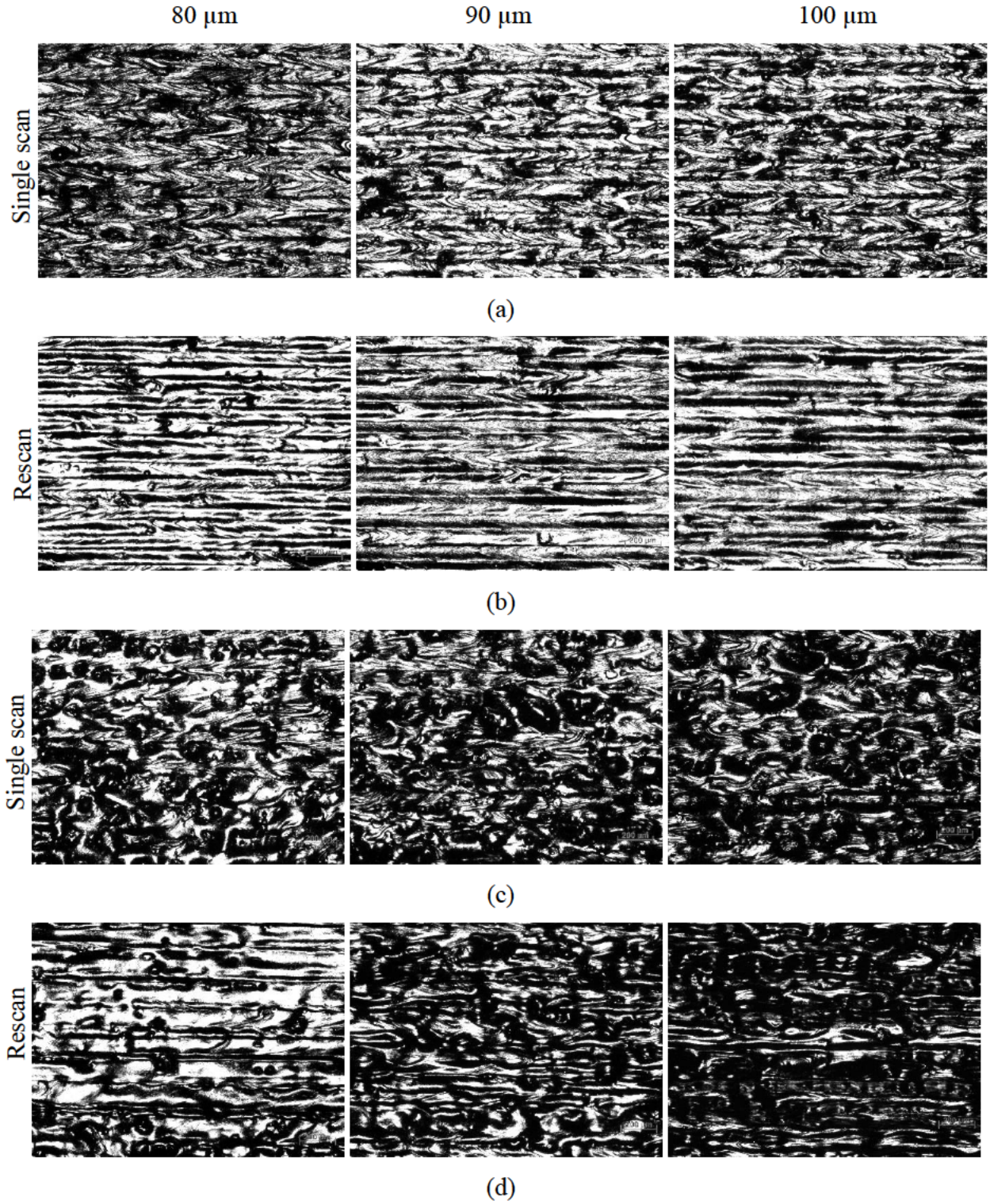

Figure 6.4.1: Top view of DMLS surfaces from Ti15Mo *in-situ* alloy (a) single scan, (b) rescan at laser power 150 W, scanning speed 1.0 m/s and 80-100 µm hatch distances. (c) single scan, (d) rescan at laser power 350 W, scanning speed 2.4 m/s and 80-100 µm hatch distances.

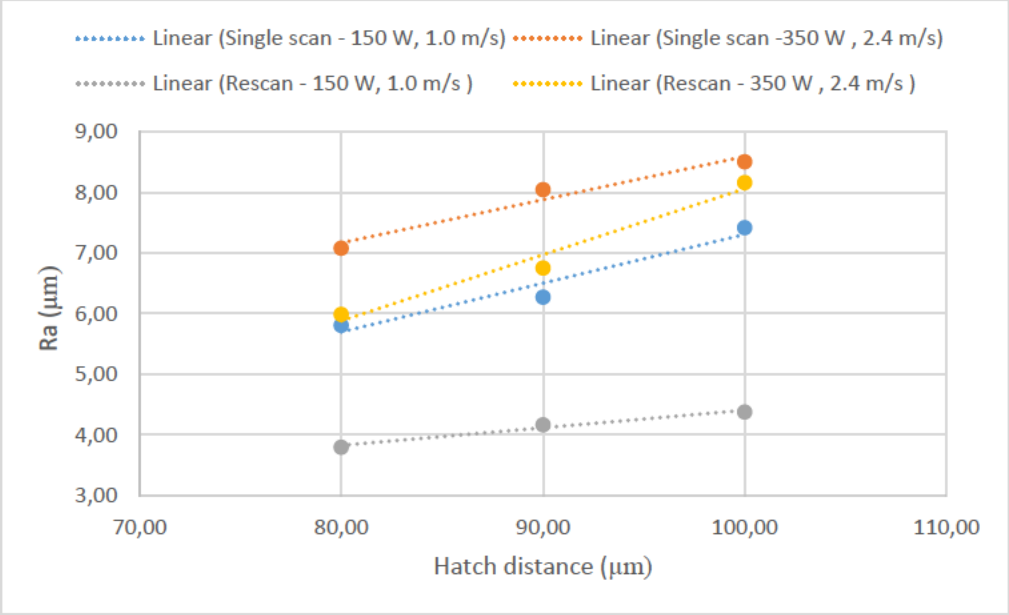

Figure 6.4.2: Surface roughness *Ra* of *in-situ* alloyed Ti15Mo at varied hatch distance, laser power and scanning speeds.

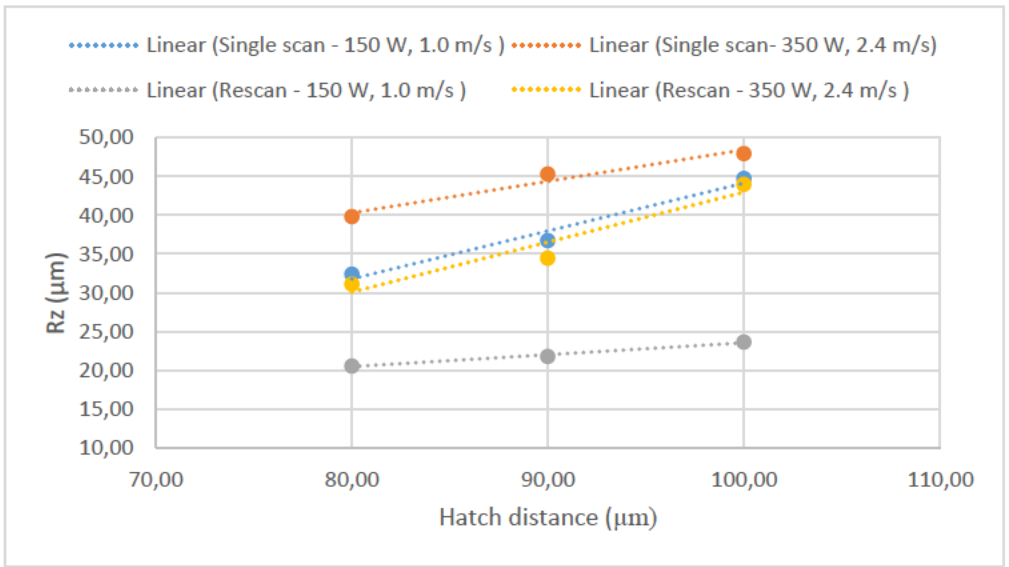

Figure 6.4.3: Surface roughness *Rz* of *in-situ* alloyed Ti15Mo at varied hatch distances, laser powers and scanning speeds for

There were a lot of satellites particles sticking to the solidified surfaces after the single scanned process (Figure 6.4.4a and c). Rescanning of the surfaces at the various hatch distances considerably reduces surface roughness by eliminating the satellites. It was shown earlier that rescanning of DMLS layers increases the surface quality (Yasa & Kruth, 2008; Kruth et al., 2009; Kruth et al., 2010; Król *et al.*, 2014; Kinnear *et al.*, 2016). It is widely reported that for DMLS parts top surface roughness is between 6-10 µm for *Ra* and >30µm for *Rz* value (Maisonneuve et al., 2007; Duleba et al., 2011; EOS, 2014; Longhitano *et al.*, 2015). The *Ra* is the arithmetic mean of all deviations of the sampling path length whereas *Rz* is the average distance between the highest peaks and the deepest valleys within the sampling length. The experimental results perfectly fall within the expected values for both *Ra* and *Rz* (Figure 6.4.2 and Figure 6.4.3, single scan surfaces). Rescanning considerably lowers, the *Ra* and *Rz* values more than 30% (Figure 6.4.2 and Figure 6.4.3, rescan surfaces) for laser power of 150 W and 350 W. However, the 150W samples showed the lowest surface roughness value. Though the laser input energy *(P/V)* is almost the same for the scan and rescan strategy, it could be stated that surface roughness increase with increasing laser power.

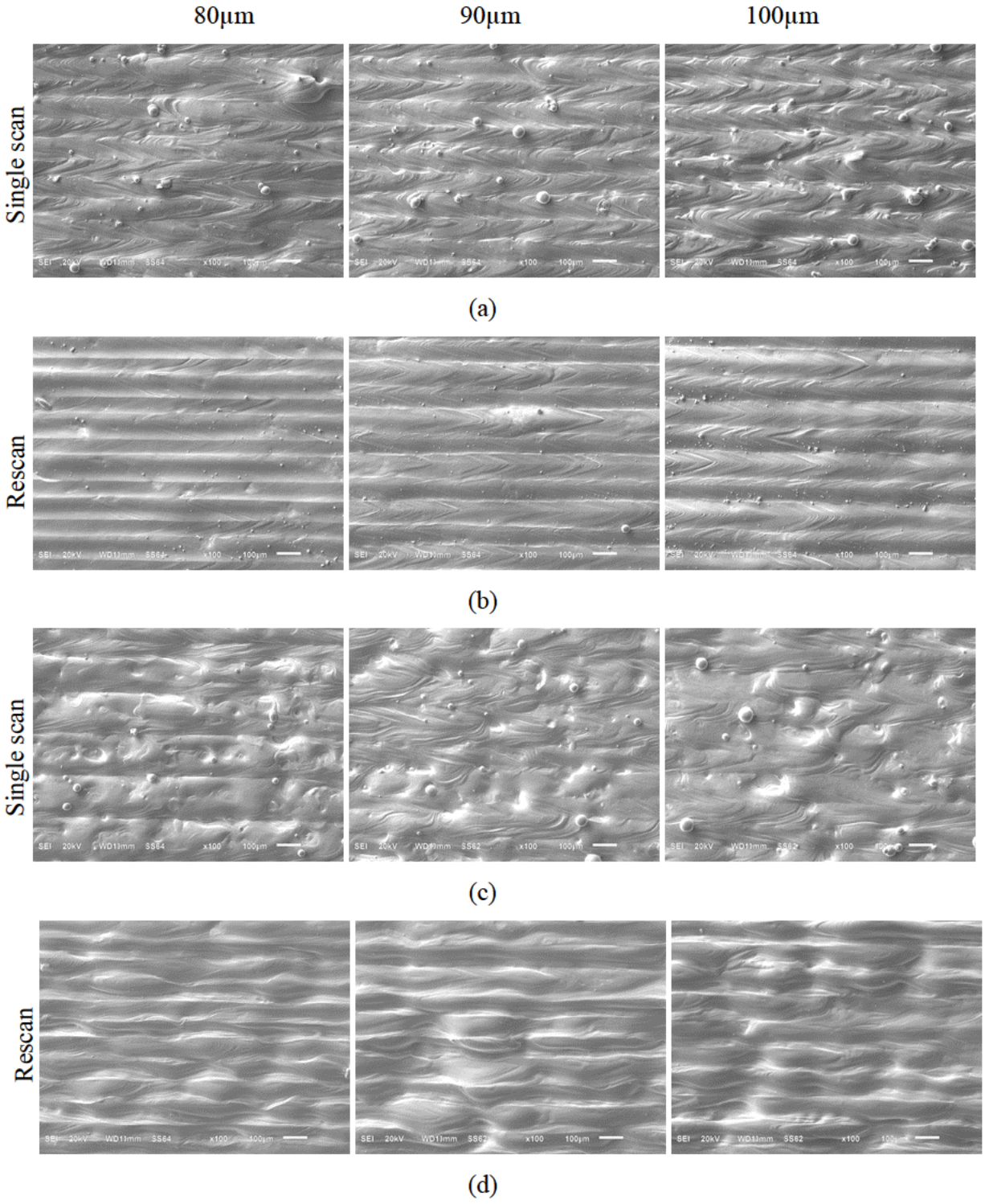

Figure 6.4.4: SEM photos of DMLS surfaces from Ti15Mo *in-situ* alloy (a) single scan, (b) rescan at laser power 150 W, scanning speed 1.0 m/s and 80-100 µm hatch distances. (c) single scan, (d) rescan at laser power 350 W, scanning speed 2.4 m/s and 80-100 µm hatch distances.

6.4.2: Cross-sectional Analysis of Single Layers

The cross-sectional examination reveals that the Mo powder particles were not completely melted especially for the single scan samples (Figure 6.4.5) The input energy was sufficient enough to melt CpTi completely but not Mo due to the thermophysical properties differences between the two materials (Table 3.2.4). The melting point of CpTi is about 1650°C and that of Mo is about 2617°C. Also, the laser radiation reflectance of Mo is higher than that of CpTi (Palik, 1985), hence CpTi would absorb more of the laser radiation. The fore mentioned factors lead to the complete melting of CpTi and partial melting of the Mo.

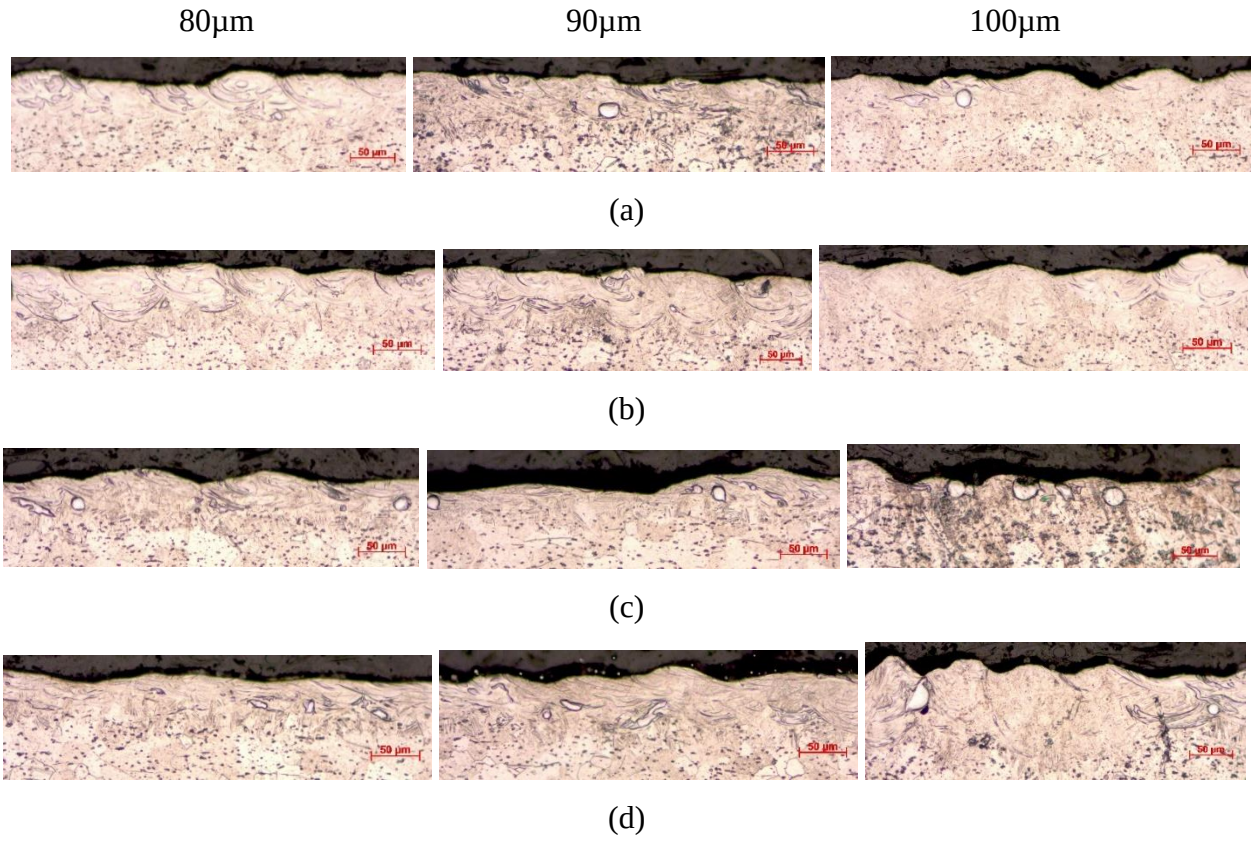

Figure 6.4.5: Cross-sectional view of DMLS from Ti15Mo *in-situ* alloy (a) single scan, (b) rescan at laser power 150 W, scanning speed 1.0 m/s and 80-100 µm hatch distances. (c) single scan, (d) rescan at laser power 350 W, scanning speed 2.4 m/s and 80-100 µm hatch distances.

The rescanning process had positive effect on the Mo particles, more Mo unmelted particles appear to melt (Figure 6.4.5a). During the rescanning process, the previously rough surface would

enhance laser radiation absorbance of the samples (Bergström *et al.,* 2007). The increase in laser absorptivity due to the rougher surface trigger both increase in temperature and more prominent flow of the molten pool. The higher temperature and the more prominent flow liquid would cause the Mo particles to melt completely. As a result of this phenomenon, the unmelted Mo particles appear to reduce in size after the rescanning process.

However, Mo has a higher atomic mass than Ti, hence it is heavier than Ti. The heavier Mo particles are more susceptible of sinking to the bottom of the molten pool during the process and been shielded from the laser radiation. As a result, some of the Mo particles could still be observed even after the rescanning process though they reduce in size especially samples manufactured at 350 W (Figure 6.4.5d).

Although not very conclusive it could be observed that the number of unmelted particles increases with increasing hatch distance (Figure. 6.4.5c-d). Vrancken *et al.* (2014) also observed unmelted Mo particles after *in-situ* alloying Ti6Al4V+10wt.%Mo.

An EDS elemental map analysis was performed to verify the distribution of the Mo in the CpTi near the surface of the alloy. It came to light that the Mo was inhomogeneously distributed in the CpTi during the single scan (Figure 5.4.6). Rescanning has improved the distribution of the Mo in the CpTi at the surface.

The effect of the varied hatch distance seems not to have any significant effect on the Mo distribution in the CpTi. All the samples demonstrate an equal level of Mo distribution at each hatch distance (80 µm, 90 µm and 100 µm) in the Ti alloy matrix. On the contrary, Kinnear *et al.* (2016) tested *in-situ* alloy Ti6Al4V-xCu and found that homogeneous distribution of Cu in Ti6Al4V decrease with increasing hatch distance.

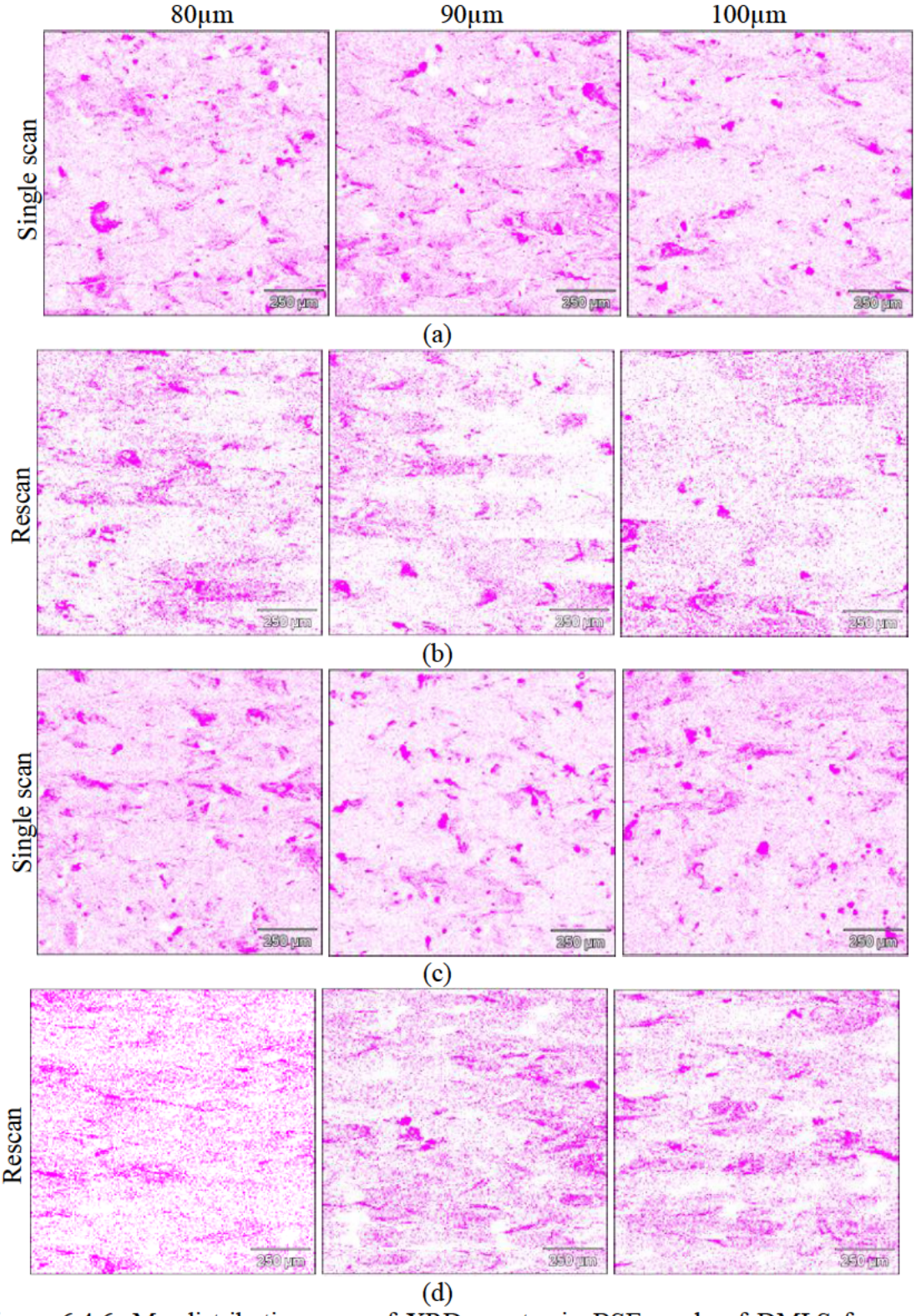

Figure 6.4.6: Mo distribution map of XRD spectra in BSE mode of DMLS from Ti15Mo *in-situ* alloy (a) single scan, (b) rescan at laser power 150 W, scanning speed 1.0 m/s and 80-100 µm hatch distances. (c) single scan, (d) rescan at laser power 350 W, scanning speed 2.4 m/s and 80-100 µm hatch distances.

It could be observed that no defects such as porosity, delamination of the layer, solidification cracks were present in both the single scan and rescan samples for all the process parameters. However, 150 W samples seem to be preferable. These specimens have the lowest surface roughness value and almost complete melting of Mo particles at the surface.

6.5: Microstructure and mechanical properties of *in-situ* alloyed DMLS Ti-15Mo samples

6.5.1: Microstructural Analysis

3D samples (cubes- Figure. 6.5.1a) were produced at laser power of 150 W and 350 W at scanning speeds of 1.0 m/s and 2.4 m/s respectively for microstructural analysis. Due to the layerwise (layer-by-layer) building process used by the DMLS technology the microstructure of DMLS build parts are different when viewed from different planes. A commonly used coordinate system is the scanning plane x-y and the built direction z (Figure. 6.5.1b). During the DMLS process, the individual scan tracks are formed in the scanning direction (Yadroitsev *et al.,* 2010; Yadroitsev *et al.,* 2015; Kruth *et al.,* 2010).

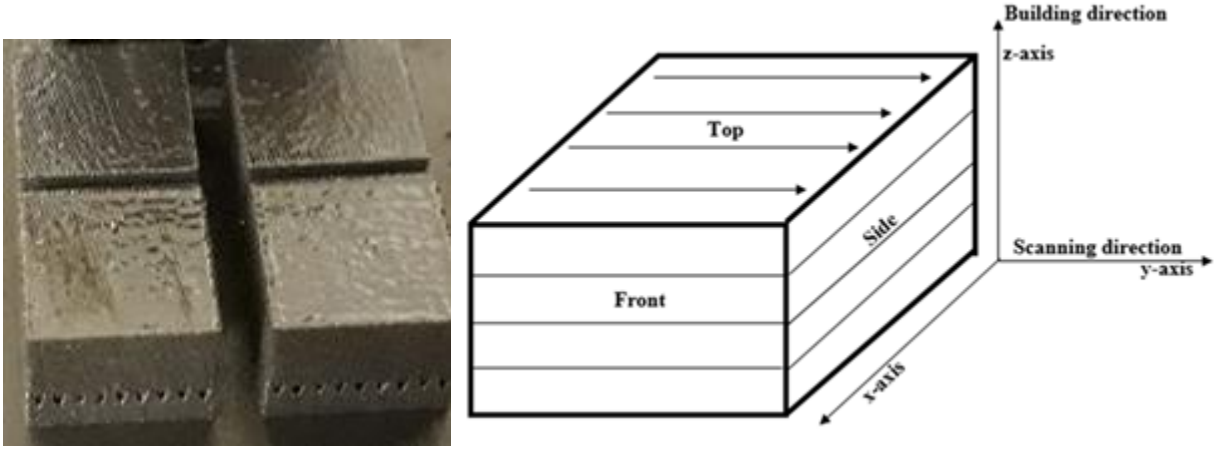

Figure 6.5.1: Cubes of Ti15Mo (a) and Scanning coordination system (b).

The directional variation in the microstructure of DMLS built parts is due to the very high rates of heating and cooling ($\sim 10^4 - 10^6$ ℃$/s$) (Roberts *et al.,* 2009; Brandl & Greitemeier, 2012) simultaneously along with the solidification mechanisms (Kruth *et al.,* 2010). It is also worth to mention that other scholars are of the view that the rate of heating and cooling during DMLS is still a matter of research (Yan & Yu, 2015).

The microstructures obtained in the current experiment generally consists of three distinct phases. With optical microscope photos it can be seen partially melted Mo particles, the gray and dark varying-contrast areas (Figure 6.5.2a–b). By SEM it was found that those grey areas represent the dissolved Mo in the Ti alloy matrix (Figures 6.5.2c–d). The white contrasting areas at BSE mode by SEM were found to be partially melted Mo particles. The concentration of Mo in grey areas (similar to the point A in Fig. 6.5.2d) was 7.5-16 wt%. Bright grey areas had higher concentration of Mo, it was 24.7wt% in the point B in Figure 6.5.2d, for example. The whole, observed average concentrations of Mo in the alloy correspond well to the α+β microstructures.

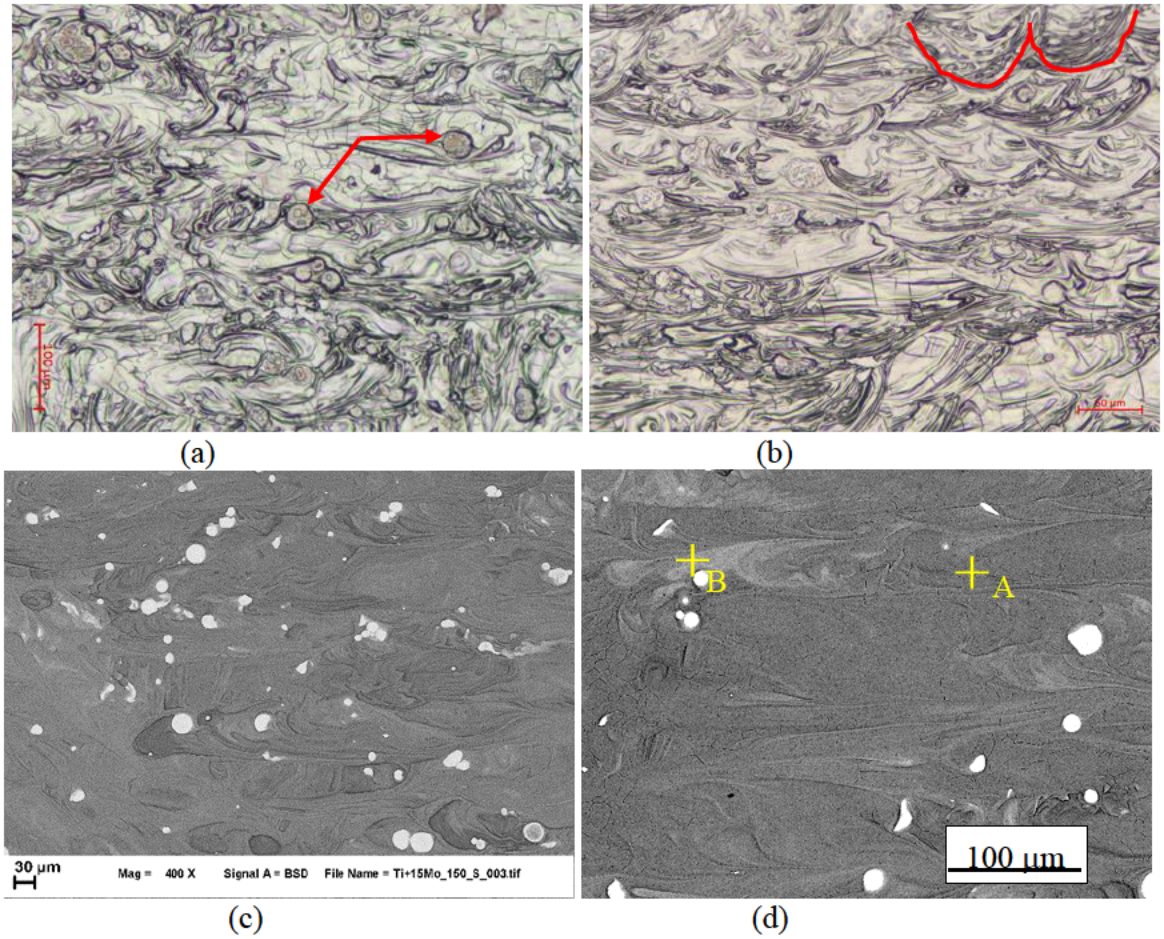

Figure 6.5.2: Ti15Mo microstructure produce at laser power of 150 W at speed of 1.0 m/s: (a) top view (unmelted Mo particles – red arrows) (b) side view, SEM image in BSE mode of top cross-section (c, d) (parabolic shape – red curves)

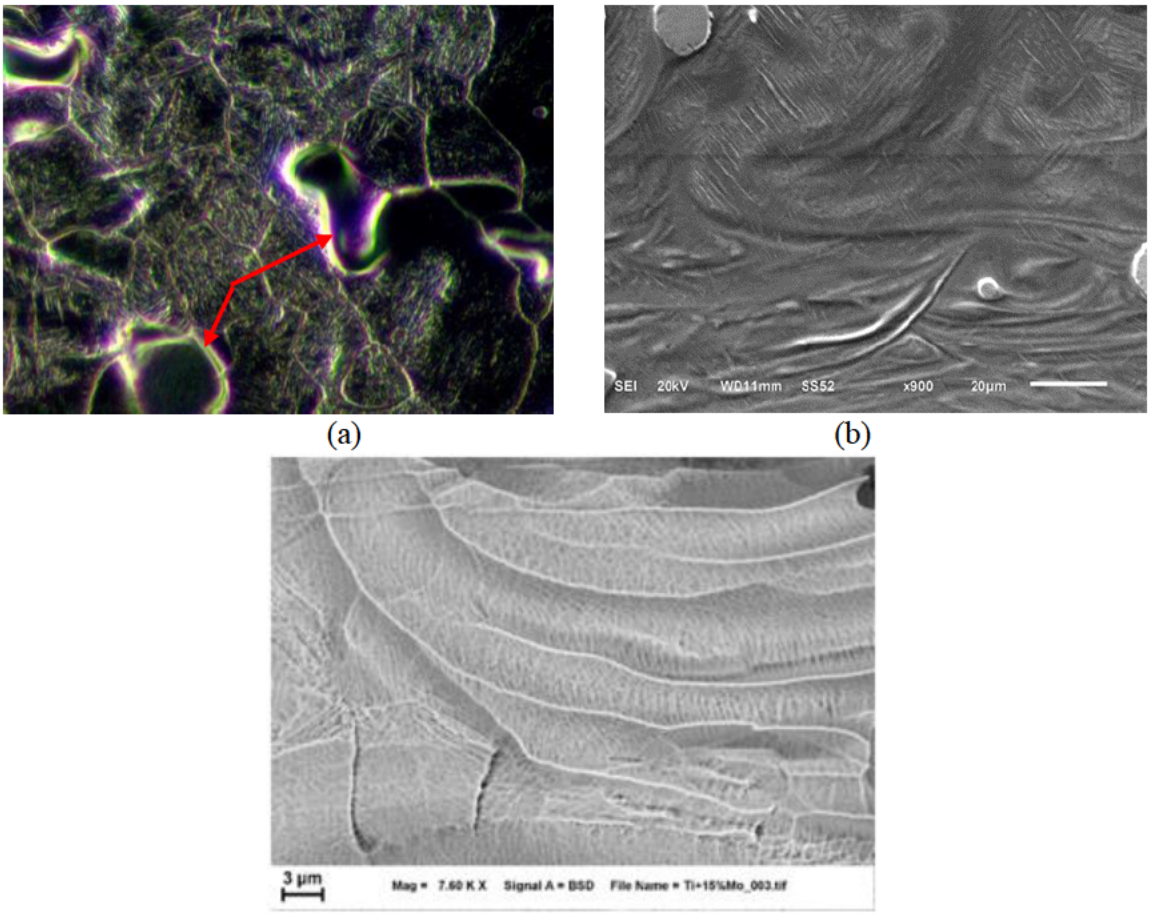

(a) (b)

(c)

Figure 6.5.3: Microstructure in dark field by optical microscope (a) (unmelted Mo particles – red arrows), SEM micrograph showing needles (b) and SEM micrograph showing cellular dendrite (c).

In the microstructure needles of fine acicular martensite inside the prior β grains of Ti alloy were found (Figure 6.5.3b) due to the high cooling rates during the DMLS process (Thijs *et al.,* 201021; Simonelli *et al.,* 2012). Regions of beta cubic phase also were formed as cellular dendritic structure during solidification (Figure 6.5.3c). A cellular dendritic structure was associated with Mo particles; it was confirmed by EDS higher concentration of Mo in these regions.

The microstructure demonstrates overlapping of subsequent scan tracks as a result of the optimum hatch distance and the selected scanning strategy employed. The overlapping edges are of curve shape from the side and front views (Figure 6.5.2b-c and Figure 6.5.3a) which signify the welding of each layer onto the layers that surround it. There were partially melted Mo particles distributed

randomly in the alloy matrix, observed from all the views (Figure 6.5.2-6.5.3). The distribution and mixing of the particles in the solidified melt pool could be related to convective flow in the liquid melt pool (Khairallah *et al.,* 2016). The Mo did not melt completely due to the difference in thermos-physical properties between the two materials. Mo has a melting point of 2623°C (AZO, 2015) while Ti has a melting point in the range of 1650-1670°C and thermal conductivity of Mo almost 7 times higher than that of pure Ti. Also the laser reflectance of Mo is higher than that of Ti. Ti would absorb more laser radiation than Mo (Lynch *et al.,* 1985). These difference in thermos-physical properties induce the partial melting of the Mo leading to the formation of Mo particle - Ti alloy matrix microstructure.

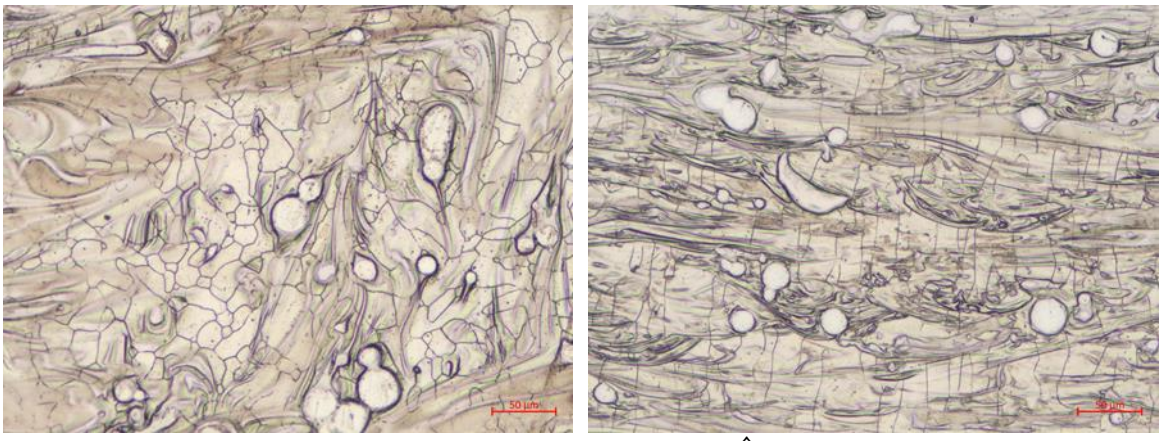

⊕ *building direction* ⇑ *building direction*

(a) (b)

Figure 6.5.4: Microstructure of Ti15Mo samples rescan at a laser power of 150 W at speed of 1.0 m-s: (a) top view (b) representing both side and front views.

The microstructure of samples produces at 350 W at scanning speed of 2.4 m/s (Figure 6.5.5) were similar to those of 150 W at a scanning speed of 1.0 m/s. However, there seems to be more unmelted Mo particle at laser power of 350 W than 150 W. This is due to the fact that at a high scanning speed, the dwelling time of the laser at a particular spot on the powder bed reduces (Manakari *et al.,* 2016). The relatively higher scanning speed of 2.4 m/s at 350 W implies an insufficient time for the laser beam to melt the Mo particles before propagating to the next spot. As a result of the shorter interaction times, fewer Mo particles were melted at the laser power of 350 W with the relatively high scanning speed of 2.4 m/s as compared to laser power of 150 W

with the slower scanning speed of 1.0 m/s. Becker *et al.* (2015) noted that the high scan speed minimises heat transfer.

From the current results it could be speculated that reducing the laser scanning speed could trigger complete melting of the Mo particles. But as pointed out by Yadroitsev *et al.* (2010) the DMLS process parameters are not linearly related, rather only a careful combination of the laser power and scanning speed that could yield optimum results.

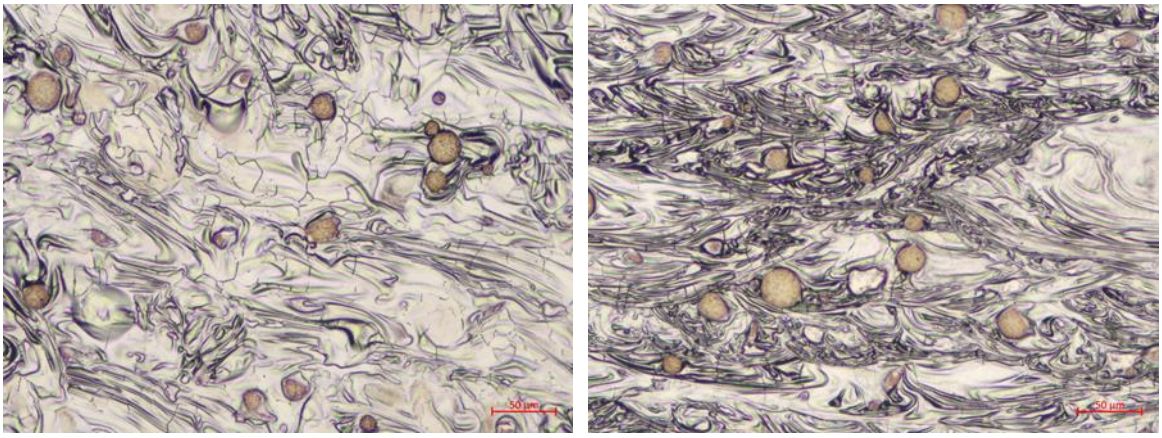

(a) (b)

Figure 6.5.5: Microstructure of Ti15Mo samples scan at a laser power of 350 W at speed of 2.4 m-s: (a) top view (b) representing side and front views.

6.5.1.1: Porosity

For all the different sets of samples produce at laser power of 150 W and 350 W pores were found in-between the solidified layers (x-y plane) (Figure 6.5.6). The location of the pores justified the assumption that the pores occur due to non-uniform powder delivery. During DMLS process when the surface of the previously solidified layer is uneven with deep valleys the next powder distribution would be uneven. The uneven powder deposition would lead to pore formation in-between the solidified layers known as interlayer porosity (Hofmeister & Griffith, 2001; Su *et al.*, 2003; Ahsan *et al.*, 2011). The interlayer pores are a detrimental feature in DMLS built parts as far as the mechanical properties and fatigue life of biomedical objects are concerned. The interlayer pores compromise structural integrity and contributes strongly to premature and unexpected structural failure of the parts (Wang, 2008).

Figure 6.5.6: Interlayer pores (white arrows) in the Ti15Mo microstructure.

6.5.2: Mechanical Properties Investigations

6.5.2.1: Microhardness Tests

The microhardness values of the front and side views of the as built Ti15Mo samples were determined in order to study the anisotropic behavior typically of DMLS build parts (Thijs *et al.,* 2010; Vrancken *et al.,* 2012; Vrancken *et al.,* 2014; Becker *et al.,* 2015). The Vickers's hardness numbers (VH) presented in Table 6.5.1 attest to the fact that DMLS build parts are not holistically homogenous throughout the bulk material. This is generally linked to the layer-wise building process and the direction of heat conduction. However, for the current experiment, the random distribution of partially melted Mo particles also contributed significantly to the varied microhardness values in the Ti15Mo material matrix.

Table 6.5.1: Microhardness values of Ti15Mo at both process parameters

Process parameters	Samples	Front (HV)	Side (HV)
150 W, 1.0 m/s	Single scan	426 ±37	441±40
	Rescan	439±32	443±45
350 W, 2.4 m/s	Singe scan	436±24	436±28
	Rescan	443±19	441±26

Nonetheless, taking the mean of the microhardness values for the scanned and rescanned samples gives almost the same results; 438 ± 36 for 150 W at a scanning speed of 1.0 m/s and 439 ± 24 for the 350 W at a scanning speed of 2.4 m/s. These values correlate with the result of Collins *et al.* (2003). They produced a compositionally graded structure of Ti-xMo (x= 0-25at.%) by laser engineered net-shaping (LENS™) and reported the highest microhardness value of 450 HV at 10wt.% Mo concentration and noted that the microhardness value of the samples reduces with increasing Mo content. Therefore, obtaining microhardness value of about 440 HV indicate a reduction in hardness with increase in Mo centration. The microhardness values recorded for the unmelted Mo particles randomly dispersed in the Ti15Mo alloy at laser power of 150 W and 350 W were almost the same (Figure 6.5.7).

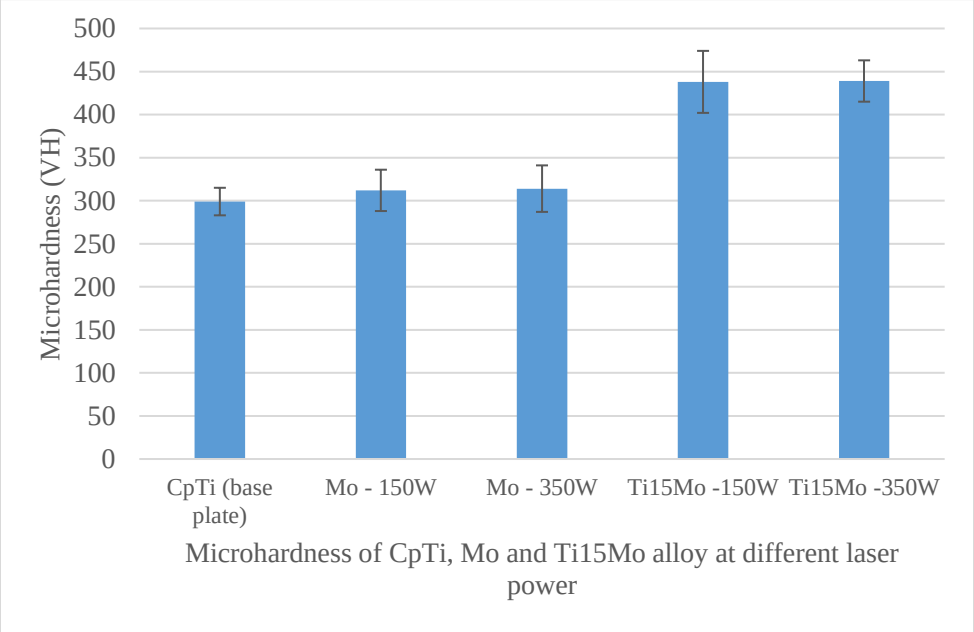

Figure 6.5.7: Microhardness of the base Cp Ti plate, and DMLS Mo and Ti15Mo alloy.

6.5.2.2: Tensile test

Based on the above detailed analysis samples (Figure 6.5.8) were produced at laser power of 150 W at a scanning speed of 1.0 m/s for tensile test analysis. The samples were rectangular in shape with 10 mm gauge length, 2 mm width and 1 mm thickness, which is described as mini sample (van Zyl *et al.*, 2016).

Figure 6.5.8: As-built Ti15Mo mini samples.

Five mini samples were investigated. The average ultimate tensile strength obtained for Ti15Mo mini sample was lower than that of Ti6Al4V mini sample reported by van Zyl *et al.* (2016), elongation at break for Ti15Mo was also lower than that of Ti6Al4V (Table 6.5.2). Though the DMLS process has a great freedom of design which makes it a prime choice for biomedical applications the fast rate of heating and cooling which lead to martensitic formation reduces the ductility of the material greatly, as in DMLS Ti6Al4V alloy. In present experiments, partially melted Mo particles were randomly distributed in Ti alloy. Inhomogeneity in sintered material and residual stress can decrease ductility.

Table 6.5.2: Comparison of tensile properties of Ti15Mo and Ti6Al4V mini-samples

Sample	UTS (MPa)	Elongation (%)	Microhardness (HV)	Roughness	
				Ra	*Rz*
Ti15Mo	894±24	2.8±1.7	441±2	21.27±0.6	123.50±3.94
Ti6Al4V van Zyl *et al.*, (2016)	1243±49	6.6±0.4	389±14.8	21.7±4.37	125.2±20.49

6.5.2.3: Fracture Analysis

The fracture surface and geometry of the fracture of a metal is dependent on the microstructure of the metal (Mandelbrot *et al.*, 1984). Generally, after a metal undergoes a tensile test the fracture surface is rough and irregular as in the case of Ti15Mo samples (Figure 6.5.10a). SEM analysis

reveals the occurrence of complex ductile/brittle fracture (Figure 6.5.9b) with brittle fracture predominance, which is attested to by the absence of gross necking before fracture (Figure 6.5.9).

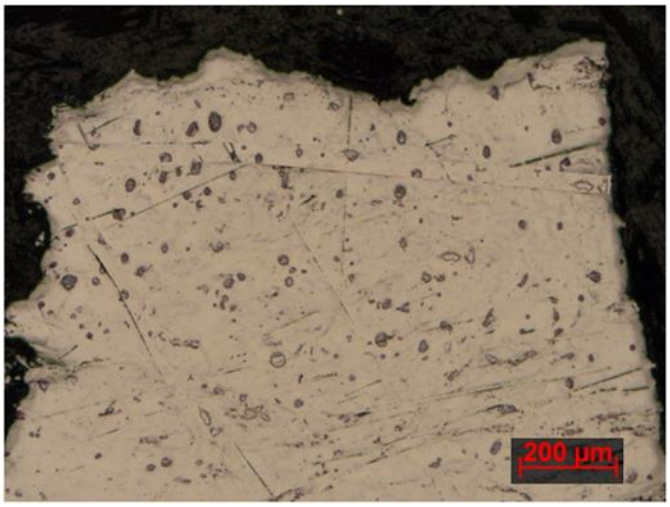

Figure 6.5.9: Optical image of tensile test specimen showing absence of gross necking before fracture.

The interior of Figure 6.5.10a reveals the predominance of brittle fracture. At a higher magnification (Figure 6.5.10b) there was evidence of areas of ductile tearing (quasi-cleavage fracture). This type of fracture is due to the occurrence of both ductile (dimples) and brittle fracture together on a single fracture surface (mixed mode). van Zyl *et al.* (2016) examined the fracture surface of Ti6Al4V mini sample produced by DMLS and observed ductile-brittle fracture with ductile predominance contrary to the brittle predominance observed for the Ti15Mo samples.

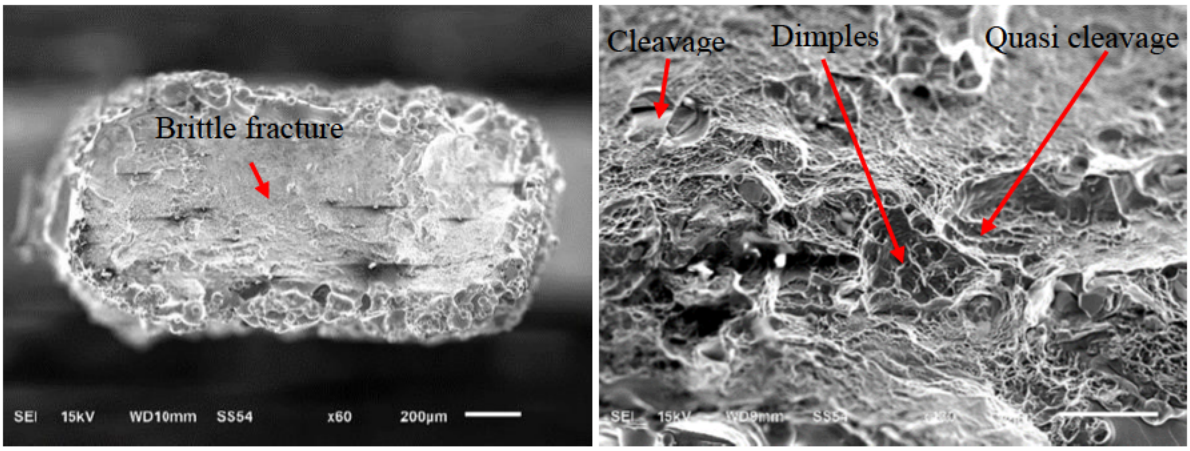

(a) (b)

Figure 6.5.10: SEM micrograph of fracture surface – total view (a) and fracture surface at higher magnification showing predominant brittle fracture with some cleavage features at fracture surface (b).

6.6: Summary

The chapter gave a vivid description of the underlining mechanisms of single tracks formation. The various process parameters that influence the molten pool and the solidification mechanisms were espoused. A process map was generated and optimum process parameters were determined after top and cross-sectional analysis of the DMLS single tracks was conducted. Single layers were formed and the optimum hatch distance was determined after surface roughness and the degree of Mo distribution in Ti was investigated. It was concluded that samples produced at the laser power of 150 W at a scanning speed of 1.0 m/s were of acceptable quality as compared to samples manufactured at a laser power of 350 W at a scanning speed of 2.4 m/s. 3D objects were manufactured for microstructural and mechanical properties analysis. The microstructural analysis reveals the presence of unmelted Mo particles in the β-Ti alloy matrix. The rescannig process did not have significant effect on the unmelted Mo particles. The ductility values of the experimental samples were below what is recommended for biomedical materials. The mechanical properties values defeat the ultimate aim of producing biomedical objects of high ductility for structural bearing implants in a single step by the DMLS process. This is due to the inherent high rate of cooling of the DMLS process which introduce significant amount of martensitic phase into the mini-sample. The martensite reduced the ductility of the samples significantly. However, post processing strategies such as heat treatment could still be employed to achieve this aim.

6.7: References

Aboulkhair, N. T., Maskery, I., Tuck, C., Ashcroft, I. & Everitt, N.M., 2016. On the formation of AlSi10Mg single tracks and layers in selective laser melting: Microstructure and nano-mechanical properties. *Journal of Materials Processing Technology*, 230, pp. 88-98.

Ahmed, T. & Rack, H., 1998. Phase transformations during cooling in α+ β titanium alloys. *Materials Science and Engineering: A,* 243(1), pp. 206-211.

Ahsan, M., Bradley, R. & Pinkerton, A., 2011. Microcomputed tomography analysis of intralayer porosity generation in laser direct metal deposition and its causes. *Journal of Laser Applications*, 23(2), p. 022009.

Allvac, A.T.I., 2004. *Ti-15Mo Beta Titanium Alloy*. Technical Data Sheet, ATI Allvac, Monroe, NC, 16.

ASM aerospace, 2016. ASM aerospace specification metals Inc. Available at: http://www.matweb.com [Accessed 28 May 2017].

AZO, 2015. AZO materials. Available at: http://www.azom.com [Accessed 28 May 2017].

Baufeld, B., Brandl, E. & Van der Biest, O., 2011. Wire based additive layer manufacturing: comparison of microstructure and mechanical properties of Ti–6Al–4V components fabricated by laser-beam deposition and shaped metal deposition. *Journal of Materials Processing Technology*, 211(6), pp. 1146-1158.

Becker, T., Van Rooyen, M. & Dimitrov, D., 2015. Heat treatment of Ti-6Al-4V produced by lasercusing. *South African Journal of Industrial Engineering,* 26(2), pp. 93-103.

Bergström, D., Powell, J. & Kaplan, A. F. H., 2007. A ray-tracing analysis of the absorption of light by smooth and rough metal surfaces. *Journal of Applied Physics*, 101(11), pp. 113504.

Brandl, E. & Greitemeier, D., 2012. Microstructure of additive layer manufactured Ti–6Al–4V after exceptional post heat treatments. *Materials Letters,* 81, pp. 84-87.

Bowen, A. 1971. Omega phase embrittlement in aged Ti-15% Mo. *Scripta Metallurgica*, 5(8), pp. 709-715.

Chan, C. L., Mazumder, J. & Chen, M. M., 1987. Three-dimensional axisymmetric model for convection in laser-melted pools. *Materials Science and Technology*, 3(4), pp. 306-311.

Chandrasekar, S., 1961. *Hydrodynamic and Hydromagnetic Stability*. New York: Clarendon Press, Oxford.

Childs, T. H. C., Hauser, C. & Badrossamay, M., 2004. Mapping and modelling single scan track formation in direct metal selective laser melting. *CIRP Annals-Manufacturing Technology,* 53(1), pp. 191-194.

Collins, P., Banerjee, R., Banerjee, S. & Fraser, H., 2003. Laser deposition of compositionally graded titanium–vanadium and titanium–molybdenum alloys. *Materials Science and Engineering: A*, 352(1), pp. 118-128.

Das, S., 2003. Physical aspects of process control in selective laser sintering of metals. *Advanced Engineering Materials,* 5(10), pp. 701-711.

Duleba, B., Greškovič, F. & Sikora, J. W., 2011. Materials and Finishing Methods of DMLS Manufactured Parts. *Transfer Inovácií*, 21, pp. 143-148.

Dzogbewu, T.C, Yadroitsev, I, Krakhmalev, P, Yadroitsava, I & Du Plessis, A. 2017. Optimal process parameters for *in-situ* alloyed Ti15Mo structures by Direct Metal Laser Sintering, *Proceedings of the 28th Annual International Solid Freeform Fabrication Symposium,* Austin Texas, August 7-9, 2017. (In press)

Eagar, T. W. & Tsai, N. S., 1983. Temperature fields produced by traveling distributed heat sources. *Welding Journal*, 62(12), pp. 346-355.

EOS, 2014. EOS Titanium Ti64. EOS GmbH - Electro Optical Systems.

Fay, J. A., 1994. *Introduction to fluid mechanics, 2nd Edition*. Cambridge: MIT press.

Fischer, P., Romano, V., Weber, H.P., Karapatis, N.P., Boillat, E. & Glardon, R., 2003. Sintering of commercially pure titanium powder with a Nd: YAG laser source. *Acta Materialia,* 51(6), pp. 1651-1662.

Gharbi, M., Peyre, P., Gorny, C., Carin, M., Morville, S., Le Masson, P., Carron, D. and Fabbro, R., 2013. Influence of various process conditions on surface finishes induced by the direct metal deposition laser technique on a Ti-6Al-4V alloy. *Journal of Materials Processing Technology*, 213(5), pp. 791-800

Gusarov, A. V. & Smurov, I., 2010. Modeling the interaction of laser radiation with powder bed at selective laser melting. *Physics Procedia,* 5, pp. 381-394.

Hann, D. B., Iammi, J. & Folkes, J., 2011. A simple methodology for predicting laser-weld properties from material and laser parameters. *Journal of Physics D: Applied Physics*, 44(44), p. 445401.

Ho, W.F., Ju, C.P. & Lin, J.C. 1999. Structure and properties of cast binary Ti–Mo alloys, *Biomaterials*, 20(22), pp. 2115-2122

Hofmeister, W. & Griffith, M., 2001. Solidification in direct metal deposition by LENS processing. *Journal of the Minerals, Metals and Materials Society*, 53(9), pp. 30-34.

Huang, Q., Hu, N., Yang, X., Zhang, R. and Feng, Q., 2016. Microstructure and inclusion of Ti–6Al–4V fabricated by selective laser melting. *Frontiers of Materials Science*, pp. 1-4.

Islam, M., Taimisto, L., Piili, H., Salminen, A. & Nyrhilä, O., 2012. Evaluation of effect of heat input in laser assisted additive manufacturing of stainless steel. *In Proceedings of the 37th International MATADOR Conference*. Manchester.

Keene, B. J., 1993. Review of data for the surface tension of pure metals. *International Materials Reviews*, 38(4), pp. 157-192.

Khairallah, S. A. & Anderson, A., 2014. Mesoscopic simulation model of selective laser melting of stainless steel powder. *Journal of Materials Processing Technology*, 214(11), pp. 2627-2636.

Khairallah, S. A., Anderson, A. T., Rubenchik, A. & King, W. E., 2016. Laser powder-bed fusion additive manufacturing: Physics of complex melt flow and formation mechanisms of pores, spatter, and denudation zones. *Acta Materialia*, 108, pp. 36-45.

King, W. E., Barth, H.D., Castillo, V.M., Gallegos, G.F., Gibbs, J.W., Hahn, D.E., Kamath, C. & Rubenchik, A.M., 2014. Observation of keyhole-mode laser melting in laser powder-bed fusion additive manufacturing. *Journal of Materials Processing Technology*, 214(12), pp. 2915-2925.

Kinnear, A., Dzogbewu, T. C., Yadroitsava, I. & Yadroitsev, I., 2016. *In-situ* alloying process of Ti6Al4V-xCu structures by direct metal laser sintering. *Proceedings of the 17th International conference Rapid Product Development Association of South Africa,* 2-4 November 2016, Vaal University of Technology Vanderbijlpark, South Africa.

Klassen, A. & Carolin, K., 2014. Modelling of electron beam absorption in complex geometries. *Journal of Physics D: Applied Physics*, 47(6), pp. 065307.

Körner, C., Attar, E. & Heinl, P., 2011. Mesoscopic simulation of selective beam melting processes. *Journal of Materials Processing Technology*, 211(6), pp. 978-987.

Körner, C., Bauereiß, A. & Attar, E., 2013. Fundamental consolidation mechanisms during selective beam melting of powders. *Modelling and Simulation in Materials Science and Engineering*, 21(8), pp. 085011.

Kou, S., Limmaneevichitr, C. & Wei, P. S., 2011. Oscillatory Marangoni flow: a fundamental study by conduction-mode laser spot welding. *Welding Journal*, 90(12), pp. 229-240.

Krehl, P. O., 2008. *History of shock waves, explosions and impact: a chronological and biographical reference.* Berlin Heidelberg: Springer Science & Business Media.

Król, M., Kujawa, M., Dobrzański, L. A. & Tański, T., 2014. Influence of technological parameters on additive manufacturing steel parts in Selective Laser Sintering. *Archives of Materials Science and Engineering*, 67(2), pp. 84-92.

Kruth, J. P., Badrossamay, M., Yasa, E., Deckers, J., Thijs, L. & Van Humbeeck, J., 2010. Part and material properties in selective laser melting of metals. *In Proceedings of the 16th international symposium on electromachining.*

Kruth, J. P., Mercelis, P., Van Vaerenbergh, J., Froyen, L. & Rombouts, M., 2005. Binding mechanisms in selective laser sintering and selective laser melting. *Rapid Prototyping Journal*, 11(1), pp. 26-36.

Kruth, J. P., Yasa, E. & Deckers, J., 2009. Experimental investigation of laser surface re-melting for the improvement of selective laser melting process. *In Proceedings of Solid Free Fabrication Symposium*, Austin, Texas.

Lee, Y. S. & Zhang, W., 2015. Mesoscopic Simulation of Heat Transfer and Fluid Flow in Laser Powder Bed Additive Manufacturing. *In International Solid Free Form Fabrication Symposium*, Austin, Texas.

Longhitano, G. A., Larosa, M.A., Munhoz, A.L.J., Zavaglia, C.A.D.C. & Ierardi, M.C.F., 2015. Surface Finishes for Ti-6Al-4V Alloy Produced by Direct Metal Laser Sintering. *Materials Research*, 18(4), pp. 838-842.

Lu, S., Fujii, H. & Nogi, K., 2004. Marangoni convection and weld shape variations in Ar–O 2 and Ar–CO 2 shielded GTA welding. *Materials science and engineering: A*, 380(1), pp. 290-297.

Lynch, D., Hunter, W. & Palik, E., 1985. *Handbook of optical constants of solids*. Orlando: Academic press.

Maisonneuve, J., Colin, C. & Aubry, P., 2007. Profile Project: direct manufacturing of aerospace components by laser cladding and laser sintering. *In Icaleo'2007 Conference*, Scottsdale, USA.

Manakari, V., Parande, G. & Gupta, M., 2016. Selective Laser Melting of Magnesium and Magnesium Alloy Powders: A Review. *Metals*, 7(1), p. 2.

Mandelbrot, B.B., Passoja, D.E. & Paullay, A.J. 1984. Fractal character of fracture surfaces of metals, Nature, 308(5961), pp. 721-722.

Matilainen, V. P., Piili, H., Salminen, A. & Nyrhilä, O., 2015. Preliminary investigation of keyhole phenomena during single layer fabrication in laser additive manufacturing of stainless steel. *Physics Procedia*, 78, pp. 377-387.

Mondal, A., Shukla A., Upadhyaya A. & Agrawal D., 2010. Effect of porosity and particle size on microwave heating of copper. *Science of Sintering*, 42(2), pp.169-182.

Mumtaz, K. & Hopkinson, N., 2010. Selective laser melting of Inconel 625 using pulse shaping. *Rapid Prototyping Journal*, 16(4), pp. 248-257.

Palik, E. D., 1985. *Handbook of optical constants of solids (Vol. 1-3).* Maryland: Academic press.

Qiu, C., Panwisawas, C., Ward, M., Basoalto, H.C., Brooks, J.W. & Attallah, M.M., 2015. On the role of melt flow into the surface structure and porosity development during selective laser melting. *Acta Materialia*, 96, pp. 72-79.

Rai, R., Elmer, J. W., Palmer, T. A. & DebRoy, T., 2007. Heat transfer and fluid flow during keyhole mode laser welding of tantalum, Ti–6Al–4V, 304L stainless steel and vanadium. *Journal of Physics D: Applied Physics*, 40(18), pp. 5753.

Rayleigh, L., 1892. On the instability of a cylinder of viscous liquid under capillary force. *The London, Edinburgh, and Dublin Philosophical Magazine and Journal of Science*, 34(207), pp. 145-154.

Rehme, O., Schwarze, D. & Emmelmann, C., 2006. Selective laser melting of customized implants with cellular surface structures for optimized elasticity and imporved osseointegration. *In procedding of Rapid Production Development 2006 Modulus Events Conference.* Marinha Grande, Portuga.

Roberts, I.A., Wang, C.J., Esterlein, R., Stanford, M. and Mynors, D.J., 2009. A three-dimensional finite element analysis of the temperature field during laser melting of metal powders in additive layer manufacturing. *International Journal of Machine Tools and Manufacture*, 49(12), pp. 916-923.

Sames, W. J., List, F.A., Pannala, S., Dehoff, R.R. & Babu, S.S., 2016. The metallurgy and processing science of metal additive manufacturing. *International Materials Reviews*, 61(5), pp.315-360.

Simchi, A. & Asgharzadeh, H., 2004. Densification and microstructural evaluation during laser sintering of M2 high speed steel powder. *Materials Science and Technology*, 20(11), pp. 1462-1468.

Simonelli, M., Tse, Y. & Tuck, C., 2012. Further understanding of Ti-6Al-4V selective laser melting using texture analysis. *In Proceedings of 23rd Annual International Solid Freeform Fabrication Symposium, Austin, Texas.*

Simonelli, M., Tse, Y. & Tuck, C., 2012. Microstructure of Ti-6Al-4V produced by selective laser melting. *Journal of Physics*, 371(1), p. 012084.

Spears, T. G. & Gold, S. A., 2016. In-process sensing in selective laser melting (SLM) additive manufacturing. *Integrating Materials and Manufacturing Innovation*, 5(1), pp. 1-25.

Su, W., Erasenthiran, P. & Dickens, P., 2003. Investigation of fully dense laser sintering of tool steel powder using a pulsed Nd: YAG (neodymium-doped yttrium aluminium garnet) laser. *Journal of Mechanical Engineering Science*, 217(1), pp. 127-138.

Tam, D., von Arnim, V. O., McKinley, G. H. & Hosoi, A. E., 2009. Marangoni convection in droplets on superhydrophobic surfaces. *Journal of Fluid Mechanics*, 624, pp. 101-123.

Thijs, L., Verhaeghe, F., Craeghs, T., Van Humbeeck, J. and Kruth, J.P., 2010. A study of the microstructural evolution during selective laser melting of Ti–6Al–4V. *Acta Materialia*, 58(9), pp. 3303-3312.

van Zyl, I., Moletsane, M., Krakhmalev, P., Yadroitsava, I. & Yadroitsev, I. 2016. Validation of miniaturised tensile testing on DMLS TI6AL4V (ELI) specimens, *South African Journal of Industrial Engineering*, 27(3), pp. 192-200.

Verhaeghe, F., Craeghs, T., Heulens, J. & Pandelaers, L., 2009. A pragmatic model for selective laser melting with evaporation. *Acta Materialia*, 57(20), pp. 6006-6012.

Vrancken, B., Cain, V., Knutsen, R. & Van Humbeeck, J., 2014. Residual stress via the contour method in compact tension specimens produced via selective laser melting. *Scripta Materialia*, 87, pp. 29-32.

Vrancken, B., Thijs, L., Kruth, J. P. & Van Humbeeck, J., 2014. Microstructure and mechanical properties of a novel β titanium metallic composite by selective laser melting. *Acta Materialia*, 68, pp. 150-158.

Vrancken, B., Thijs, L., Kruth, J. P. & Van Humbeeck, J., 2012. Heat treatment of Ti6Al4V produced by Selective Laser Melting: Microstructure and mechanical properties. *Journal of Alloys and Compounds*, 541, pp. 177-185.

Wang, Y., 2008. *Mechanical properties and microstructure of laser sintered and starch consolidated iron-based powders*. Doctoral dissertation: Karlstads universitet.

Xie, F., He, X., Lv, Y., Wu, M., He, X. & Qu, X. 2015. Selective laser sintered porous Ti–(4–10) Mo alloys for biomedical applications: Structural characteristics, Mechanical properties and corrosion behaviour. *Corrosion Science*, 95, pp. 117-124

Yadroitsau, I., 2009. *Selective laser melting: Direct manufacturing of 3D-objects by selective laser melting of metal powders*. Saarbrucken: LAP Lambert Academic Publishing AG & Co. KG.

Yadroitsava, I., Els, J., Booysen, G. & Yadroitsev, I., 2015. Peculiarities of single track formation from TI6AL4V alloy at different laser power densities by selective laser melting. *South African Journal of Industrial Engineering*, 26(3), pp. 86-95.

Yadroitsev, I., Bertrand, P. & Smurov, I., 2007. Parametric analysis of the selective laser melting process. *Applied Surface Science*, 253(19), pp. 8064-8069.

Yadroitsev, I., Gusarov, A., Yadroitsava, I. & Smurov, I., 2010. Single track formation in selective laser melting of metal powders. *Journal of Materials Processing Technology*, 210(12), pp. 1624-1631.

Yadroitsev, I., Krakhmalev, P. & Yadroitsava, I., 2015. Hierarchical design principles of selective laser melting for high quality metallic objects. *Additive Manufacturing*, 7, pp. 45-56.

Yadroitsev, I., Krakhmalev, P., Yadroitsava, I., Johansson, S. & Smurov, I., 2013. Energy input effect on morphology and microstructure of selective laser melting single track from metallic powder. *Journal of Materials Processing Technology*, 213(4), pp. 606-613.

Yadroitsev, I., Yadroitsava, I., Bertrand, P. & Smurov, I., 2012. Factor analysis of selective laser melting process parameters and geometrical characteristics of synthesized single tracks. *Rapid Prototyping Journal*, 3(18), pp. 201-208.

Yan, M. & Yu, P., 2015. An Overview of Densification, Microstructure and Mechanical Property of Additively Manufactured Ti-6Al-4V—Comparison among Selective Laser Melting, Electron Beam Melting, Laser Metal Deposition and Selective Laser Sintering, and with Conventional Powder. *In Sintering Techniques of Materials. InTech.*

Yang, J., Han, J., Yu, H., Yin, J., Gao, M., Wang, Z. & Zeng, X., 2016. Role of molten pool mode on formability, microstructure and mechanical properties of selective laser melted Ti-6Al-4V alloy. *Materials & Design*, 110, pp. 558-570.

Yasa, E. & Kruth, J. P., 2008. Experimental study of the combined process of selective laser melting and selective laser erosion. *In Proceedings of the RAPID 2008 Conference & Exposition*.

Zinoviev, A., Zinovieva, O., Ploshikhin, V., Romanova, V. and Balokhonov, R., 2016. Evolution of grain structure during laser additive manufacturing. Simulation by a cellular automata method. *Materials & Design*, 106, pp. 321-329.

CHAPTER 7: *IN-SITU* ALLOYING OF Ti6Al4V-xCu STRUCTURES BY DMLS

7.1: Introduction

The medical industry has successfully utilized the layer-by-layer nature of DMLS to manufacture complex shapes from biocompatible materials to produce implants using CAD geometry based on Computer Tomography scan data. Ti6Al4V Extra Low Interstitials (ELI) is a commonly used biomaterial because of its suitable mechanical and biocompatible properties (Niinomi, 2008). Infection at the bone–implant interface is the most probable reason for implant failure directly after implantation (Geetha *et al.*, 2009). Coating the interface with materials that have antibacterial properties is a promising approach to infection prevention. Material such as silver, zinc and copper have shown such antibacterial properties. Though medication helps to cure infection, antibacterial materials are more efficient as they act locally and continuously at the site of infection. Copper is a proven antibacterial agent and in small amounts is not toxic to the human body (Nan *et al.*, 2008). Implants can be constructed to have a biocompatible Ti6Al4V structure with Cu additions at the bone–implant interface to reduce the risk of bacterial infection and implant failure.

Jung *et al.* (2014) electrochemically deposited small amounts of Cu onto Ti discs to show the effect of Cu as an antibacterial agent. After 10 days of exposure to the Cu, bacteria such as Escherichia coli (E. coli) and Staphylococcus aureus (S. aureus) experienced a dramatic decrease in growth. Demonstrating that antibacterial functionalization of Ti implants by Cu also was suggested by Shirai *et al.* (2009) which used Ti-Cu alloy as an anti-bacterial implant interface. It was indicated that 1% Cu addition retained the samples biocompatibility and inhibited the growth of bacterial microbes.

In a pilot study by Kinnear *et al.* (2015) was compared *in-situ* alloyed Ti6Al4V-1at.%Cu surface and a surface that had Cu areas on a Ti6Al4V substrate so that the surface contains 1% Cu by means of surface area.. Results showed that the *in-situ* alloyed Ti6Al4V-1at.%Cu surface was more efficient at inhibiting the growth of E. coli and S. aureus. Scanning Electron Microscope (SEM) and Energy Dispersive X-ray Spectroscope (EDS) analysis showed that the *in-situ* alloyed Ti6Al4V-1%Cu surface had inhomogeneous surface composition (Figure 7.1.1a) and high surface

roughness of 54.4±3.94 µm (Figure 7.1.2b). The current study aims to optimize the layer formation of *in-situ* alloyed Ti6Al4V-1at.%Cu.

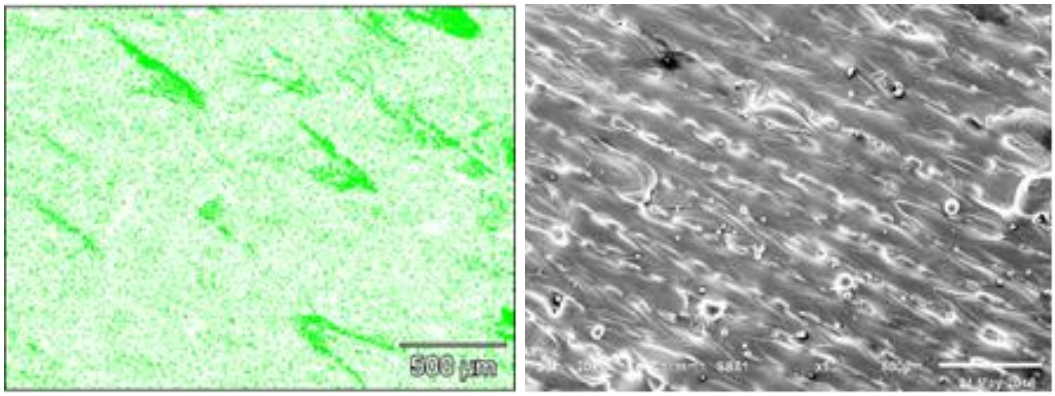

(a) (b)

Figure 7.1.1: *In-situ* alloyed Ti6Al4V-1at.%Cu: (a) EDS mapping of Cu and (b) SEM of top view.

In-situ alloying allows for the manipulation of microstructures, producing material with superior properties and facilitating easier processing of certain materials by adding alloying elements. *In-situ* DMLS alloying from elemental powders would be a cost and time effective means to produce a wide range of alloy compositions. Vrancken *et al.* (2004) highlighted the capabilities of DMLS to *in-situ* processing of powder mixtures Ti6Al4V-ELI and 10 wt.% Mo powders. Krakhmalev & Yadroitsev (2014) showed that an increase in laser power or a re-melting strategy are effective methods of improving homogeneity of Ti and SiC alloying. Fischer *et al.* (2016) produced Ti–26Nb alloy by DMLS of elemental titanium and niobium mixed powders, noting that energy input has a significant effect on porosity and homogeneity of the produced part. Dadbakhsh & Hao (2014) formed an Al/5 wt.%Fe2O3 alloy by *in-situ* DMLS, noting that the layer thickness had a strong influence on the microstructural outcome.

7.2: Experimental Procedure

To produce the Ti6Al4V-1 at.`%Cu (1.38 wt%) powder alloy 1.36 g of Cu powder is mixed with 98.64 g of Ti6Al4V(ELI) (Extra Low Interstitials) powder and mixed for 1 hour.

To determine the effect of hatch distance and scanning speed on surface quality and homogeneity of the alloy, sintered single layers (4.5 mm x 12 mm) were manufactured by EOSINT M280

machine. Laser power was kept constant at 170 W and spot size was about 80 µm. Three intervals of scanning speed (0.7 m/s, 1.0 m/s and 1.3 m/s) and four values of hatch distance (70 µm, 80 µm, 90 µm and 100 µm) were applied.

To investigate distribution of elements in the bulk, 3D disc specimens of 10 mm in diameter and 5 mm in height were fabricated. Manufacturing was done at 170 W, 0.7 m/s and 80 µm hatch distance process parameters, layer thickness was 30 µm.

The metallography examination was conducted according to the recommended protocols discussed in Chapter 3. Determination of chemical composition at the surface and 3D specimens was dome by means of scanning electron microscopy at 20 kV accelerating voltage with JEOL JSM-6610 scanning electron microscope with Thermo Scientific Ultradry energy-dispersive spectrometer and, LEO 1350 FEG-SEM equipped with Oxford Instruments INCAx-sight EDX detector.

7.3: Results and Discussion

To investigate DMLS single layers manufactured at different hatch distance, images from SEM and cross-sections of the layers were analysed. Defects such as porosity, delamination of layer and solidification cracks have not been found in DMLS single layers before and after rescanning. At chosen process parameters, laser power density which is the ratio of laser power to the laser beam spot area, was constant. For 60 µm layer thickness and chosen process parameters, total average remelted depth was about 60 µm for single layers sintered at different hatch distances (Figure 7.3.2a). Roughness of the surfaces is shown in Table 7.3.1.

Table 7.3.1: Roughness of DMLS surfaces

Hatch distance	70 µm		80 µm		90 µm		100 µm	
	R_a	R_z	R_a	R_z	R_a	R_z	R_a	R_z
Scanning speed	Single scan							
0.7 m/s	4.6±0.66	24.9±2.43	5.1±0.05	33.5±4.44	6.6±0.7	37.5±1.8	7.4±0.39	46.2±1.53
1.0 m/s	6.4±0.63	38.7±0.57	7.1±0.63	41.5±2.7	7.99±0.98	43.9±1.94	8.6±0.24	51.1±3.2
1.3 m/s	6.9±0.81	38.2±0.64	7.4±0.68	44.7±4.38	8.3±0.55	51.2±1.83	9.4±0.33	54.4±3.94
Rescanning								
0.7 m/s	4.4±0.1	24.8±1.12	5.4±0.7	26.5±2.74	6.4±0.31	36.1±1.29	7.3±1.24	40.3±4.4
1.0 m/s	5.9±0.86	35.6±2.22	6.3±0.92	35.7±0.59	7.3±1.39	40.3±2.18	7.5±0.48	50.5±1.39
1.3 m/s	6.8±0.3	37±1.05	7.4±0.46	37.4±1.83	9.4±0.45	50.4±4.8	9.3±1.04	51. 3±5.1

The surface roughness increased with an increase in hatch distance and scanning speed. More satellites were observed at the surface manufactured at higher scanning speeds and hatch distances which dramatically decreased the surface quality. Rescanning removed the satellites from the surfaces. Rescanning showed some improvement of the surface quality. This was expected due to the fact that the single tracks where rescanned on the same position as the previous tracks (Figure 7.3.1). Further rescanning strategies need to be investigated to further improve the surface quality of *in-situ* DMLS alloying.

Investigation of homogeneity distribution of Cu in Ti6Al4V near the surface at various scanning speed (0.7-1.3 m/s) and hatch distances (70-100 µm) was performed by analysis of an EDS elemental maps. For a single scan at 0.7 m/s scanning speed and 70 µm hatch distance, the surface composition was homogeneous. An increase in scanning speed and hatch distance resulted in a decrease in surface homogeneity. Rescanning had a profound effect on the surface homogeneity (Figure 7.3.3). The rescanning strategy removed the segregation of copper that formed at the peripheries of the single tracks. Similarly, to single scan, at rescanning the Cu inhomogeneity increased with scanning speed and hatch distance. An increase in input energy has a positive effect on surface homogeneity. A rescanning strategy provides an effective means to improving the surface homogeneity.

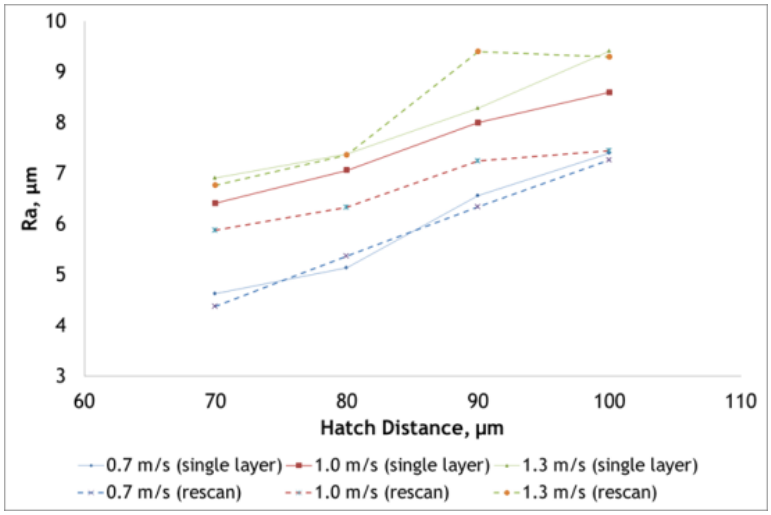

(a)

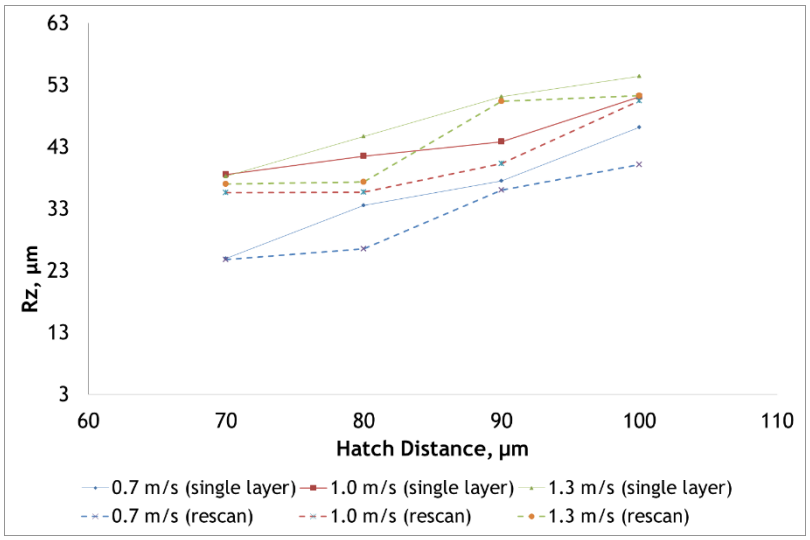

(b)

Figure 7.3.1: Surface roughness of *in-situ* alloyed Ti6Al4V-1 at.%Cu at laser power 170 W, scanning speed 0.7-1.3 m/s and 70-100 µm hatch distances for a single layer

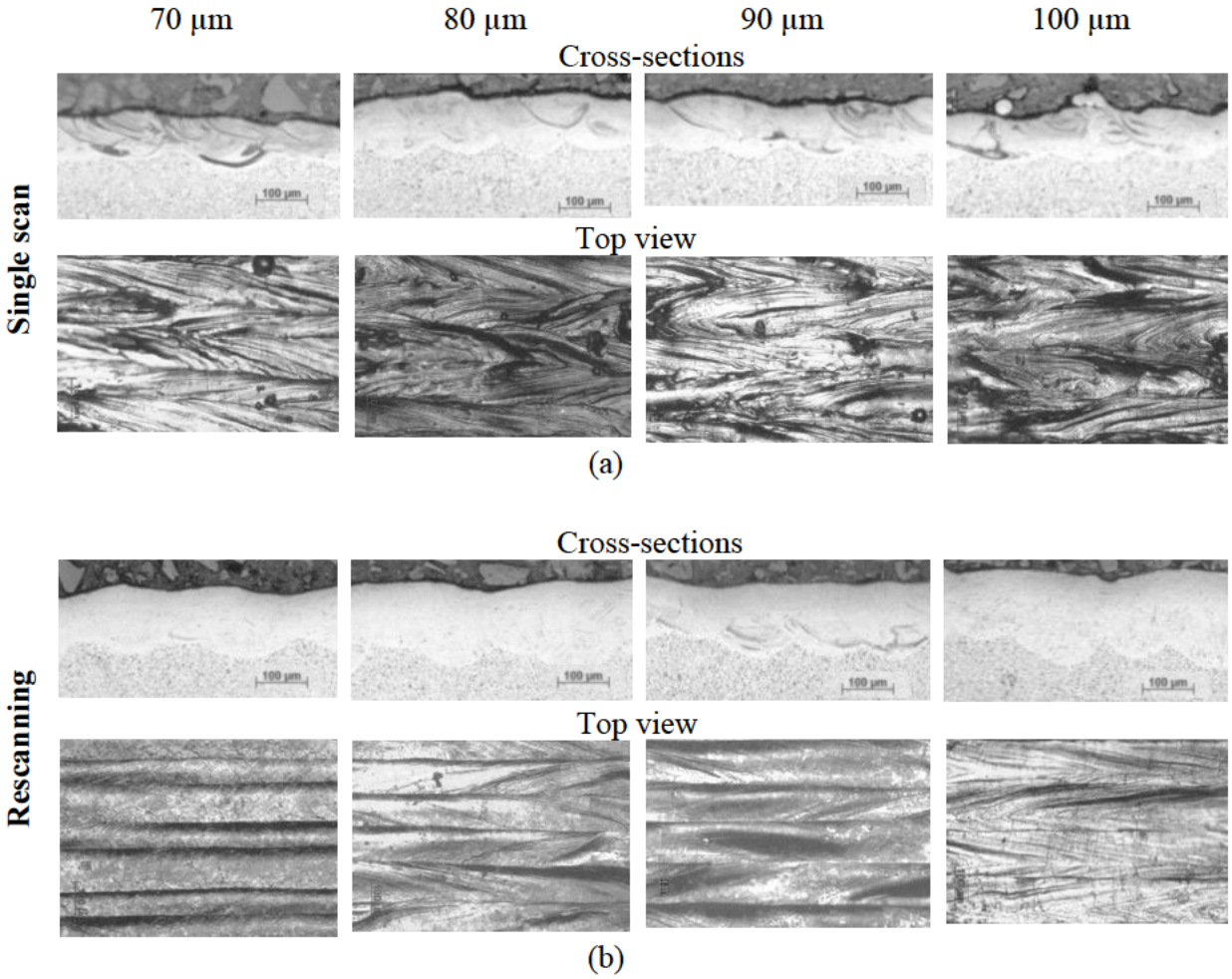

Figure 7.3.2:. Cross-sections and top view of DMLS surfaces from mixture Ti6Al4V (ELI) and 1 at.% Cu at laser power 170 W, scanning speed 1.0 m/s and 70-100 µm hatch distances: (a) single scan, (b) after rescanning.

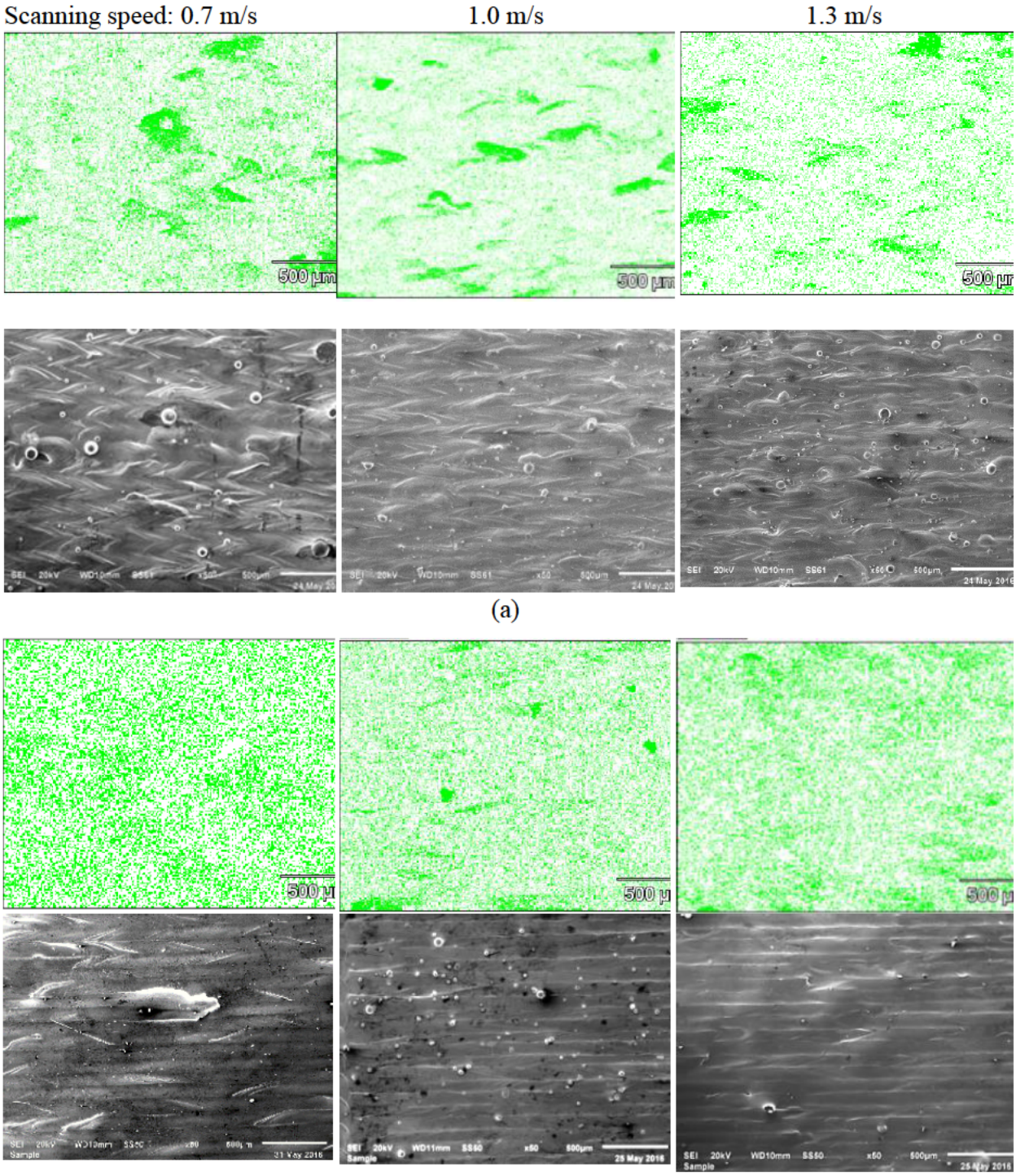

Figure 7.3.3: Cu distribution map by XRD spectra and top view photos in SE mode of DMLS surfaces from mixture Ti6Al4V (ELI) and 1 at.% Cu at laser power 170 W, scanning speeds 0.7-1.3 m/s and 90 µm hatch distances: (a) single scan, (b) after rescanning.

In Figure 7.3.4 the surface composition of Cu (%wt) for *in-situ* Ti6Al4V-Cu alloyed layers is shown. For a single exposure at 0.7 m/s scanning speed and 70 µm hatch distance the surface composition was 1.05% Cu, and 2.31% for at scanning speed and hatch distance of 1.3 m/s and 100 µm, respectively. With an increase in scanning speed and hatch distance, the surface composition of Cu increased.

Rescanning improved the surface Cu concentration of the *in-situ* alloyed layer. This difference in of surface concentration is the result to the vast difference in the material properties of Ti6Al4V and Cu. Ti6Al4V and Cu have a specific heat capacity 560 J/kg/K and 387 J/kg/K, thermal conductivity; 7.2 W/m/K and 401 W/m/K, density; 4430 kg/m/3 and 8940 kg/m/3, melting temperature of 1649°C and 1083°C respectively and viscosity in liquid state 5 mPa×s and 4.75 mPa×s. When the powder is exposed to the laser beam, the powder mixture melts. However, due to the rapid solidification of the DMLS process Cu could not uniformly distribute in the molten pool before it solidifies. Better results of surface homogeneity and surface composition were obtained at higher energy inputs because the Cu has more time to alloy the Ti6Al4V before the molten pool solidifies. Rescanning dramatically improves the surface homogeneity because the molten pool is completely re-melted. At 0.7 m/s scanning speed and 70 µm hatch distance there is sufficient input energy and overlapping of single tracks to exhibit similar surface homogeneity.

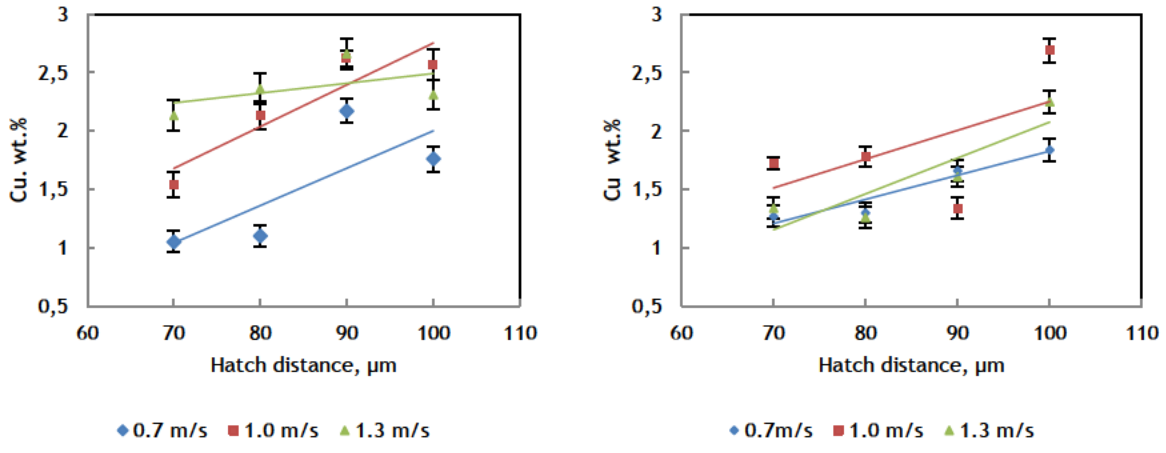

(a) (b)

Figure 7.3.4: Average wt.% of Cu near the DMLS surface of Ti6Al4V+1at%Cu powder at different scanning speeds and hatch distances: single scan (a) and rescanning (b).

7.4: Microstructure and Mechanical Properties

Observed effects of energy input on homogeneity and a deviation of surface concentration of the Ti6Al4V-1%Cu alloy could be explained taking into account vast difference in the material properties of Ti alloy and Cu. Estimated time of direct interaction laser beam–powder under laser spot size is tD.I.=d0/V, where d0 is laser beam spot size and V is scanning speed. For 80 μm spot size and scanning speed *V*=0.7–1.3 m/s, time of laser-powder direct interaction is 114–61.5 μs. Ti6Al4V and Cu have a latent heat of fusion of 370 and 205 kJ/kg. Taking into account latent heat of melting, heat capacity and density, energy for melting of unit volume of employed material can be estimated. For bulk Cu and Ti6Al4V, this values are close: 5.49 J/mm^3 and 5.67 J/mm^3 respectively. Homogenization time calculated as ratio of squared powder particle radius to the thermal diffusivity of a bulk metal is about 40 times higher for Cu than for the Ti6Al4V. For 37 μm powder particle, the time of homogenization of Cu particle is 3 μs and 106 μs in case of similar size of Ti6Al4V powder particle. It can be assumed that thin high-reflective Cu film will shield the laser radiation.

Distribution of Cu in the bulk *in-situ* alloyed DMLS material was investigated with SEM EDS on cross-sections of 3D specimens manufactured of the same initial powder mixture. Investigations have shown that Cu is quite well dissolved in the Ti alloy, although some areas enriched with Cu were observed.

Figure 7.4.2 illustrates distribution of Cu in the bulk. It is seen that Cu-rich areas have characteristic shapes, which can easily be associated with molten pool boundaries. Microstructure in these areas also differed from the regular surrounding structures. Regular microstructure has typical for martensite needle-like structure, commonly observed in Ti6Al4V manufactured by DMLS (Thijs *et al.*, 2010; Yadroitsava & Yadroitsev, 2015; Becker *et al.*, 2015). Cu-rich regions could be divided into two groups, in one structure is also martensitic, in the others rather dendritic (Figure 7.4.2).

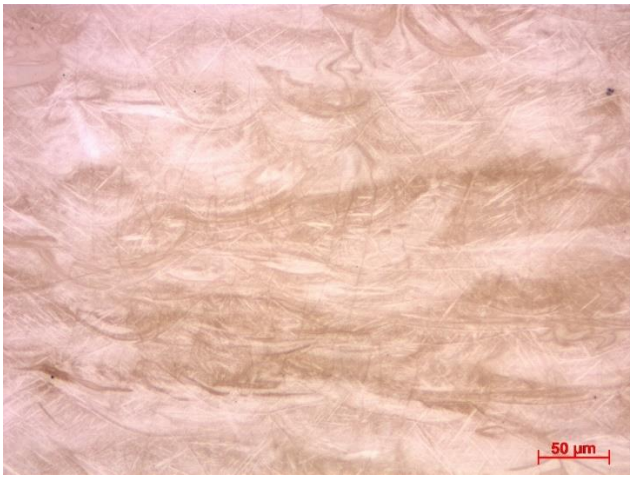

Figure 7.4.1: Optical photo of DMLS Ti6Al4V–1at.% Cu disc fabricated at laser power 150 W, 0.7 m/s and hatch distance of 80 µm.

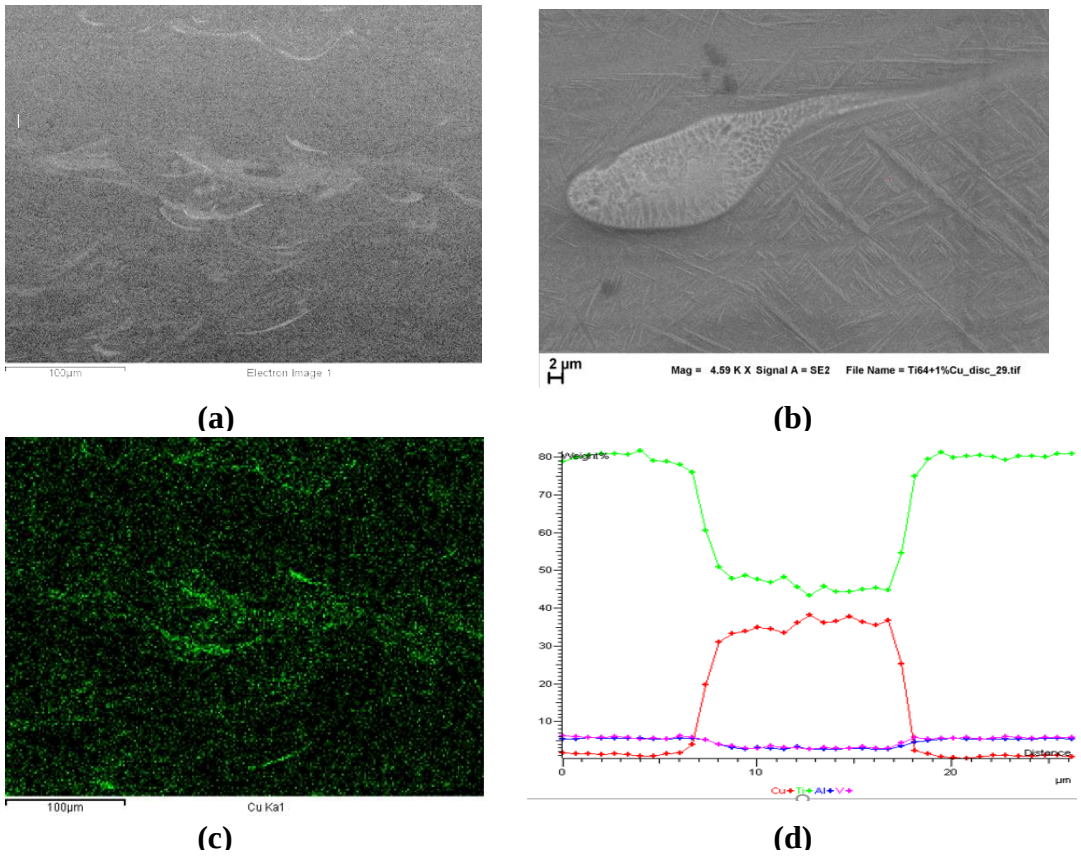

Figure 7.4.2: Cu distribution map by XRD spectra (a) EBSD image, (b) Cu EDS map, (c) SE illustration of typical microstructures and, (d) elemental concentration of Ti, Al, V and Cu in the Cu-rich area

EDS analysis of chemical composition of areas with different microstructures showed that regular martensitic structure is not pure Ti6Al4V, but a material alloyed with Cu. Cu content in these areas varied in range of 1–1.5%. This concentration is quite close to the nominal concentration of pure Cu powder in the initial powder mixture. In the areas enriched with Cu but still having martensitic structure, even within one single area, concentration of Cu varied remarkably between 2 and 5 wt%. Highest concentration of Cu, up to 35 wt% was observed in areas that have different microstructure. Nevertheless, it is possible to conclude that these areas are not unmolten particles of pure Cu, as concentration of Ti in those areas is high (Figure 7.4.2d.)

Cu is well-known as a beta stabilizer in titanium. Therefore, it is possible that in the areas with highest concentration of Cu, high-temperature beta Ti phase is formed. This statement, nevertheless, has to be proven in the future by experimental investigations and phase identification. A microhardness value of 455.60 HV was measured.

7.5: Summary

In-situ alloying of Ti6Al4V (ELI) and 1at.% Cu powder was successfully performed utilizing DMLS. Produced single layers exhibited no signs of porosity, delamination, or solidification cracks. The surface quality of the produced layers was improved with a decrease in scanning speed and hatch distance.

The applied rescanning strategy removed surface satellite particles, improving the surface quality. Surface homogeneity was achieved by an increase in input energy.

Rescanning had a profound improvement on surface homogeneity and surface composition; this is attributed to the complete re-melting of the single layer. It can be concluded that the surface quality and homogeneity of *in-situ* alloyed Ti6Al4V-1at.%Cu can be improved by decreasing the scanning speed and hatch distance, within the optimal process window, or applying the rescanning strategy.

In the bulk state some inhomogenieties also observed. Areas of enhanced Cu concentrations are associated with fusion boundaries. Enrichment with Cu differs from area to area, nevertheless,

surrounding material contains about 1at% Cu which indicated, although incomplete but sufficient allotting of Ti6Al4V with Cu *in-situ* at DMLS of powder mixtures.

7.6: References

Bergström, D., Powell, J. & Kaplan, A. H., 2007. A ray-tracing analysis of the absorption of light by smooth and rough metal surfaces. *Journal of Applied Physics*, 101(11), pp. 113504-113511.

Becker, T., van Rooyen, M. & Dimitrov, D., 2015. Heat treatment of Ti-6Al-4V produced by lasercusing. *South African Journal of Industrial Engineering*, 26(2), pp. 93-103.

Dadbakhsh, S. & Hao, L., 2014. Effect of layer thickness in selective laser melting on microstructure of Al/5 wt.% Fe2O3 powder consolidated parts. *The Scientific World Journal*, 2014(6), pp.106129.

Fischer, M., Joguet, D., Robin, G., Peltier, L. & Laheurte, P., 2016. *In-situ* elaboration of a binary Ti–26Nb alloy by selective laser melting of elemental titanium and niobium mixed powders. *Materials Science and Engineering*, 62, pp. 852-859.

Geetha, M., Singh, A. K., Asokamani, R. & Gogia, A. K., 2009. Ti based biomaterials, the ultimate choice for orthopaedic implants–a review. *Progress in Materials Science*, 54(3), pp. 397–425.

Gharbi, M., Peyre, P., Gorny, C., Carin, M., Morville, S., Le Masson, P., Carron, D. & Fabbro, R., 2013. Influence of various process conditions on surface finishes induced by the direct metal deposition laser technique on a Ti-6Al-4V alloy. *Journal of Materials Processing Technology*, 213(5), pp. 791-800.

Jung, C., Straumann, L., Kessler, A., Pieles, U. & de Wild, M., 2014. Antibacterial copper deposited onto and into the oxide layer of titanium implants. *BioNanoMat*, 15, pp. S180.

Kinnear, A. W., 2015. *Direct metal laser sintering of multiple material structures for biomedical applications*. Master's thesis. Central University of Technology, Free State, South Africa.

Krakhmalev, P. & Yadroitsev, I., 2014. Microstructure and properties of intermetallic composite coatings fabricated by selective laser melting of Ti–SiC powder mixtures. *Intermetallics*, 46, pp. 147-155.

Nan, L., Yang, W.C., Liu, Y.Q., Xu, H., Li, Y., Lu, M.Q. & Yang, K., 2008. Antibacterial mechanism of copper-bearing antibacterial stainless steel against E. coli. *Journal of Materials Science and Technology*, 24(2), pp. 197–201.

Niinomi, M., 2008. Mechanical biocompatibilities of titanium alloys for biomedical applications. *Journal of the Mechanical Behavior of Biomedical Materials*, 1(1), pp.30-42.

Shirai, T., Tsuchiya, H., Shimizu, T., Ohtani, K., Zen, Y. & Tomita, K., 2009. Prevention of pin tract infection with titanium-copper alloys. *Journal of Biomedical Materials Research Part B: Applied Biomaterials,* 91(1), pp. 373-380.

Thijs, L., Verhaeghe, F., Craeghs, T., Van Humbeeck, J. & Kruth, J.P., 2010. A study of the microstructural evolution during selective laser melting of Ti–6Al–4V. *Acta Materialia*, 58(9), pp. 3303-3312.

Vrancken, B., Thijs, L., Kruth, J. P. & Van Humbeeck, J., 2014. Microstructure and mechanical properties of a novel β titanium metallic composite by selective laser melting. *Acta Materialia*, 68, pp. 150-158.

Yadroitsava, I., Els, J., Booysen, G. & Yadroitsev, I., 2015. Peculiarities of single track formation from TI6AL4V alloy at different laser power densities by SLM. *The South African Journal of Industrial Engineering*, 26(3), pp. 86-95.

Yadroitsev, I., 2009. *Selective laser melting: direct manufacturing of 3D-objectsby selective laser melting of metal powders.* Saarbrucken: LAP Lambert Academic Publishing AG & Co. KG.

Yadroitsava, I. & Yadroitsev, I., 2015. Residual Stress in Metal Specimens Produced by Direct Metal Laser Sintering. *In Proceedings of the SFF Symposium*, Austin, TX, USA (pp. 10-12).

Yadroitsev, I., Yadroitsava, I., Bertrand, P. H. & Smurov, I., 2012. Factor analysis of selective laser melting process parameters and geometrical characteristics of synthesized single tracks. *Rapid Prototyping Journal,* 18(3), pp. 201-208.

CHAPTER 8: CONCLUSIONS AND FUTURE WORKS

8.1: Conclusions

The experimental procedures and design were carefully constituted and a series of experiment were carried out to understand the intricate laser-powder interactions that control and influence the melting process of the metallic powder. Single tracks and single layers were produced and optimum process parameters were determined. 3D objects were produced and their mechanical properties were investigated to make sure that they are suitable for biomedical applications. FEA analysis was also conducted to obtain a foreknowledge of the biomechanical behaviour of various graded/gradient implant design for a specific biomedical application. The various numerical and experimental investigations and their respective contributions are elucidated below:

8.1.1: Finite Element Analysis (FEA)

The use of numerical simulation as a feasible alternative for predicting the response of bone under a variety of loading conditions have made biomechanics and orthopedic research more robotic and repeatable with great accuracy. In the current study (chapter 4), FEA was used to predict the biomechanical behaviour of different grade/gradient mandible CAD model implant designs. The models were designed taking into consideration the geometry and anatomical (biomechanics) characteristics of a human mandible. The material properties that were used to defined the CAD models were selected based on the natural (biomimetic) properties of human mandible. Half of the symmetric mandible bone was used in the simulation to reduce computational time. The principles of mastication were meticulously followed in setting the boundary conditions for the simulation. The simulation results indicated that implants with low Elastic modulus in the range of bone are much desirable for the replacement of a damaged hard tissue. The stress distribution between the implant and the bone was more uniform when the supposed implants have a similar mechanical property like that of the bone. It was recognized that for bone-implant contact interlocking and avoiding of the stress shielding effect, replacing a damaged part of a mandible with a relatively lower Elastic modulus would probably prevent implant failure since the stress/strain induced by the mastication forces are most likely to be distributed uniformly. An advanced lightweight mandible implant was proposed based on each patient specific functional requirements of the damaged bone.

Contributions

- Using FEA to envisage how stresses would be transferred between the implant and the bone interface and selection of the appropriate mechanical properties for implants would greatly prevent trial-and-error methods and implant failure.
- Demonstrating the capability of cellular structures as a potential candidate for biomedical applications.
- Reinforcing the idea of producing graded/gradient structures (biomimetic) for biomedical applications.
- Providing a solution to implant failure (due to the stress shielding effect, bone resorption, and implant loosening) which would contribute to better quality of life for implant patients.

8.1.2: Cellular Structures

The potential material saving combined with multi-functionalities of cellular structures makes them suitable for biomedical applications. It was found that the manufacturability (by DMLS) and mechanical properties of the cellular structure are greatly influenced by the cellular topology (i.e. cell shape, cell size, and percentage of volume fraction). Attached powder particles and micropores less than 20 µm were visible in the analyzed cross-sections of the cellular structures. Ti6Al4V ELI stress-relieved cellular structures had stable mechanical properties when loading was applied co-axially to the building direction. The mechanical properties of the structures increase with an increase in volume fraction of the strut. Compressive tests showed that the proposed DMLS cellular structures are suitable for fabrication of light-weight implants because their mechanical properties are close to the properties of human bone. There was no change in the microstructure of the cellular structures after stress-relieving heat treatment.

Contributions

- Demonstrate the possibility of using DMLS technology to manufacture cellular structures with controlled cell sizes.
- Provide the type of nodes and strut size which could yield optimum mechanical properties for biomedical applications.

- Provide a refined method for mechanically testing of cellular structures by putting a thin layer of dense material on the top and bottom of the cellular structures to ensure even distribution of the loading throughout the whole material before fracture.

8.1.3: DMLS Process Parameters for *in-situ* alloying

The top surface analysis reveals that some of the tracks were continuous whiles others were discontinuing (pre-balling and balling effect). It was observed that the molten pool dives (laser spatter) onto the powder bed and form droplets (satellites) at the edge of the tracks. It was noted that the number of satellites was much higher at a lower laser power at similar energy input. For each selected laser power and the corresponding scanning speeds, pre-balling or balling effects begins at higher scanning speeds due to a reduction in linear energy density at a higher scanning speed at the same laser power. For almost all the selected process parameters under investigation, the single tracks formation starts from optimum (conduction mode), then proceeds to pre-balling and the subsequent balling effect. The widths of the tracks also decrease as the scanning speed increase at the same laser power.

The plates were cross-sectioned to determine the extent of the re-melted depth (penetration depth) and the height of the tracks. The penetration depth increase with increasing laser power and decrease with increasing scanning speed. The heights of the tracks were irregular which was attributed to inhomogeneous deposition of powder layer and melt hydrodynamics. It was also observed that if the combination of the processing parameters exceeds a certain threshold the mode of thermal conduction in the molten pool could change to the so-called keyhole mode. As opposed to most previous experiments there were no pores in the keyhole mode conduction in the current experiments.

After the top surface and cross-sectional examination, optimum process parameters were determined for Ti15Mo and Ti6Al4V+1a t.%Cu. The optimum process parameters values were used to produce single layers for both alloys. It was generally observed that surface roughness increase with increasing hatch distance. Rescanning strategy was found to improve the surface quality of the samples. An EDS elemental map analysis also reveals that rescanning strategy improves the surface homogeneity and composition of the solute elements in the master alloy.

Contributions

- Provide a methodology for determining optimum process parameters for Ti15Mo and Ti6Al4V+1at.%Cu. The procedure could be used to determined optimum process parameters for other alloys.
- The *in-situ* alloying strategy of different powder mixtures would broaden the material database of DMLS technology.

Specific contributions for Ti15Mo

- A high laser energy input $\Delta H/h_s$ >70 leads to V-shape molten pool deep penetration and the probability of the keyhole mode is very high for Ti alloys.
- The most preferred optimum process parameters are laser power of 150 W and 350 W with a corresponding scanning speed of 1.0 m/s and 2.4 m/s.
- Hatch distance of 80 µm would produce the best surface quality, homogeneity, and composition of the bulk material (Ti15Mo).

Specific constructions for Ti6Al4V+1%Cu

- The most preferred optimum process parameters for Ti6Al4V+1%Cu are laser power of 170 W at a scanning speed of 0.7 m/s.
- Hatch distance of 70 µm would be optimal hatch distance.

8.1.4: Microstructure and Mechanical Properties of Ti15Mo and Ti6Al4V+1%Cu

Due to the difference in thermophysical properties between Ti and Mo, there were unmelted Mo particles distributed randomly in the Ti alloy material matrix. Rescanned strategy was applied to melt the unmelted Mo particles, but no significance change was observed in the volume fraction of the unmelted Mo particles after the rescanned process.

The microhardness investigation reveals the anisotropic nature of DMLS samples. From all the surfaces investigated the microhardness values varied considerable. However, the unmelted particles aggravate the anisotropic behaviour of the bulk Ti15Mo alloy material. The ductility obtained (2.8±1.7%) was below what was recommended for biomedical applications. The martensitic phase due to the high rates of heating and cooling was responsible for the low ductility. The ultimate tensile strength (UTS) for the as-built DMLS Ti15Mo mini-samples was lower than Ti6Al4V DMLS samples: 894±23.6 MPa and 1243±49 MPa respectively. The fracture surface analysis demonstrated mixed fracture mode.

For the current experiment, it was obvious from the microstructure examination that copper dissolves quite well in Ti-alloy with pockets of copper-enriched areas. The copper-rich areas have characteristic shapes, which can easily be associated with molten pool boundaries. The copper-rich areas present two distinct microstructures – martensitic and dendritic microstructures which are different from the typical martensite needle-like structure for Ti6AL4V alloy. The composition of copper in the martensitic region of the microstructure ranges from 1-1.5% of Cu which is very close to the nominal concentration of pure Cu powder in the initial powder mixture. The copper-enriched part of the microstructures demonstrates disparate composition of copper between 2-5%. The areas with the highest concentration of Cu up to 35 wt% had a different microstructure, however, it was concluded that these areas are not unmolten particles of pure Cu.

8.1.5: Biomedical Applications

The DMLS process used in this study has demonstrated the capability of manufacturing 3D objects for biomedical applications. Optimum process parameters were determined for the selected alloys which were used to manufacture 3D objects. Complex shapes such as cellular structures with thin struts size were successfully manufactured. The procedure could be used to manufacture implants with intricate shape with internal configurations characterize close to that of bone structures. Manufacturing biomimetic structures such as cellular structures with tailored mechanical properties by varying strut size would serve the analogous function of epiphysis and metaphysis found in the human limbs. As simulated by the FEA, low Elastic moduli implant in the range of bone properties would aid the homogenous load transferred stress stimulation of the bone which would enhance osseointegration. Implants could be manufactured with tailored properties with different metallic powders for specific functional requirement of a damaged body parts. The addition of copper to the Ti-based alloys would definitely enhance the antibacterial properties of the material matrix. Alloying with Cu was successful and therefore there are promising ways to manufacture materials with embedded antibacterial properties. Issues of delamination of the antibacterial coating from the metal matrix, faster rate of elution of the incorporated drugs, relatively low drug concentration at the target site, inability to produce coatings that can load and release enough bactericides in a controllable fashion throughout the lifetime of the implant, would be completely avoided by *in-situ* alloying with the DMLS technology.

8.1.6: Verification of the Research Objectives

The research objectives that triggered the current studies are enumerated below with the possible solutions arrived at after the intensive numerical and experimental engagement.

1. ***To identify Ti alloys for the fabrication of the various implants by DMLS***

Two major titanium alloys were identified in the current studies – Ti15Mo and Ti6Al4V+1at.%Cu. The novelty lies in using DMLS to *in-situ* alloy the various powder mixture. Systematic experimental procedures were followed to determined optimum process parameters at which these metal mixtures could be *in-situ* alloy by DMLS to obtained the required mechanical properties for biomedical applications. Chapters 6 and 7 gave a vivid description of the *in-situ* alloying process of the identified alloys for biomedical applications.

2. ***To simulate suitability of using cellular structures mechanical properties for implants and to compare numerical simulation with experimental data.***

The suitability of using cellular structures for biomedical applications was demonstrated by the FEA analysis of the mandibular CAD model in the fourth chapter, which was experimental proven in the fifth chapter of the studies. It came to light that using the inherent capabilities of lightweight, material saving, structural bearing nature of cellular structures as demonstrated by nature would lead to the production of advanced lightweight implants with high strength.

3. ***To produce by DMLS non-porous and lattice structured samples***

The production of the cellular structures in the fifth chapter demonstrate the capabilities of using the DMLS technology to manufacture intricate thin walls (~1 mm) for biomedical applications. The micropores found in the cross-sections of the cellular structures were less than 20 µm. Biomimetic non-porous structures could easily be manufactured with the DMLS technology.

4. ***To study microstructure and mechanical properties of DMLS samples***

The later part of Chapters Six and Seven of the studies were devoted to microstructural and mechanical properties of the alloys produced by DMLS. It was identified that the microstructure of the alloys (Ti15Mo and Ti6Al4V+1%Cu) were different from the typical martensite needle-like

structure which is normally obtained for Ti6Al4V alloy manufactured by DMLS. The ductility of the alloy (Ti15Mo) was found to be below what was recommended for biomedical applications. The ultimate tensile strength value obtained for the as-built DMLS Ti15Mo mini-samples was similar as recommended for the conventional Ti15Mo α/β alloy.

5. ***To suggest ways for the development of the next generational implants with add-value functionality by DMLS***

The study aims to suggest ways for the development of the future generation implants with add-value functionality by DMLS. 3D objects of cellular structures, cubes, and tensile test piece which were manufactured, clearly demonstrate that any complex shape of implants could be manufactured by the DMLS technology. The principal objective of producing samples from titanium alloys and establishing a relationship between the process parameters, microstructure and mechanical properties for biomedical applications has been perfectly demonstrated.

8.2: Future Work

The research has discussed many important issues, of prime importance is the variation of the DMLS processing parameters to produce particular microstructure/mechanical properties during the rapid melting/sintering and solidification process. The fundamental studies of the intricate laser-matter interactions of the powder bed reveal that the principal processing parameters such as laser power, scanning speed, laser spot diameter, etc. determined the final microstructure/ mechanical properties of DMLS build parts. However, the current researcher had limited access to changing machine parameters such as laser spot size independently due to safety issues. As a result, the process parameters that were investigated were manipulated within the permissible range set by the machine manufacturer.

For the lattice structures, the effects of powder particle size and distribution on the manufacturability of cellular structures by DMLS should be considered in future studies. Simulation of the cellular structures itself to understand the stress distribution/transfer within the lattice should be investigated. A comprehensive future study about regenerative properties of tissue cells on the selected cellular structures (selected nodes, shapes and strut size) in this study should be conducted.

The cellular structures studies in this current research did not involve support structures. A future study involving support structures and the effects of removing the support structures on the mechanical properties and surface roughness of the cellular structures is important. Such a study would enhance the designing of delicate geometrical objects for biomedical applications. The zig-zag scanning strategy is used in the current studies. Investigating optimum scanning strategies for cellular structures could be considered in future studies.

In the current study, the compressive strength test was conducted in a uniaxial direction along the building direction of the cellular structures. A further investigation with respect to different loading direction is required to completely understand the behaviour of cellular structures for biomedical application under different loading directions in the human body.

The current research focused on tensile and microhardness mechanical properties of the DMLS Ti-based alloys. Further work to establish the fatigue life and crack growth resistance is very crucial. Studying how the non-conventional microstructure of DMLS build parts influences the initiation and growth of fatigue cracks would give a comprehensive understanding about mechanical properties of the selected alloys under investigation.

In-situ alloying was found to be an efficient way to manufacture new materials, nevertheless, to manufacture homogeneous alloy was a challenge. For efficient *in-situ* DMLS alloying processes, not only laser power and scanning speed should be optimized. Powder properties (size, shape, flowability, surface area, porosity, impurity content etc.) should also be optimised in order to guarantee efficient melting and intermixing of both materials. In the present investigations, sizes of the powder particles are too large especially for the Mo particles, which contributed to the incomplete melting of Mo powder particles. A future investigation with smaller power particle size (~10 μm) is recommended.